Punching strength of continuous flat slabs

THÈSE N^{O} 6928 (2016)

PRÉSENTÉE LE 11 MARS 2016

À LA FACULTÉ DE L'ENVIRONNEMENT NATUREL, ARCHITECTURAL ET CONSTRUIT
LABORATOIRE DE CONSTRUCTION EN BÉTON
PROGRAMME DOCTORAL EN GÉNIE CIVIL ET ENVIRONNEMENT

ÉCOLE POLYTECHNIQUE FÉDÉRALE DE LAUSANNE

POUR L'OBTENTION DU GRADE DE DOCTEUR ÈS SCIENCES

PAR

Jürgen EINPAUL

acceptée sur proposition du jury:

Prof. N. Geroliminis, président du jury
Prof. A. Muttoni, Dr M. Fernández Ruiz, directeurs de thèse
Prof. R. Vollum, rapporteur
Prof. A. Pinho Ramos, rapporteur
Prof. J.-F. Molinari, rapporteur

ÉCOLE POLYTECHNIQUE
FÉDÉRALE DE LAUSANNE
Suisse
2016

Foreword

The punching design of flat slabs has traditionally been performed in design codes on the basis of the properties of the slab-column connection (such as the size of supported area or the amount of moment transfer) as well as those of the slab in the vicinity of the supported area (such as the reinforcement ratio or the utilization ratio of the bending reinforcement). This approach has been inspired by the experimental evidence, mostly based on isolated slab specimens supported on columns and consequently only characterised by these data. This evidence has also shown that the deformations in the vicinity of the supported area are governing for the punching shear strength, with larger punching shear strengths associated to lower strains and crack widths.

Contrary to isolated test specimens, actual flat slabs are usually continuous systems where redistributions of bending moments can occur between the regions subjected to hogging and sagging bending moments. In addition, in plane (membrane) compressive forces may develop due to the dilatancy in bending of concrete. The slab continuity thus influences the deformations and the inner forces in the slab near the column connections, normally increasing its stiffness with respect to isolated specimens. This has an influence on the punching shear strength, as it potentially increases the actual resistance with respect to the estimates provided by design provisions.

The work developed by Mr. Einpaul is mostly aimed at this question. It investigates the role of slab continuity on the deformations at the critical punching areas. These results are used in combination with the strain-based approach of the Critical Shear Crack Theory (CSCT) to obtain enhanced predictions of the strength in actual (continuous) flat slabs. To that aim, Mr. Einpaul has performed a very large experimental programme which has helped in understanding the role of some parameters (as the column size and slenderness) on the strain state (rotations) of the slab and on the punching shear strength. In addition, refined numerical analyses have been performed to assess the role and significance of these effects. These investigations have been completed with detailed experimental measurements performed within the slab specimens allowing tracking the development of punching cracks inside the slab. These novel measurements confirm the basic assumptions and pertinence of the CSCT and constitute a significant contribution to the state-of-the-art. The work of Mr Einpaul is finally completed with some investigations on the strength that the inclined strut carrying shear may have as well as on the size effect and influence of column size.

The research developed by Mr. Einpaul has significant practical consequences as it allows for refined assessments of the strength of actual flat slabs. On the basis of this work, beneficial influences on the punching strength neglected by codes of practice can be assessed, and this may potentially avoid unnecessary retrofitting of punching-critical existing structures.

Lausanne, February 2016

Prof. Dr. Aurelio Muttoni Dr. Miguel Fernández Ruiz

Acknowledgements

My research work was carried out under the supervision of Prof. Dr. Aurelio Muttoni and Dr. Miguel Fernández Ruiz at the Structural Concrete Laboratory (IBETON) at Swiss Federal Institute of Technology in Lausanne (EPFL). I am sincerely grateful to both of the supervisors for the support, advice and inspiration they provided me during my years at EPFL.

I would also like to thank the members of my thesis jury, namely Prof. Jean-François Molinari, head of the Computational Solid Mechanics Laboratory at EPFL, Prof. Antonio Pinho Ramos, director of the Structures Laboratory of the Civil Engineering Department at Universidade Nova de Lisboa and Dr. Robert Vollum, a Reader in concrete structures at Imperial College London for their engagement, valuable comments and interesting discussion. The role of Prof. Nikolaos Geroliminis, head of the Urban Transport Systems Laboratory at EPFL, as the president of the jury is also gratefully acknowledged.

My work was funded by Swiss National Science Foundation (project no. 200021 137658), for which I would like to express my sincere gratitude.

A large part of my time during the first three years at EPFL was spent in the testing laboratory. I had the joy of doing it together with its excellent staff. In particular, I would like to thank Gilles Guignet, Gérald Rouge and Sylvain Demierre for teaching me how to use the tools and the equipment and how to solve problems on the fly. The role of Thibault Clément and Marina Fraccaro in developing the internal measurement system should not be undervalued. I would also like to thank João Simões for helping me with the experimental campaign that is presented in the thesis.

João should also be thanked for proofreading my thesis and giving valuable comments. Maléna and Pia are thanked for translating the abstract to French and German respectively, and giving advice regarding some parts of the thesis. I would also like to express my gratitude to Dr. Olivier Burdet, whom I cooperated with on several projects. Our lengthy conversations on various topics turned out to be quite interesting in many cases. Yvonne, our secretary, is sincerely thanked for taking care all of the administrative matters, as well as social events, and making the life for all of us simpler and more enjoyable.

I am extremely happy having met Sarah, Pia, Galina, Raluca, Francisco, Marie-Rose, Maléna, Ioannis, Hadi, Fabio, Shenghan, Filip and many more interesting, smart and fun people. Our common moments, from coffee-breaks and lunches to hiking or skiing trips, were always enjoyable. My special thanks go to Stefan, my first officemate, for the interesting, although not always work-related, discussions.

Thanks also go to all my friends and former colleagues from Estonia, especially Rando and Marika, with whom I worked for several years before joining IBETON. Their practical questions have always been helpful for reminding me the purpose of our research. However, my most sincere gratitude goes to Dr. Ahti Lääne, whose encouragement undoubtedly had the biggest influence on my wish to look for answers through research.

Finally, I would like to thank my family for their support and love, and for teaching me to never settle without giving my best (*Viis miinus!? Miks miinus?*).

Abstract

Reinforced concrete slabs with uniform thickness are common in residential and commercial buildings but can also be found in other types of structures. Such slabs are susceptible to punching shear failures, where a supporting column penetrates through the slab and leads to an immediate local failure that may trigger a progressive collapse of the building. Provisions for punching shear in most codes of practice are still mainly empirical, calibrated on the basis of experiments on test specimens that traditionally model only an isolated part of the slab within the points of contraflexure around the column. However, the punching behavior of actual continuous slabs may be influenced by effects that cannot occur in isolated specimens, such as moment redistribution between hogging and sagging moments, which changes the location of the points of contraflexure, and compressive membrane action. These effects can lead to higher punching strengths of actual continuous slabs compared to isolated specimens.

The first part of the thesis introduces an axisymmetric model to analyze the influence of these effects on the flexural deformations of continuous flat slabs. Combined with the failure criterion of the Critical Shear Crack Theory, the model can be used to predict the punching capacities of such slabs. Good agreement was found between the model predictions and the results of some unconventional punching tests from the literature. A simplified method, sufficiently straightforward to be used in design or assessment and given in a format compatible with the punching provisions of the Model Code 2010, is also proposed for calculating the load-rotation curves of continuous slabs.

The second part of the thesis contains the results of a test campaign comprising 13 isolated symmetric punching specimens. The study focuses on the influence of the size of the supported area and the slenderness of the slab. Other investigated parameters are the flexural reinforcement ratio and the presence of shear reinforcement. A novel experimental approach is used for tracking the formation and development of internal cracks. Measurement points were installed inside small holes drilled on the slab soffit on two sides of the column in the regions were punching cracks were expected to appear. Displacements of these points at various stages of loading were followed with a high-precision coordinate measuring arm. In most cases, the punching failure cracks were seen to develop independently of the flexural cracks, either appearing at the moment of failure or, in some cases, already at earlier stages of loading. Although the slabs were nominally axisymmetric, different crack development patterns could be observed on the two monitored sides of the columns.

On the basis of the experimental evidence, a new punching model is proposed for slabs without shear reinforcement. Punching failures are assumed to occur due to reaching a critical triaxial stress state below the flexural cracks in the compression strut and a consequent formation and

propagation of a failure crack. The proposed model uses the theory of plasticity with a general triaxial yield criterion together with an effectiveness factor based on fracture mechanics that is a function of the depth of the compression zone and the size of the column. The influence of membrane forces in continuous slabs on their punching strength is taken into account by adjusting the depth of the compression zone.

Keywords

continuous slabs, compressive membrane action, Critical Shear Crack Theory, interior slab-column connections, Model Code 2010, moment redistribution, punching shear model, punching tests, reinforced concrete flat slabs

Résumé

Les dalles de béton armé d'épaisseur constante sont fréquemment utilisées, entre autres, pour la construction de bâtiments commerciaux et résidentiels. L'un des modes de rupture de ce type de dalles est le poinçonnement qui se produit à la connexion avec une colonne. La colonne pénètre dans la dalle ce qui cause une rupture locale qui peut entraîner un effondrement progressif de tout le bâtiment. Les recommandations des codes de construction pour le calcul de la résistance au poinçonnement des connexions dalle-colonne ont traditionnellement été calibrées à l'aide de résultats d'essais sur des spécimens isolés. Ces spécimens représentent la partie de la dalle continue qui se trouve entre les points de contreflexion, autour de la colonne. Toutefois, la résistance au poinçonnement d'une dalles continue réelle peut être influencée par des effets non présent dans un spécimen isolé tel que la redistribution des moments positifs et négatifs, qui modifie la position des points de contreflexion, et l'effet de membrane, due au confinement du reste de la dalle. Ces deux effets peuvent mener à une résistance au poinçonnement plus élevée et une capacité de déformation réduite.

La première partie de cette thèse introduit un modèle axisymétrique pour analyser l'influence de ces effets sur les déformations de dalles plates continues en flexion. Combiné avec le critère de rupture de la théorie de la fissure critique, le modèle peut être utilisé pour prédire la résistance au poinçonnement de dalles continues. Les prédictions du modèle et les résultats d'essais non-conventionnels trouvés dans la littérature montrent une bonne concordance. Une méthode simplifiée est proposée pour calculer la courbe force-rotation de dalles continues dans un format compatible avec les dispositions du Model Code 2010 pour le calcul de la résistance au poinçonnement. Cette méthode est suffisamment explicite pour être utilisée lors de la conception ou l'évaluation de dalles.

La seconde partie de la thèse contient les résultats d'une campagne d'essais sur treize dalles axisymétriques et isolées représentants une connexion dalle-colonne intérieure. L'étude se concentre sur l'influence de la taille de la zone de support et l'élancement de la dalle. Les autres paramètres étudiés sont le taux de renforcement en flexion et la présence de renforcement à l'effort tranchant. Une nouvelle méthode expérimentale est utilisée afin de suivre la formation et le développement de fissures à l'intérieur de la dalle. Des points de mesure ont été installés à l'intérieur de petits trous percés à l'intrados de la dalle, sur deux côtés de la colonne, dans les régions où les fissures de poinçonnement sont attendues. Le déplacement de ces points à différentes étapes du chargement a été suivi à l'aide d'un bras de mesure des coordonnées spatiales à haute précision. Dans la plupart des cas, les fissures de rupture au poinçonnement se sont développé indépendamment des fissures de flexion. Elles apparaissent soit au moment de la rupture, soit, dans certains cas, déjà à des ni-

veaux de chargement plus faibles. Bien que les dalles testées fussent supposément axisymétrique, différents patrons de développement des fissures ont été observés sur les deux côtés de la colonne où les mesures étaient réalisées.

Sur la base des évidences expérimentales, un nouveau modèle pour le calcul de la résistance au poinçonnement est proposé pour les dalles sans renforcement à l'effort tranchant. Il est supposé que la rupture au poinçonnement se produit à la base de la bielle de compression, soumise à un état de contraintes triaxial, par la formation d'une fissure de rupture. Le modèle proposé utilise la théorie de la plasticité avec un critère de plastification triaxial général et un facteur d'efficacité qui est fonction de la hauteur de la zone comprimée et de la taille de la colonne. L'influence de l'effet de membrane sur la résistance au poinçonnement des dalles continues est prise en compte en ajustant la hauteur de la zone comprimée.

Mots-clés

dalles continues, effet de membrane, théorie de la fissure critique, connexion dalle-colonne intérieure, Model Code 2010, redistribution des moments, modèle de résistance au poinçonnement, essais de poinçonnement, planchers-dalles en béton armé

Zusammenfassung

Stahlbetonflachdecken mit konstanter Dicke sind häufig in Wohn- und Bürogebäuden, aber auch anderen Bauwerken, vorzufinden. Solche Decken sind anfällig für Durchstanzversagen, bei dem eine Stütze die Decke durchdringt und zu sofortigem lokalem Versagen führt, welches einen progressiven Einsturz des Gebäudes nach sich ziehen kann. Normative Regelungen zur Berechnung des Durchstanzwiderstandes von Stützen-Decken Verbindungen wurden gewöhnlich an Versuchen kalibriert, die mit dem Bereich innerhalb der Momentennullpunkte nur einen begrenzten Teil der Decke abbilden. Das Durchstanzverhalten echter, durchlaufender Decken kann aber sowohl durch Umlagerung zwischen positiven und negativen Momenten, welche die Lage der Momentennullpunkte ändert, als auch durch Druckkräfte, welche durch die Membranwirkung entstehen, beeinflusst werden. Diese Effekte können bei Versuchen an Plattenausschnitten nicht auftreten, können aber zu einer Erhöhung des Durchstanzwiderstandes und einer Verminderung der Verformungskapazität führen.

Im ersten Teil dieser Dissertation wird ein achsensymmetrisches Modell vorgestellt, mit welchem der Einfluss der genannten Effekte auf die Biegeverformungen durchlaufender Flachdecken analysiert werden kann. Kombiniert mit dem Versagenskriterium der Theorie des kritischen Schubrisses kann das Modell dazu benutzt werden die Durchstanzkapazität solcher Decken zu berechnen. Bei Vergleichen der mit dem Modell gemachten Vorhersagen mit den Ergebnissen unkonventioneller Durchstanzversuchen aus der Literatur wurde eine gute Übereinstimmung (zwischen Berechnung und Versuchsbeobachtung) erzielt. Zur Berechnung der Last-Rotations-kurve durchlaufender Decken wird eine vereinfachte Methode vorgeschlagen, die ausreichend direkt ist, um bei Bemessung und Überprüfung eingesetzt zu werden und in einem mit dem Model Code 2010 kompatiblen Format präsentiert wird.

Der zweite Teil der Dissertation enthält die Resultate eine Testreihe an 13 isolierten symmetrischen Durchstanzkörpern, die innere Decken-Stützen Verbindungen darstellen. Diese Studie konzentriert sich auf den Einfluss der Auflagergrösse und der Schlankheit der Decke. Ausserdem untersucht werden der Einfluss des Biegebewehrungsgehaltes und des Vorhandenseins von Schubbewehrung. Eine neuartige Messtechnik wurde angewendet, um die Entstehung und Ausbreitung der Risse im Inneren des Versuchskörpers zu verfolgen. Dazu wurden Messpunkte in kleinen Löchern fixiert, die auf zwei Seiten der Stützen, dort, wo die Rissbildung erwartet wurde, in die Unterseiten der Platten gebohrt wurden. Die Verschiebungen dieser Punkte in verschiedenen Laststufen wurden mit einem hochpräzisen Messarm aufgenommen. In den meisten Fällen wurde beobachtet, dass die Risse, die zum Durchstanzversagen führten, sich unabhängig von den Biegerissen entweder im Augenblick des Versagens oder manchmal auch

schon in früheren Laststufen bildeten. Obwohl die Versuchskörper nominell achsensymmetrisch waren, konnten auf den beiden Seiten der Stützen an denen gemessen wurde verschiedene Muster der Rissbildung beobachtet werden.

Basierend auf den experimentellen Ergebnissen wird ein neues Durchstanzmodell für Flachdecken ohne Schubbewehrung vorgeschlagen. Darin wird angenommen, dass Durchstanzversagen durch eine Lokalisierung des Schadens in einem Riss in der Druckzone, die sich in einem dreiachsigen Spannungszustand befindet, ausgelöst wird. Im vorgeschlagenen Modell wird die Plastizitätstheorie mit einem generellen dreiachsialen Fliesskriterium unter Berücksichtigung eines Effektivitätsfaktors verwendet, der von der Tiefe der Druckzone und der Grösse der Stütze abhängt. Der Einfluss der Membrankräfte auf den Durchstanzwiderstand kontinuierlicher Decken wird durch eine Anpassung der Tiefe der Druckzone berücksichtigt.

Stichworte

durchlaufende Decken, Druck-Membranwirkung, Theorie des kritischen Schubrisses, innere Decken-Stützen Verbindungen, Model Code 2010, Momentenumlagerung, Durchstanzmodell, Durchstanzversuche, Stahlbetonflachdecken

Kokkuvõte

Ühtlase paksusega punkttoetusega raudbetoonplaadid on tavapärased konstruktsioonielemendid nii elamute ja ärihoonete vahelagedes kui ka muudes hoonetes ja rajatistes. Raudbetoonplaatide dimensioneerimisel on määravaks faktoriks tihti plaadi ja posti ühendussõlme läbisurumiskandevõime. Et läbisurumispurunemise, mis oma hapruse tõttu võib kaasa tuua kogu hoone varingu, mehaanikat pole siiani täielikult mõistetud, on ehitusnormides toodud läbisurumiskandevõime valemid enamjaolt tuletatud empiiriliselt, katsetulemuste põhjal. Läbisurumiskatsekehad esindavad tavapäraselt ainult plaadi negatiivse paindemomendiga osa, kus plaadi serv vastab momendi nulljoone asukohale modelleeritavas jätkuvplaadis. Jätkuvplaatides võib paindemoment aga ümber jaotuda, mille käigus momendi nulljoone asukoht muutub. Lisaks võib jätkuvplaatide põikjõukandevõimet suurendada survemembraaniefekt. Neid nähtuseid tavapäraste katsekehade põhjal uurida ei saa ja seega normide empiirilised valemid nendega harilikult ei arvesta.

Käesoleva doktortöö esimene osa kirjeldab telgsümmeetrilist arvutusmudelit, mis võimaldab analüüsida paindemomentide ümberjaotumise ja survemembraaniefekti mõju paindedeformatsioonidele jätkuvplaatide poste ümbritsevates piirkondades. Kriitilise nihkeprao teooria kohaselt määrab plaadi pööre momendi nulljoonel posti ja plaadi ühendussõlme läbisurumiskandevõime. Esitletud telgsümmeetriline model koos kriitilise nihkeprao teooriaga võimalab edukalt ennustada teaduskirjandusest leitud ebaharilike katsekehade käitumist. Lisaks pakub käesolev doktoritöö välja lihtsa valemi läbisurumiskontrollil plaadi jätkuvusega arvestamiseks, mis on mõeldud kasutamiseks koos Model Code 2010 arvutusvalemitega.

Doktoritöö teine osa sisaldab kolmeteistkümne tavapärase, negatiivse paindemomendiga plaadiosa modelleeriva läbisurumiskatse mõõtmistulemusi ja nendel põhinevaid tähtsamaid järeldusi. Peamised uurimisalused parameetrid olid toetuspinna (posti) läbimõõt (83 kuni 660 mm) ja katseplaadi suurus (1.7 kuni 3.9 m). Lisaks uuriti paindearmatuuri koguse ja põikarmatuuri olemasolu mõju. Plaadisisese pragunemise jälgimiseks arendati välja uudne monitoorimissüsteem. Plaadi alapinda posti lähedusse puuriti enne katse alustamist erineva sügavusega augud, mille põhja liimiti mõõtmispunktid, mille koordinaate mõõdeti koormamise käigus korduvalt kõrgtäpse mõõtekäega. Mõõtesüsteem võimaldas jälgida plaadisiseste pragude teket ja kasvamist ilma plaadi telgsümmeetrilist geomeetriat oluliselt häirimata. Tänu uudsele monitooringusüsteemile selgus, et kaldsed nihkepraod, mis põhjustavad plaadi läbisurumispurunemise, arenesid enamasti eraldiseisvalt plaadi pinnal jälgitavatest paindepragudest. Nihkepraod ilmusid kas plaadi põikjõupurunemise hetkel või mõnel juhul juba enne seda. Kuigi katseplaadid olid nominaalselt telgsümmeetrilised, võis pragunemise areng olla posti erinevatel külgedel küllaltki erinev.

Töö kolmas osa pakub põikarmatuurita plaatidele välja uue läbisurumismudeli. Vaatlusandmete põhjal oletatakse, et läbisurumise põhjustab kriitiline ruumiline pingeolukord postiäärse kaldsurvevarda paindepragude aluses osas, kust saab seetõttu alguse kaldpragu, mis levib survetsooni välist betooni lõhestades plaadi ülapinnani. Kriitiline pingeolukord defineeritakse sõltuvalt plaadi geomeetiast, armeerimistegurist ja materjalide omadustest plastsusteooria alampiiri teoreemi ja üldise kolmtelgse betooni voolavustingimuse abil. Betooni purunemise haprus võetakse arvesse, kasutades efektiivsustegurit, mis arvestab purunemismehaanikast tuleneva betooni plastsete omaduste sõltuvusega plaadi paksusest ja posti suurusest. Jätkuvplaatide survemembraaniefekt suurendab uue läbisurumismudeli kohaselt kandevõimet paindepragude sügavuse vähendamise kaudu.

Märksõnad

jätkuvplaat, kriitilise põikjõuprao teooria, läbisurumise mudel, läbisurumiskatse, Model Code 2010, paindemomendi ümberjagunemine, raudbetoonplaat, survemembraaniefekt, sümmeetriline plaadi-posti ühendussõlm

Contents

Notation

A_i	surface area of element i
A_s	cross-section area of a reinforcement bar
A_{sw}	total area of shear reinforcement between the column face and a perimeter at distance d from the column
B	side length of a square test slab; inner circle diameter of an octagonal test slab; diameter of a round test slab
D	characteristic dimension of a structural element
D_0	reference element size
EA_0	longitudinal stiffness before cracking, per unit width
EA_s	longitudinal stiffness of the reinforcing bars alone, per unit width
EI_0	flexural stiffness before cracking, per unit width
EI_1	flexural stiffness after cracking, per unit width
EI_s	flexural stiffness of the reinforcing bars alone, per unit width
E_c	modulus of elasticity of concrete (taken as $E_c = 10\,000\, f_c^{1/3}$)
E_s	modulus of elasticity of reinforcement (taken as E_s = 205000 MPa)
F	external force
G_F	fracture energy
I_1	first invariant of stress tensor
J_2	second invariant of deviatoric stress tensor
L	distance between the axes of the columns in a continuous slab (slab span)
N_r	radial in-plane force in the slab
N_t	tangential in-plane force in the slab between r_a and r_c
$N_{0,\varphi}$	horizontal force in the compression strut over an angular width $\Delta\varphi$
$N_{\alpha,\varphi}$	normal force on the critical surface in the compression strut over an angular width $\Delta\varphi$
P	total force in the inclined compression strut (or a conical shell) around the column
$T_{0,\varphi}$	force in the tension chord over an angular width $\Delta\varphi$

V	shear force
V_0	vertical force in the compression strut
$V_{0,\varphi}$	vertical force in the compression strut over an angular width $\Delta\varphi$
V_{dow}	shear force carried by the dowel action of a reinforcing bar
V_R	punching shear capacity
$V_{R,cont}$	punching shear capacity, continuous model
$V_{R,crush}$	punching shear capacity, failure due to crushing of the concrete strut between the edge of the column and the first shear reinforcement unit
$V_{R,isol}$	punching shear capacity, isolated model
$V_{R,out}$	punching shear capacity, failure outside of the shear-reinforced area
$V_{R,test}$	experimental punching shear capacity
$V_{R,pred}$	predicted punching shear capacity
$V_{R,within}$	punching shear capacity, failure within the shear-reinforced area
V_{flex}	shear force at the flexural capacity
$V_{flex,beam}$	shear force in the center of a beam at the flexural capacity
$V_{flex,cont}$	shear force at the flexural capacity of a continuous slab
$V_{flex,isol}$	shear force at the flexural capacity of an isolated slab
$V_{flex,s\text{-}c}$	shear force at the flexural capacity of a self-confined continuous slab, accounting for the influence of in-plane forces
$V_{flex,confined}$	shear force at the flexural capacity of a confined continuous slab
$V_{\alpha,\varphi}$	shear force on the critical surface in the compression strut over an angular width $\Delta\varphi$

a	crack length; distance between the loading point and the edge of the support in a beam; coefficient in the Ottosen yield criterion
a_{eff}	effective shear span
b	width of an element; coefficient in the Ottosen yield criterion
b_0	perimeter of the critical section at $d/2$ from the column edge
b_{col}	perimeter of the column
$b_{per}(r_i)$	width of a slab sector at a distance r_i from the column
b_s	width of the support strip according to Model Code 2010

c	side length of a square column
c_1, c_2	length of the longer side and the shorter side of a rectangular column
c_I, c_{II}	boundary conditions
c_{top}	concrete cover of top reinforcement
d	effective depth of a slab (distance from the tension reinforcement to the extreme compressed fiber)
d_c	diameter of a round column
d_g	maximum aggregate size (diameter)
d_{g0}	reference aggregate size (d_{g0} = 16 mm)
e	eccentricity of prestressing cables
f_c	average compressive strength of concrete (cylinder)
f_{cp}	plastic concrete compressive strength
f_{ct}	tensile strength of concrete (taken as $f_{ct} = 0.3\, f_c^{2/3}$ MPa if not shown otherwise)
f_{ctm}	mean tensile strength of concrete
f_y	yield strength of reinforcement
h	depth of an element; slab thickness
k_1, k_2	coefficients in the Ottosen yield criterion
k_{col}	effectiveness factor on the plastic strength of concrete in the compression strut depending of the column size
k_{max}	factor that limits the maximum increase of shear capacity for slabs with shear reinforcement in Eurocode 2 (amended in 2014)
k_{sys}	CSCT coefficient describing the efficiency of a shear reinforcement system
$k_{s\text{-}c}$	factor of proportionality for load-rotation relationship of self-confined slabs
k_x	effectiveness factor on the plastic strength of concrete in the compression strut depending of the depth on the compression zone
k_ψ	factor of proportionality for rotation at the onset of yielding in a continuous slab relative to the corresponding rotation in an isolated specimen
l	length of an element; effective length of a dowel
m	bending moment per unit width
m_R	moment capacity per unit width
$m_{R,hog}$	hogging moment capacity per unit width

$m_{R,sag}$	sagging moment capacity per unit width
m_S	acting bending moment due to the applied load, per unit width
m_{cr}	cracking moment per unit width
m_r	radial bending moment per unit width
m_t	tangential bending moment per unit width
n_R	tensile strength of a cross-section at zero moment, per unit width
n_{cr}	tensile cracking force of a cross-section, per unit width
n_{edge}	in-plane applied force at the edge of a slab specimen, per unit width
n_r	radial axial force per unit width
n_t	tangential axial force per unit width
n_{tang}	numbers of transverse reinforcing bars in one perimeter
q	distributed load
r	distance from the center of the column
r_0	radius of the critical shear crack at the level of tensile reinforcement
r_c	column radius
r_{cr}	distance between the center of the column and the line separating the cracked and uncracked parts in a self-confined slab
r_i	distance from the center of the column to a point i
r_q	distance between the center of the column and the point of application of load
r_s	distance between the center of the column and the line of moment contraflexure
r_{slab}	distance between the center of the column and the symmety line in mid-span of the slab
r_{yl}	distance between the center of the column and a circular sagging yield line
r_α	distance between the center of the column and the cross-section where the critical surface intersects the neutral axis of the slab
s	transverse slip of a dowel
s_0	distance between the edge of the column and the first perimeter of transverse reinforcing bars
s_1	spacing of transverse reinforcing bars in radial direction
s_{cr}	spacing of cracks
s_{max}	transverse slip corresponding to the plastic strength of a dowel

s_{top}	spacing of top flexural reinforcing bars
u_i	horizontal radial displacement of a point *i* in the slab
u_{edge}	horizontal displacement of the slab edge
v	nominal shear stress at the control perimeter
v_R	nominal shear capacity at a control perimeter
$v_{R,c}$	nominal shear capacity at a control perimeter for slabs without shear reinforcement
$v_{R,max}$	nominal shear capacity at a control perimeter located at the column face according to Eurocode 2
v_S	acting nominal shear stress at the control perimeter due to applied load
v_i	shear force per unit width at point *i* of the slab
w	maximum vertical displacement (deflection) of the slab
w_{cr}	crack width
w_i	vertical displacement (deflection) of a point *i* in the slab
x	depth of the compression zone (distance between the compressed edge of the cross-section and the neutral axis in bending)
x_{pl}	depth of the rectangular compression block
x_α	depth of the compression zone at a distance r_α from the center of the column, accounting for the inclination of the compression field

$\Delta\varphi$	angle of a slab sector
$\Delta\chi$	change of curvature
$\Delta\chi_N$	change of curvature due to the presence of normal forces
$\Delta\chi_{T\text{-}S}$	change of curvature due tension stiffening
Π	potential energy
ϕ	creep coefficient of concrete
Φ	diameter of a reinforcing bar
Φ_{top}	diameter of top flexural reinforcing bars
Φ_{stud}	diameter of shear stud reinforcing bars

α	inclination of the critical surface in the compression strut from the horizontal
α_P	inclination of the resultant force of the compression strut from the horizontal
α_R	inclination of the critical surface corresponding to the punching capacity
β	efficiency factor of the bending reinforcement (due its orthogonal placement)
ε	axial strain on the central axis of a cross-section
ε_c	axial strain of the most compressed fiber of a cross-section
ε_{cr}	axial strain on the central axis immediately before cracking
ε_r	radial axial strain
ε_s	axial strain in the level of tensile reinforcement
ε_t	tangential axial strain
η	ratio between sagging and hogging moment capacities
η_{fc}	brittleness factor of concrete
θ	angle of similarity of a stress in Haigh-Westergaard coordinates
θ_p	angle between the critical surface in the compression strut and the principal direction of stresses
$\theta_{p,R}$	angle between the critical surface in and the principal direction of stresses corresponding to the punching capacity
ν	efficiency factor in the theory of plasticity
ξ	hydrostatic stress in Haigh-Westergaard coordinates
ρ	tension reinforcement ratio; deviatoric stress in Haigh-Westergaard coordinates
ρ_2	compression reinforcement ratio
ρ_{hog} (ρ_{top})	hogging (top) flexural reinforcement ratio
ρ_{sag} (ρ_{bot})	sagging (bottom) flexural reinforcement ratio
σ	axial stress; average axial stress in a cross-section
σ_0	plastic material strength
σ_N	nominal size-dependent material strength
σ_1, σ_2, σ_3	maximum, average and minimum principal stresses
σ_{b0}	axial stress in the slab at the control perimeter
$\sigma_{c,dow}$	average stress on the contact surface between a reinforcing bar subjected to dowel action and concrete
σ_{ct}	stress in the outermost tension fiber of a cross-section

σ_{edge}	axial stress in the slab at the edge of the slab
σ_{mcr}	average compressive stress that prevents flexural cracking
σ_n	axial stress in the cross-section at the control perimeter
σ_r	radial average stress in the slab
σ_s	stress in tension reinforcement
$\sigma_{s,R}$	stress in tension reinforcement at punching capacity
σ_t	tangential average stress in the slab
σ_α	normal stress on the critical surface in the compression strut
$\sigma_{\alpha,R}$	normal stress on the critical surface in the compression strut at punching capacity
$\sigma_{//}$	stress parallel to the critical surface in the compression strut
τ_α	shear stress on the critical surface in the compression strut
$\tau_{\alpha,R}$	shear stress on the critical surface in the compression strut at punching capacity
φ	angle of internal friction in the Mohr-Coulomb yield criterion
χ	curvature of a cross-section
χ_{cr}	curvature of a cross-section immediately before cracking
χ_r	radial curvature
χ_t	tangential curvature
$\chi_{y,hog}$	curvature of a cross-section at the flexural limit for hogging moment
$\chi_{y,sag}$	curvature of a cross-section at the flexural limit for sagging moment
ψ	rotation of slab at the line of moment contraflexure or at the edge of an isolated specimen
ψ'	modified rotation to take into account the axial compression at the control perimeter
ψ_R	rotation of slab at the line of moment contraflexure at punching failure
ψ_{cont}	rotation of a continuous slab at the line of moment contraflexure
ψ_{crack}	relative rotation between the lips of the critical crack
ψ_{edge}	rotation of the edge of a slab specimen
ψ_i	rotation of slab at point i
ψ_{isol}	rotation of an isolated slab at the line of moment contraflexure (edge of the slab)
ψ_y	rotation at the flexural limit
$\psi_{y,isol}$	rotation of an isolated slab at the flexural limit

$\psi_{y,cont}$ rotation of a continuous slab at the flexural limit, in-plane forces neglected

$\psi_{y,s\text{-}c}$ rotation of a self-confined continuous slab at the flexural limit, accounting for the influence of in-plane forces

Chapter 1 Introduction

Reinforced concrete flat slabs, often supported on columns without capitals or drop panels, are very common structural elements in both residential and commercial buildings. In addition to offering great architectural flexibility, these elements have simple formworks and are thus easy and fast to construct. Slabs with large permanent or temporary concentrated loads can also be found in other types of structures, such as cut-and-cover tunnels or slab bridges supported on columns. In many cases, such slabs are only equipped with flexural reinforcement and no transverse rebars are provided.

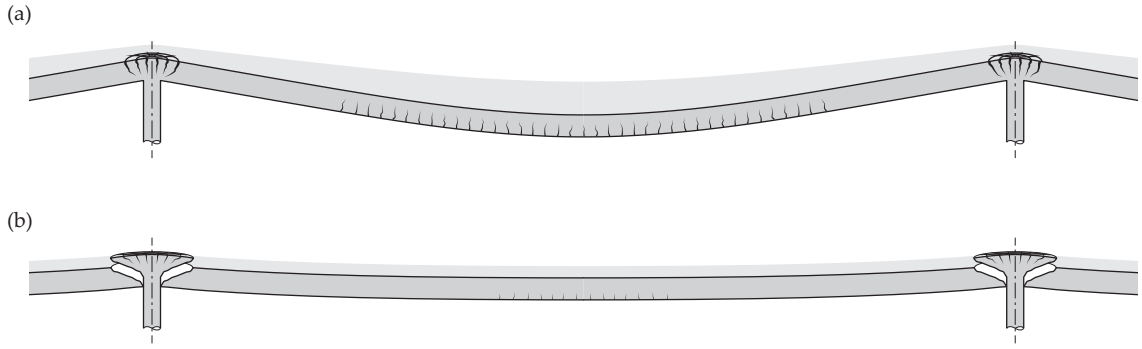

Figure 1.1 Potential failure modes of flat slabs: (a) flexural failure; (b) punching shear failure

Capacity of flat slabs in the vicinity of columns is governed either by flexural or shear strength. Flexural failures occur after large deformations (Fig. 1.1(a)). This can provide warning signs for the users and may allow, in the case of unforeseen or accidental loadings or support settlements, the internal forces to be redistributed between the different load-carrying actions in the slab. Several analytical methods, from simple strip method to linear or non-linear finite element method or yield line theory, exist to design and verify slabs against flexural failures. In contrast, deformations of shear-critical elements are typically very limited before a failure occurs, especially when no shear reinforcement is used (Fig. 1.1(b)). This makes punching shear a particularly dangerous failure mode.

Punching tests are typically conducted on slab elements with load applied at the edges and support reaction concentrated on a column in the center of the specimen (Fig. 1.2). More than 500 such tests have been performed. The provisions for punching design and verification in several codes of practice comprise empirical formulas developed on the basis of these experiments.

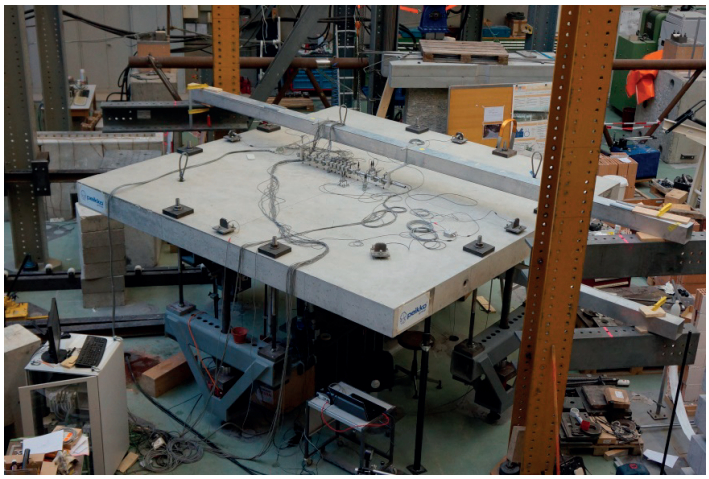

Figure 1.2 Full-scale punching test on an isolated specimen, supported on a column in the center an loaded at 8 points close to the perimeter [Ein16a]

The unitary shear strength of specimens subjected to two-way action (such as flat slabs supported on columns) has been observed to be higher than the shear capacity of one-way elements (such as slabs on linear supports). The very few experiments that have been conducted on continuous slabs (such as the test by Ladner *et al.* [Lad77] shown in Fig. 1.3) have suggested that actual slab-column connections may have even higher capacities than predicted on the basis of isolated specimens. However, due to the lack of experimental data and because the mechanism of punching is still not completely understood, this increase is typically not accounted for in engineering practice. A better understanding of the punching phenomenon is therefore needed in order to develop more precise and physically sound design methods for the evaluation of existing structures as well as for developing new and innovative designs.

Figure 1.3 Reduced-scale punching test on a continuous slab by Ladner *et al.* [Lad77], supported on 16 columns and loaded uniformly on the top surface (picture courtesy to Mr. Heini Lippuner and Dr. Marc Ladner)

1.1 Objectives

The objective of this research is to improve the knowledge about the phenomenon of punching of reinforced concrete slabs. Several different theories exist that can in some cases provide conflicting design outcomes. While in the case of one-way elements, the formation of cracks and the development of strains can be directly observed on the specimen's side surfaces, in punching tests, the cracks appear inside the slab and therefore cannot be directly followed. For the present research, a measurement system was developed that allowed measuring the propagation of internal cracking during a punching test and validate the previously made assumptions regarding the punching failure mechanism.

From previous experiments, it is known that continuous or edge-restrained specimens, which model actual slab-column connections more precisely, show smaller flexural deformations and higher punching capacities than conventional isolated specimens. The empirical models that have been calibrated on the basis of test results on isolated specimens are therefore believed to give conservative predictions. While this can be considered suitable for the design of new structures, assessment of existing structures may require more precise estimates of the actual capacities. The present thesis therefore also studies the strength enhancement of actual slab-column connections in continuous slabs in comparison to isolated specimens.

1.2 Scope

Only axisymmetric loading conditions and geometries are discussed in this thesis. Extensions to non-axisymmetric cases, such as edge or corner columns, unequal reinforcement ratios and span lengths or the cases where significant moment transfer occurs between the columns and the slab, are not considered. However, the punching strength enhancement due to slab continuity is also expected to occur in the case on non-axisymmetric punching of interior columns. These effects are less significant in edge and corner column connections or in the presence of large openings in slabs close to the supports.

The study on punching of continuous slabs is performed using the Critical Shear Crack Theory. According to this theory, the punching capacity of a slab-column connection is a function of flexural deformations of the slab around the connection. The enhanced punching strength of continuous slabs can thus be estimated by studying the influence of slab continuity on its flexural deformations.

Regarding the comparisons between experimental results and provisions of the design codes, as well as development of calculation models, all the safety factors are taken equal to unity. The safety format against failures is not discussed in this thesis. Furthermore, loading is assumed to be short-term, unless specifically noted otherwise.

This thesis considers reinforced concrete flat slabs made of normal or high strength concrete (excluding ultra-high-performance and fiber-reinforced concretes) and ordinary reinforcing steel with

sufficient ductility. The detailing of reinforcement (bar spacing, development lengths and anchorage) is assumed to correspond to the requirements of the codes of practice. All the failure modes associated to anchorage or bond failures or rebars are thus neglected.

1.3 Organization

The present thesis covers two main topics. Firstly, the punching behavior of slab-column connections in continuous flat slabs is investigated with respect to the possible differences compared to typical punching test specimens, which only model an isolated part of the slab in the vicinity of the connection. Secondly, the mechanisms of punching failures are studied on the basis on experimental results obtained by measuring the coordinates of points inside the slab during tests. A new punching model based on the experimental observations is thereafter proposed.

The thesis is organized into eight chapters. After the first introductory chapter, the contents are as follows:

- Chapter 2 presents a brief overview of the state of the art. Various proposed physical approaches to punching design are described. The state of the art regarding punching of continuous and confined slabs is also presented.

- Chapter 3 introduces an axisymmetric numerical model that can simulate the flexural behavior of slabs on small supports, taking into account the influence of compressive membrane action. Depending on applied edge conditions, the model can analyze continuous slabs with various levels of confinement as well as edge-restrained test specimens. The model is validated by comparing its predictions to the results obtained from unconventional punching tests. This chapter is based on two papers, one published in *Engineering Structures* and one accepted for publication in *ACI Structural Journal*.

- Chapter 4 shows the derivation of a simple analytical relationship to predict the load-rotation response of continuous slabs without external confining elements. Slabs with and without membrane action (where the emergence of membrane forces is hindered) are considered. The results of this analysis are presented in a paper accepted for publication in *ACI Structural Journal*.

- Chapter 5 gives the principal results of a test campaign performed within the current research. The test results are compared to the main codes of practice. This chapter is based on a paper published in *ACI Structural Journal*.

- Chapter 6 describes a novel internal measurement technique and the results obtained by applying it to follow the development of flexural cracks and the localization of shear failure cracks inside punching test specimens. This chapter is based on paper "Measurements of internal cracking in punching test slabs without shear reinforcement" submitted for publication in *Magazine of Concrete Research*.

- Chapter 7 proposes a new punching failure model based on the lower bound theorem of the theory of plasticity that is applied to predict the failure load of the compression zone. A general stress-based failure criterion is used together with an effectiveness factor accounting for the size effect. The predictions of the model are compared to test results from the literature.

- Chapter 8 presents the conclusions drawn from the previous chapters and gives an outlook for further research.

1.4 Personal contributions

The main personal contributions of the author were:

- Implementing and improving an axisymmetric numerical model that predicts the flexural response of flat slabs, accounting for the influence of membrane forces in the slab, and validating the model by comparing its predictions the results of tests on various edge-restrained slabs from the literature;

- Performing a series of parametric studies with the numerical model to study the differences between the flexural behaviors and predicted punching strengths of actual continuous slabs and isolated test specimens;

- Deriving a simplified analytical relationship, in a format compatible with the punching provisions of Model Code 2010, for calculating the load-rotation response of continuous slabs, taking into account either only the redistribution between hogging and sagging moments or also accounting for the influence of compressive membrane action;

- Carrying out a series of full-scale symmetric punching tests on slabs with and without shear reinforcement (slab depths 250 mm and sizes from 1.7 x 1.7 to 3.9 x 3.9 m) and comparing their results to various codes of practice and the CSCT;

- Developing a measurement system to track the coordinates of points inside a specimen during a punching test and programming a number of tools to analyze the measured data;

- Performing the internal measurements (in total, on 20 specimens for various research projects) and treating the test results to obtain an overview of crack initiation and development which then allowed identifying the mode of failure of the specimens;

- Proposing a new punching model where the capacity of the slab-column connection is assumed to be governed by the strength of the compression zone, which can be calculated based on the lower bound theorem of the theory of plasticity, and comparing the proposed model to the experimental results from the literature.

Chapter 2 State of the art

Punching of reinforced concrete flat slabs under concentrated loads has been in the focus of research for several decades. This chapter gives a short overview of the state of the art in the field and describes some of the previously suggested analytical models regarding punching shear behavior of symmetric interior slab-column connections. The scope of this review is not to give a complete overview of all the proposed models but to briefly describe only the models that have inspired or influenced the approach of the present thesis. Empirical calculation formulas as well as numerical approaches (such as finite element analyses with three-dimensional solid elements) are also not presented in this chapter.

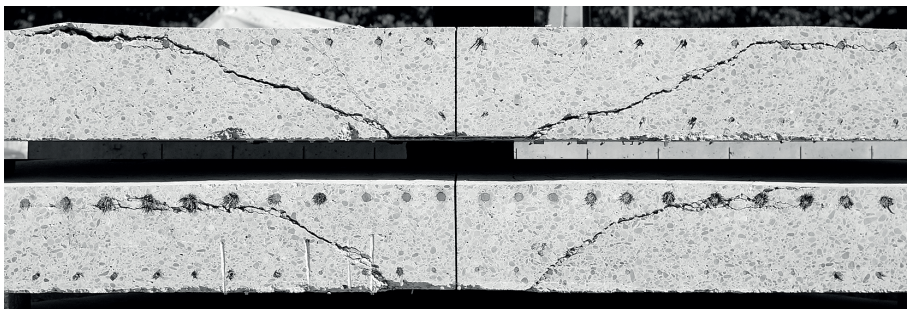

Figure 2.1 Typical cracking patterns on saw-cuts through the column region after punching failures (Specimens PE9 (ρ = 0.75%) and PE8 (ρ = 1.50%) of Einpaul *et al.* [Ein16a])

In order to study the resistance of flat slabs without shear reinforcement, more than 500 large-scale punching tests have been performed, mostly on symmetric specimens supported on a column stub in the center and loaded along the perimeter of the slab. Such specimens normally fail either in bending or in punching. Bending failures are accompanied by yielding of reinforcement and crushing of concrete, showing large deformations and a long plateau of residual strength. In contrast, punching failures typically occur suddenly with formation of a diagonal crack that separates a punching cone from the rest of the slab (Fig. 2.1). Slab deformations prior to failure are often small and residual strength after punching low. Whereas flexural failures are well understood and both the strength and deformations can be predicted with sufficient precision, predicting shear failures as precisely is still a challenge.

2.1 Shear resistance models

The analytical models of shear resistance in reinforced concrete have to include several simplifications due to the complex actual behavior that combines the response of two materials, concrete and reinforcement. In addition, the behavior of concrete depends strongly on three-dimensional state of stresses and strains and is also different before and after cracking. Therefore, physically precise

modeling of the response (for example, with non-linear finite element method) has not yet been successful. Various simplified approaches are mostly used in practice and in research.

2.1.1 Upper bound and lower bound models of plasticity

Simplified models based on the theory of plasticity have been successfully applied to many different problems related to the design and verification of reinforced concrete structures. The constitutive material law is assumed as rigid-plastic with stresses equal to either zero or the compressive or tensile strength of concrete or reinforcing steel (Fig. 2.2(a)). Because the actual material behavior is not rigid-plastic, stresses on the failure surface have to be corrected with an effectiveness factor ν that accounts for the softening of the material, cracking and local stress concentrations [Hoa98].

Regarding punching shear, both upper bound and lower bound models have been suggested. According to upper bound models, the failure occurs when a kinematically admissible failure mechanism forms along yield surfaces. Figure 2.2(b) shows a possible mechanism for punching as suggested by Nielsen [Nie84]. The load causing the mechanism of failure can be determined from the requirement of energy equilibrium of the work performed by external loads and the work performed by internal forces. According to the upper bound theorem of plasticity, an actual failure load cannot be higher than the load calculated with any of the kinematically admissible mechanisms. Therefore, to determine the load-bearing capacity of a structure, a mechanism has to be found that gives the lowest failure load. It should be noted that, the effectiveness factor ν has to be recalibrated for each type of problem as it is dependent on both material and geometric parameters.

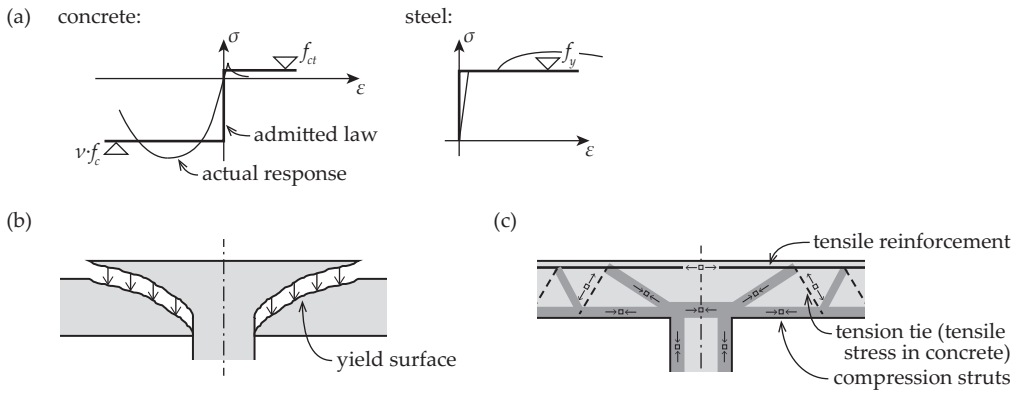

Figure 2.2 Upper bound and lower bound plasticity models: (a) admitted material laws for concrete and reinforcing steel; (b) an admissible failure mechanism for punching [Nie84]; (c) strut-and-tie model for elements without transverse reinforcement

Alternatively, lower bound models of plasticity have been suggested (for example, by Alexander and Simmonds [Ale87]). According to the lower bound theorem of the theory of plasticity, if a distribution of stresses can be found that satisfies static equilibrium and does not exceed material strength at any point of the element, the element does not fail. This approach forms the theoretical basis of the strut-and-tie and stress field models [Mut96]. In the case of shear in elements without

transverse reinforcement, a statically admissible strut-and-tie model requires that some ties rely on tensile stresses in concrete (Fig. 2.2(c)). As the actual tensile behavior of concrete differs considerably from the rigid-plastic assumption, the choice of a suitable efficiency factor ν is very important in these models in order to obtain reasonable predictions. However, for slabs with shear reinforcement, where all tension ties are provided with reinforcement, strut-and-tie models may be appropriate [And81]. Also, these models can be relatively easily modified to account for moment transfer or non-axisymmetric geometries (such as edge and corner columns) [Sim87].

2.1.2 Kinematic models

Models based on the theory of plasticity make very rough simplifying assumptions regarding the material behavior of concrete. In order to use physically more precise constitutive laws, strains in the materials have to be known. Kinematic models attempt to predict the deformations by dividing the structure into elements that are assumed to act as rigid bodies and establishing laws for the relative displacements along the boundaries of the elements.

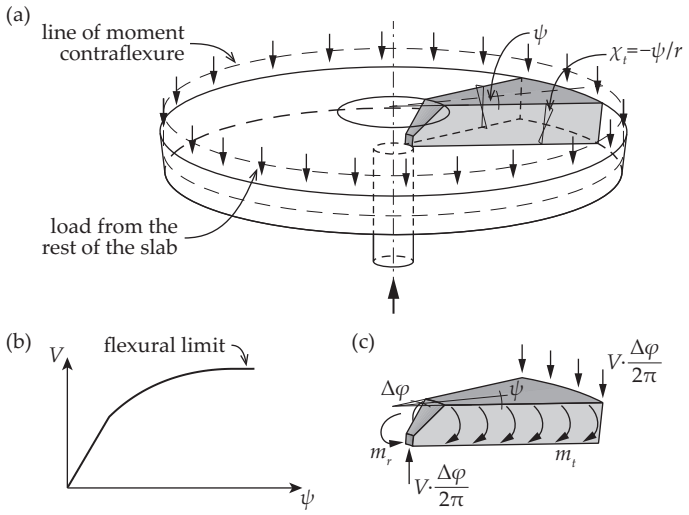

Figure 2.3 Kinematic model of an isolated hogging moment area around a small support [Kin60]: (a) division of the slab into sector elements; (b) load-rotation curve calculated from the equilibrium equations of the element; (c) forces and moments acting on the element

A widely accepted kinematical model of the deformations of a reinforced concrete slab around interior slab-column connections in regular span slabs was proposed by Kinnunen and Nylander [Kin60]. Their model describes the deformations of a hogging moment area around the column that is isolated form the rest of the slab by the line of moment contraflexure. The deformed shape of this area resembles a truncated cone (Fig. 2.3(a)). Radial curvature χ_r in the conical part of the slab is zero and tangential curvature χ_t is proportional to the slab rotation ψ. A relationship between load V and slab rotation ψ (Fig. 2.3(b)) can be calculated from the moment equilibrium equation of a sector element (Fig. 2.3(c)), where the tangential and radial moments m_t and m_r are calculated from the curvatures χ_t and χ_r using non-linear moment-curvature laws. More details about this model are given in Chapters 3 and 4 of the present thesis.

According to Kinnunen and Nylander, shear force is carried to the column by a conical compression strut. This strut is predicted to fail and cause a punching failure when tangential strains on the compressed concrete surface reach a critical value. These strains depend on the flexural deformations of the slab, making the predicted punching strength effectively a function of the flexural capacity of the isolated hogging moment area.

The model of Kinnunen and Nylander has been extended and improved by several researchers [Kin63, She89, Bro90, Hal96, Mut08b]. The improvements have been focused on refining the criterion at which the punching failure is predicted to occur. Among them, the Critical Shear Crack Theory (CSCT) proposed by Muttoni [Mut08b] will be more thoroughly described in Section 2.2.

2.1.3 Size effect in punching shear

Tensile and shear failures of reinforced concrete elements, if governed by the failure of concrete as opposed to reinforcing steel, are known to exhibit size effect: if geometrically similar specimens of different sizes are tested, the obtained nominal stresses at failure are higher in smaller specimens than in larger specimens. This effect has a high practical importance, as many laboratory experiments are performed on smaller scale than the actual structures that they are modeling and may thus potentially give overestimated capacities. It has been attempted to explain the size effect using the concepts of fracture mechanics, namely energy equilibrium at the process of crack propagation [Baž84].

An example of a brittle tensile failure is shown in Figure 2.4. An external applied force F causes a tensile stress σ in the element. When at some point of the element the tensile strength of the material is reached (in section A-A Fig 2.4(a), $\sigma = f_{ct}$), the element starts to crack and the applied force F begins to decrease (Fig. 2.4(b)). In the uncracked portion of section A-A, the stress remains at $\sigma = f_{ct}$. In the rest of the element (for example, in section B-B), the stress decreases due to the reduction of the applied force. Therefore, the elastic strains also decrease ($\varepsilon_{B\text{-}B}$ in Fig. 2.4(c)) and the potential energy stored in the material at loading is released ($-d\Pi$ in Fig. 2.4(d)). The process of crack propagation consumes energy because new material surfaces are created. This spent energy has to be in equilibrium with the released potential energy. As the volume of the material where the stress release occurs depends on the element size, the energy that is available for propagating the crack is also size-dependent. In linear-elastic fracture mechanics (assuming that the stress release is elastic and linear and occurs in the whole length of the element), size effect turns out to be proportional to $h^{-1/2}$, where h is the height of the cross-section of the specimen. In quasi-brittle materials such as concrete, the release of stress is localized into a crack band, the width of which depends on the properties of concrete (such as maximum aggregate size). This reduces the influence of size effect for smaller element sizes, as in this case the width of the crack band constitutes a larger part of the element [Baž84].

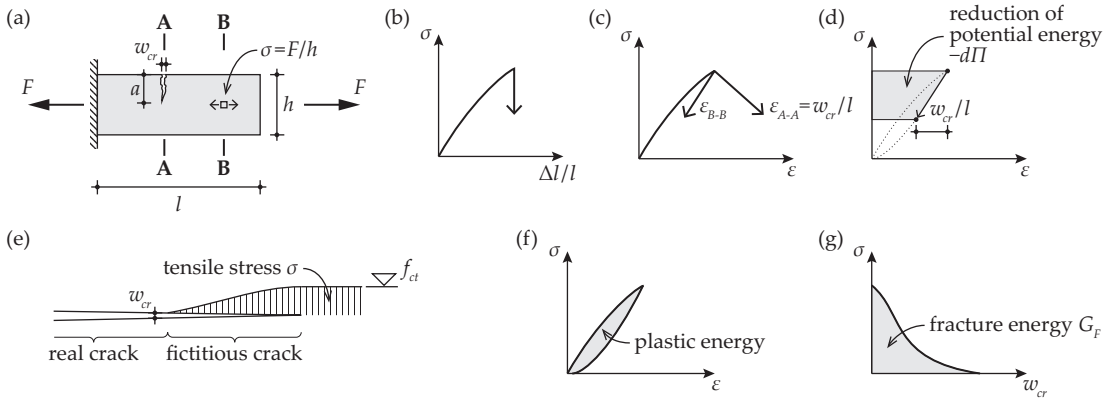

Figure 2.4 Size effect in fracture mechanics: (a) tensile failure of a brittle element; (b) stress-strain curve for the whole element; (c) stress-strain curves for sections A-A (with a crack) and B-B (without a crack); (d) released potential energy in section B-B; (e) tensile stress transfer in fictitious cracks according to Hillerborg [Hil83]; (f) stress-strain law in uncracked concrete; (g) stress-crack opening law in the crack

Consumption of energy at crack propagation can also be expressed as a work of a fictitious tensile force that resists the opening of the crack. This interpretation is often used in finite element modeling of cracking in concrete where transmission of tensile stresses is assumed between crack lips (as suggested by the fictitious crack model of Hillerborg [Hil76, Hil83], Fig. 2.4(e)). It is important to note that whereas stresses in uncracked concrete are related to strains (Fig. 2.4(f)), the residual tensile stress transferred between the crack lips is a function of crack width w_{cr} (Fig. 2.4(g)). The residual stress multiplied with crack opening gives fracture energy G_F that may be considered a material parameter.

Plastic punching models account for a size effect through the efficiency factor ν that varies as a function of slab depth [Nie84, Nie11]. Several empirical models, such as the model used in the punching provisions of the current Eurocode 2 [CEN04], account for size effect as a function of the effective depth of the slab. The punching failure criterion in the kinematical model of Kinnunen and Nylander [Kin60] does not include a factor for size effect. Instead, the failure criterion accounts for strain effect, as the failure is predicted to occur when concrete surface strain reaches a critical value. This strain depends on, in addition to slab rotation, the height of the compression zone, which is proportional to slab depth.

The models of Shehata [She89] and Broms [Bro90] modify the failure criterion and introduce a size effect factor that increases the allowable concrete strains for smaller elements. In Hallgren's model [Hal96], also fracture energy of concrete is taken into account and the size effect factor is formulated on the basis of experiments on unreinforced concrete beams used to determine the fracture energy. The CSCT of Muttoni [Mut08b] described in the next section considers size and strain effects together.

2.2 Critical Shear Crack Theory

2.2.1 Assumed kinematics of shear failures

According to the Critical Shear Crack Theory (CSCT), the shear failure is assumed to occur along a critical shear crack. For one-way beams without shear reinforcement, a comprehensive model describing the kinematics and the contributions of different shear transfer actions was proposed by Fernández Ruiz *et al.* [Fer15] with kinematics shown in Figure 2.5(a). The assumed center of rotation of the relative displacement between the two rigid bodies is located at the tip of the crack. The load is transferred between the bodies by dowel action of tensile reinforcement, aggregate interlock and residual tensile strength along the crack as well as the inclined compression in the compression zone above the crack tip. Stress-displacement laws allow quantifying the contribution of each action and establishing their dependency on the opening width w_{cr} of the crack. It is shown that the load transfer capacity between the two bodies decreases with increasing crack opening. The crack opening is then correlated to a reference axial strain $\varepsilon_{0.6d}$ that can be obtained from cross-sectional analysis of the element (Fig. 2.5(b)).

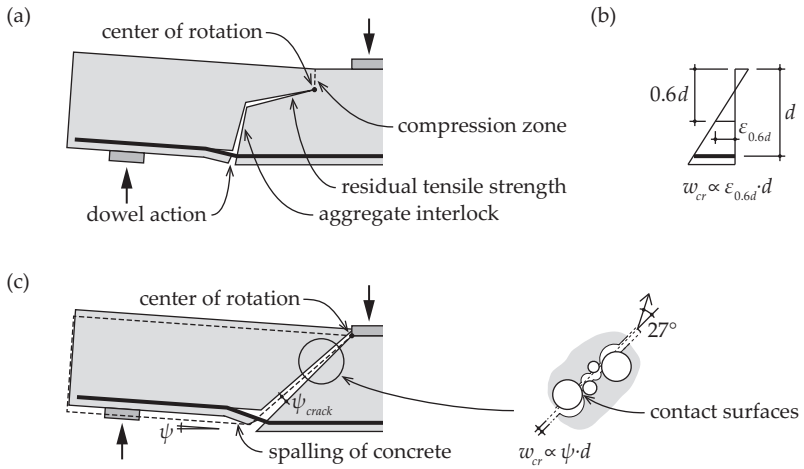

Figure 2.5 The CSCT for one-way elements: (a) assumed kinematics of the critical crack in one-way elements by Fernández Ruiz *et al.* [Fer15]; (b) reference strain ε; (c) assumed kinematics of the critical crack in two-way elements by Guidotti [Gui10a]

Guidotti [Gui10a] proposed a simpler kinematic failure mechanism for two-way slabs without shear reinforcement. The critical crack is assumed to be straight and inclined at 45 degrees. The center of relative rotation between the rigid bodies is taken at the edge of the support (Fig. 2.5(c)). With the assumed kinematics, the average crack width is proportional to the relative rotation between the rigid bodies (crack lips) ψ_{crack} times the effective depth d. It is further assumed that the rotation between crack lips is proportional to the slab rotation ψ. The flexural deformation (slab rotation) can be calculated with any physically based model that accounts for the non-linear behavior of reinforced concrete and thus models correctly the moment redistribution between radial and tangential mechanisms. In axisymmetric cases, the model of Kinnunen and Nylander [Kin60]

can be used. As the center of rotation is assumed to be located at the edge of the column, the contribution of the compression zone is not accounted for. The capacity of dowel action of tensile reinforcing bars to transfer forces between the rigid bodies is greatly reduced by spalling cracks at the level of tensile reinforcement. Therefore, this contribution is also neglected. Shear force is assumed to be transferred through residual tensile stresses in the crack (in the part of the crack where its opening is small) or through aggregate interlock action. The contribution of aggregate interlocking depends on the kinematics (width and the direction of opening) of the crack, as well as the size of aggregates and their packing density. With these parameters, the area of contact between the crack lips can be calculated that gives an estimate of the magnitude of stresses transferred through the crack. In the model of Guidotti, the punching failure crack is assumed to slide at an angle of 27 degrees relative to the crack surface (Fig. 2.5(c)) as was observed in the push-off experiments performed by Walraven [Wal80]. With these assumptions, Guidotti established a law that relates the capacity of the crack to carry shear forces to $\psi \cdot d$, as the failure criterion of Muttoni [Mut08b].

2.2.2 Failure criterion

As described above, the shear strength of an element without shear reinforcement depends on its state of flexural deformations – reference strain $\varepsilon_{0.6d}$ in the control section in the case of one-way elements or slab rotation ψ in the case of two-way elements. In order to verify the punching capacity of a slab-column connection, slab rotation due to the applied load has to be determined first. Then, the shear strength for the determined rotation v_{crit} can be calculated. The shear capacity is sufficient if the shear stress due to applied load is lower than the calculated shear capacity ($v_S < v_{crit}$ in Fig. 2.6(a)). The exact shear capacity v_R can be found where the load-rotation curve intersects the failure criterion (Fig. 2.6(b)).

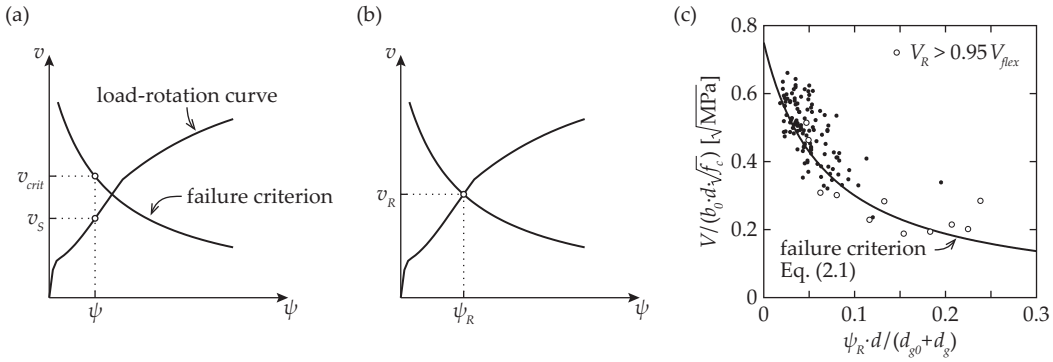

Figure 2.6 (a) Verification of punching strength according to the CSCT; (b) determination of punching capacity; (c) failure criterion of Eq. (2.1) [Mut08b] and experimental results of 128 tests from the literature ([Gua09], [Kin60], [Els56], [Moe61], [Tol88], [Hal96], [Ram96], [Gui10b], [Tas11], [Ein16a], [Sis97], [Lip12], [Tom93])

Based on the results of 99 punching tests, Muttoni [Mut08b] proposed a failure criterion as a function of a parameter $\psi \cdot d$. This parameter is related to the opening width of flexural cracks in the shear-critical region. The failure criterion was given as:

$$\frac{V_R}{b_0 d\sqrt{f_c}} = \frac{0.75}{1+15\dfrac{\psi \cdot d}{d_{g0}+d_g}} \tag{2.1}$$

where d is the effective depth of the slab, b_0 is the length of the control perimeter located at a distance $d/2$ from the column face, f_c is the concrete cylinder compressive strength, ψ is the rotation of the conical slab portion (at the edge of an isolated specimen or, in a general case, at the line of moment contraflexure), d_g is the maximum aggregate size and d_{g0} = 16 mm is a reference aggregate size. The maximum aggregate size in Equation (2.1) accounts for the roughness of the crack surfaces that influences the capacity of shear transfer by aggregate interlock [Gui10a]. The consistency of the CSCT with the fracture mechanics approach is further described and discussed elsewhere [Fer15].

The general approach of the CSCT can also be used to treat slabs with irregular column layout and uneven loading [Sag11] as well as punching of rectangular columns [Sag14]. However, in the current research, only cases that can be approximated by an axisymmetric model (interior column connections in regular span slabs under uniform loading) are considered.

2.2.3 Influence of in-plane forces

Clément *et al.* [Cle14] proposed that the influence of prestressing on punching behavior of flat slabs can be accounted for by considering three potentially beneficial phenomena. Firstly, if the placement of tendons is eccentric, the bending moments they introduce can reduce the rotation due to the applied load. This reduction can be taken into account in the calculation of slab rotation. Secondly, if the tendons are inclined, part of the shear force can be carried by the vertical component of the axial force in the tendons. Finally, the axial compression at the column perimeter can increase the punching capacity by reducing the width of the critical shear crack. This effect was suggested to be accounted for in the failure criterion [Cle14]:

$$\frac{V_R}{b_0 d\sqrt{f_c}} = \frac{0.75}{1+15\dfrac{\psi' \cdot d}{d_{g0}+d_g}} \tag{2.2}$$

where ψ' is a modified rotation:

$$\psi' = \psi + 45 \cdot \frac{\sigma_n}{E_c} \geq 0 \tag{2.3}$$

where σ_n is an axial stress at the column perimeter (compression is negative) and E_c is the modulus of elasticity of concrete.

2.2.4 Punching of slabs with shear reinforcement

Fernández Ruiz and Muttoni [Fer09] have extended the CSCT to also cover slabs with shear reinforcement. Different failure modes that have to be verified are summarized in Figures 2.7(a–c).

According to this approach, shear reinforcement that intersects the critical crack carries part of the shear force. In this case, the punching capacity V_R can be found by summing the concrete and reinforcement contributions (Fig. 2.7(a)). The contribution of concrete can be calculated in the same manner as for slabs without shear reinforcement (Eq. (2.1)). Thus, it decreases with increasing slab rotation (due to increasing crack opening). The shear force carried by shear reinforcement depends on the strains in them, which increase with increasing opening of the critical shear crack, which these elements intersect (Fig. 2.7(a)). Thus, with increasing rotation, the concrete contribution decreases and the steel contribution increases. The maximum contribution of the transverse units is limited by the yield strength of shear reinforcement or their anchorage conditions in the case of some reinforcement systems. The described failure mode is referred to as failure within the shear reinforced area and it is usually governing for low amounts of shear reinforcement.

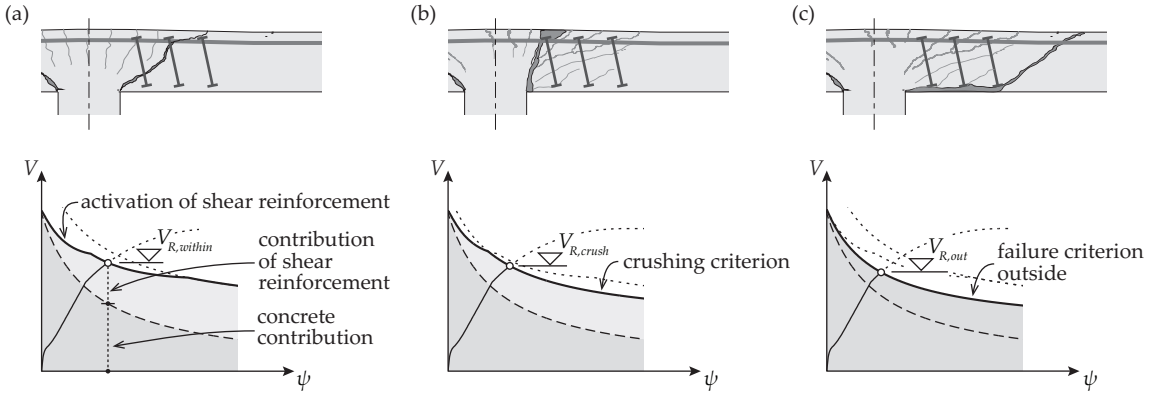

Figure 2.7 Punching failure modes of slabs with shear reinforcement: (a) failure within the shear-reinforced area; (b) failure inside the shear-reinforced area (between the edge of the column and the first shear unit perimeter; (c) failure outside of the shear-reinforced area

In the case of large amounts of shear reinforcement, shear failure may also occur by crushing of the concrete strut between the edge of the supported area and the first perimeter of shear reinforcement units. This failure typically occurs before transverse reinforcement reaches yielding and is assumed to be independent of the shear reinforcement ratio (Fig. 2.7(b)). According to the CSCT, the punching capacity in this failure mode is influenced by the same parameters as punching without shear reinforcement since both are governed by the strength of concrete in shear. This is considered in the CSCT by multiplying the concrete contribution failure criterion with a factor k_{sys}. Position and anchoring properties of shear reinforcement also have and influence on this failure mode so that k_{sys} depends on the performance of the shear reinforcement system. Its value should be determined, specifically for each system, by testing.

Punching failure may also occur outside the shear-reinforced area (Fig. 2.7(c)). In this case, relatively good estimates in comparison to the experimental results have been obtained by considering the shear-reinforced zone as supported area with a control perimeter outside the last perimeter of transverse reinforcement units. In this case, the compression strut is supported on the anchorage zone of the last shear units. Therefore, the part of the cross-section that is below this anchorage

zone has to be subtracted from the effective depth of the slab in Equation (2.1). If the radial spacing of the transverse elements is too large, the failure can also occur between the perimeters of shear reinforcement units.

2.3 Behavior of continuous slabs

2.3.1 Redistribution between hogging and sagging moments

Most punching tests are performed on specimens that model an isolated hogging moment area according to the suggestion of Kinnunen and Nylander [Kin60]. Such specimens are round or square, supported on a small column stub in the center and loaded close to the perimeter (Fig. 2.8(a)). Size of the hogging moment area is usually determined by means of an elastic analysis. In the case of small columns, this leads to the location of the line of moment contraflexure at $r_s \approx 0.22\ L$ (Fig. 2.8(a)). When cracking of concrete or yielding of reinforcement occurs in the vicinity of the column, bending moments can be redistributed between radial and tangential directions (Fig. 2.8(b)). In this regard, isolated specimens are suitable to model the region of the slab around a slab-column connection.

However, in continuous slabs, moment redistribution can also occur between hogging moments around the column and sagging moments in mid-span. This redistribution shifts the location of the line of contraflexure (Fig. 2.8(c)). This phenomenon cannot occur in isolated specimens where the line of moment contraflexure of a prototype slab is represented by the edge of the specimen. Therefore, it can only be experimentally studied by testing real continuous slabs or larger specimens with rotationally restrained edges. However, such experiments are significantly more time-consuming and expensive to perform and are thus rarely done.

Kinnunen and Nylander [Kin60] justified the applicability of the isolated specimen's results on continuous slabs by requiring that sagging reinforcement should be designed so that it remains in the elastic phase up to a punching failure. Thus, the curvatures and moments in the sagging moment area can be assumed to vary in a parabolic manner. This approach requires increasing the amount of reinforcement in mid-span compared to the results of conventional design for bending.

According to the strip model of continuous slabs proposed by Alexander [Ale99], shear forces are carried to the column through support strips. Shear stresses on the surfaces between the rest of the slab and the support strips can be redistributed in a fully plastic manner. Capacity of the slab-column connection is assumed to be limited by the flexural resistance of the support strips, which are calculated as continuous beams. This way, the influence of the amount of sagging reinforcement on the punching strength is accounted for.

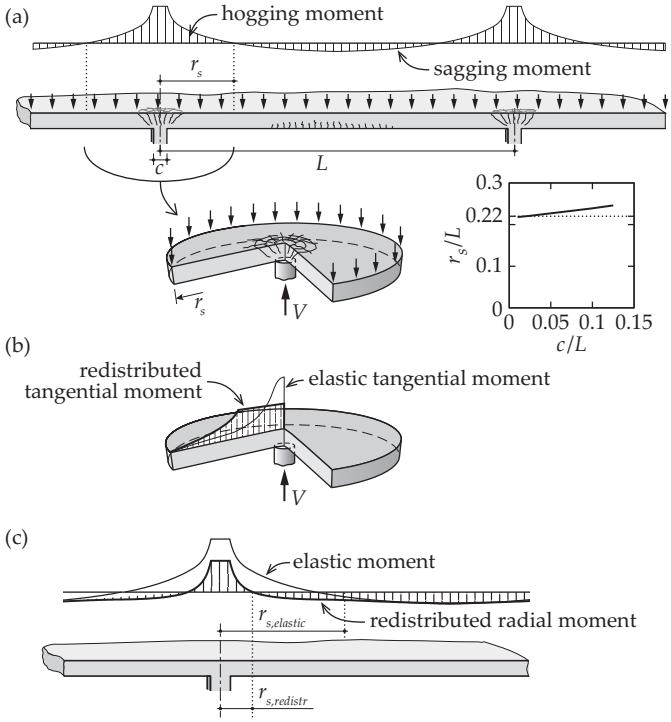

Figure 2.8 (a) Continuous slab and a corresponding isolated test specimen; (b) Redistribution of tangential moments in an isolated element after reinforcement yielding; (c) Redistribution of radial moments in a continuous slab due to cracking and/or reinforcement yielding

2.3.2 Compressive membrane action

Compressive membrane action is a phenomenon where the flexural strength (m_R) of a reinforced concrete element is enhanced by compressive axial forces in the slab ($-n$) (Fig. 2.9(a)) that appear due to rigid lateral supports that restrain the expansion of the element, which is caused by shifting of its neutral axis at flexural cracking. An example of a structure where the influence of lateral supports is important is a bridge deck slab that is confined between stiff beams linked with diaphragms shown in Figure 2.9(b). The in-plane forces significantly increase both the flexural strength and also the flexural stiffness of such structures.

Lateral expansion (dilation) of isolated punching test specimens after cracking (Fig. 2.9(c)) has been observed in the experiments (an example of slab PG19 of Guidotti [Gui10b] is shown in Fig. 2.9(d)). In continuous slabs, this expansion is constrained by surrounding slab portion that is uncracked and therefore does not dilate. To resist the dilation, tangential tensile stress (a tension ring) appears around the cracked zone (Fig. 2.9(e)) and induces axial compressive stress within the hogging moment area (Fig. 2.9(f)) that increases the flexural stiffness and strength of the slab. In this thesis, this effect is called self-confinement, as it is provided by the continuous slab itself without any external confining elements.

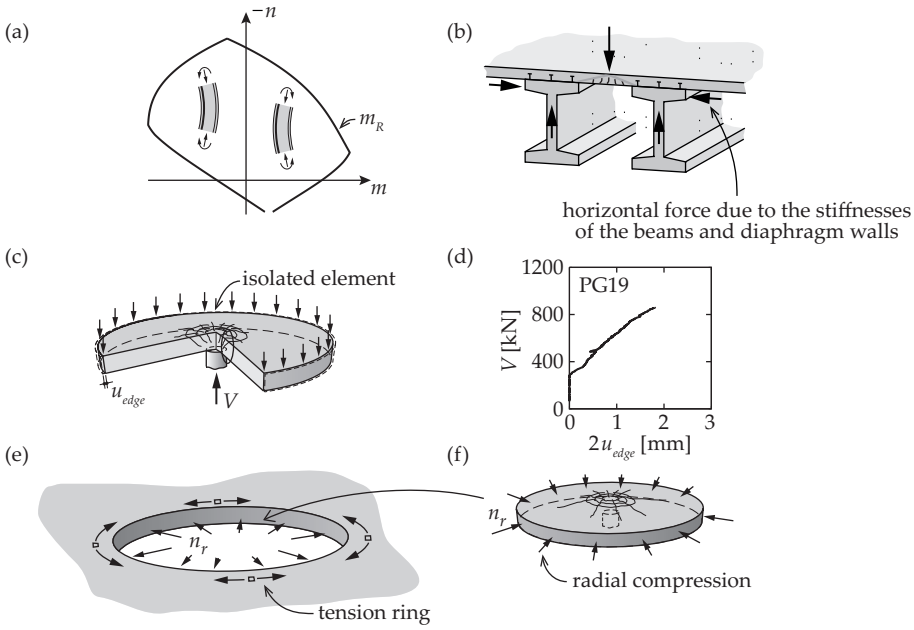

Figure 2.9 Compressive membrane action: (a) influence of normal force on the flexural strength of a reinforced concrete element; (b) compression arch in confined slabs; (c) dilation of an isolated slab; (d) measured dilation of specimen PG19 [Gui10b]; (e) formation of a tension ring in the slab portion around the hogging moment area; (f) compressive forces in the hogging moment area due to restrained expansion

Although Wood [Woo61] argued that if the compressive in-plane forces in the hogging moment area have to be equilibrated with tension around it, additional reinforcement is required, and concluded that accounting for compressive membrane action in slabs without external confining elements therefore does not result in any reduction in the total quantity of required reinforcement, later researchers have attempted to study the influence of self-confinement on the flexural capacity and deformations of continuous slabs more precisely.

An ASCE-ACI report described the appearance of self-generated compressive in-plane stresses in continuous flat slabs in a qualitative manner in 1974 [ASC74]. Significant effort has thereafter been made by researchers to evaluate the influence of these in-plane stresses quantitatively. Traditional yield line analysis (that neglects the influence of in-plane forces) results in plastic flexural strength V_{flex} that is independent on the deflection of the center point of the slab (Fig. 2.10(a)). Methods based on rigid-plastic analysis [Par80, Bra80a] allow modeling the dome effect of the forces arising from the changes of geometry. Assuming infinite in-plane stiffness, these methods lead to a maximum flexural strength value at zero deflection and a subsequent decrease of strength with increasing deflection due the reduction of the height of the compression arch (Fig. 2.10(b)). When the magnitude of the deflection is similar to the thickness of the slab, the flexural strength approaches the yield line strength of an unconfined slab as the height of the compression arch reduces to zero. If the slab is equipped with sufficient amount of longitudinal reinforcement that is properly anchored at the supports, tensile membrane action may arise (Fig. 2.10(c)). However, this resisting mechanism can only be activated in the presence of very large deformations and can be used in the

engineering practice only for extreme cases as post-failure behavior [Mel98]. This kind of membrane action is not a subject of the present thesis.

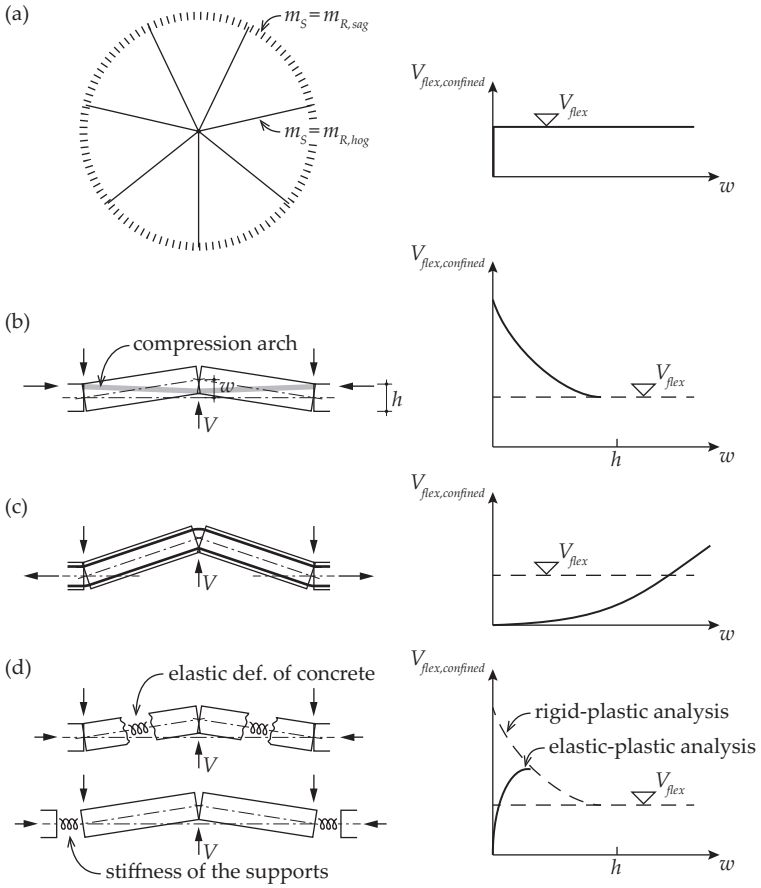

Figure 2.10 Rigid-plastic and elastic-plastic analysis of confined slabs: (a) flexural strength of a slab in the vicinity of the support according to yield line analysis (V_{flex} is independent of the deflection); (b) influence of compressive membrane action, rigid-plastic analysis; (c) tensile membrane action; (d) compressive membrane action, elastic-plastic analysis.

The rigid-plastic analyses assumed that the influence of the in-plane deformations of the slab and the lateral displacement of the supports are negligible compared to the second order effects due to the slab deflection. Therefore, in the case of small deflections (which is the most relevant regime for engineering applications and the main interest of this thesis), an elastic-plastic analysis [Bra80b] has to be performed. If the surrounding structural elements are significantly stiffer than the slab, an assumption can be made that the stiffness of the lateral supports is infinite. Therefore, only the elastic deformations of the concrete slab itself have to be taken into account in order to determine the ascending branch of the load-deflection curve [Kir84] (Fig. 2.10(d)). This approach has been accepted by some codes of practice [UKH02] as a basis of a design formula for designing bridge deck slabs between laterally stiff beams (such as shown in Fig. 2.9(b)). However, these assumptions are not valid in the cases where the surrounding elements are not significantly stiffer than the slab. In these occasions, the stiffness of the supports has to be taken into account. In a simplified

manner, this can be done by attributing the lateral supports a stiffness value that describes both the rigidities of the tension ring in the slab and the restraining elements (Fig. 2.10(d)). In that case, the horizontal support reaction necessary to create the compression arch is only generated at non-zero deflections. However, determining a suitable stiffness is in most cases still performed empirically [Hew75, Kua93, Eyr07].

In the present thesis, both redistribution between hogging and sagging moments as well as self-generated compressive membrane action are analyzed on the basis of an axisymmetric numerical model. A load-rotation curve of a slab-column connection in a continuous slab is obtained from the analysis. Punching strength of the connection is thereafter predicted using the failure criterion of the CSCT.

Chapter 3 Numerical model for continuous slabs

This chapter, based on a paper published in *Engineering Structures* [Ein15], describes a numerical model that allows analyzing the flexural deformations and, by applying the failure criterion of CSCT, punching strengths of slabs with various edge conditions, such as unconventional configurations for symmetric punching tests but also interior slab-column connections in continuous flat slabs. The model is validated by comparing its predictions to uncommon punching test specimens found from the literature.

3.1 Description of the numerical model

3.1.1 Equilibrium equations and compatibility conditions

The numerical approach presented in this section assumes axisymmetric conditions (extension of the model for non-axisymmetric geometries is discussed in Section 3.1.4). A region of the slab around an interior column is divided into sector elements (Fig. 3.1(a)) [Gua05, Gui10a]. For each element, equations for the equilibrium of moments (3.1) and forces (3.2) as well as for the geometrical compatibility of deformations due to bending (3.3) and normal forces (3.4) are written (notation in Fig. 3.1(b) and (c)):

$$m_{r,i+1} \cdot r_{i+1} - m_{r,i} \cdot r_i - m_{t,i} \cdot \Delta r_i + v_{i+1} \cdot \Delta r_i \cdot r_{i+1} + q_i A_i \left(r_{q,i} - r_i \right) = 0 \tag{3.1}$$

$$n_{r,i+1} \cdot r_{i+1} - n_{r,i} \cdot r_i - n_{t,i} \cdot \Delta r_i = 0 \tag{3.2}$$

$$\chi_{t,i} = \frac{-\psi_i + \chi_{r,i} \cdot \Delta r_i / 2}{r_i + \Delta r_i / 2} \tag{3.3}$$

$$\varepsilon_{t,i} = \frac{u_i + \varepsilon_{r,i} \cdot \Delta r_i / 2}{r_i + \Delta r_i / 2} \tag{3.4}$$

The relationship between forces and deformations can be provided by any suitable moment-curvature and moment-dilation law for the considered level of axial load. Such law can be generally obtained using a layered non-linear sectional analysis. To facilitate the calculation procedure, in the current thesis, a simpler multi-linear law is used (Fig. 3.2), where different linear branches of the law are related to uncracked, cracked and reinforcement yielding regimes:

$$(m,n) = f_{multilin}(\chi,\varepsilon) \tag{3.5}$$

For the details about the derivation of the multi-linear law, refer to Section 3.1.3. The sectional response is calculated independently in tangential and radial directions (thus the value of the Poisson's ratio is taken as 0).

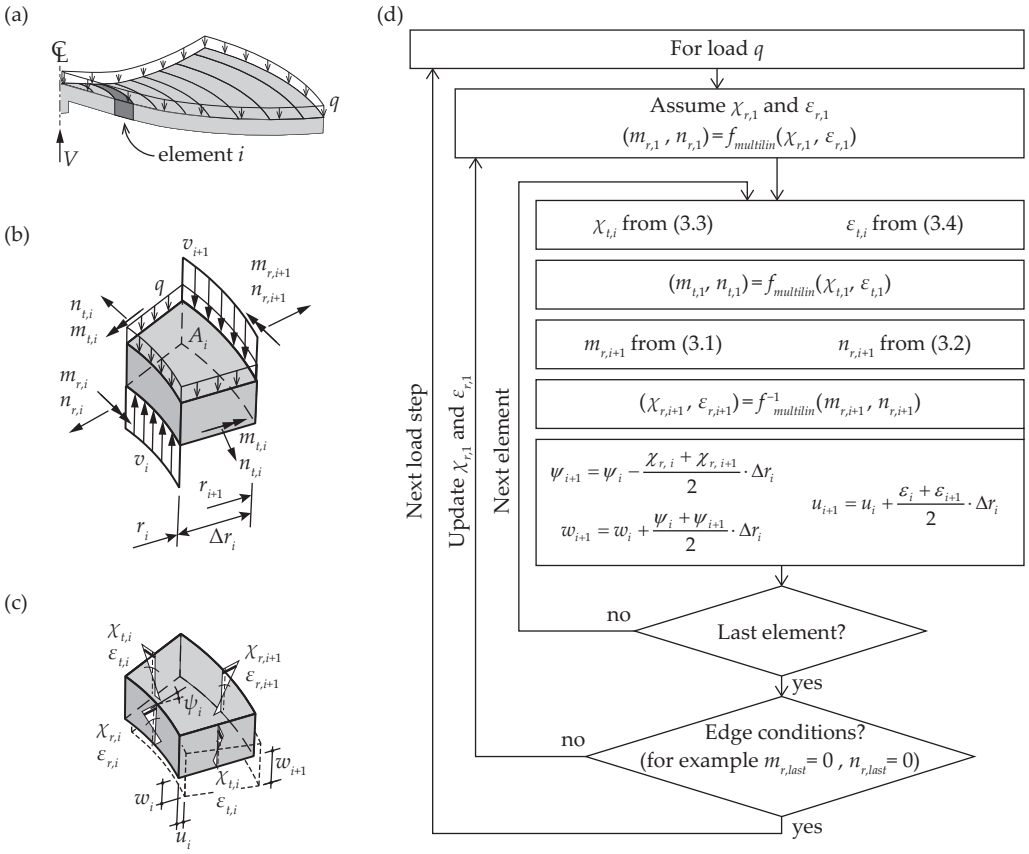

Figure 3.1 (a) Sector of an axisymmetric slab; (b) internal forces acting on an element; (c) deformations and displacements of the element; (d) numerical solution procedure

A block diagram of the numerical solution procedure is shown in Figure 3.1(d)). For each element, Equations (3.1)–(3.5) can be used to find the internal forces and deformations at the outer edge of the element if the internal forces at the inner edge of the element are known. The increase of rotation and vertical as well as horizontal displacements within an element can also be obtained. By assuming a state of deformations (χ, ε) at the inner edge of the centermost element and repeating the calculation for each subsequent element, taking into account the external loads q applied on the slab, two boundary conditions are reached at the edge of the slab. The response of the slab can thus be determined by finding for each loading case the state of deformations in the center that leads to the appropriate boundary conditions. This is done by means of an iterative calculation procedure.

A simpler calculation can be performed by neglecting the influence of in-plane forces in the multilinear sectional law (Eq. (3.5)) so that only the equilibrium of moments (Eq. (3.1)) and compatibility of flexural deformations (Eq. (3.3)) is required.

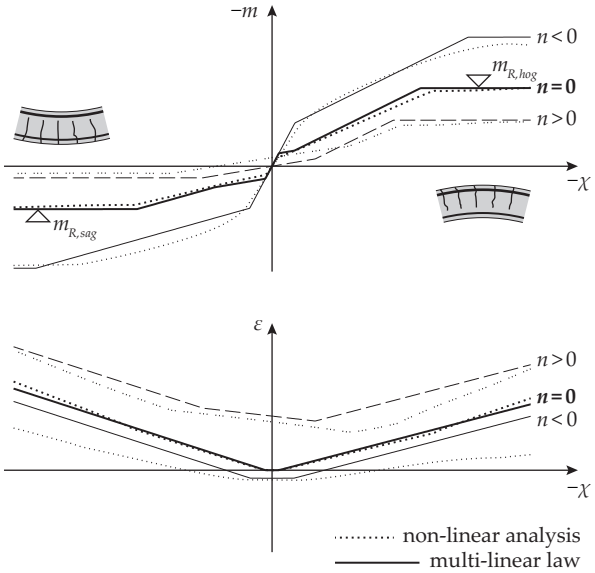

Figure 3.2 Moment-curvature (m-χ) and dilation-curvature (ε-χ) relationships for different levels of axial force (n): results of a non-linear sectional analysis and the simplified multi-linear law (calculated with Response 2000 [Ben00])

3.1.2 Boundary conditions

The boundary conditions in at the edge of the slab are:

- for an isolated specimen, the radius of the axisymmetric calculation model corresponds to the radius of the specimen. Radial moment at specimen's edge has to be zero ($m_{r,edge} = 0$) and if the loading system is designed as to avoid in-plane forces and no prestressing is applied, the radial normal force at the edge of the slab has to be zero as well ($n_{edge} = 0$) (Fig. 3.3(b));

- for a continuous slab, the radius of the model r_{slab} corresponds to the distance between the column and the symmetry line in mid-span. The first boundary condition is therefore zero rotation at the edge of the model ($\psi_{edge} = 0$). The radius of the slab r_{slab} is selected so that in the elastic uncracked phase, the axisymmetric model has to yield the same radius of moment contraflexure r_s of 0.22 L as it is in a regular continuous slab. This leads to the choice of $r_{slab} \cong 0.7\ L$ (refer to Section 3.1.4 for discussion). The second boundary condition may be:

  - for a flat slab on supports that carry only vertical reactions (a self-confined slab), the second boundary condition is $n_{edge} = 0$ (Fig. 3.3(c));

  - for a flat slab that is perfectly confined between external elements (like, for example, very stiff shear walls), the second boundary condition is $u_{edge} = 0$ (Fig. 3.3(d)).

Other cases can also be easily modeled, including tests on additionally confined isolated slabs, slabs with partially rotation-restrained edges, or slabs with bending moments applied at some distance from the center.

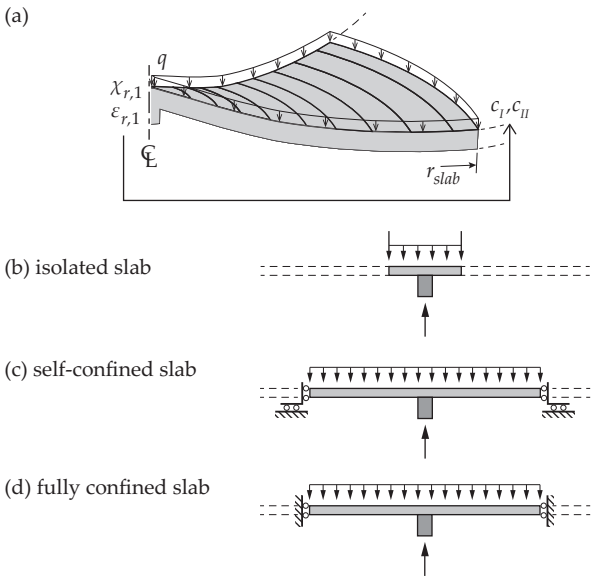

Figure 3.3 (a) Axisymmetric calculation model; (b) Boundary conditions for an isolated slab; (c) Boundary conditions for a slab without external confining elements (self-confined); (d) Boundary conditions for a slab with perfectly rigid external confining elements

3.1.3 Multi-linear sectional analysis

A simplified multi-linear relationship between the internal forces acting on a cross section and its deformations is used in this numerical model. The internal forces considered are the bending moment m and the axial force n, whereas the related deformations are curvature χ and dilation of the axis ε. The law is based on an approach used by Muttoni [Mut08b] and Clément *et al*. [Cle14] but it is modified to describe the dilation of the axis and to approximate the response of a section under high tensile forces in a more suitable manner. The resulting curves and a comparison with a layered non-linear analysis are presented in Figure 3.2.

A number of simplifications are made to ensure the continuity of the curves and to facilitate the use of the multi-linear law in the iterative calculations of the numerical model. The moment-curvature and the curvature-dilation relationships are assumed to consist of linear phases, as shown in Figure 3.4 for some different levels of axial load:

- In the uncracked phase, the slope of the moment-curvature relationship is equal to the stiffness of a full concrete cross-section EI_0. The influence of the tension and compression reinforcement can be normally neglected (Fig. 3.5(a)). This phase describes the response between zero moment and cracking moment (m_{cr}). Cracking moment is defined, depending on the level axial force, as a bending moment that induces a tensile force equal to f_{ct} in the outermost tension fiber of the cross-section [Cle14]. Compressive axial force increases the cracking moment, whereas tensile axial force decreases it. In the presence of high tensile forces, the tensile stress in concrete may exceed the tensile strength in the whole cross-section ($n > n_{cr}$). In this case, the cross-section is cracked in tension at zero bending moment and the uncracked phase does not apply (Fig. 3.4(c)).

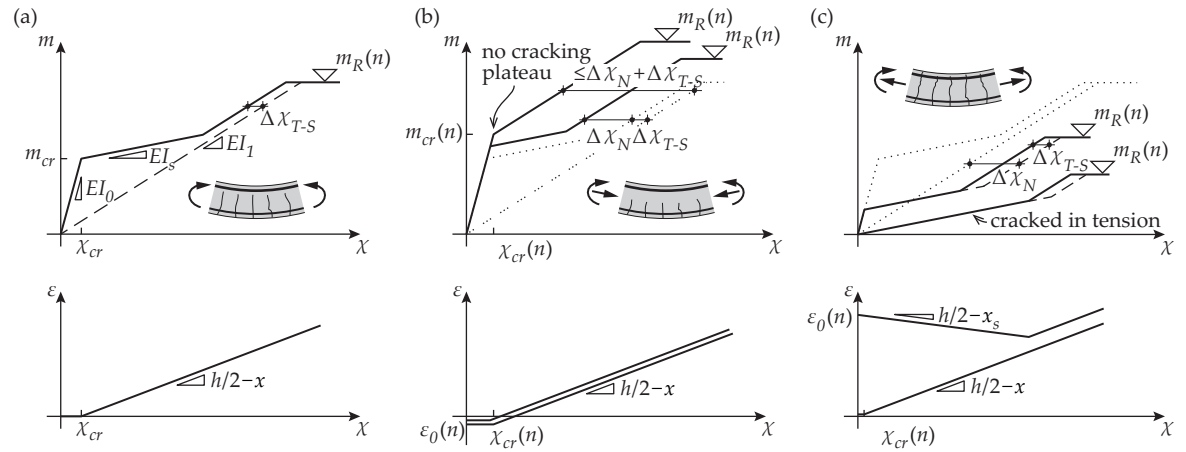

Figure 3.4 Moment-curvature and moment-dilation relationships for different levels of axial load: (a) no axial force; (b) axial compression; (c) axial tension

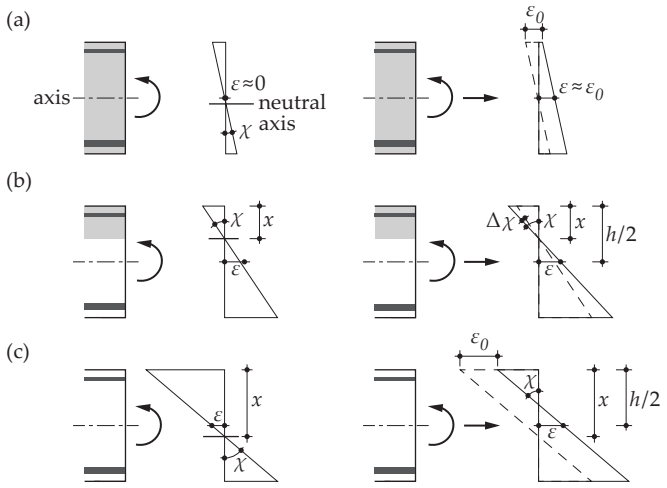

Figure 3.5 Sectional analysis: (a) uncracked phase; (b) partially cracked phase; (c) fully cracked phase

The dilation of the axis ε in the uncracked phase mainly depends on the deformation due to the axial force ε_0 (Fig. 3.5(a)).

– If the applied moment exceeds the cracking moment, a cracked phase applies. In this phase, the m-χ relationship is assumed to be linear with a slope equal to the stiffness of a fully cracked cross-section (βEI_1) that is composed of the compression zone and the reinforcing bars (Fig. 3.5(b)) multiplied by an efficiency factor β. The efficiency factor takes into account the orthogonal placement of the reinforcing bars, which is not equivalent with the polar placement that is assumed in the axisymmetric model. A suitable value of β has been shown to be 0.6 [Mut08b]. The contribution of concrete in tension is neglected when calculating EI_1. However, the contribution of the tensile stresses in the concrete around steel re-

bars due to bond between the reinforcing bars and concrete are taken into account with a tension stiffening factor [Mut08b]:

$$\Delta\chi_{TS} = \frac{f_{ctm}}{\rho \cdot \beta \cdot E_s} \cdot \frac{1}{6 \cdot h} \tag{3.6}$$

Applying an axial force on the cross-section affects the height of the compression zone. As a simplification, however, this change is neglected in the present multi-linear law. The influence of the axial forces is taken into account by modifying the curvature due to different stiffness of the tension tie and the compression chord (Fig. 3.5(b)). The change of the curvature due to the axial load is [Cle14]:

$$\Delta\chi_N = \frac{-n}{(d - x/3)^2} \cdot \left(\frac{h/2 - x/3}{\rho \cdot d \cdot E_s \cdot \beta} - \frac{2 \cdot (d - h/2)}{x \cdot E_c} \right) \tag{3.7}$$

The total contribution of the aforementioned effects is thus:

$$\Delta\chi = \Delta\chi_{T-S} + \Delta\chi_N \tag{3.8}$$

The contribution of tension stiffening $\Delta\chi_{T\text{-}S}$ is always positive (decreasing the curvature). The contribution of the normal force $\Delta\chi_N$ can be positive (decreasing the curvature) in the case of compression (Fig. 3.4(b)) or negative (increasing the curvature) in the case of tensile axial forces (Fig. 3.4(c)). In the case of high compressive forces, $\Delta\chi$ may be so large that the curvature at cracking χ_{cr} is less in the cracked phase than in the uncracked phase. In this case, the value of $\Delta\chi$ is limited to yield the same in the χ_{cr} cracked phase as in the uncracked phase [Cle14] (leading to no cracking plateau in Fig. 3.4(b)).

At the onset of cracking, the dilation of an element is known to increase abruptly while the cracks are formed. After their initial formation, the cracks will start growing and the increase of dilation will become more stable. In the current analysis, this phenomenon is neglected and the dilation in the cracked phase is assumed to increase linearly from the dilation in the uncracked phase ε_0 (Fig. 3.5(b)):

$$\varepsilon = \varepsilon_0 + (\chi - \Delta\chi) \cdot (h/2 - x) \tag{3.9}$$

As seen in Equation (3.9), the dilation is calculated using the modified curvature ($\chi - \Delta\chi$). In this manner, the effect of tension stiffening is taken into account.

– In presence of high tensile axial forces ($n > n_{cr}$), the whole concrete cross-section may be cracked in tension. In this case (Fig. 3.4(c)), the stiffness of the cross-section consists of the stiffness of only rebars $\beta\, EI_s$ (Fig. 3.5(c)). In the case of different compression and tensile reinforcement ratios, the influence of this asymmetry on the location of the neutral axis should be taken into account. It should be noted that the slope can be negative if the amount of compression reinforcement exceeds the amount of tensile reinforcement.

– Between the uncracked and cracked phases, a crack development plateau is usually assumed. In the current paper, the slope of the plateau is taken equal to EI_s as in the previously described phase (Fig. 3.4) to ensure continuity between different levels of axial load. However, as a simplification, the curvature-dilation relationship is found with Equation (3.9) similarly to the cracked phase.

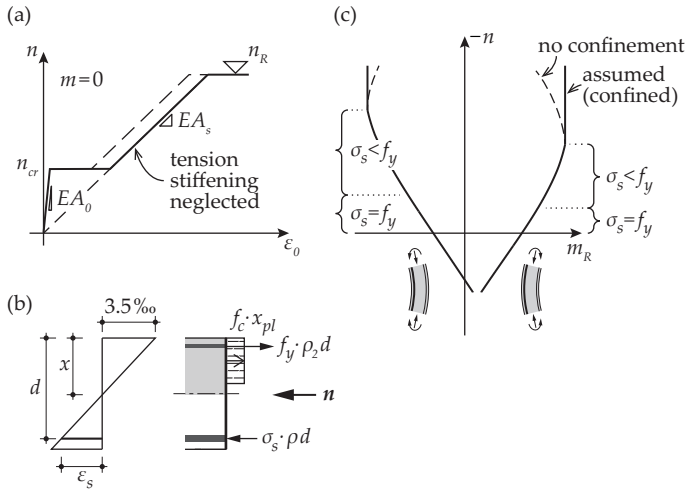

Figure 3.6 (a) Axial force-dilation relationship with no bending moment; (b) Strains and forces at the cross-section in the case of high compressive axial forces; (c) adapted axial load-moment capacity relationship

The multi-linear law used for determining the dilation at zero moment ε_0 (Fig. 3.5(a)) is shown in Figure 3.6(a). Similarly to the moment-curvature relationship, uncracked and cracked phases are distinguished with the respective stiffnesses of βEA_0 and βEA_s. As a simplification, tension stiffening is neglected in this law. The tensile capacity of the cross-section at zero moment n_R is reached when the bars on the side with lower reinforcement ratio start to yield.

The flexural capacity of the cross-section (m_R) is calculated assuming yielding of tensile reinforcement and a rectangular compression block in concrete:

$$m_R = \rho \cdot d \cdot f_y \left(d - h/2\right) + \rho_2 \cdot d \cdot f_y \left(d - h/2\right) + f_c \cdot x_{pl} \left(h/2 - x_{pl}/2\right) \tag{3.10}$$

where the depth of the rectangular compression block x_{pl} depending on the level of axial force can be found as:

$$x_{pl} = \left(\left(\rho - \rho_2\right) \cdot d \cdot f_y - n\right) / f_{cp} \tag{3.11}$$

In the case of high compressive axial force, tensile reinforcement may not be yielding at the flexural limit ($\varepsilon_s < f_y/E_s$ in Fig. 3.6(b)). In this case, the moment capacity is limited by the strength of the compression zone. By assuming that the ultimate compressive strain of concrete is 3.5‰, stress in tension reinforcement can be calculated (Fig. 3.6(b)):

$$\sigma_s = \frac{d-x}{x} \cdot 0.0035 \cdot E_s \tag{3.12}$$

By further assuming that the depth of the rectangular compression block is $0.8x$, the moment capacity can be found:

$$m_R = \rho \cdot d \cdot \sigma_s \cdot (d - h/2) + \rho_2 \cdot d \cdot f_y (d - h/2) + f_c \cdot 0.8x \cdot (h/2 - 0.8x/2) \tag{3.13}$$

The equilibrium of normal forces yields an equation:

$$n = -\rho \cdot d \cdot \sigma_s + \rho_2 \cdot d \cdot f_y + f_c \cdot 0.8x \tag{3.14}$$

The depth of the compression zone x and moment capacity m_R can be determined by solving the system of Equations (3.13) and (3.14). This leads to increasing moment capacity with increasing axial compression but with a slower increase than in the previous phase (Fig. 3.6(c)).

If the depth of the compression zone reaches the height of the cross-section, increasing the axial force will start to decrease the moment capacity. However, in the current research, high axial compression is only found in the center of the slab and it appears simultaneously in radial and tangential direction. Therefore, the ultimate strain and stress of concrete can be significantly higher due to the biaxial compression (confinement). Due to this, for the current analysis it is assumed that the moment capacity does not decrease with increasing axial force (the confined case in Fig. 3.6(c)).

In Figure 3.2, the simplified multi-linear law was compared to the results of a non-linear layered sectional analysis [Ben00]. The approaches yield similar results, except for a larger discrepancy regarding the dilation of the cross-section in the case of compressive normal forces and large curvatures. The difference is caused by neglecting concrete compression softening in the simplified law (which reduces the total normal force in the non-linear analysis). However, in the present analysis, large curvatures combined with high axial compressive forces occur in the center of the slab, where the concrete is bi-axially confined and the softening effect is therefore reduced.

3.1.4 Conversion of a regular-span continuous slab to an axisymmetric model

Compared to the geometry of actual slabs and conventional placement of reinforcing bars, the axisymmetric model is developed assuming several simplifications.

Firstly, in the axisymmetric case, the deflection of the slab at its outer edge is considered constant along the whole edge. However, in the case of a continuous slab supported on a regular grid of columns, the deflection is smaller on the axes and larger in the middle of the fields (Fig. 3.7(a)). Therefore, the choice of the radius for the continuous model that would predict correctly the deformations of the slab in the vicinity of the column is not as straightforward as in the case of the radius for an isolated element.

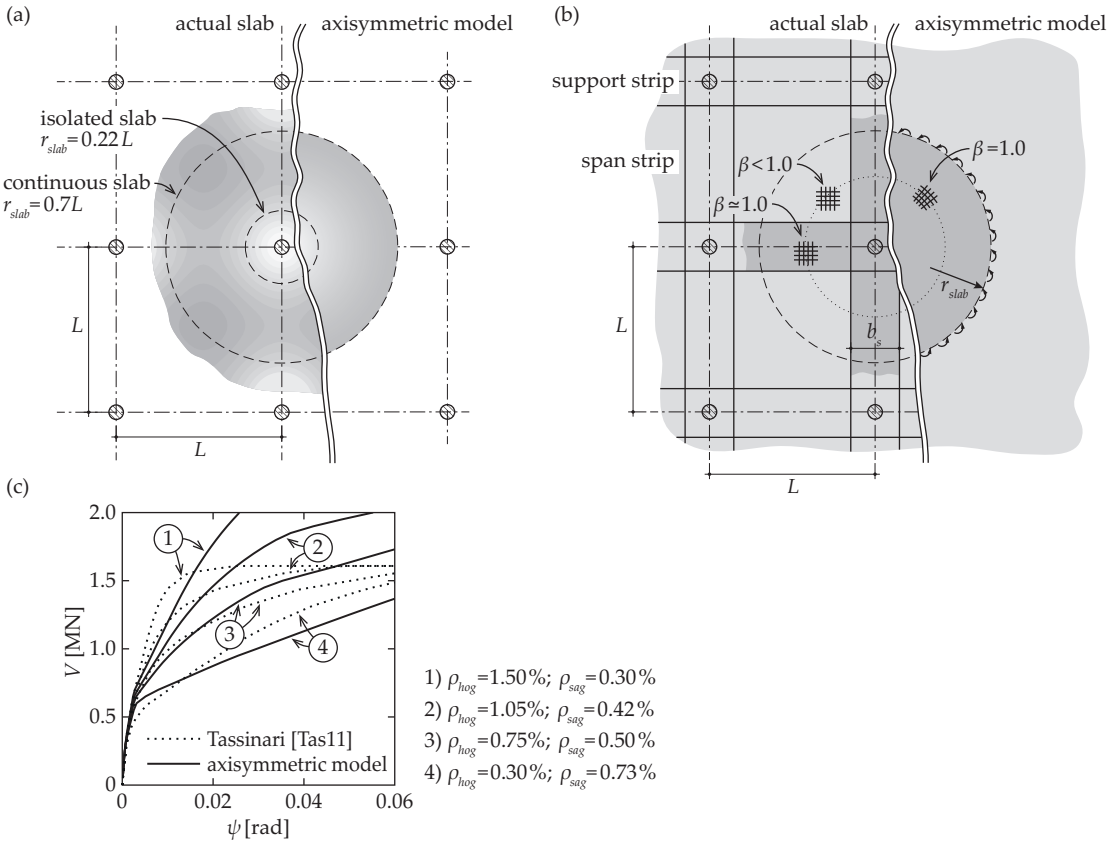

Figure 3.7 Conversion of an actual slab to an axisymmetric model: (a) comparison of slab deflections (represented by shading); (b) simplification of the reinforcement layout; (c) comparison with a non-linear parametric study by Tassinari [Tas11]

In this research, the radius of the slab r_{slab} has been chosen so that in the elastic uncracked phase, the axisymmetric continuous model has to yield the same radius of moment contraflexure r_s of 0.22 L as an elastic analysis of a regular-span slab. This leads to $r_{slab} \cong 0.7\ L$. The radius is larger than it would be based on purely geometrical considerations (the same contributive area, for instance) because of the overestimate of the tangential curvature in the outer part of the axisymmetric model, which leads to overestimating the contribution of tangential moments in comparison to the sagging moment area of an actual slab. The overestimate of the radial stiffness can be compensated for by increasing the extent of the slab in the axisymmetric model. The distributed load on the slab is correspondingly decreased by a factor of $0.7^2 \cdot \pi = 1.54$ to yield an equal column reaction.

Secondly, in the axisymmetric model, the reinforcement is assumed to be laid in the radial and in the tangential directions. In actual slabs, however, the reinforcement is placed orthogonally and may therefore cross the radial and the tangential planes at oblique angles. In these cases, the stiffness of the tension chord of the cross-section is reduced. This effect is taken into account in the multilinear moment-curvature law with an efficiency factor β that reduces the stiffness of a cracked cross-section (refer to Section 3.1.3). For uniformly reinforced isolated test specimens, an average

value of $\beta = 0.6$ gives good results in comparison to the test results [Mut08b] and the same value has been used in the current research.

Thirdly, in the axisymmetric model, top and bottom reinforcement ratios are considered constant over the whole slab. However, in actual slabs, top reinforcement is usually concentrated in strong bands (support strips) between the supports (Fig. 3.7(b)) and significantly lower amounts of flexural reinforcement are provided in the areas between these strips. This results in redistribution of internal forces and concentration of bending moments on the support strips due to the higher flexural stiffness of these strips after cracking.

When applying the present model for actual slabs, the influence of the distribution of hogging reinforcement can be taken into account analogously to the Model Code 2010 [FIB13], where the width of the support strip b_s for interior columns is defined as 75% of the width of the elastic hogging moment area ($1.5 \cdot r_s$). As a practical rule, it is suggested that the sagging reinforcement ratio be also defined as an average ratio over the width of the column strip. This value may be higher than the geometrically weighted average over the whole sagging moment area. However, considering firstly the concentration of bending moments on the stiffer support strips and secondly, the higher β-factor of these strips compared to the span strips (as the reinforcement in the strong strips is placed parallel to the direction of principal moments (Fig. 3.7(b)), this approach is believed to be reasonable and realistic. A comparison with numerical non-linear solutions [Tas11] for square-spanned slabs with the reinforcement concentrated in strips shows a reasonable (possibly slightly prudent) agreement with the axisymmetric model (Fig. 3.7(c)).

3.2 Modeling results

3.2.1 One-way, isolated two-way and continuous elements

Figure 3.8 shows the unitary shear force-rotation curves for a one-way member (a beam), an isolated two-way slab specimen and a continuous slab (or a slab with flexural edge restraints), calculated using the axisymmetric numerical model described in Section 3.1, not accounting for the influence of in-plane forces. All the compared elements have the same thicknesses and flexural reinforcement ratios. The beam (Fig. 3.8(b)) and the isolated slab (Fig. 3.8(d)) have identical values of shear slenderness (r_q/d, where r_q is the distance from the load application point to the support). The model of the continuous slab is subjected to uniformly distributed loading and extends to the mid-span symmetry line where the slab rotation is required to be zero. The span of the continuous slab L (Fig. 3.8(f)) is selected based on the consideration explained in the previous section. The shear force associated to the flexural capacity of each element (V_{flex}) can be found with yield line method based on kinematic mechanisms shown in Figure 3.8(b, d, f). The isolated slab has higher flexural capacity than the beam due to the radial plastic hinges that activate the reinforcement in the whole slab (Fig. 3.8(e)). In turn, the continuous slab has higher flexural capacity than the isolated slab due to a circular plastic hinge that also activates the sagging reinforcement (Fig. 3.8(g)). It is worth noting that the stiffnesses of the different contributions are not equal and the rotation ψ_y at which V_{flex}

is reached varies for the three cases (Fig. 3.8(a)). Due to the lower stiffness of the sagging mechanism, the load-rotation curves for the isolated and continuous slabs are similar until the first yielding of hogging reinforcement occurs. After that, however, stiffness of the hogging mechanism starts to decrease and the difference between the isolated and the continuous slabs becomes more significant. After full yielding of hogging reinforcement, the load on the continuous slab can still increase, although with lower stiffness than in the previous phase, as the additional load is only being resisted by sagging reinforcement.

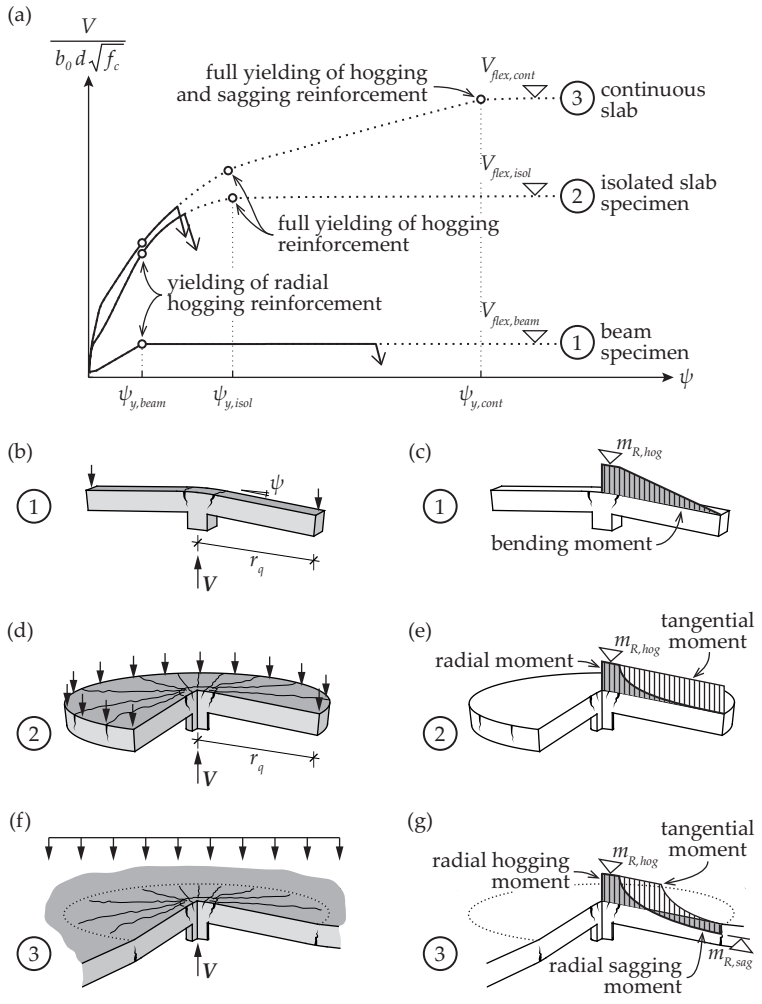

Figure 3.8 Comparison of a beam, an isolated slab and a continuous slab with equal shear slenderness factors (r_q/d): (a) normalized shear stress-rotation curves; (b) flexural failure mechanism of a beam; (c) distribution of bending moments in a beam at the flexural limit; (d) failure mechanism of an isolated slab; (e) bending moments in an isolated slab at the flexural limit; (f) failure mechanism of a continuous slab; (g) bending moments in a continuous slab at the flexural limit

3.2.2 Location of the line of moment contraflexure

Flexural reinforcement of flat slabs is nowadays conventionally designed using linear-elastic finite element programs (with or without a redistribution of hogging moments) or simplified analytical methods, as the "direct design method" [ACI14]. Both approaches normally result in placing relatively large amounts of flexural reinforcement in the support regions. However, many existing flat slabs have also been designed using the theory of plasticity (yield line method or strip method), which allows the designer freely choose the amount of moment redistribution. This leads to potentially large variation in the ratios between the amount of reinforcement at the support and in midspan. The method described in the present research allows taking into account the influence of the actual reinforcement distribution and is thus a very useful tool to investigate existing flat slabs with unusual hogging-to-sagging reinforcement distributions.

Due to the different stiffnesses of various mechanisms described in Section 3.2.1, redistribution of bending moments takes place in slabs when concrete cracks or reinforcement yields. In isolated specimens, the only possible redistribution of moments is that of between tangential and radial directions. In continuous slabs, bending moments can also be redistributed between hogging and sagging contributions. This redistribution is accompanied by changes in the location of the line of moment contraflexure. A common approach for selecting a representative specimen size in punching tests is to determine this location by assuming linear-elastic material response with uncracked concrete behavior. In this manner, for a continuous slab supported on regularly spaced small supports and assuming an elastic uncracked behavior, the line of moment contraflexure is located approximately at a radius of 0.22 L from the column axis (Fig. 3.9) [Kin60].

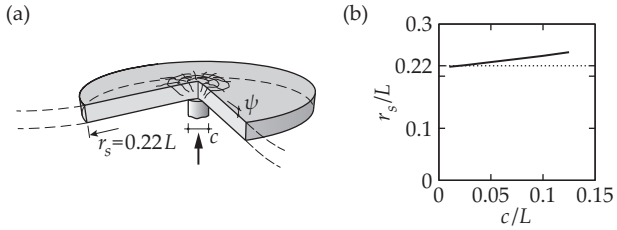

Figure 3.9 (a) isolated hogging moment area; (b) radius of the hogging moment area depending on the size of the column

As will be shown in Chapter 5, a correct choice of the slenderness ratio of a test specimen is important in order to model the behavior of an actual slab suitably. As the actual response of reinforced concrete is non-linear and redistribution of bending moments develops, the choice made according to elastic calculation might not be correct for all load levels. Figure 3.10(a), shows the distance r_s between the column axis and the line of moment contraflexure depending on the load level (shown as the support reaction), calculated using the axisymmetric numerical model with distributed load. In-plane forces are neglected in this analysis in order to investigate only on the influence of moment redistribution. It can be seen that after an initial elastic uncracked phase, the line of moment contraflexure shifts closer to the column (shear slenderness decreases) due to the loss of stiffness in the hogging moment area near the column. After cracking of concrete due to

sagging moment in mid-span, shear slenderness starts to increase again. At the load levels where the radial reinforcement in the hogging moment area has started to yield, the line of moment contraflexure approaches once again the elastic estimate. This occurs because in this range, the stiffnesses of the hogging and sagging moment areas (at column and mid-span, respectively) are similar. The shear slenderness starts to decrease again once that all the hogging reinforcement is yielding (which would correspond to the flexural failure of an isolated specimen). Similar results regarding the changes of shear slenderness due to the non-linear behavior of reinforced concrete were obtained using a non-linear finite difference analysis of continuous flat slabs [Tas11].

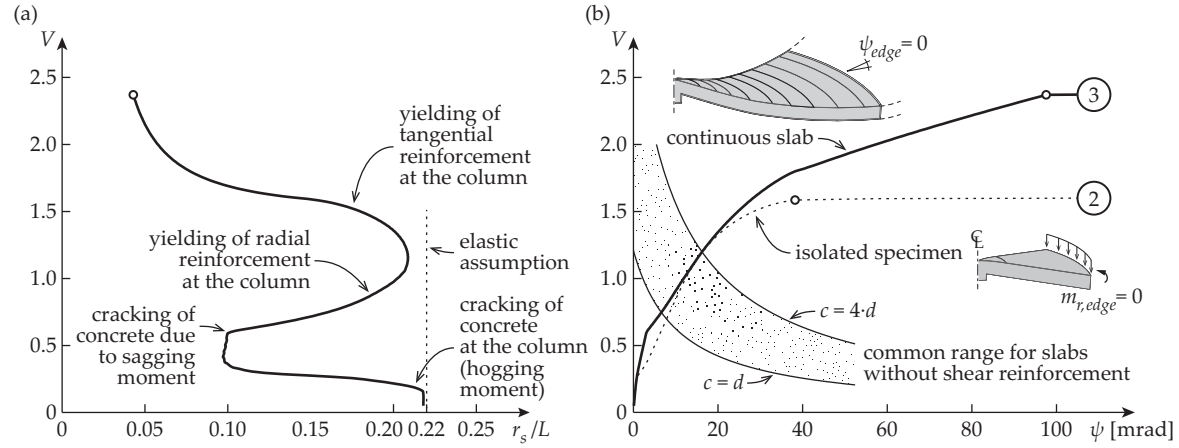

Figure 3.10 Radius of the line of moment contraflexure (influence of the in-plane forces neglected): (a) radius of the line depending on the load; (b) load-rotation relationship for an isolated specimen and a continuous slab (parameters: L = 7 m, h = 250 mm, d = 210 mm, c = 260 mm, f_c = 35 MPa, f_y = 550 MPa, d_g = 16 mm; ρ_{hog} = 1.0%; ρ_{sag} = 0.5%)

3.2.3 Influence of moment redistribution

Figure 3.10(b) presents a load-rotation curve that is calculated using the axisymmetric model representing a continuous slab with twice the amount of hogging reinforcement compared to the sagging reinforcement. As a comparison, the load-rotation curve of a corresponding isolated specimen with $r_s = 0.22\,L$ is also shown. The continuous slab is loaded with distributed load, whereas the isolated specimen is loaded with an identical distributed load and a linear load at the edge of the specimen that corresponds to the shear force of the distributed load on the rest of the slab. It can be seen that the rotation of the continuous slab for a given level of load (compared to the one of an isolated specimen) depends on its actual shear slenderness r_s/d at that load level (Fig. 3.10(a)). For load levels where the shear slenderness of a continuous slab is smaller than the size of the isolated specimen, the rotation is also lower. It is also evident that the ultimate flexural strength of a continuous slab is higher than that of an isolated specimen due to the contribution of sagging yield lines in the failure mechanism (Fig. 3.8(d, f)). However, in a wide range of practical cases, punching occurs at loads below the flexural strength of an isolated specimen. The failure criteria of CSCT [Mut08b] for punching of slabs without shear reinforcement around columns with diameters of $c = d$ and $c = 4 \cdot d$ are shown in Figure 3.10(b) as examples. It can be seen that in these cases, the

strength and the deformation capacity of an isolated specimen are very similar to the behavior of a continuous slab.

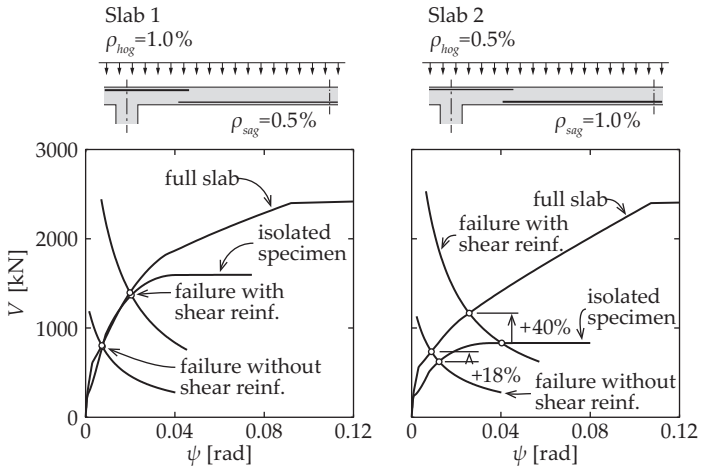

Figure 3.11 Comparison of punching strengths of two slabs with equal plastic moment capacity but different support and span reinforcement distribution (parameters: refer to Fig. 3.10)

On the other hand, in the case of slabs with very low amount of hogging reinforcement, neglecting the influence of sagging reinforcement can lead to a significant underestimate of the punching strength. Figure 3.11 shows an example of two slabs with equal yield line capacities. In the case of slab 1, the flexural reinforcement is placed according to an elastic calculation (leading to relatively high hogging moments), thus the amount of hogging reinforcement is chosen as twice the amount of sagging reinforcement in mid-span. Slab 2 is designed assuming significant plastic moment redistribution, with twice less hogging reinforcement on the support than sagging reinforcement in the span. It can be seen that the prediction of punching strength of the isolated element corresponds reasonably well to the strength of the continuous slab in the first case. In the case of the second slab, the flexural stiffness and therefore the punching strength are underestimated by the analysis based on the isolated element. The difference is even more significant for slabs with shear reinforcement (calculated with $k_{sys} = 2.8$ [FIB13, Fer09]). The isolated specimen representing only the hogging moment area may reach its flexural limit at a load level lower than the punching strength of a continuous slab. This kind of failure has been observed in punching tests of slabs with shear reinforcement even when using high flexural reinforcement ratios [Lip12]. Stein, Ghali and Dilger [Ste07] argued that the flexural capacity of a specimen should be chosen at least 70% higher than the predicted punching strength. However, this would lead to unrealistically high flexural reinforcement ratios for slabs with large amounts of highly efficient shear reinforcement, and lead to misleading conclusions about the necessary amount of flexural reinforcement in column regions. The current analysis demonstrates that the distinction between a punching shear and flexural failure cannot be made only based on isolated specimens as suggested by Stein *et al.* [Ste07].

3.2.4 Influence of compressive membrane action

Compressive in-plane forces delay the cracking of reinforced concrete in bending and stiffen the moment-curvature response of a cracked cross-section. The compression may result from prestressing [Cle14] or from restrained lateral expansion due to external rigid elements (like shear walls) or the rigidity of the surrounding slab portion. The numerical model allows analyzing all these cases by varying the boundary conditions of the axisymmetric slab.

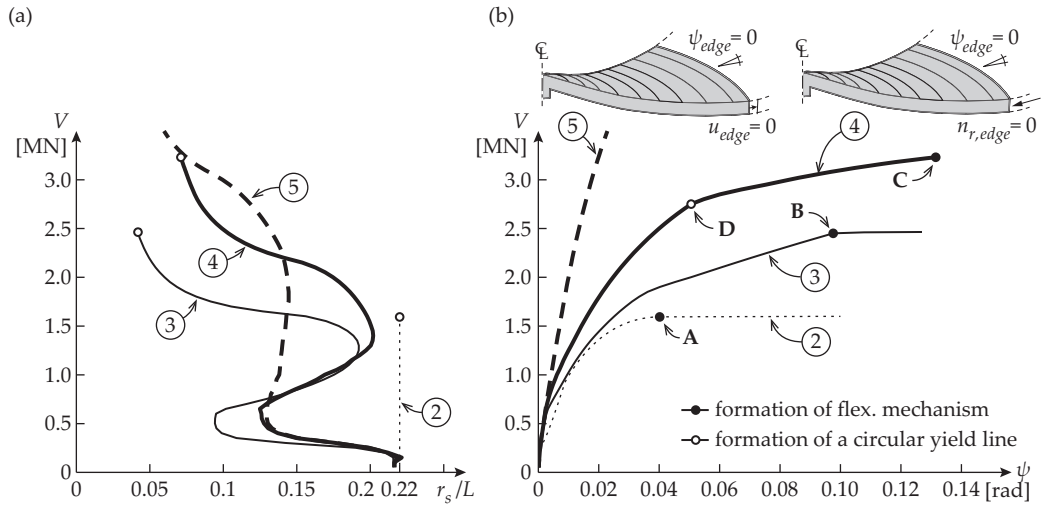

Figure 3.12 Effect of various levels of confinement on the response of a slab: (a) radius of the line of moment contraflexure; (b) load-rotation curves (parameters: refer to Fig. 3.10)

Figure 3.12(b) shows load-rotation curves for different boundary conditions. Curves 2 and 3 represent an isolated slab and a continuous slab with the influence of membrane effect neglected (Fig. 3.10(b)). Points A and B represent the formation of the flexural mechanism for the slabs (Fig. 3.8(d)). Curve 4 in Figure 3.12(b) shows the load-rotation response of a self-confined flat slab (free to dilate, no in-plane force applied at the outer edge). In this case, the compressive membrane force in the center part of the slab results from the tangential tensile forces in the outer portion of the slab (the tension ring). The flexural limit of the slab is reached when a full yield line mechanism (Fig. 3.8(f)) forms (point C). This occurs at both higher load and larger rotation than in the case of curve 3 due to the increased flexural capacity and curvature at yielding of a reinforced concrete slab (Fig. 3.4(b)). The stiffness of the response is also significantly higher up to the point D, which corresponds to the formation of a circular yield line due to yielding of radial sagging reinforcement. The yield line appears further from the column than in the case of curve 3 (point B) (Fig. 3.12(b)) because of the radial compression in the region closer to the column. The formation of this yield line does not produce a flexural mechanism because the radial hogging yield lines are not yet formed inside the circular one. The significantly reduced rotation at point D on curve 4 compared to the point B on curve 3 is explained by the presence of a region in the slab which is under radial compression that is high enough to prevent the cracking of concrete, therefore reducing the maximum rotation.

Curve 5 in Figure 3.12(b) shows the load-rotation response of a perfectly confined slab. Dilation is not allowed at the edges and therefore significant compressive forces are induced which increase towards the center of the slab. Unlike in the case of prestressed slabs where the normal force in the slab can be considered independent of the load, the compressive stress in the center of a perfectly confined slab increases with a rising load level and rotation. If concrete softening for large compressive strains was considered, the load would start decreasing because of the decreasing moment capacity under high axial compression. However, in the current analysis, this effect is neglected because of the bi-axial state of compression in the center of the slab. Geometrical second order effects are also not considered in this analysis. These effects would start decreasing the flexural strength at very large deflections [Bra80a].

3.3 Validation of the numerical model

Most punching tests found in literature have been performed on specimens that model the isolated hogging moment area of an actual continuous slab. Shear force can be applied by loading the column while the specimen is supported along its edges or by applying the load at the edges and supporting the specimen on a column in the center. This type of slab specimens only allows for redistribution between radial and tangential hogging moments (Fig. 3.8(e)). In order to also permit redistribution between hogging and sagging moments (that changes the location of the line of moment contraflexure as shown in Fig. 3.10(a)), multi-span slabs or members with in-plane and/or rotational restraints along the slab edges have to be tested.

In this section, the numerical model is applied to predict the deformations of specimens in some unconventional punching tests reported in the literature. Only the tests on slabs thicker than 100 mm are considered as the punching shear phenomenon is known to exhibit significant size effect and the results of experiments on very thin elements are difficult to extrapolate to a realistic scale (also, small variations in placing of reinforcement may lead to significant strength variations). Tests on isolated slabs with confining elements (like [Bel15]) are also excluded from the analysis because the stiffness of a steel confinement ring is typically much smaller than the stiffness of a reinforced concrete tension ring in a continuous slab. Therefore, the arising axial forces are low and do not influence the response of the slab in a significant manner. The contribution of such elements can mainly be seen as related to an increase of the flexural strength.

The punching strengths are predicted using failure criterion of CSCT [Mut08b]. The failure criterion may be modified to include the beneficial influence of the axial compressive forces acting on the control perimeter [Cle14], which can also be obtained from the numerical analysis. The capacity obtained in this manner is also presented for the applicable cases. For comparison purposes, the slabs are also modeled as conventional isolated specimens, where the size of the specimen r_s is chosen to correspond to the edge of the elastic hogging moment area.

3.3.1 Test by Ospina *et al.*

One such test was performed by Ospina *et al.* at the University of Alberta (Canada) as a part of an experimental study on the behavior of concrete slabs strengthened or rehabilitated after punching failure [Osp01]. The test slab ER1-VS was square with side length of 4.2 m, thickness h = 152 mm and had a measured average effective depth d = 109 mm and 119 mm for top and bottom reinforcement, respectively. The slab had 400 mm square column stubs in the center protruding 300 mm above and 330 mm below the slab. Mean cylinder (152 x 304 mm) concrete strength at the time of testing was 29.8 MPa and maximum aggregate size 19 mm.

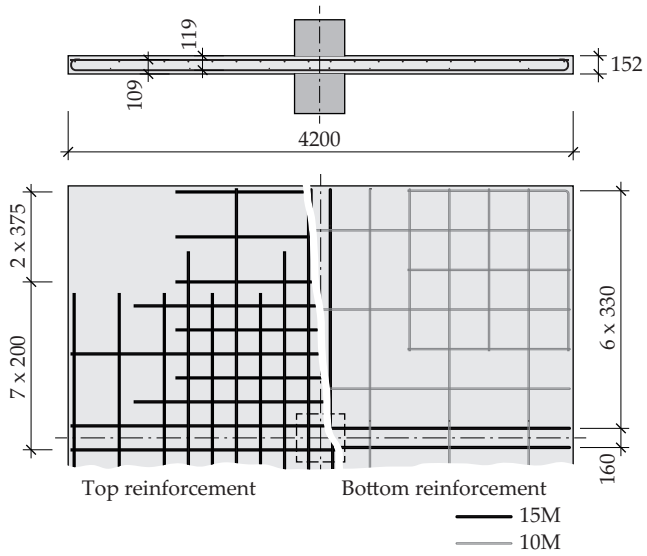

Figure 3.13 Reinforcement layout of the specimen (dimensions in mm)

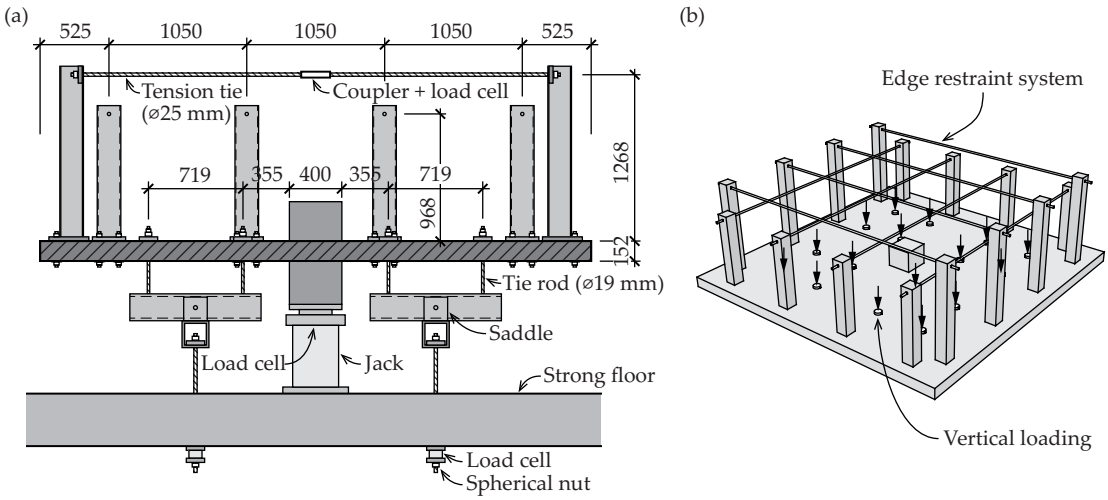

Figure 3.14 Test setup: (a) section cut; (b) view of the test specimen and the edge restraint system (dimensions in mm)

As the study was focused on rehabilitation of old structures, the flexural reinforcement of the slab was designed to comply with the requirements of ACI 318-71 [ACI71] in terms of minimum slab thickness and amount of reinforcement as well as distribution of design flexural moments (using the direct design method) and per CSA A23.3-94 [CSA94] in terms of cut-off points, development length and integrity steel. Top reinforcement (refer to Fig. 3.13) consisted of 15M (A_s = 200 mm²) and 10M (A_s = 100 mm²) bars (with yield strengths of 428 MPa and 441 MPa, respectively). The top reinforcement was concentrated in the center of the slab, so that the reinforcement ratio varied from 0.92% within column-wide strips to 0.25% close to the edges. The bottom reinforcement was more uniformly distributed – the reinforcement ratio was 0.25%, except in the column strips where two 15M (A_s = 200 mm² each) integrity bars were placed. However, only half of the bottom bars were continuous along the whole slab with the other half being cut in the middle. All bottom bars were developed with 180 degree hooks, whereas the top bars had straight ends.

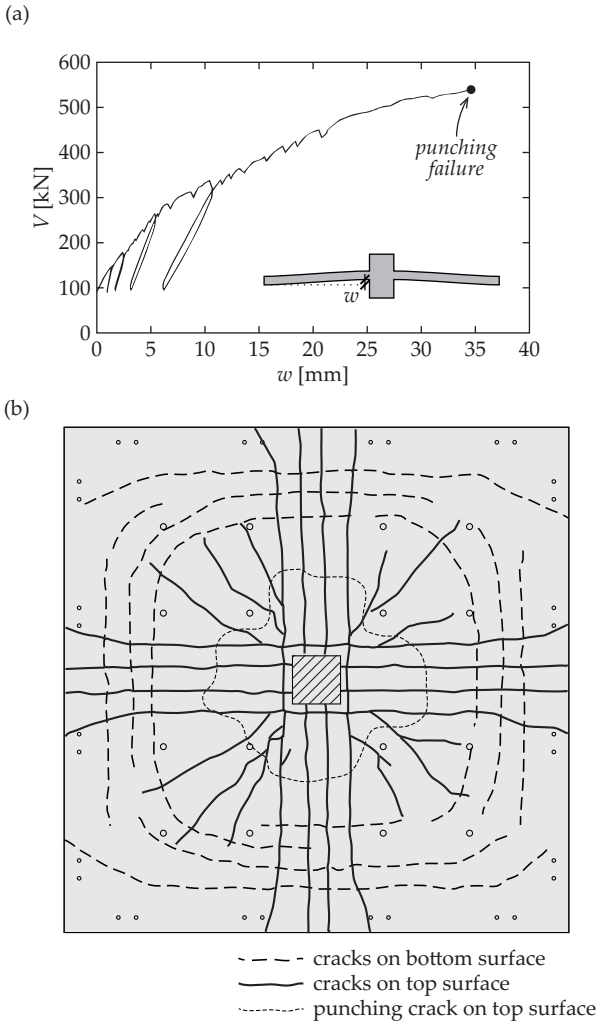

Figure 3.15 Specimen ER1-VS [Osp01]: (a) load-deflection response; (b) cracking pattern after the punching failure

Rotations of the edges of the test slab were restrained by a system consisting of four steel square hollow columns bolted down to the slab along each side and connected at the top with steel tie rods (Fig. 3.14). The load was applied by jacking up the central column stub and restraining the displacement in 16 equally loaded points. Prior to the start of the test, the edge restraining system was prestressed to provide moment distribution similar to that in a corresponding continuous slab under self-weight (assuming that the sections where the steel columns were fixed represented span center lines). The test slab was brought up to punching failure after imposing five load cycles. The cyclic loading intended to simulate conditions in an actual slab due to service loads.

The first observed cracks were flexural cracks that formed on the slab top surface at a load of 96 kN, barely above the self-weight of the slab and the testing apparatus (89 kN). The cracks formed along the two centermost bars of the topmost reinforcement layer. These cracks progressed from the column towards outer slab regions followed by similar cracks along the other axis and reached the edge of the slab at approximately 260 kN. This point can be seen as a change in the slope of the load-deflection curve (Fig. 3.15(a)). The first yielding of top reinforcement according to strain gauge measurements was observed around the column at 386 kN and the first yielding of bottom bars occurred at 448 kN. A sudden punching failure took place at a load of 542 kN. The crack pattern after the failure is shown in Figure 3.15(b).

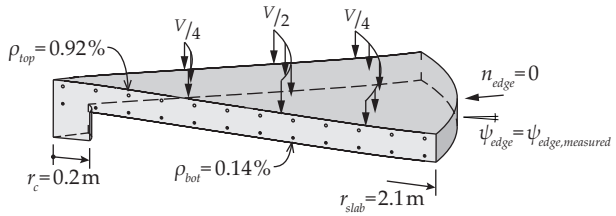

Figure 3.16 Axisymmetric numerical model of ER1-VS [Osp01]

The behavior of the test specimen ER1-VS was compared to the response calculated with the numerical model. The geometry of the slab, including the distribution of reinforcement, was assumed to be axisymmetric (with the radius of the axisymmetric model r_{slab} equal to half of the slab width) and top and bottom reinforcement ratios constant over the whole slab (Fig. 3.16). The influences of rotational edge restraint and compressive membrane action (CMA) were analyzed separately by performing two numerical analyses. At first, a simpler model was considered that did not account for in-plane forces and deformations. The only applied edge condition was edge rotation (that was required to correspond to the measured value). Therefore, only the effect of redistribution between sagging and hogging moments was modeled. In the second model, the influence of axial deformations due to cracking of concrete and consequent membrane forces (with their influence on axial deformations) was taken into account as well. The second edge condition applied was that the axial force at the edge of the slab was required to be zero (actually, a negligibly small axial compression equal to the force in the tension ties was present in the tested slab).

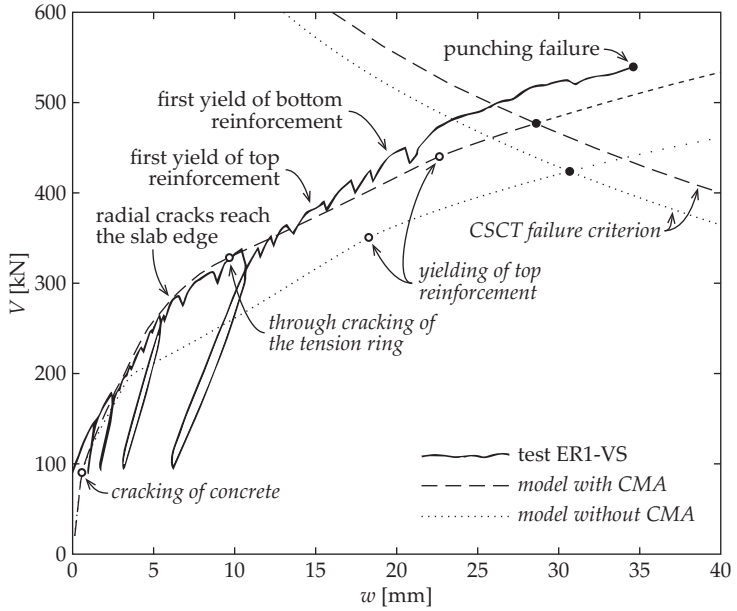

Figure 3.17 Comparison of measured and predicted response (slab ER1-VS [Osp01]) with the failure criterion of CSCT (the failure criterion curves are different for the models with CMA and without CMA due to the different deformed shapes of the slabs, where an equal rotation at the line of moment contraflexure ψ leads to different deflections w)

Figure 3.17 shows the resulting load-deflection curves from the two analyses together with the observed response curve. Prior to first flexural cracking (predicted at 91 kN), dilation of the slab is zero and no membrane force is generated. Therefore, in this range, both models predict the same response. After cracking, the cracked portion of the slab starts to dilate but the dilation is restrained by the uncracked part of the slab around it. Thus, in the model with CMA, a tension ring develops close to the edge of the slab. This induces compressive forces in the hogging moment area which stiffens the response compared to the model without CMA. At 325 kN, stresses in the tension ring reach the tensile strength of concrete over the whole slab thickness, leading to through cracking of the tension ring. After this, the rate of increase of compressive stress in the hogging moment area decreases significantly. The tangent stiffnesses of the curves are similar, but the second model shows considerably smaller deformations at a given level of load. Yielding of top reinforcement at the face of the column is predicted at 350 kN in the first model and at 440 kN in the second. Punching failure is predicted to occur at the intersection between the response curve and the failure criterion of the CSCT [Mut08b] at 420 kN when CMA is neglected and at 475 kN when CMA is accounted for (the failure criterion is defined as a function of slab rotation but plotted for deflection of the prediction models in Figure 3.17). The actual punching failure occurred at 542 kN, slightly higher than predicted, possibly due to the effect of compressive stresses in the punching perimeter that were not accounted for in the failure criterion.

A comparison between the observed and predicted load-deflection curves in Figure 3.17 shows a very good agreement between the experimental results and the calculation that includes the CMA effect. Differences between the predicted and observed cracking and yielding loads can be ex-

plained by the differences between the axisymmetric simplification of the numerical model and the actual geometry, where column corners, orthogonal layout of reinforcement and load application points can cause concentrations of stresses and deformations. Local stress concentrations may also explain the observed yielding of bottom reinforcement, although the numerical model does not predict it before the punching failure.

The numerical model predicts the formation of a thoroughly cracked tension ring along the perimeter of the specimen. This effect explains the observed propagation of top surface radial cracks to the specimen's edge, even though the measured edge rotation is small and thus the tangential moment should not cause cracking. The cracks at the edge of the slab at rather low levels of load therefore indicate that tensile axial force is present in the cross-section.

Table 3.1 Modeling parameters of tests of Ospina *et al.* [Osp01], Choi and Kim [Cho12], Clément *et al.* [Cle14], Chana and Desai [Cha92] and Ladner *et al.* [Lad77]

Ref.	Test	f_c, [MPa]	f_y, [MPa]	A_{sw}, [mm²]	ρ_{hog}, [%]	ρ_{sag}, [%]	h (d), [mm]	r_c, [mm]	r_{slab} (r_s), [mm]	Edge conditions
[Osp01]	ER1-VS	29.8	428	-	0.92	0.14	152 (109)	200	2100 (1500)	ψ_{edge} [rad] = $9.0 \cdot 10^6 \cdot V$ [MN] n_r =0
[Cho12]	MRA	37.0	404	-	1.06	0.31	152 (121)	178	2100 (1500)	ψ_{edge} [rad] = $6.67 \cdot 10^6 \cdot V$ [MN] n_r =0
	MRB	30.5			0.83	0.43				
	MRC	34.6			0.58	0.57				
[Cle14]	PC1	44.0	583	-	0.84	1.06	250 (192)	130	1611	
	PC2	45.3	549		1.64	1.05	250 (192)			
	PC3	43.8	591		0.83	1.65	250 (194)			
	PC4	44.4	602		1.65	2.00	250 (190)			
[Cha92]	FPS1	21.4	500*	-	0.85 0.27**	0.85 0.55**	250 (210)	200	4500 (1320)	$m_{r,edge}$ = 0 n_{edge} = 0 w_{edge} = 0
	FPS2	27.4		942						
	FPS3	27.2		402						
	FPS4	30.7		1257						
	FPS5	25.8		1570						
[Lad77]	C6	44.4	550	-	1.80	0.94	110 (80)	50	1680 (528)	$m_{r,edge}$ =0 n_{edge} =0
	C7							120		
	C10							100		
	C11							160		

* – nominal value, ** – outside of r = 1925 mm

3.3.2 Tests by Choi and Kim

Choi and Kim [Cho12] performed three tests on 4.2 x 4.2 m slabs with rotationally restrained edges using the same test setup as Ospina *et al.* [Osp01] (Fig. 3.14). The test campaign focused on studying the effect of moment redistribution in continuous slabs. The amounts of reinforcement of the slabs were designed to provide similar flexural capacities but the proportions between the sagging and hogging reinforcement ratios varied significantly, from 3.5:1 to 1:1 (refer to Table 3.1 for details). The load was applied in three steps, on each step in a cyclic manner (ΔV = 100 kN). The rotation of the edges was partially restrained by steel columns connected by steel ties on top identical-

ly to the experiments of Ospina *et al.* [Osp01] (Fig. 3.14). The edge rotation and the forces in the ties were measured which allowed calculating edge moments.

Despite the variation in the distribution of reinforcement, the observed punching strengths for the three specimens were similar (refer to the results given in Table 3.2). This observation contradicts the predictions of empirical design models (such as the one used in Eurocode 2 punching provisions [CEN04]) that have been established on the basis of isolated elements and thus consider only the influence of hogging reinforcement, predicting lower capacities for slabs with lower amount of reinforcement (such as MRC in comparison to MRA in Fig. 3.18). The influence of sagging reinforcement was, however, correctly predicted by the numerical model (that took into account the influence of in-plane forces). For the slabs tested by Choi and Kim, the increase of the amount of sagging reinforcement and compressive membrane action were sufficient to compensate for the decrease of hogging moment capacity and provide similar punching shear strengths in spite of the very different hogging reinforcement ratios. It should be noted that the experimental failure loads were consistently lower than predicted (Table 3.2), likely due to the influence of the cyclic loading sequence – all specimens failed during cycling the applied load between 80–100% of the maximum load (even a low number of cycles at load levels close to the shear capacity is known to noticeably reduce the shear strength [Nat15]).

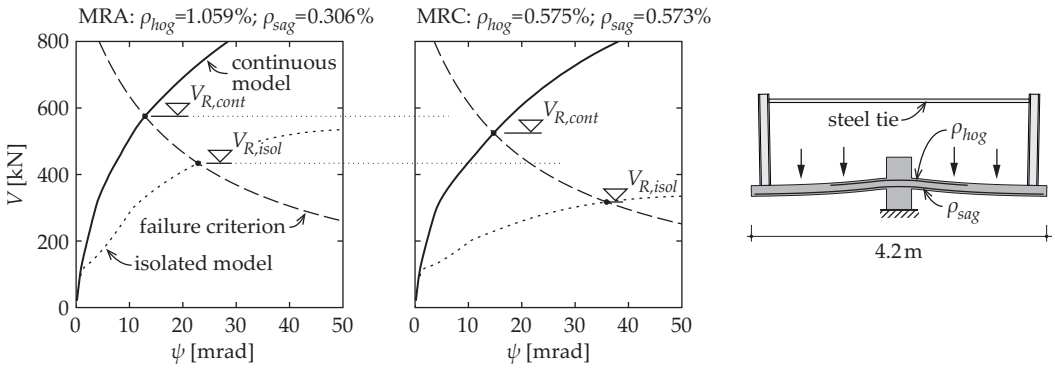

Figure 3.18 Comparison of the numerical model to the experimental results, specimens MRA and MRC of Choi and Kim [Cho12]

3.3.3 Tests by Clément *et al.*

Clément *et al.* [Cle14] performed four tests on square 3 x 3 m slabs with thickness of 250 mm (Table 3.1). Sagging moment was applied at the edges of specimens by means of stiff L-shaped steel elements and hydraulic jacks between them (refer to Fig. 3.19(a)). Shear force was applied close to the edge of the slab with a separate set of jacks. The moment was increased proportionally to the shear force up to a previously defined limit. The numerical model is able to predict the flexural response of the slabs with a very satisfactory precision (Fig. 3.19(b)). It can also be noted that the influence of in-plane forces is less significant in this test series due to the smaller extent of the sagging moment area and therefore a narrower tension ring. A parametric analysis with variable edge moment and a comparison to the test results on Figure 3.19(c) show that for this series, the edge

moment has a significant influence on the punching strength. The influence of accounting for the in-plane forces becomes more significant with increasing edge moment. In addition, due to the beneficial influence of edge moment (sagging moment in actual slabs) and in-plane compression, punching strength of continuous slabs is less dependent on the hogging reinforcement ratio than in the case of isolated specimens without edge restraints (refer to the decreasing gap between the curves for ρ = 1.64% and 0.84%).

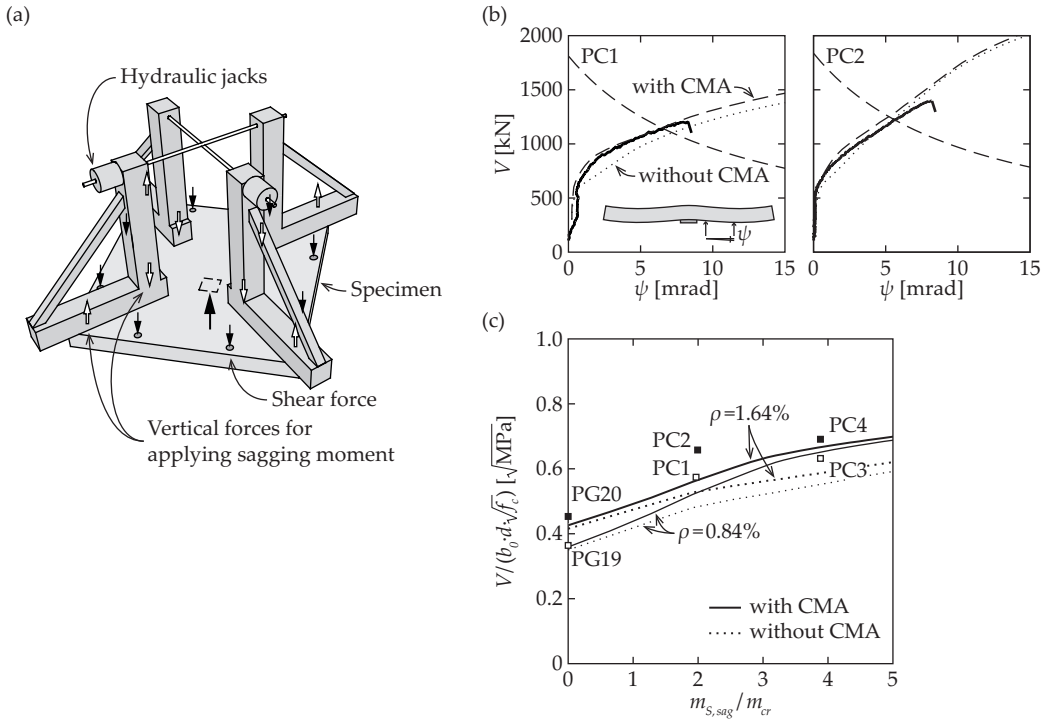

Figure 3.19 Tests by Clément *et al.* [Cle14]: (a) moment application frame; (b) comparison between the flexural responses of the test specimens and the model predictions; (c) punching strength of the specimens as a function of applied edge moment

3.3.4 Tests by Chana and Desai

Chana and Desai [Cha92] tested five 9 x 9 m full-size slabs; four of which were equipped with shear reinforcement. The slabs were supported on a column in the center and on a linear support at the perimeter (Fig. 3.20). The perimeter support allowed both rotation and horizontal displacement. The load was applied in eight points placed at a radius of 1.2 m from the center. All the slabs had similar concrete strengths, the other parameters were identical. Figure 3.20 shows the predicted load-deflection response from the numerical model compared to the measured deflections. A load-deflection curve for the corresponding isolated element is also shown. It can be seen that the edge-restrained model predicts the deflections correctly, whereas the deflections of the isolated specimens exceed the measured values several times. Due to this, all the punching loads are significantly underestimated by the isolated model (Table 3.2). The edge-restrained model slightly overestimates the strength of the slab without shear reinforcement. Regarding the slabs with shear rein-

forcement, where the stresses in shear reinforcement units are predicted to remain low due to small slab rotation (refer to the activation phase of shear reinforcement in Fig. 2.7(a)), the capacitites of the specimens are underestimated by the CSCT.

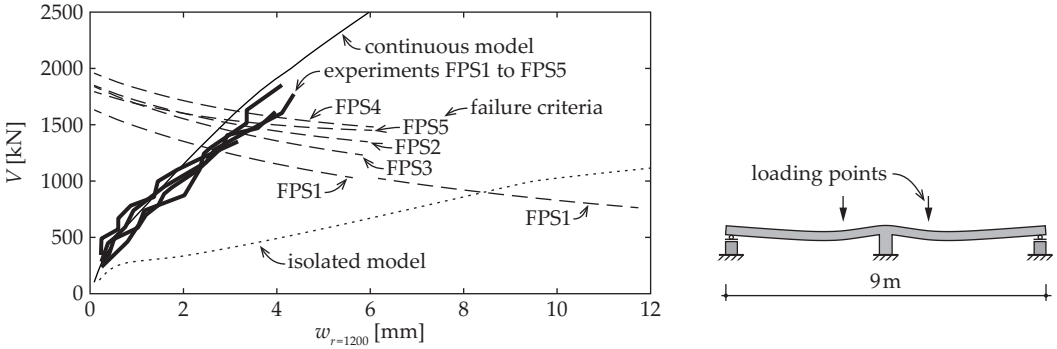

Figure 3.20 Load-deflection curves of specimens of Chana and Desai [Cha92]

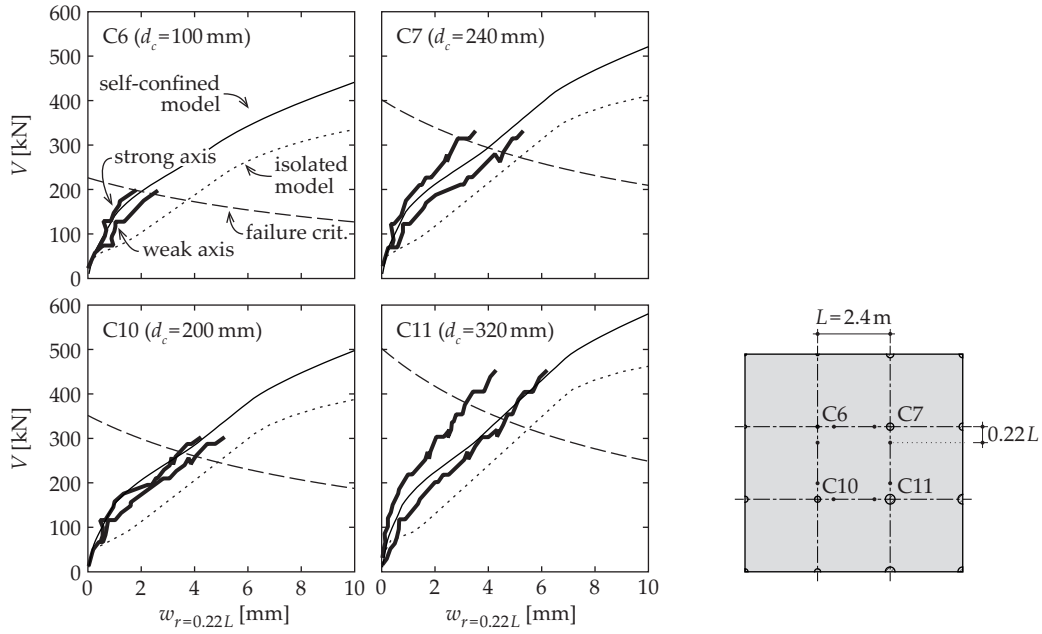

Figure 3.21 Column reaction-deflection curves of the experiment of Ladner *et al.* [Lad77]

3.3.5 Tests by Ladner *et al.*

Ladner *et al.* [Lad77] performed tests on a 7.2 x 7.2 m slab supported on 16 columns of different sizes. The slab was loaded with uniform pressure to the failure of a slab-column connection. After each failure, the slab was repaired and the loading was continued, until all the connections had failed in punching. In addition to the reaction force at each column, the deflection of the slab was measured at different points under the slab. Figure 3.21 compares the measured deflections around the interior columns on the strong and on the weak axis to the curves predicted by the numerical model. Also presented are the failure criterion of CSCT and the load-rotation curves of corresponding isolated elements [Mut08b]. It can be seen that the numerical model predicts the

deflections very well, whereas the calculations that are based on isolated elements always underestimate the stiffness. The predictions of punching strength that are based on the deformations of isolated hogging moment areas are more conservative because of the deflections that are overestimated in this model (Table 3.2).

3.3.6 Summary of the comparisons

A comparison of the punching strengths predicted using differnet models is given in Table 3.2. The calculations are performed using the following approaches:

- V-ψ according to the Model Code 2010 [FIB13];
- V-ψ of an isolated element according to the 4-linear model [Mut08b];
- V-ψ of the presented continuous model, taking into account the effect of moment redistribution but neglecting the influence of in-plane forces;
- V-ψ of the presented continuous model, taking into account both the effect of moment redistribution and the membrane action;
- V-ψ of the presented continuous model, taking into account both the effect of moment redistribution and the membrane action, with a failure criterion with modified rotation ψ' [Cle14] (Eq. 2.2).

Table 3.2 Comparison between the test results and predictions based on isolated elements and continuous slabs

Ref.	Test	$V_{R,test}/b_0 d \sqrt{f_c}$ [√MPa]	$V_{R,test}/V_{R,pred}$ (isolated)	$V_{R,test}/V_{R,pred}$ (continuous, without CMA)	$V_{R,test}/V_{R,pred}$ (continuous, with CMA)	$V_{R,test}/V_{R,pred}$ (continuous, modified crit.)
[Osp01]	ER1-VS	0.469	1.53	1.29	1.14	1.13
[Cho12]	MRA	0.345*	1.06*	0.88*	0.80*	0.76*
	MRB	0.327*	1.07*	0.87*	0.77*	0.73*
	MRC	0.335*	1.36*	1.00*	0.82*	0.77*
[Cle14]	PC1	0.574	-	1.17	1.10	1.04
	PC2	0.658	-	1.24	1.20	1.11
	PC3	0.632	-	1.07	0.98	0.83
	PC4	0.690	-	1.12	1.05	0.85
[Cha92]	FPS1	0.558	1.36	1.13	0.94	-
	FPS2	0.608	1.29	1.23	0.99	-
	FPS3	0.716	1.68	1.34	1.21	-
	FPS4	0.771	1.61	1.41	1.25	-
	FPS5	0.805	1.50	1.35	1.26	-
[Lad77]	C6	0.574	1.18	1.09	1.03	0.94
	C7	0.658	1.27	1.22	1.15	1.07
	C10	0.632	1.28	1.22	1.14	1.08
	C11	0.690	1.46	1.44	1.33	1.26
		mean	1.42	1.24	1.13	1.03
		COV	12 %	9 %	10 %	13 %

* – cyclic tests, not included in the calculation of mean and coefficient of variation

3.4 Parametric analysis

In the previous sections, a model was introduced that allowed describing how slab continuity and compressive membrane action influence the flexural deformations and punching capacity of actual flat slabs. In the current section, results of a parametric study are presented, which analyzes the influence of several factors on the prediction of the punching capacity of a self-confined (without external confining elements) continuous slab. The punching strengths are calculated using the same five approaches listed in Section 3.3.6.

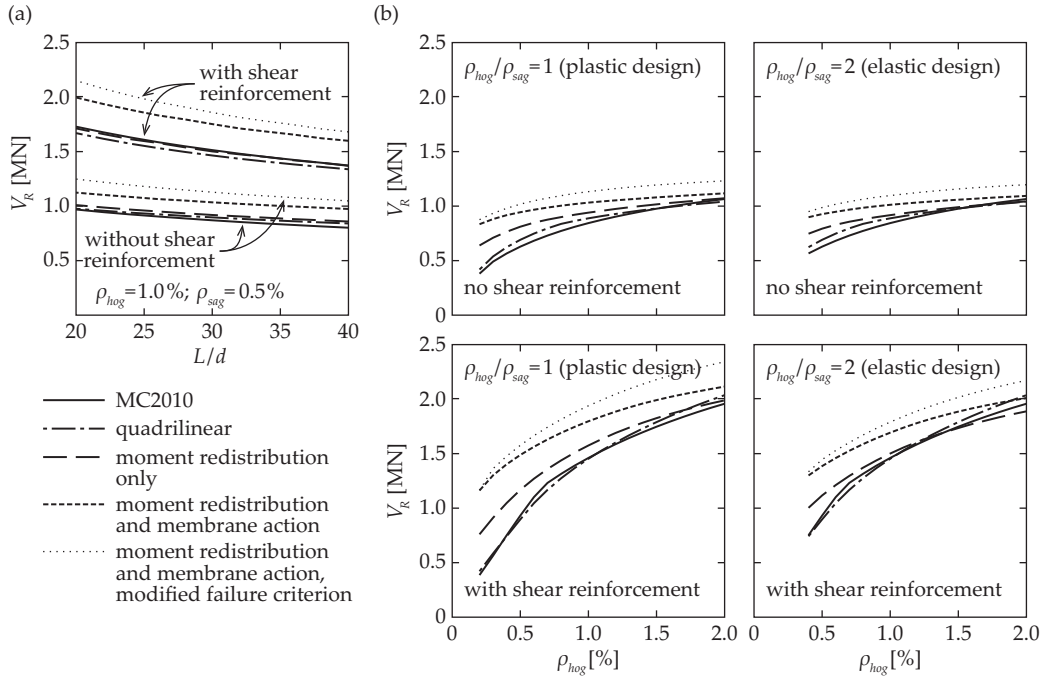

Figure 3.22 Parametric study: (a) influence of slenderness; (b) influence of the hogging reinforcement ratio and the amount of sagging reinforcement, for slabs without shear reinforcement and for slabs with large amounts of double-headed stud shear reinforcement (parameters: L = 7 m; h = 250 mm; d = 210 mm; c = 350 mm; f_c = 35 MPa; f_y = 550 MPa; β = 0.6; d_g = 16 mm)

Figure 3.22(a) shows the influence of slab slenderness L/d on the punching capacity. Although the slenderness effect is not taken into account in many codes of practice [CEN04, ACI14], it is well known [Sta01] and can be successfully accounted for by using the CSCT [Mut08b] or the Model Code 2010 [FIB13]. All the studied methods show a similar influence of the slab slenderness on the punching strength. The effect can be seen to be more important for slabs with shear reinforcement.

Figure 3.22(b) shows the influence of the hogging reinforcement ratio on the punching strength. The presented curves are for slabs without and with shear reinforcement (maximum punching shear resistance due to concrete crushing (k_{sys} = 2.8)). Two possible design cases are investigated. First, a case where the amount of sagging reinforcement equals to the amount of hogging reinforcement (plastic design) and a second case where the amount of sagging reinforcement is half of

the amount of hogging reinforcement (corresponding to a typical elastic design). The ratio of hogging reinforcement is known to have an important influence on the stiffness and punching strength of isolated test specimens and the influence is considered in many codes of practice [CEN04, FIB13]. However, other design codes [ACI14] neglect its influence. The present analysis shows that in the case of low hogging reinforcement ratios, the flexural and axial stiffness of the surrounding portion of the slab might be able to stiffen the load-rotation response in a considerable manner and therefore reduce the influence of hogging reinforcement ratio on the punching capacity of continuous slabs.

The influence of the amount of sagging reinforcement on punching strength is currently not included in design codes [CEN04, ACI14, FIB13]. However, comparing the curves corresponding to plastic and elastic designs in Figure 3.22(b) indicates this factor may nevertheless have an importance. In the presented example, doubling the amount of sagging reinforcement led to a punching strength increase of approximately 5% for slabs without shear reinforcement and up to 10% for slabs with shear reinforcement. This increase may be useful, for example in the assessment of existing structures.

3.5 Influence of shrinkage and creep

The present model of self-confined slabs assumes that the axial force at the edge of the slab is zero and the compressive membrane action arises only by the confinement provided by the slab itself. In actual non-prestressed slabs, compressive in-plane stresses can also arise when the dilation of the slab is restricted to some extent by adjoining structural elements such as walls, stiff columns or edge beams that induce compressive axial force at the edge of the slab. Therefore, the actual behavior of a slab should mainly fall between that of a perfectly confined and a self-confined slab (Fig. 3.23(a)).

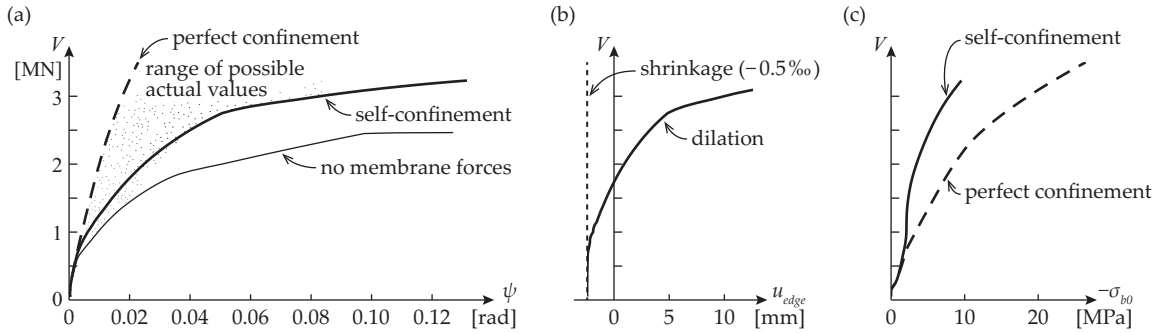

Figure 3.23 Influence of shrinkage: (a) load-rotation curves; (b) edge displacements due to shrinkage and due to slab dilation caused by cracking; (c) compressive stresses in the center of the slab in self-confined and fully confined cases (parameters: refer to Fig. 3.10)

However, it should be noted that shrinkage of concrete may reduce the compressive force in the slab. In the case where lateral shrinkage (relative to that of adjoining elements) is larger than the dilation caused by cracking, tensile restraining forces may appear at the edge of the slab instead of

compressive forces. This reduces the efficiency of the compressive membrane action (the actual response tends to the curve with no membrane action in Figure 3.23(a)). The influence of this phenomenon is illustrated in Figure 3.23(b), where the dilation of a self-confined slab is compared to the corresponding displacement at its edge due to a shrinkage strain of 0.5‰. For low levels of load, the influence of shrinkage exceeds that of dilation, thus potentially reducing the compressive membrane forces (which will be smaller than those shown in Fig. 3.23(c) for self-confined slabs). In these cases, curve with no membrane forces provides a safe estimate of the actual behavior. For higher levels of rotation, the shrinkage strains will be compensated by the dilation of cracked concrete and compressive membrane forces may again appear. However, in many cases, a self-confined model with zero axial force at the edge of the slab can be regarded as a lower bound of the confinement effect for actual flat slabs.

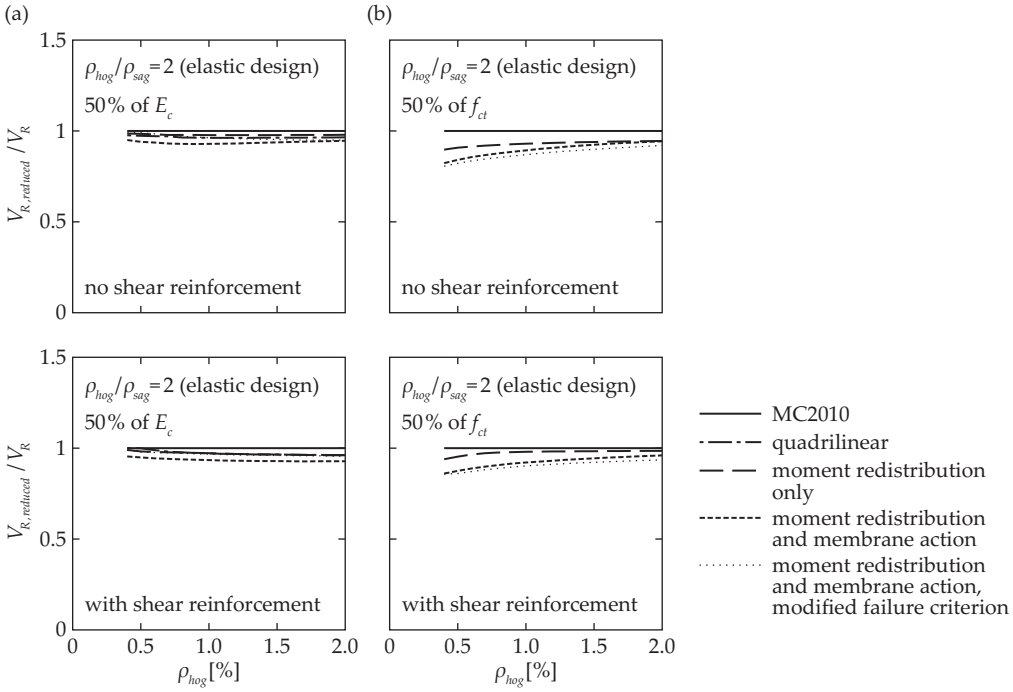

Figure 3.24 Parametric study: (a) influence of reduced modulus of elasticity of concrete; (b) influence of reduced tensile strength of concrete, for slabs without shear reinforcement and for slabs with large amounts of double-headed stud shear reinforcement (k_{sys} = 2.8, concrete crushing criterion governing) (parameters: refer to Fig. 3.22)

Long-term behavior of flat slabs is influenced by creep of concrete that will lead to an increase of slab rotation and potential decrease of the punching strength (as follows from the failure criterion of CSCT), at least in the case when the increase of strength of concrete in time is not taken into account. The presented approach can be used in a simplified manner to model the effect of creep by using a reduced value of modulus of elasticity of concrete $E_c/(1+\phi)$ (where ϕ refers to the creep coefficient and low variations of concrete stresses are assumed during the creep process) for calculating the deformations due to long-term loads. In Figure 3.24(a), the predicted punching resistances calculated with E_c are compared to predictions obtained with 50% E_c (to account for a

reduced influence of creep effects in the cases where the ratio between permanent and maximum loads is lower than one). The reduced stiffness is observed to reduce the punching strength similarly for both isolated slabs (up to 4%) as well as for continuous slabs with no membrane effect (up to 5%) and self-confined slabs (up to 7%). Therefore, it seems that tests on isolated specimens could be suitable for further studies on the influence of creep on punching strength of flat slabs.

The axial stiffness of the tangential tension ring that confines the hogging moment area in a self-confined slab is largely provided by the contribution of uncracked concrete in the tension ring. This effect is referred to as tension stiffening [Mar98] and it can significantly increase the axial stiffness of the slab. It follows that the value of the tensile strength of concrete f_{ct} has a significant influence on the punching strength predictions for continuous slabs. In order to illustrate this, Figure 3.24(b) shows the influence of reducing the value of f_{ct} two times. However, for design purposes, average value of concrete tensile strength (f_{ctm}) should be used.

3.6 Summary and conclusions

In this chapter, a numerical method was presented for determining the load-deformation response of axisymmetric slabs. This model allows quantifying the influence of moment redistribution and the development of compressive membrane action in a continuous flat slab around interior columns. The model was validated by comparing its predictions to the results of punching tests with unconventional edge conditions. In combination with the failure criterion of the CSCT, the presented method is able to predict the punching strength of interior columns in continuous flat slabs.

The main conclusions are:

- Flexural behavior may be different in actual flat slabs than in isolated test specimens. Therefore, punching tests on such specimens may not always correctly represent the strength of actual slabs, especially in the case of large columns and the presence of shear reinforcement.

- The flexural capacity of a continuous slab is higher than of an isolated element for the same amount of hogging reinforcement. The stiffness of the load-deformation response also normally increases due to a reduction of the shear slenderness and the influence of compressive membrane action. Nevertheless, these effects do not seem to be accounted for in the punching provisions of current design codes.

- Compressive membrane action may arise from the restraint against the expansion of the slab provided by stiff surrounding structural elements but also due to the restraint against the expansion of the hogging moment area provided by the in-plane stiffness of the sagging moment area. This effect does not require any external confinement, is not sensitive to imposed deformations such as shrinkage and can therefore be considered as a lower bound of the behavior for actual continuous flat slabs.

- Due to the effects described above, the deflections of a continuous flat slab are smaller than the ones of a corresponding isolated specimen. This leads to lower crack widths and potentially larger punching strength.
- These aspects lead to potentially higher safety margins on the design for punching strength around interior columns of actual flat slabs than presumed in the current codes of practice as the provisions of those have been calibrated using tests on isolated specimens. Such increase in strength should be considered, particularly for the assessment of existing structures in order to avoid unnecessary strengthening.
- The Model Code 2010 punching previsions that are based on the CSCT can be adapted to take these effects into account. A numerical approach is presented in the current chapter. Comparisons to test results confirm the pertinence of these aspects.

Chapter 4 Simplified analytical model

The numerical model introduced in the previous chapter is able to succesfully predict the flexural response of edge-restrained specimens. This chapter presents background information for a simplified analytical approach derived on the basis of the numerical model that can predict the load-rotation response of continuous self-confined slabs. The model was also presented in a paper accepted for publication in *ACI Structural Journal* [Ein16c]. It is derived using idealized distribution of internal forces and deformations in flat slabs around inner slab-column connections. The predictions of the simplified analytical model are also compared to the results of numerical modeling.

4.1 Isolated specimens

4.1.1 Load-rotation curve

According to the Critical Shear Crack Theory (CSCT), punching failure of a slab-column connection occurs when the slab rotation, caused by loading, reaches a critical value [Mut08b]. For continuous or confined slabs, the load-rotation relationship can be calculated using the numerical model presented in the previous chapter. In the case of isolated test specimens, the flexural response can also be calculated from the moment equilibrium equation of an axisymmetric slab sector [Kin60, Mut08b]:

$$V = \frac{2\pi}{r_q - r_c}\left[m_r\left(\frac{\psi}{r_0}\right)\cdot r_0 + \int_{r_0}^{r_s} m_t\left(\frac{\psi}{r}\right)dr \right] \tag{4.1}$$

However, for using the CSCT in engineering practice, a simpler model was needed. Muttoni has thus proposed a simplified relationship for approximating the load-rotation curve of isolated slab elements [Mut08b, Mut13]. This formula is also used for predicting the slab rotation is the punching provisions of Model Code 2010 [FIB13]:

$$\psi_{isol} = 1.5\cdot\frac{r_s}{d}\frac{f_y}{E_s}\cdot\left(\frac{V}{V_{flex}}\right)^{3/2} \tag{4.2}$$

Equation (4.2) includes physical parameters r_s (radius of the hogging moment area) and V_{flex} (flexural strength the isolated hogging moment area). These parameters can be adapted for continuous or confined slabs. The radius of the isolated element r_s can be substituted with the distance to the line of moment contraflexure in continuous slabs which, as shown in the previous chapter, actually varies as a function of slab deformations. The flexural capacity V_{flex} can be calculated accounting for the influence compressive in-plane forces due to compressive membrane action (CMA) on the flexural capacity. The level of in-plane compression also varies depending on slab deformations.

For continuous or confined slabs, Equation (4.2) thus becomes:

$$\psi_{isol} = 1.5 \cdot \frac{r_s(\psi)}{d} \frac{f_y}{E_s} \cdot \left(\frac{m_{S,hog}}{m_{R,hog}(\psi)} \right)^{3/2} \tag{4.3}$$

where $r_s(\psi)$ and $m_{R,hog}(\psi)$ are non-linear functions of slab rotation ψ. In Equation (4.3), the ratio (V/V_{flex}) is expressed as the ratio of average acting hogging moment in the support strip (calculated with a linear-elastic model) to the hogging moment resistance of the slab ($m_{S,hog}/m_{R,hog}$), as $V_{flex,isol}$ is proportional to $m_{R,hog}$ when linear-elastic slab response is assumed.

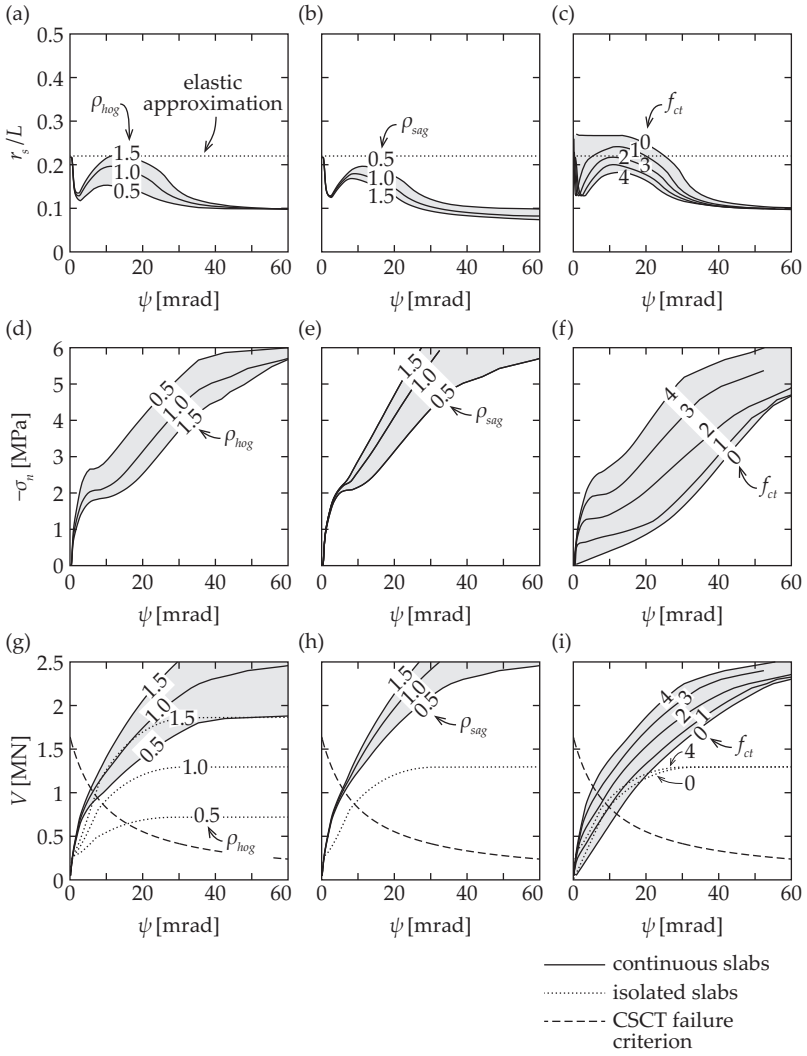

Figure 4.1 Parametric analysis on continuous self-confined slabs in comparison to isolated specimens: (a–c) influence of ρ_{hog} [%], ρ_{sag} [%], and f_{ct} [MPa] on the position of the line of moment contraflexure; (d–f) influence of ρ_{hog} [%], ρ_{sag} [%] and f_{ct} [MPa] on the development of compressive stresses in the perimeter of the column; (g–i) influence of ρ_{hog} [%], ρ_{sag} [%] and f_{ct} [MPa] on the load-rotation curves (parameters, if not shown otherwise: L = 7 m, h = 250 mm, d = 210 mm, c = 350 mm, f_c = 35 MPa, f_{ct} = 3.2 MPa, f_y = 420 MPa, d_g = 16 mm; ρ_{hog} = 1.0%; ρ_{sag} = 0.5%)

Figure 4.1 shows the influence of the amount of reinforcement and its distribution, as well as the tensile strength of concrete, on the response of self-confined continuous slabs. The first row shows, as a function of slab rotation, the distance between the center of the column and the line of moment contraflexure (r_s) due to non-linear response of the slab. As was also shown in the previous chapter, this distance is close to the elastic approximation of $0.22\,L$ in the elastic phase before cracking and also in the phase where both hogging and sagging moment areas are cracked and the stiffnesses are therefore similar. In the phases where the stiffness of the hogging moment area is smaller compared to that of the sagging moment area (due to concrete cracking or reinforcement yielding), its size also decreases.

The second row shows the generated in-plane average compressive stresses (that could potentially increase the hogging moment resistance) in a slab around the slab-column connection. This compression only appears after cracking of the slab and increases with increasing slab rotation as it is generated by the dilation of the slab due to cracking (unlike prestressing that delays the cracking and is not significantly influenced by the deformations of the slab). The compressive stress is strongly influenced by the tensile strength of concrete because the tensile strength affects the cracking and stiffness of the tension ring around the hogging moment area.

In the third row in Figure 4.1, load-rotation curves are shown together with the failure criterion of the CSCT. As a comparison, with dotted lines, the load-rotation curves for corresponding isolated slabs are also shown. It can be seen that the difference between continuous and isolated slabs is especially significant for the case of low amounts of hogging reinforcement (Fig. 4.1(g)).

It can be seen in Figure 4.1 that the parameters $r_s(\psi)$ and $m_{R,hog}(\psi)$ are complex functions of ψ that additionally depend on several other parameters. In order to model the flexural response of a continuous or confined slab suitably, both parameters have to be determined with a sufficient accuracy. In addition, as the rotation ψ is not known, applying Equation (4.3) would require iterations that are not desirable in design formulas. Therefore, a different approach is considered in the present research.

4.1.2 Internal forces and deformations at the flexural limit

In order to simplify Equation (4.3), the internal forces and deformations of an axisymmetric isolated slab at the flexural limit are compared to those of edge-restrained elements. The load-rotation curve for a slab submitted to a load at the edge and supported in the center is shown in Figure 4.2(a). A flexural mechanism of such slab is reached when the top reinforcement (corresponding to hogging reinforcement in an actual continuous slab) in the whole slab yields. The last part of the slab to reach its flexural resistance is the outermost tangential strip of the specimen [Kin60, Mut08b] (Fig. 4.2(c)). At that moment, the tangential curvature at the edge of the slab (which can be calculated as $\chi_t = \psi/r_s$ because the deformed shape of the slab part outside the immediate vicinity of the support is conical) equals the curvature at the onset of yielding due to hogging moments

$\chi_{y,hog}$ (Fig. 4.2(e)). From these two equations, the slab rotation at the onset of the flexural plateau can be calculated as (Fig. 4.2(f)):

$$\psi_{y,isol} = \chi_{y,hog} \cdot r_s \tag{4.4}$$

where $\chi_{y,hog} = m_{R,hog}/EI_I - \Delta\chi_{TS}$. Alternatively, in a simpler manner, the curvature of a reinforced concrete cross-section at a flexural limit (χ_y) can be assumed to be proportional to the yielding strain in the reinforcement (f_y/E_s) divided by the effective depth d (when the depth of the compression zone is neglected). Replacing this into Equation (4.4) yields an equation for the slab rotation at the flexural limit ($V = V_{flex}$) that is consistent with the simplified relationship proposed by Muttoni [Mut08b] (Eq. (4.2)):

$$\psi_{y,isol} = k_m \cdot \frac{r_s}{d} \frac{f_y}{E_s} \tag{4.5}$$

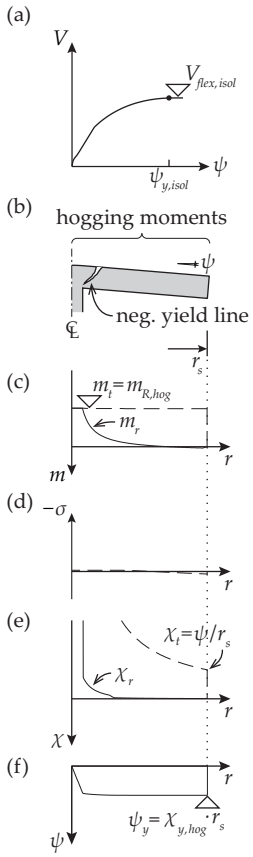

Figure 4.2 Internal forces and deformations in an axisymmetric isolated slab at the onset of a flexural plateau, calculated with the numerical model: (a) quadrilinear load-rotation curve; (b) slab deformations; (c) bending moments (radial – continuous lines, tangential – dashed lines); (d) in-plane forces; (e) curvatures (radial – continuous lines, tangential – dashed lines); (f) slab rotation

4.2 Continuous slabs with the influence of CMA neglected

4.2.1 Internal forces and deformations at the flexural limit

In order for the flexural limit in an axisymmetric edge-restrained slab element to be reached, both hogging and sagging yield lines need to develop (Fig. 4.3(b)). The load leading to a flexural failure $V_{flex,cont}$, according to yield line analysis, is proportional to the sum of hogging and sagging flexural strengths ($V_{flex,cont} \propto m_{R,hog} + m_{R,sag}$). The rotation at the flexural limit cannot be calculated with Equations (4.4) or (4.5) similarly to isolated elements, because yielding of tangential hogging reinforcement at r_s does not yet imply reaching a flexural limit of the slab (Fig. 4.3(c)), as the sagging yield line might not be fully developed at this stage.

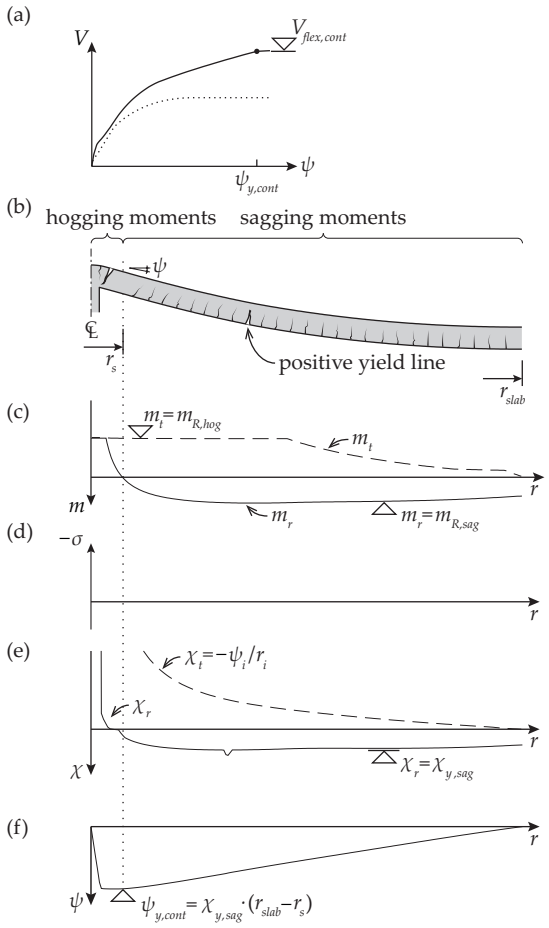

Figure 4.3 Internal forces and deformations in an axisymmetric continuous slab element at the onset of a flexural plateau, calculated with the numerical model neglecting the influence of in-plane forces and deformations: (a) load-rotation curve; (b) slab deformations; (c) bending moments (radial – continuous lines, tangential – dashed lines); (d) in-plane forces (neglected); (e) curvatures (radial – continuous lines, tangential – dashed lines); (f) slab rotation

It is known that the rotation at the outer edge of the element is zero (representing a mid-span symmetry line of a continuous slab). Thus, the rotation at the line of moment contraflexure can be,

in a general manner, determined by integrating radial sagging curvatures between the edge of the element (r_{slab}) and the line of moment contraflexure (r_s). As seen in Figure 4.3(c), at the flexural limit (just before the formation of a a circular sagging yield line), the radial moment in most of the sagging moment area is close to the flexural resistance $m_{R,sag}$. If the radial sagging moment is assumed to be constant at $m_{R,sag}$, the corresponding curvature may also be taken constant at $\chi_{y,sag}$ (Fig. 4.3(e)). Under these assumptions, the slab rotation at r_s can be calculated:

$$\psi_{y,cont} = \chi_{y,sag} \cdot \left(r_{slab} - r_s\right) \tag{4.6}$$

It may be interesting to compare the hypothesis of a constant (plastified) radial sagging moment with the assumption of Kinnunen and Nylander [Kin60] that the radial sagging moments remains in the elastic range until the punching failure (as described in Chapter 2). However, it should be noted that the present hypothesis is made for the limit state at the onset of flexural yielding (formation of a circular sagging yield line) and does not attempt to describe the slab behavior in the earlier stages of loading.

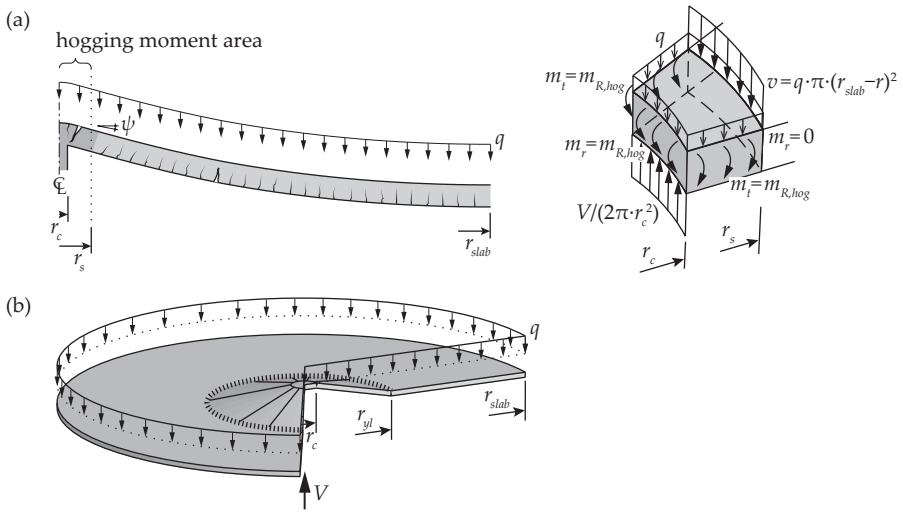

Figure 4.4 (a) Equilibrium of a slab sector inside the line of moment contraflexure (r_s);
(b) Failure mechanism of an axisymmetric slab element

The size of the hogging moment area at the flexural limit (radius r_s) can be determined by solving the equilibrium equation (Eq. 3.1) of a slab sector inside the line of moment contraflexure (Fig. 4.4(a)):

$$m_{R,hog} \cdot r_c - m_{R,hog} \cdot \left(r_s - r_c\right) + q \cdot \pi \cdot \left(r_{slab} - r_s\right)^2 \left(r_s - r_c\right) \cdot r_s + qA_i\left(r_s - r_c\right) = 0 \tag{4.7}$$

Flexural capacity of the element can be determined with yield line method. The governing yield line strength $V_{flex,cont}$ is the lowest one obtained by varying the distance from the center of the slab to the yield line r_{yl} (Fig. 4.4(b)):

$$V_{flex,cont} = \frac{2\pi \cdot \left(m_{R,hog} + m_{R,sag}\right) \cdot r_{yl}}{\left(r_{yl} - r_c\right) \cdot \left[\pi \cdot r_{slab}^2 - \pi/3 \cdot \left(r_{yl}^2 - r_{yl} r_c + r_c^2\right)\right]} \cdot \pi \cdot r_{slab}^2 \tag{4.8}$$

4.2.2 Load-rotation curve

As shown in Chapter 3, in continuous slabs with CMA neglected, the stiffnesses of hogging and sagging mechanisms are different. The hogging mechanism develops fully at a rotation $\psi_{y,isol}$ (Eq. (4.4)), whereas the sagging mechanism reaches its capacity at a rotation $\psi_{y,cont}$ (Eq. (4.6)). The full load-rotation response can be calculated by adding the contributions of sagging and hogging mechanisms (Fig. 4.5(a,b)):

$$\psi_{cont}(V) = \psi_{isol}(V) + \psi_{sag}(V) \tag{4.9}$$

where the function $\psi_{isol}(V)$ can be calculated with (Eq. (4.1)) and the function $\psi_{sag}(V)$ describing the response of the sagging mechanim is assumed to be linear with $V_{flex,sag}$ (determined as $V_{flex,cont} - V_{flex,isol}$) reached at rotation $\psi_{y,cont}$ (Fig. 4.5(a)).

A comparison presented in Figure 4.5(c–d) between the load-rotation curves obtained with the numerical analysis (with in-plane forces neglected) and the simplified analytical formula (Eq. (4.9)) with hogging contribution calculated with the quadrilinear model (Eq. (4.1)) shows very good agreement.

A simpler load-rotation relationship can be established when the simplified parabolic curve given by Equation (4.2) [Mut08b] is used for calculating the contribution of hogging mechanism (ψ_{isol}) in Equation (4.9). In addition, when calculating the rotation at the flexural limit (both hogging and sagging reinforcement yielding) with Equation (4.6), it is assumed that $r_s \to 0$ (refer to Fig. 4.1(a–c)). In this case, the ratio $\psi_{y,isol}/\psi_{y,cont} \cong r_s/r_{slab} \cdot \chi_{y,hog}/\chi_{y,sag}$. When $\chi_{y,hog}$ and $\chi_{y,sag}$ are taken equal and $r_s/r_{slab} = 0.22/0.7 \cong 0.3$ (refer to Chapter 3), the load-rotation relationship can be written as:

$$\psi_{cont} = \max\left\{ \begin{array}{l} 1.5 \cdot \dfrac{r_s}{d} \cdot \dfrac{f_y}{E_s} \left(\dfrac{m_S}{m_{R,hog} + 0.3 \cdot m_{R,sag}} \right)^{3/2} \\ 4.8 \cdot \dfrac{r_s}{d} \cdot \dfrac{f_y}{E_s} \cdot \dfrac{m_{R,hog}}{m_{R,sag}} \left(\dfrac{m_S}{m_{R,hog}} - 1 \right) \end{array} \right. \tag{4.10}$$

Simplified curves calculated with Equation (4.10) compare reasonably well to the numerical ones in Figure 4.5(e–f). A curve based on isolated specimens (Eq. 4.2) is also shown. It can be seen that the contribution of sagging reinforcement, albeit limited, decreases the slab rotation for a given level of load. However, at loads exceeding the flexural strength of an isolated specimen (cases where significant moment redistributions between hogging and sagging mechanisms are accounted for), the slab rotation calculated with Equation (4.2) may not be conservative.

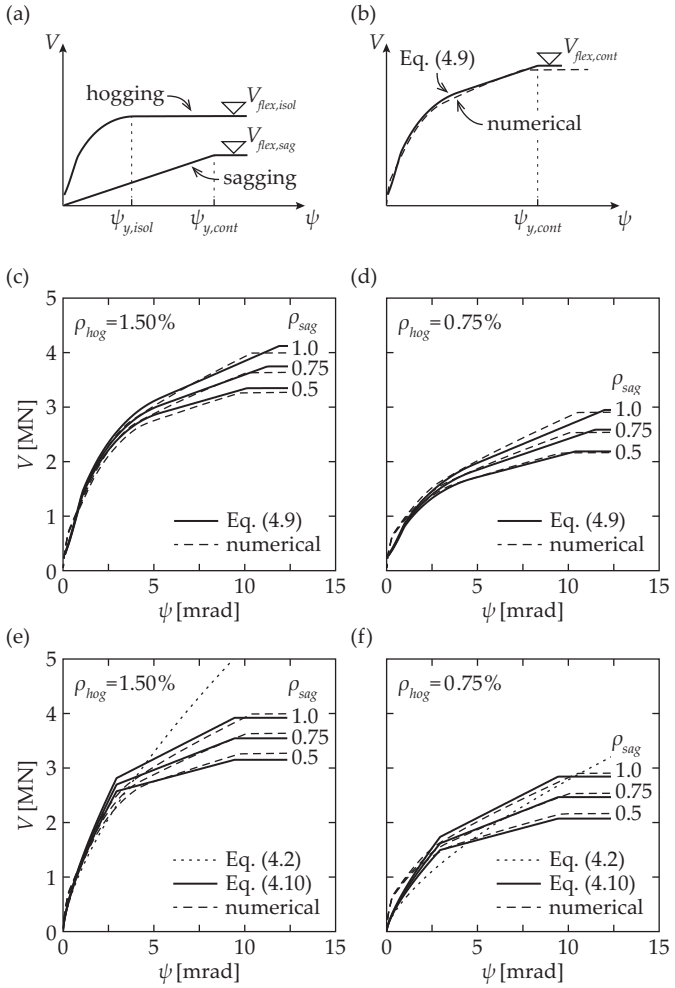

Figure 4.5 Load-rotation curves for continuous slabs with CMA neglected, comparison of the simplified analytical approach (Eq. (4.10)) and the numerical model: (a) contributions of hogging and sagging mechanisms; (b) total load-rotation response; (c–d) comparisons of the analytical and numerical curves, ρ_{hog} = 1.50% and ρ_{hog} = 0.75%; (e–f) comparisons of the simplified analytical and numerical curves, ρ_{hog} = 1.50% and ρ_{hog} = 0.75% (parameters, if not shown otherwise: L = 7 m, h = 250 mm, d = 210 mm, c = 350 mm, f_c = 35 MPa, f_{ct} = 3.2 MPa, f_y = 550 MPa)

4.3 Continuous slabs with CMA

4.3.1 Internal forces and deformations at the flexural limit

In continuous slabs with no external confining elements (self-confined slabs), the edge conditions at r_{slab} (representing a mid-span symmetry line) are zero rotation and zero in-plane force. Therefore, the in-plane compression that appears in around the slab-column connection is only generated by the restraint provided by the tension ring in the external part of the slab element.

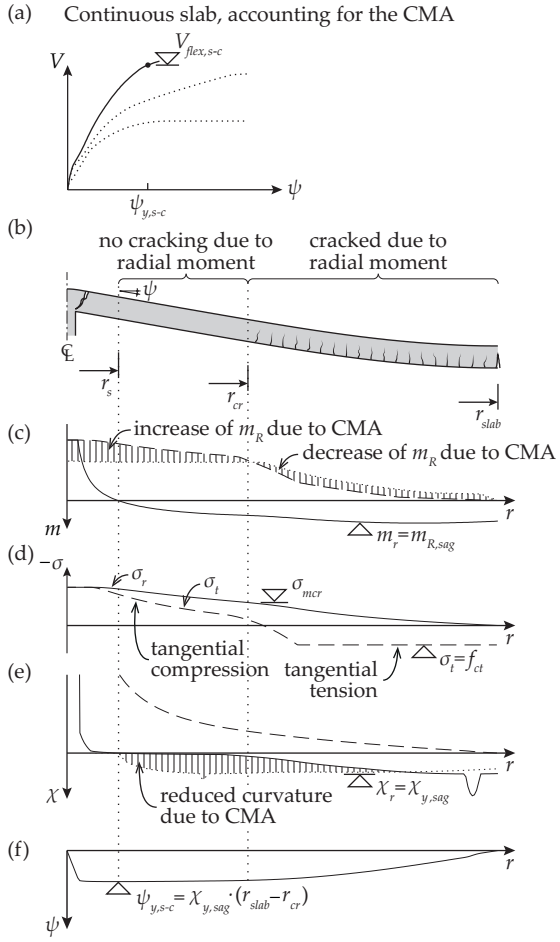

Figure 4.6 Internal forces and deformations in an axisymmetric continuous slab element at the onset of a flexural plateau, calculated with the numerical model that accounts for the influence of in-plane forces and deformations: (a) load-rotation curve; (b) slab deformations; (c) bending moments (radial – continuous lines, tangential – dashed lines); (d) in-plane forces (neglected); (e) curvatures (radial – continuous lines, tangential – dashed lines); (f) slab rotation

Figure 4.6 shows the internal forces and deformations of an axisymmetric portion of a self-confined slab. The tangential compression in the middle of the slab has to be equilibrated with tangential tension at the outer edge (Fig. 4.6(d)). Due to CMA, the tangential moment is increased in the parts of the slab under tangential compression and decreased in the parts under tangential

tension (Fig. 4.6(c)). These two effects partly compensate for each other and thus the total influence of self-confinement on the flexural capacity of a slab is not very significant.

However, another effect has an important influence on the slab rotation at the flexural limit. As shown in Figure 4.6(e), radial curvatures in a central part of the slab are significantly decreased compared to a model where the in-plane forces are neglected (Fig. 4.3). This reduction is caused by compressive stresses in the slab that arise from the tensile stresses in the tension ring (Fig. 4.6(d)). The reduction of radial curvatures is especially significant in sections where the radial compression is sufficiently high in order to avoid flexural cracking (refer to the moment-curvature law presented in Fig. 3.4). In a simplified manner, the radial curvature can be assumed to be zero in the part of the slab that is not cracked due to radial sagging moments (Fig. 4.6(b)). Outside of this part, the radial curvature is estimated to be constant at the yielding curvature $\chi_{y,sag}$ as in the case of the analysis where the in-plane forces are neglected (Fig. 4.6(c) and Fig. 4.3(c)). If the limiting radius between the cracked and the uncracked parts is r_{cr}, the rotation at flexural limit at the line of moment contraflexure, calculated by integrating the curvatures between r_{slab} and r_s, is:

$$\psi_{y,s-c} = \chi_{y,sag} \cdot \left(r_{slab} - r_{cr}\right) \tag{4.11}$$

Comparing Equations (4.6) and (4.11), it can be seen that the rotation at the flexural limit decreases considerably if in-plane forces are accounted for, as $r_{cr} > r_s$ (Fig. 4.6(b)).

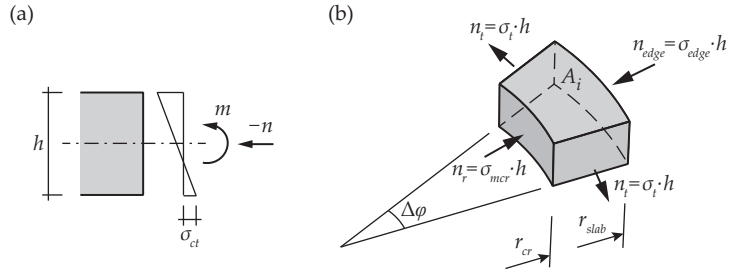

Figure 4.7 (a) Stresses in an elastic cross-section (b) Equilibrium of in-plane forces in a slab sector between r_{cr} and r_{slab}

The value of r_{cr} is estimated by making the following assumptions. In an uncracked reinforced concrete cross-section (with the influence of reinforcing bars neglected), stress in the outermost tension fiber σ_{ct} can be calculated as (Fig. 4.7(a)):

$$\sigma_{ct} = \frac{6 \cdot m}{h^2} + \sigma \tag{4.12}$$

where m is a bending moment per unit width and $\sigma = n/h$ is an in-plane stress (compression is negative). Cracking occurs when this stress reaches the tensile strength of concrete f_{ct}. Necessary in-plane compressive stress σ_{mcr} that prevents cracking due to a bending moment m can thus be determined from Equation (4.12):

$$\sigma_{mcr} = f_{ct} - \frac{6 \cdot m}{h^2} \tag{4.13}$$

The equilibrium equation of axial forces for a slab sector limited by r_{cr} and r_{slab} is (Fig. 4.7(b)):

$$\sigma_{edge} \cdot h \cdot \Delta\varphi \cdot r_{slab} - \sigma_{mcr} \cdot h \cdot \Delta\varphi \cdot r_{cr} - \sigma_t \cdot h \cdot \Delta\varphi \cdot (r_{slab} - r_{cr}) \tag{4.14}$$

The force in the tension ring n_t (Fig. 4.8(a)) is dependent on both on the dilation of the cracked central part of the slab (larger dilation generates higher stresses) as well as the axial stiffness of the ring (higher stiffness causes higher stresses). The tensile stiffness of the ring decreases considerably after cracking of concrete (Fig. 4.8(b)). After that, much larger dilation of the central slab portion is needed to reach the same compressive stresses in the ring. However, the stiffness of the ring after cracking does not drop abruptly but a crack formation phase occurs where the force stays at a constant level due to tension stiffening effect [Mar98]. The force starts increasing again only when the dilation is sufficiently large to cause higher stresses with fully cracked stiffness of the ring.

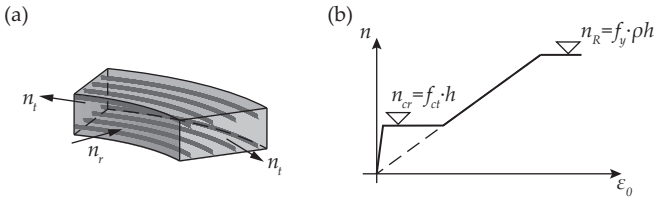

Figure 4.8 Tensile stresses in the tension ring: (a) tangential and radial in-plane forces; (b) stress-strain relationship for the tensile ring

Therefore, it is conservative to assume that the tangential tensile stress σ_t is equal to f_{ct} and the limiting radius r_{cr} where the concrete is cracked due to radial sagging moment can be calculated from Equation (4.14):

$$-\left(f_{ct} - \frac{6 \cdot m_{R,sag}}{h^2}\right) \cdot r_{cr} - f_{ct} \cdot (r_{slab} - r_{cr}) - \sigma_{edge} \cdot r_{slab} = 0 \tag{4.15}$$

From Equation (4.15):

$$r_{cr} = \frac{(f_{ct} - \sigma_{edge}) \cdot h^2}{6 \cdot m_{R,sag}} \cdot r_{slab} \tag{4.16}$$

By noting that $(f_{ct,eff} \cdot h^2)/6$ is equal to the cracking moment m_{cr} of the slab without an axial force and effective tensile strength of concrete $f_{ct,eff} = f_{ct} - \sigma_{edge}$, where σ_{edge} is the radial stress at the edge of the element (corresponding to a mid-span symmetry line of an actual continuous slab), Equation (4.16) becomes:

$$r_{cr} = \frac{m_{cr}}{m_{R,sag}} \cdot r_{slab} \tag{4.17}$$

It can be seen that the reduction of slab deformations due to the influence of in-plane forces is especially significant for slabs with low amounts of sagging reinforcement (when $m_{R,sag} \rightarrow m_{cr}$). Also, a compressive stress ($\sigma_{edge} < 0$) at the edge of the element increases the size of the uncracked slab portion r_{cr} whereas a tensile stress ($\sigma_{edge} > 0$) reduces it. Slab rotation at the flexural limit can be thus calculated from Equations (4.11) and (4.17):

$$\psi_{y,s-c} = \chi_{y,sag} \cdot r_{slab} \cdot \left(1 - \frac{m_{cr}}{m_{R,sag}}\right) \tag{4.18}$$

4.3.2 Load-rotation relationship

As explained in the previous section, in-plane forces influence the load-rotation response of continuous slabs in two ways. Firstly, in-plane compression increases the flexural strength in the parts of the slab where compressive stresses are induced. However, in the case of self-confinement, parts of the slab (the tension ring) are under axial tension, where the flexural strength is reduced. Therefore, these effects partly counteract each other. Secondly, it was shown that the slab rotation at the flexural limit of a self-confined slab is reduced compared to a case where the in-plane forces and deformations are neglected. In addition, the two phases of first activating the hogging reinforcement and then the sagging reinforcement cannot be distinguished in confined slabs (compare Figures 4.3(a) and 4.6(a)). This is caused by the fact that the sagging portion of a self-confined slab also contributes to the load-bearing mechanism by generating compressive stresses in the hogging moment area and it is therefore activated at lower load levels. This phenomenon allows describing the load-rotation relationship of self-confined slabs with a single-phase law.

Therefore, the load-rotation curve of continuous self-confined slabs can be approximated with a parabolical curve, analoguosly to isolated elements (Eq. (4.2)):

$$\psi_{s-c} = \psi_{y,s-c} \cdot \left(\frac{V}{V_{flex,s-c}}\right)^{3/2} \tag{4.19}$$

where rotation at the flexural limit $\psi_{y,s-c}$ is given by Equation (4.18). If $\chi_{y,sag}$ is approximated similarly to isolated slabs (Eq. (4.5)) and the fact that the flexural strength $V_{flex,s-c}$ is proportional to $m_{R,hog} + m_{R,sag}$ is taken into account (the possible influence of membrane action on the flexural strength is neglected), Equation (4.19) becomes:

$$\psi_{s-c} = k_{s-c} \cdot \left(1 - \frac{m_{cr}}{m_{R,sag}}\right) \cdot \frac{r_{slab}}{d} \cdot \frac{f_y}{E_s} \cdot \left(\frac{m_S}{m_{R,hog} + m_{R,sag}}\right)^{3/2} \tag{4.20}$$

Denoting the ratio between sagging and hogging moment capacities as $m_{R,sag}/m_{R,hog} = \eta$, Equation (4.20) can be rewritten as:

$$\psi_{s-c} = k_{\psi} \cdot \left(1 - \frac{m_{cr}}{\eta \cdot m_{R,hog}}\right) \cdot \frac{r_s}{d} \cdot \frac{f_y}{E_s} \cdot \left(\frac{m_S}{m_{R,hog}}\right)^{3/2} = k_{\psi} \cdot \left(1 - \frac{m_{cr}}{\eta \cdot m_{R,hog}}\right) \cdot \psi_{isol} \tag{4.21}$$

where

$$k_\psi = \frac{k_{s-c}}{1.5} \cdot \frac{r_{slab}}{r_s} \cdot (1+\eta)^{-3/2} \tag{4.22}$$

For practical purposes, Equation (4.21) can be further simplified by using a constant value of η chosen for a case where the reinforcement is designed according to the direct design method of ACI 318 [ACI14] ($\eta = 0.5$, which indicates that the amount of hogging reinforcement is twice the amount of sagging reinforcement) and by assuming that in this case, the factor k_ψ is equal to one. The influence of redistribution between hogging and sagging moments and CMA can then be accounted for by modifying the expression suggested by Muttoni [Mut08b] and utilized in Model Code 2010 punching provisions (Eq. (4.2)) with a factor $(1 - 2 \cdot m_{cr}/m_{R,hog})$:

$$\psi_{s-c} = \left(1 - \frac{2 \cdot m_{cr}}{m_{R,hog}}\right) \cdot 1.5 \cdot \frac{r_s}{d} \cdot \frac{f_y}{E_s} \cdot \left(\frac{m_S}{m_{R,hog}}\right)^{3/2} \tag{4.23}$$

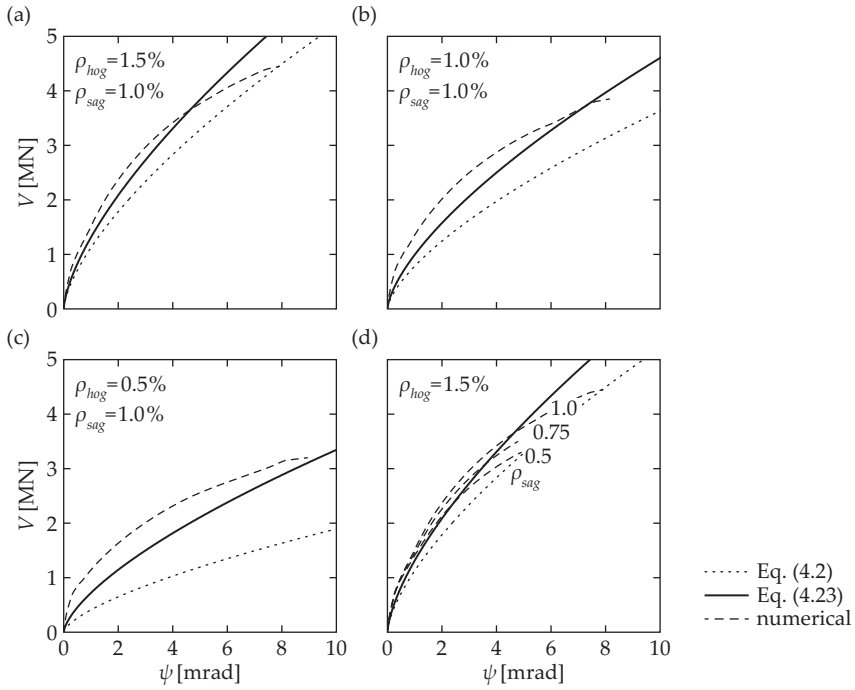

Figure 4.9 Load-rotation curves for continuous slabs with accounting for the influence of in-plane forces, comparison of the simplified analytical approach (Eq. (4.23)) and the numerical model: (a–c) variable hogging reinforcement ratio ρ_{hog} = 1.50%; (d) variable sagging reinforcement ratio (parameters: L = 7 m, h = 250 mm, d = 210 mm, c = 260 mm, f_c = 35 MPa, f_{ct} = 3.2 MPa, f_y = 550 MPa)

Figure 4.9(a–c) shows a comparion between the load-rotation curves calculated with the isolated approach (Eq. (4.2)), Equation (4.23) and the numerical analysis. It can be seen that the stiffness increase of the load-rotation response of continuous slabs compared to that of isolated specimens is more significant for lower hogging reinforcement ratios. This is due to the larger dilation and

higher induced compressive stresses in the hogging moment area in the case of larger flexural deformations of that area. Also, the difference between the numerical and the simplified approaches increases with more overestimated rotations (thus being more conservative for punching calculations) for decreasing ρ_{hog}. This is due to the previously made assumption when deriving Equation (4.23) that tensile stress in the tension ring does not exceed f_{ct}.

It should be noted that Equation (4.23) does not account for the influence of sagging reinforcement ratio. Whereas it is true that the flexural strength of continuous slabs is significantly influenced by this parameter, the present analysis has shown that the influence is much less important on the stiffness of the response at lower levels of load (Fig. 4.9(d)). This is explained by the fact that the in-plane force in the tension ring (that induces in-plane forces in the hogging moment area) is normally governed by tensile stresses of concrete and not by the amount of reinforcement in the tension ring. Therefore, the stiffness enhancement of the slab on lower levels of load is not significantly influenced by the sagging reinforcement ratio. Therefore, for simplicity, this parameter is omitted in Equation (4.23). However, it can be taken into account in the future improvements of the model by modifying the parameter k_ψ.

It can also be remarked that Equation (4.23) does not allow for distinction between the effects of moment redistribution and compressive membrane action. In fact, the possible redistribution between hogging and sagging moments is already considered in the Model Code 2010 formula (Eq. (4.2)) by not limiting its application range to the cases where $m_S/m_{R,hog} < 1$.

When applying Equation (4.23) in practice, the cracking moment m_{cr} should be calculated using a value of concrete tensile strength that can be activated by tension stiffening in the crack development phase (normally the average value f_{ctm} can be used). As given by Equation (4.16), possible radial tensile forces at the edges (for example, caused by restrained shrinkage of the slab) have to be substracted from the tensile strength. When these forces exceed the tensile cracking capacity of the slab, the isolated approach (Eq. (4.2)) provides a lower bound for the load-rotation curve.

A minimum value for the factor $(1 - 2m_{cr}/m_{R,hog})$ has to be provided in order to avoid underestimated rotations in the case of very low hogging reinforcement ratios (where $m_{R,hog} \rightarrow m_{cr}$). In the following parametric study, a value of 0.4 is used as this limit.

4.4 Parametric study

Figure 4.10 compares the punching strengths calculated with Equation (4.23) to the strengths of self-confined slabs determined using load-rotation relationships from the numerical model. Predictions for corresponding isolated specimens (radius of specimens 0.22 L, load-rotation curve determined with Eq. (4.2)) are also shown. All the strengths are calculated in combination with a failure criterion of the CSCT [Mut08b].

Figures 4.10(a) and (b) show the influence of hogging reinforcement ratio on the punching capacity of slab-column connections. Experiments on isolated specimens have shown that increasing the

amount of hogging reinforcement increases the punching strength. Following this observation, flexural reinforcement ratio in the vicinity of the column is taken into account in the punching provisions of several codes of practice [FIB13, CEN04], although also neglected by some [ACI14].

The present analysis indicates, consistently with the experimental observations of Choi and Kim [Cho12], that in the case of continuous slabs, the amount of hogging reinforcement has a lower influence on punching capacity than in isolated specimens. This can be explained by the fact that the influence of compressive membrane action and the contribution of sagging reinforcement are both more significant in the case of low amounts of hogging reinforcement and considerably increase the flexural stiffness of such slabs (as seen by comparing the continuous and dotted load-rotation curves in Fig. 4.1(g)). The proposed formula for continuous self-confined slabs (Eq. (4.23)) increases the Model Code 2010 punching strength predictions in the case of low reinforcement ratios and can be of particular interest for assessment of existing slabs. The constant punching shear strength used in ACI 318 is seen to be conservative for all the reinforcement ratios in the analyzed range.

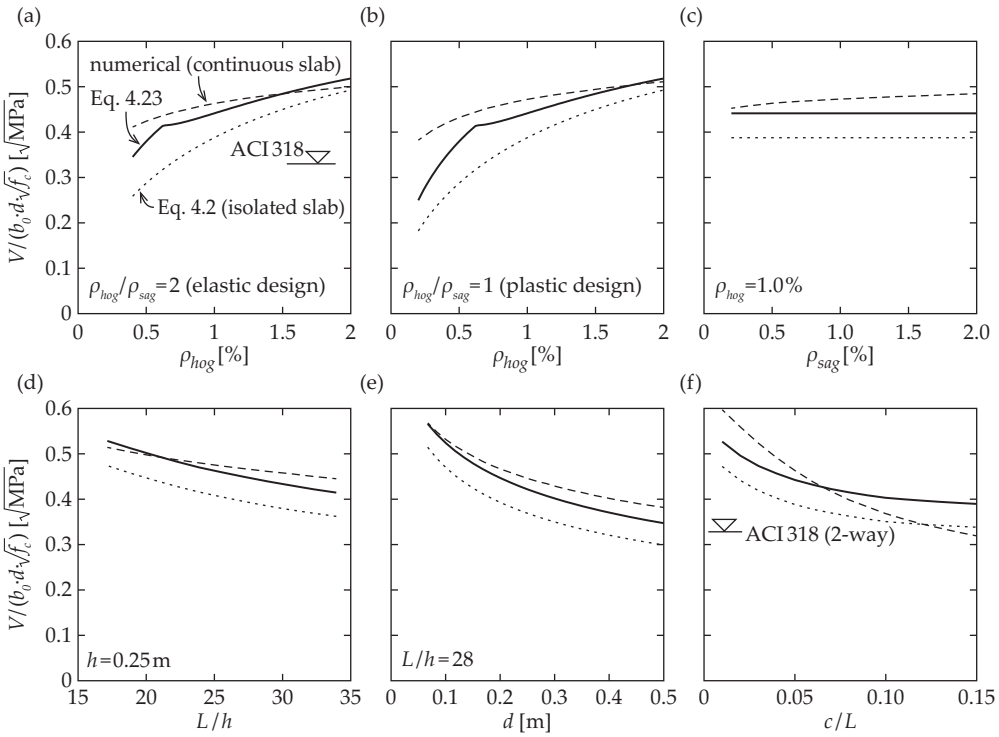

Figure 4.10 Comparison of the punching strengths calculated with load-rotation relationships from Model Code 2010 (dashed line), the proposed expression (continuous line) and the numerical model (dotted line): (a, b) influence of the hogging reinforcement ratio; (c) influence of the sagging reinforcement ratio; (d) influence of the slab slenderness with constant h (slenderness effect); (e) influence of the effective depth with constant slenderness (size effect); (f) influence of the column size (parameters, if not shown otherwise: L = 7 m, h = 250 mm, d = 210 mm, c = 350 mm, f_c = 35 MPa, f_{ct} = 3.2 MPa, f_y = 420 MPa, d_g = 16 mm; ρ_{hog} = 1.0%; ρ_{sag} = 0.5%)

As explained in the previous section, the amount of sagging reinforcement does not have a significant influence on the stiffness of the flexural response (Fig. 4.9(d)). Thus, as shown in Figure 4.10(c), the influence of this parameter on punching strength is also limited and neglecting it in the simplified formula (Eq. (4.23)) is justified.

Figures 4.10(d–f) show the influence of different geometrical parameters on the punching shear strength of self-confined slabs. The slenderness effect [Mut08b] that exists in isolated specimens is shown to be also present in continuous slabs in Figure 4.10(d). According to this, when slab depth and column size are kept constant, punching shear strength of the slab-column connection decreases with increasing slab span. The influence of size effect in the analyzed models (with respect to slab depth) is shown in Figure 4.10(e). The depth of the slab as well as slab span are varied (with a constant slab slenderness $L/h = 28$) while the column size is kept constant. Accounting for the size effect is especially important for the cases where predictions for actual structures are made on the basis of experiments performed on reduced-scale models. The proposed approach considers the size effect similarly to Model Code 2010 because it is taken into account in the failure criterion of CSCT. ACI 318 does not account for the size effect and provides conservative predictions for thinner slabs.

Figure 4.10(f) shows the influence of column size on the punching shear strength. Whereas the total punching capacity of a slab-column connection increases with column size, the unitary strength on the control perimeter decreases according to the CSCT because a higher total load leads to larger rotations and wider cracks around the column (note that the column size does not influence slab rotation in either of the simplified Equations (4.2) and (4.23). The difference between the numerical and the simplified models is caused by the assumption made in the simplified approaches that the size of the hogging moment area is independent of column size ($r_s = 0.22\,L$). In the numerical model, r_s increases with increasing column size, leading to larger rotations and lower unitary punching strengths. In the punching provisions of ACI 318, influence of column size on the unitary shear strength is only accounted for very large columns (providing a transition from two-way to one-way shear strength), which is outside of the range of the present parametric study. For small columns, the predictions of ACI 318 are conservative.

4.5 Summary and conclusions

The present chapter describes the derivation of simplified analytical formulas for predicting the load-rotation response of continuous and self-confined slabs. The main conclusions of this chapter are:

- An approach based on the slab rotation at the flexural limit gives consistent results with the parabolic load-rotation curve proposed by Muttoni [Mut08b] that is used in the punching provisions of Model Code 2010 [FIB13]. Therefore, it can be extended to account for the effects of moment redistribution between hogging and sagging mechanisms and compressive membrane action that are present in actual continuous slabs;

- Slab rotation that is needed to activate the sagging mechanism is larger than the rotation to activate the hogging mechanism. In the cases where the compressive membrane action cannot be relied on, this has to be taken into account by considering separate phases of the load-rotation response before and after full yielding of hogging reinforcement;
- Compressive membrane action that occurs due to the tangential tensile stresses generated in the sagging moment area allows activating the sagging portion of the slab at lower levels of load. Therefore, a simpler single-phase load-rotation curve can be used in this case;
- The proposed formula to predict the load-rotation relationship of continuous self-confined slabs compares very well to the curves obtained from the numerical analysis described in Chapter 3.

Chapter 5 Experimental study

This chapter is based on a paper published in *ACI Structural Journal* [Ein16a]. It presents the results of a systematic experimental campaign consisting of thirteen symmetric punching tests on interior slab-column connections. The study focuses on the influence of varying the size of the supported area and the slenderness of the slab. Other investigated parameters are the flexural reinforcement ratio and the presence of shear reinforcement. The results of the present campaign and of previous tests are compared to the predictions of different codes of practice and to the CSCT.

5.1 Introduction

The punching provisions in several codes of practice [CEN04, ACI14] are based on empirical formulas developed on the basis of experimental data. Nevertheless, in some cases they can lead to very different strength predictions. In *fib* Model Code 2010 [FIB13], the punching provisions are based on the Critical Shear Crack Theory (CSCT) developed by Muttoni [Mut08b, Mut13], which has shown wide consistency and generality. Similarly to the first mechanical model of Kinnunen and Nylander [Kin60] it assumes that the punching shear strength of a slab is a function of its flexural deformations (referring to a strain effect on punching shear). Larger flexural deformations (slab rotation ψ), such as in the case of lower amount of flexural reinforcement or more slender slabs (Fig. 5.1(a)), lead to wider cracks in the vicinity of the column and thus decrease the strength of a shear-carrying concrete strut, thereby lowering the punching capacity (V_R). Some empirical formulas, as those of Eurocode 2 [CEN04] punching provisions, account for the influence of the flexural reinforcement ratio. Yet, the effect of slab slenderness is neglected in Eurocode 2 as in most codes of practice [CEN04, ACI14].

The mechanical model of the CSCT also provides a physical explanation for the effect observed by Vanderbilt [Van72] that increasing column size decreases the nominal punching shear strength per unit length of a control perimeter close to the column face. This is explained by the fact that when the length of the shear-critical perimeter increases, punching failures occur at higher loads. However, increasing the column size has only a limited influence on the load-rotation response of a slab (Fig. 5.1(b)). Therefore, higher loads lead to increased rotations and larger crack widths in the critical zone of the slab around the column that decrease the capacity of concrete to transfer shear stresses between the slab and the column. This is, again, related to a strain effect. As a consequence, the CSCT predicts that the unitary punching shear strength on a control perimeter of a slab-column connection decreases with increasing column size in agreement to the observations of Vanderbilt.

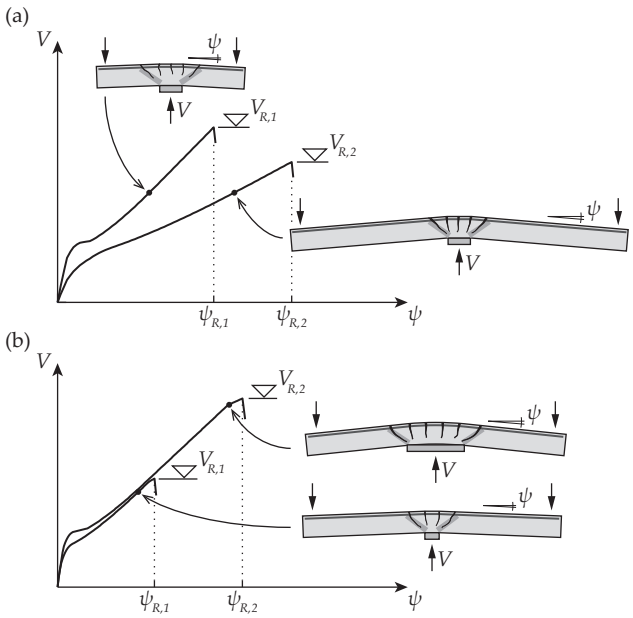

Figure 5.1 Load-rotation response and punching strength of slab specimens: (a) influence of specimen slenderness; (b) influence of column size

Another effect that may reduce the punching capacity of large square or rectangular columns is related to possible stress concentrations in the column corners [Sag14]. Figure 5.2 shows the shear fields [Vaz08] and distribution of shear stresses (calculated assuming linear-elastic slab behavior) in a slab at a distance $d/2$ from the column edge for different column sizes and shapes. Whereas the distribution for small square columns (Fig. 5.2(a)) as well as for circular columns (Fig. 5.2(c)) can be assumed as uniform, higher stresses in column corners can be noted in the case of large square columns (Fig. 5.2(b)). To account for this effect, the CSCT recommends assuming that only the parts of the control perimeter that are close to the column corners (at distances smaller than $1.5d$) are active in carrying shear stresses.

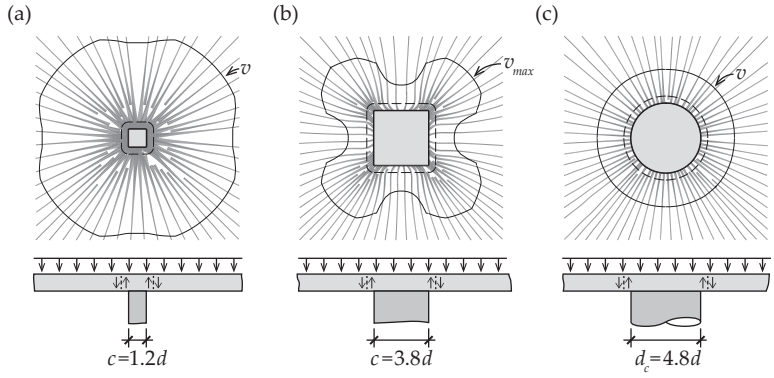

Figure 5.2 Linear-elastic shear fields in the vicinity of columns and distribution of shear stresses on a control perimeter at $d/2$ from the column edge: (a) small square column; (b) large square column; (c) large round column

The predictions of CSCT for punching of slab-column connections with variable column sizes, related to the described phenomena, have been confirmed by previous test results [Lip12] (refer to Fig. 5.3(a)). It should yet be noted that all these tests were performed using square columns. In order to avoid stress concentrations in the column corners, a new test series that is presented in this chapter is performed using round columns. Very wide range of column diameters is used (83 mm to 660 mm). Four of the slabs have a flexural reinforcement ratio of 0.75% and four slabs 1.50%. All other parameters are kept constant.

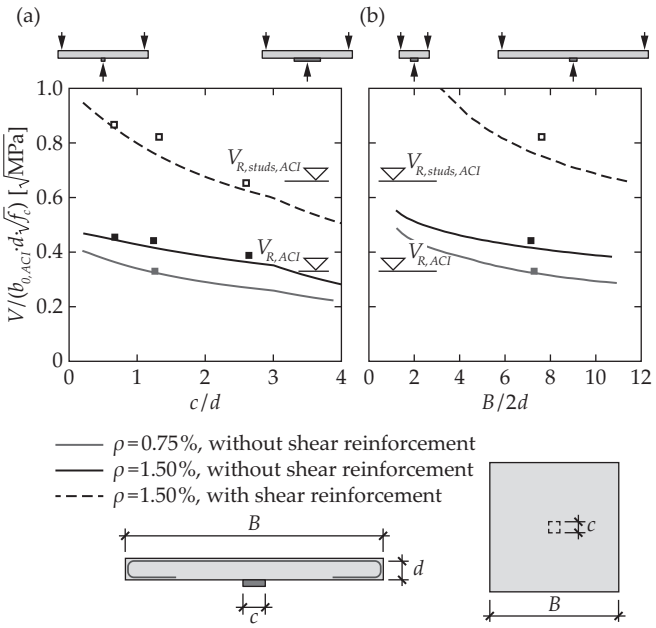

Figure 5.3 Predicted punching strengths according to the CSCT [Mut08b] and the results of previous tests [Lip12, Fer10b]: (a) influence of column size; (b) influence of specimen size

As previously explained (Fig. 5.1(a)), slenderness of a specimen also has an influence on the punching strength. This is shown in Figure 5.3(b) where available tests results are compared to the CSCT. Unfortunately, tests on specimens with constant thicknesses but varying slendernesses (defined as $B/2d$) are scarce in the scientific literature [Sis97] (Fig. 5.3(b)). In order to provide extended test data on this topic, a second test series is presented in this chapter where the size of the column and slab thickness are kept constant but the specimen slenderness ratio $B/2d$ is varied between 4.0 and 9.6. Three of the second series slabs are also equipped with shear reinforcement. In this cases, the predicted influence of slenderness is especially strong (refer to the corresponding curve in Fig. 5.3(b)).

5.2 Punching provisions in codes of practice

In all major codes of practice, punching strength of flat plates is verified by comparing the nominal shear strength of an element to a nominal shear stress on a unit length of a control perimeter around a column or a loaded area (Fig. 5.4):

$$v = \frac{V}{b_0 \cdot d} \leq v_R \tag{5.1}$$

The control perimeter b_0 should be defined in a manner that allows using nominal shear strengths that are independent of the column shape and size. It should be noted that, for this reason, the control perimeter and the actual failure surface are not directly related. Therefore, the definition of a control perimeter may be governed by very different rules depending on the code. Its location may vary between the edge of the loaded area and a distance 2d from it, its corners may be rounded or sharp and the length may be reduced in the vicinity of openings, slab edges or in the case of long straight edges of the loaded area (Fig. 5.4).

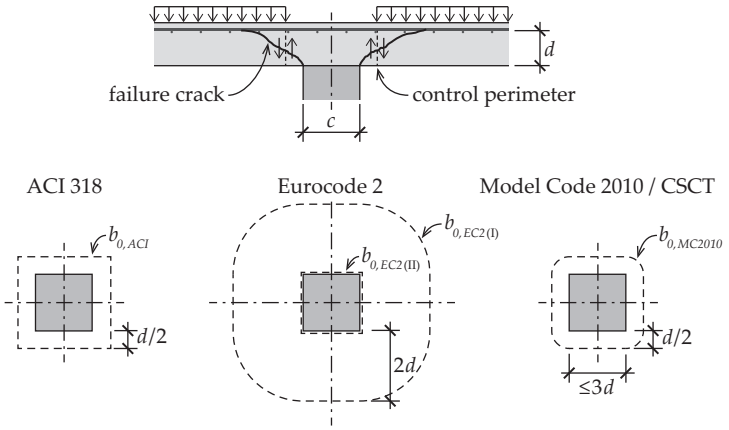

Figure 5.4 Control perimeters for punching verification in codes of practice

5.2.1 Influence of column size

The different location of control perimeters in various codes affects the influence of the loaded area size on their punching shear strength predictions. In addition, the codes account for different parameters in their punching strength formulas. Figure 5.5 shows the resistance of a continuous slab to a concentrated load (as nominal shear strength on the ACI 318 control perimeter) as a function of the size of the loaded area with respect to the slab depth according to different codes of practice and for two different reinforcement ratios. The capacity of the slabs may be governed by punching shear or flexural failure. The flexural strengths are calculated using the yield line method with a fan-shaped mechanism (Fig. 5.6), where the location of the positive yield line is r_{yl} that had to be optimized in order to obtain the minimal flexural strength. To that purpose, the amount of positive flexural reinforcement in the slab investigated in Figure 5.5 is assumed to be half the amount of negative reinforcement. It should be noted that, depending on the geometry of the slab, folding

mechanisms may also be governing. Punching failure can be avoided in the case of using sufficiently large columns (relative to slab depth) and low reinforcement ratios, or when using shear reinforcement. In these cases, bending may limit the load-bearing capacity of the slab (with enhanced deformation capacity). However, in many cases, a brittle shear failure is predicted before the full development of yield lines.

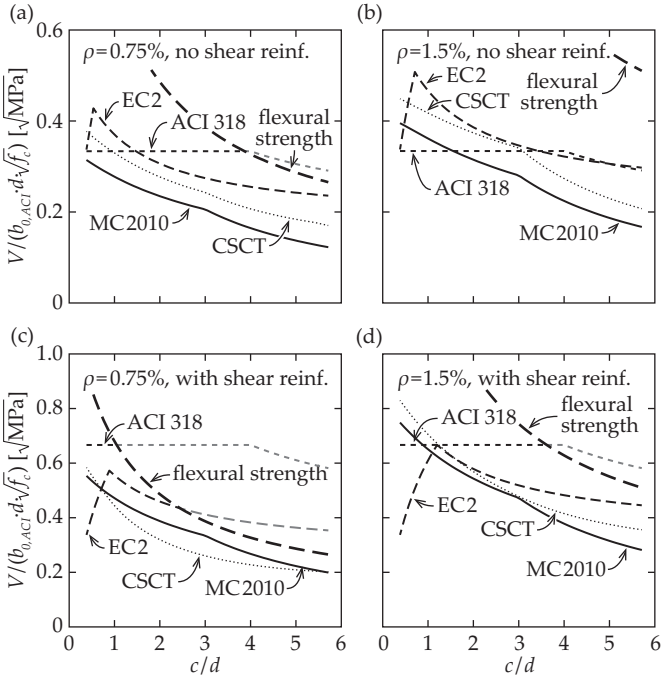

Figure 5.5 Comparison of the punching predictions of Eurocode 2, ACI 318 and Model Code 2010, without shear reinforcement and with large amounts of shear reinforcement (double-headed studs), depending on the column size to slab depth ratio (for square columns): (a) slabs with $\rho = 0.75\%$ and no shear reinforcement; (b) slabs with $\rho = 1.5\%$ and no shear reinforcement; (c) slabs with $\rho = 0.75\%$ and double-headed shear studs; (d) slabs with $\rho = 1.5\%$ and double-headed shear studs (parameters: $L = 7$ m; $d = 210$ mm; $f_c = 35$ MPa; $f_y = 420$ MPa; $\rho = 0.75\%$ or $\rho = 1.5\%$; $d_g = 16$ mm)

Since 1963, the punching or two-way shear provisions of ACI 318 [ACI14] are largely based on the work of Moe published in 1961 [Moe61]. For cases in-between one-way and two-way slab action, such as rectangular or very large loaded areas, modifications were made in 1977 where the predictions tend towards one-way shear strengths for elongated columns ($c_1/c_2 > 2$) or large column size to slab depth ratios ($c/d > 4$) [ASC74]. In comparison to the other codes, it can be seen that ACI 318 predicts significantly higher shear capacities for slabs with lower reinforcement ratios and medium c/d ratios (between 2 and 4) (Fig. 5.5(a)). In these cases (corresponding to typical floor slabs with low slenderness that do not require large quantities of flexural reinforcement), the column size does not lead to the reduction of nominal shear strength. Such reduction is based on the tests of Vanderbilt [Van72] that were performed on very thin slabs ($h = 51$ mm). As the phenomenon of punching is known to exhibit significant size effect (a decrease in nominal shear strength for in-

creasing slab thickness), these tests may have overestimated the punching strength of slabs on large supports (such as drop panels).

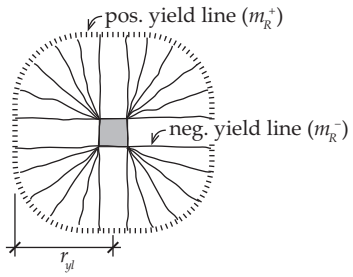

Figure 5.6 Yield line pattern for a flexural failure of a continuous slab

The punching provisions of Eurocode 2 [CEN04] are based on Model Code 1990 [CEB93] and due to the location of the control perimeter further than in ACI 318, exhibit less significant influence on column size to slab depth ratio. In 1986, Regan [Reg86] reported that the British standard of that time [BSI85], which used a control perimeter at 1.5d from the column edge, provided unsafe predictions in the case of very small c/d ratios (less than 0.75) and recommended that additional verification on a smaller control perimeter be introduced. Similar verification was also added in Eurocode 2 that checks the shear stress at a control perimeter located at a column face (refer to $b_{0,EC2(II)}$ in Fig. 5.4) with a higher nominal strength ($v_{R,max}$). This verification is governing in the case of very small values of c/d can be seen in Figure 5.5 as different regime in the Eurocode 2 predictions. This formula only considers the concrete strength and the slab depth as parameters and does not account for other influences, including the flexural reinforcement ratio. Therefore, the provisions of Eurocode 2 lead to more conservative results for slabs with large amounts of flexural reinforcement supported on small columns.

The punching provisions of Model Code 2010 [FIB13] are based on the CSCT [Mut08]. A consistent approach for all column sizes is used. The CSCT directly accounts for the flexural deformations of the slab and allows accounting for the size and strain effects on its punching strength model [Fer15]. The control perimeter is located at $d/2$ similarly to ACI 318, but the nominal shear strength is dependent on slab rotation ψ, decreasing for increasing column size. Therefore, the influence of column size is more similar to the predictions of Eurocode 2 than to ACI 318. By accounting for the influence of the flexural deformations, it allows a gradual reduction of the punching strength when flexural limit is approached, describing the transition between shear and flexural failures.

Differences between the codes of practice are even more important in the case of slabs with shear reinforcement (Fig. 5.5(c,d)). Such slabs fail at higher load levels and at larger deformations than slabs without shear reinforcement [Fer09]. For low or moderate amounts of transverse reinforcement, increasing the shear reinforcement ratio also increases the punching capacity. However, tests [Lip12] have indicated that for very large amounts of shear reinforcement, concrete close to the edge of the loaded area governs the behavior and may crush before the shear reinforcement yields. For such cases, the punching capacity no longer increases with larger amounts of transverse rein-

forcement [Fer09]. In this failure mode, punching strength depends on the type of shear reinforcement and detailing rules (anchorage type, rebar spacing). Therefore, design codes define a limit on the maximum punching strength of shear-reinforced slabs. In ACI 318 and Model Code 2010, the limit depends on the shear reinforcement system with highest resistances for double-headed studs. In Eurocode 2, the maximum punching resistance of shear-reinforced slabs is limited by the same verification of $v_{R,max}$ at the edge of the column as for slabs without shear reinforcement. This leads to lower predictions compared to the other codes for small column size to slab depth ratios (up to approximately 1), as according to this approach, using shear reinforcement does not increase the punching resistance. Predictions for larger column sizes, however, lead to higher strengths. Until recently, Eurocode 2 punching provisions did not include any other limitation on the punching strength of slabs with shear reinforcement. In 2014, an amendment [CEN14] to Eurocode 2 punching provisions was published (to be implemented by the end of 2015) so that the punching resistances of shear-reinforced slabs were limited to 1.5 times the resistances of similar slabs without shear reinforcement. That leads to similar predictions to those of Model Code 2010. However, the limitation of $v_{R,max}$ remained unchanged and thus the punching strength predictions of Eurocode 2 for the connections of slabs to columns having small sizes with respect to slab depth (that are common in European practice) are more conservative than the provisions of ACI 318 and Model Code 2010 (Fig. 5.5(c,d)).

5.2.2 Influence of slab slenderness

Punching tests are normally performed on isolated test specimens that represent a negative moment area of a continuous slab, separated from the rest of the slab by the line of moment contraflexure. In slender slabs with regular spans L, according to a linear-elastic calculation, the distance from the center of the column to this line is approximately $0.22L$ [Kin60] (in the non-linear analysis presented in Chapter 3, this was also observed to be a reasonable approximation for cracked continuous slabs). Therefore, the slenderness of a specimen ($B/2d$) corresponds to 0.22 times the slenderness of an actual flat plate (L/d). Experimental results have shown that increasing specimen slenderness reduces both its flexural stiffness and shear capacity [Sta01]. This suggests that punching shear strength of an actual slab decreases with increasing span if the depth of the member remains constant. It is thus instrumental to select the size of a specimen considering the slenderness of the actual slab that is modelled in the experiment. Despite this fact, in many experimental campaigns, the size of specimens is chosen only based on existing laboratory conditions.

The mechanical model of Kinnunen and Nylander [Kin60] as well as a design method based on their model from Swedish concrete handbook of 1990 [Nyl90] account for the slenderness effect. Also the CSCT [Mut08b] (Fig. 5.7(a,b)) and the codes that base their punching provisions on this theory (Model Code 2010 [FIB13] and since 2003 the Swiss code for concrete construction [SIA03]) take this effect into account. However, slenderness is not accounted for as a parameter in the design equations of ACI 318 [ACI14] and Eurocode 2 [CEN04] (Fig. 5.7(c,d)). It only affects the flexural strength of a slab, which may become the governing failure mode for more slender slabs with

fairly low amounts of flexural reinforcement or for slabs with shear reinforcement. According to those codes, the shift from shear to flexural failure is considered without a transition phase. According to Model Code 2010, a pure flexural failure is predicted for much more slender slabs with a transition phase where the governing failure mode is still punching but with large flexural deformations due to yielding of flexural reinforcement in the column area. Increasing the slab slenderness has a similar influence as reducing the flexural reinforcement ratio, as the punching strength is based on the state of flexural deformations. This allows calculating the reduction of strength and deformation capacity close to the flexural limit in a more refined manner.

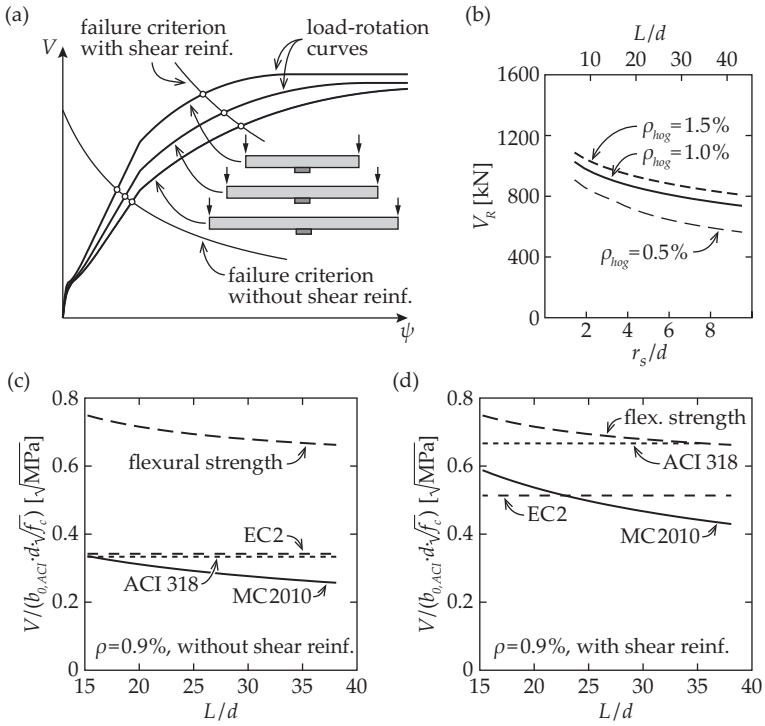

Figure 5.7 Influence of slab slenderness on punching shear strength: (a) load-rotation curves of specimens with different slenderness ratios and the failure criterion of the CSCT; (b) punching shear strength predictions of the CSCT; (c) comparison of the punching strength predictions of Eurocode 2, ACI 318 and Model Code 2010, slabs with ρ = 0.9% without shear reinforcement; (d) comparison in the case of slabs with large amounts of shear reinforcement (double-headed studs) (parameters: refer to Fig. 5.5; c = 350 mm)

5.3 Experimental campaign

The punching tests were performed in the Structural Concrete Laboratory at École Polytechnique Fédérale de Lausanne (EPFL). In total, 13 slabs were tested. The test series is complemented by two previous punching tests performed in the laboratory with similar parameters (PL7 [Lip12], PV1 [Fer10b]). The tested specimens (refer to Table 5.1) are grouped in two series, the first one investigating the influence of column size, while keeping the size of the slab constant, as the second one varies the size of the slab, while keeping the column size constant (Fig. 5.8(a)). In the first series, the columns were round in order to avoid the influence of possible stress concentrations in the

corners of large columns [Sag14]. The shapes of the first series' slabs were octagonal to be more comparable to an axisymmetric geometry. In the second series, the columns and the slabs were square.

For applying the load, eight round openings formed by steel tubes were left in the slabs at casting. The centers of these openings were located 120 mm from the slab edge. Thus, the distance r_q from the loading points to the center of the column also varied together with the specimen size. The slab thickness, in all cases, was 250 mm, representing a typical flat plate in buildings.

All the slabs were cast with normal strength concrete (f_c = 30.8 – 44.1 MPa) with mainly limestone alluvial gravel aggregate with maximum size of 16 mm. Compressive strength of concrete f_c was determined experimentally for each specimen by compression testing concrete cylinders (150 x 300 mm) cast at the same time and from the same batch of concrete as the test specimens. Concrete tests were performed at 7, 14 and 28 days after casting as well as on the day of the slab test (Table 5.1) in order to follow the development of concrete strength.

Tensile (top surface) reinforcement consisted in all the cases of conventional hot-rolled reinforcing steel rebars that had a clearly defined yielding plateau (ductility class C of Eurocode 2 [CEN04]). Yield strength of reinforcement f_y (Table 5.1) was determined by tension testing four samples of each diameter bars. The flexural reinforcement was uniformly distributed over the whole slab. The rebars were placed in four orthogonal layers, two on the bottom and two on the top surface. The top-most and the bottom-most reinforcement layers were oriented in the same direction. This is referred to as the strong axis, whereas the other direction is referred to as the weak axis. Close to the edge of the slab, the top reinforcement was anchored with 180° bends. The diameter of top surface rebars was 16 mm (for 4 slabs in the first series) or 20 mm (for 4 slabs in the first series and for all the second series slabs) and the spacing correspondingly 125 mm or 100 mm, which gives a nominal flexural reinforcement ratio of 0.75% or 1.5%. The bottom reinforcement consisted of cold-formed 10 mm rebars with spacing equal to that of the top reinforcement.

In the first series, the shape of the specimens was octagonal (with overall width of 3000 mm) whereas the columns were round (with diameters ranging from d_c = 83 mm to d_c = 660 mm) (Fig. 5.8(a)). The reinforcement layout was orthogonal. In the second series, both the slabs and the columns were square. The columns had a side length of c = 260 mm while the side length of the slabs varied from B = 1700 mm to B = 3900 mm. Two of the slabs of the second series and a reference slab PV1 [Fer10b] did not have shear reinforcement, whereas three slabs were equipped with double-headed studs as shear reinforcement (made of ordinary 16 mm ribbed reinforcing steel with yield strength of f_y = 560 MPa and hot-formed heads with diameters equal to 3 times the diameter of the shaft), fixed on rails in the bottom end to facilitate their installation. The stud rails were placed radially in a star-like pattern (according to the European practice) with 12 studs in each perimeter (Fig. 5.8(b)). The distance from the edge of the column to the first stud was s_0 = 80 mm (0.38 d) and the radial distances between subsequent studs s_1 = 150 mm (0.71 d). The number of stud perimeters was 4, 6 and 8 for slabs PP4, PP5 and PP6, respectively. The amount of shear rein-

forcement was selected to achieve the highest possible performance of the system that would lead to concrete crushing failure between the column and the first perimeter of studs [FIB13, Lip12, Fer09].

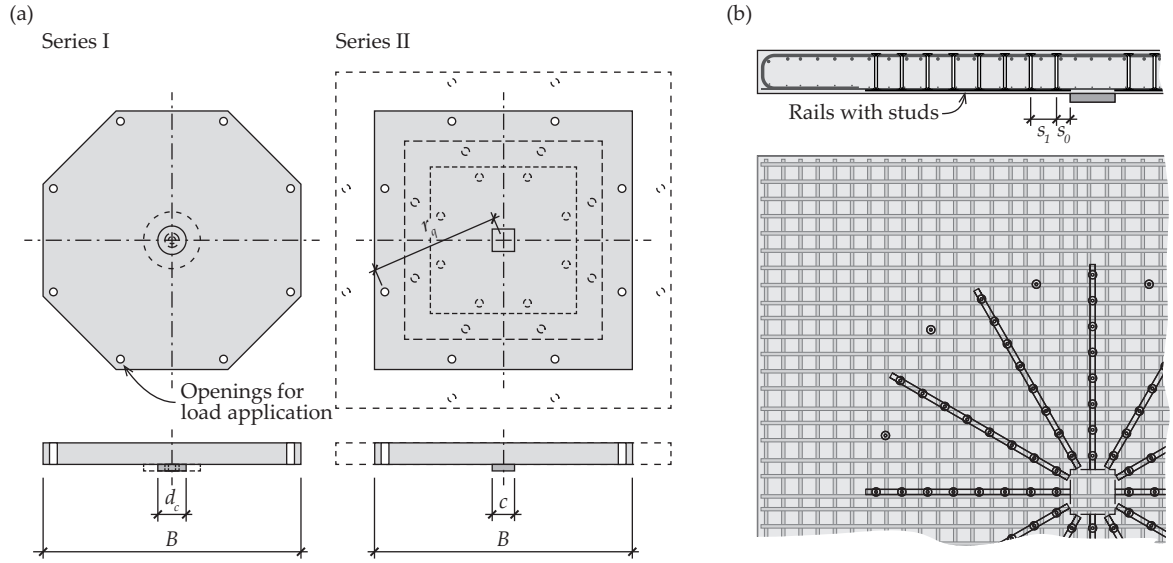

Figure 5.8 Test specimens: (a) geometric parameters; (b) placement of double-headed shear studs in specimens PP4, PP5 and PP6

Table 5.1 Main parameters of test specimens

Slab	B, m	r_q, m	c, mm	d_c, mm	d, mm	ρ, %	f_y, MPa	f_c, MPa
PE10	3.0	1.505	-	83	210	0.77	538	40.4
PE11	3.0	1.505	-	166	215	0.75	538	37.5
PE9	3.0	1.505	-	330	218	0.74	538	44.1
PE12	3.0	1.505	-	660	212	0.76	538	37.6
PE6	3.0	1.505	-	83	215	1.46	542	38.4
PE7	3.0	1.505	-	166	213	1.47	542	42.5
PE8	3.0	1.505	-	330	214	1.47	542	42.0
PE5	3.0	1.505	-	660	210	1.50	542	36.7
PE4	1.7	0.765	260	-	197	1.59	517	35.1
PV1 [Fer10b]	3.0	1.505	260	-	210	1.50	709	31.1
PE3	3.9	1.926	260	-	204	1.54	517	34.2
PP4	1.7	0.765	260	-	211	1.49	510	30.9
PP5	2.3	1.120	260	-	205	1.53	510	31.5
PL7 [Lip12]	3.0	1.505	260	-	197	1.59	583	35.9
PP6	3.9	1.926	260	-	203	1.55	510	32.7

A view of the test setup is shown in Figure 5.9. For all specimens (except for PV1, for which the details can be found elsewhere [Fer10b]), the load was applied by means of 4 hydraulic jacks connected to a common oil circuit under a strong 800 mm laboratory floor. The load was spread to eight loading points close to the perimeter of the slab at a distance r_q from the slab center. The slab was supported on a central steel column, on which a steel plate representing the column was

placed. A thin layer of plaster was placed on the steel plate before placing the specimen to avoid stress concentrations due to possible surface irregularities. The load was applied by manual pumping at a rate of approximately 25 kN/min.

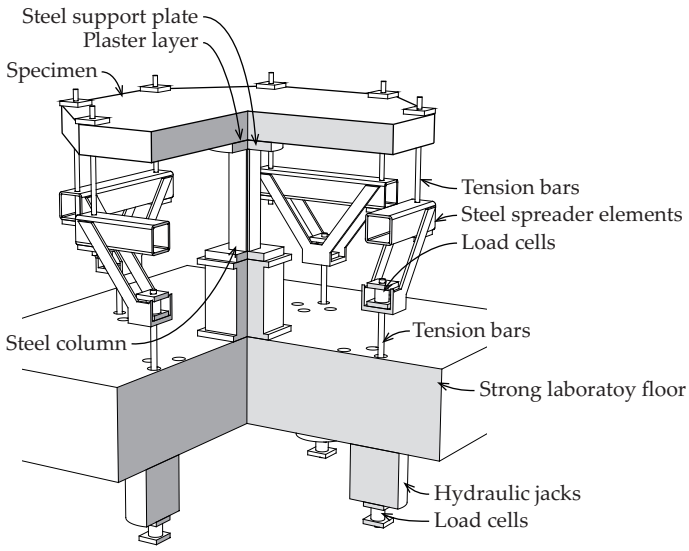

Figure 5.9 Test setup

The applied load was measured with two independent sets of load cells on the hydraulic jacks as well as on the load distribution elements (Fig. 5.9) and by strain gauges on the steel column. The differences between the results obtained with the three measurement systems were negligible. The slab rotation was measured with 4 digital inclinometers located on the main axes at a distance of 1380 mm from the center of the slab. Vertical displacements of the slab surface were measured with linear variable displacement transducers (LVDTs).

5.4 Test results

The main results of the tests are shown in Table 5.2 and the load-rotation curves in Figure 5.10. Slabs without shear reinforcement failed with a sudden drop of load. The rotations at failure varied between 5 and 35 mrad, indicating a transition from brittle to a more ductile failure type (it can be noted that slab PV1 had reinforcement with higher yield strength, but no yielding occurred and thus the load-rotation curve is not affected by this issue). At failure, the steel plate simulating the column suddenly penetrated into the slab with a loud noise. Exceptions were the slabs supported on the smallest columns (PE6 and PE10), where the failure was more gradual and accompanied by quieter cracking sound during few seconds. A diagonal failure crack was revealed after saw-cutting the specimens (Fig. 5.11). The failure cracks were irregular, with an average angle between the slab surface and the failure crack of approximately 45° or lower in most cases (refer to the photo of a typical crack in Fig. 5.12(a)). In some specimens, the failure cracks had different shapes and

angles on different sides of the column. In addition to the failure crack, several flexural cracks were seen on the saw-cuts that were inclined towards the column.

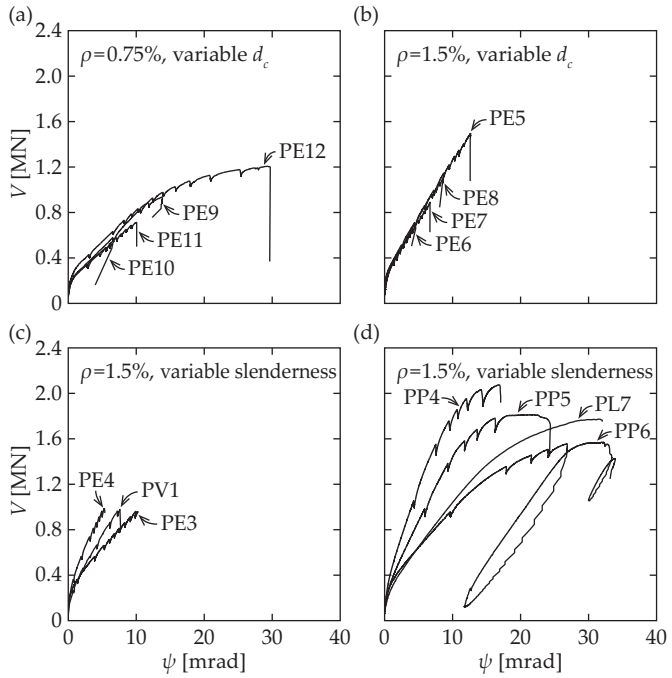

Figure 5.10 Load-rotation curves of the specimens: (a) slabs with round columns, ρ_{nom} = 0.75% and no shear reinforcement, variable column diameter; (b) slabs with round columns, ρ_{nom} = 1.5% and no shear reinforcement, variable column diameter; (c) slabs with ρ_{nom} = 1.5% and no shear reinforcement, variable specimen size (slenderness); (d) slabs with ρ_{nom} = 1.5% and double-headed shear studs, variable specimen size (slenderness)

The slabs with shear reinforcement failed at much larger flexural deformations. In slabs PP5 and PL7, the load-rotation curve reached a short plateau before failing with a sudden decrease of the load, whereas in the case of PP6 (the most slender slab), the testing system did not allow reaching sufficiently large deformations in order to achieve a punching failure. The cracking patterns on the saw-cuts of all slabs with shear reinforcement showed that the failure zone was severely damaged by flexural and shear cracks as well as by cracks in the anchorage zones of shear studs (Fig. 5.12(b)). The column plates penetrated also deeper in these slabs. Failure cracks (the cracks with the widest opening after the failure) were located either between the first perimeter of studs and the edge of the column plate or between the first two stud perimeters. The cracks crossing the shear reinforcement had much smaller widths. This suggests that shear reinforcement did not yield prior to failure which was also indicated by strain gauge measurements close to the top and bottom heads on the studs. Similarly to the slabs without shear reinforcement, the cracking patterns were not symmetric around the columns.

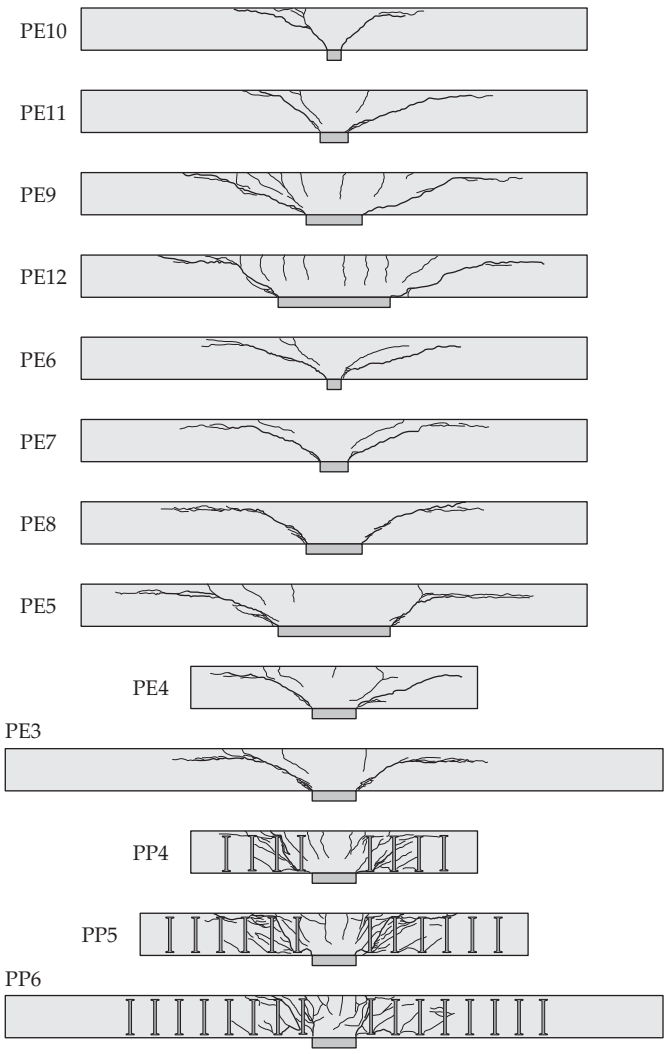

Figure 5.11 Saw-cuts of the slabs along the weak axis

Figure 5.13 shows the obtained punching shear strengths for series I (normalized with respect to concrete strength, control perimeter of ACI 3181 and effective depth) as a function of the column diameter (Fig. 5.13(a)) and for series II, as a function of the slab slenderness (Fig. 5.13(b)). The shear strengths predicted by ACI 318 and CSCT are also plotted (in dashed and in continuous lines, respectively). In the case of round columns, the predicted nominal strength according to ACI 318 is constant up to column diameters of 5.4d (for square columns, the limit is at $c = 4d$). In the experimental results, a decrease of the nominal punching shear strength with increasing column size can already be seen for smaller d_c/d ratios. Although the ACI 318 predictions were conservative for all the slabs in the present test campaign, the margin of safety decreased with increasing column sizes and decreasing reinforcement ratios.

Table 5.2 Experimental results and predicted punching strengths of test specimens, present study and the experiments of Lips *et al.* [Lip10], Regan [Reg86] and Sistonen *et al.* [Sis97]

Series	Slab	d mm	c/d	d_c/d	$B/2d$	$\psi_{R,test}$ mrad	$V_{R,test}$ kN	$V_{R,test}$ / V_{flex}	$V_{R,test}$ / $V_{R,ACI}$	$V_{R,test}$ / $V_{R,EC2}$	$V_{R,test}$ / $V_{R,CSCT}$	$V_{R,test}$ / $V_{R,MC}$
present study	PE10	210	-	0.40	7.14	6.5	530	0.53	1.29	1.19**	0.92	1.12
	PE11	215	-	0.77	6.98	10.1	712	0.67	1.36	0.96	1.05	1.29
	PE9	218	-	1.51	6.88	13.8	935	0.79	1.12	1.01	1.04	1.29
	PE12	212	-	3.11	7.08	29.4	1206	0.84	1.02	1.11	1.09	1.41
	PE6	215	-	0.39	6.98	4.5	656	0.33	1.58	1.50**	0.99	1.10
	PE7	213	-	0.78	7.04	6.7	871	0.42	1.58	0.93**	1.07	1.21
	PE8	214	-	1.54	7.01	8.7	1091	0.48	1.38	0.98	1.05	1.20
	PE5	210	-	3.14	7.14	12.7	1476	0.53	1.27	1.10	1.12	1.32
	PE4	197	1.32	-	4.31	5.3	985	0.38	1.38	1.03	0.98	1.14
	PV1*	210	1.24	-	7.14	7.6	978	0.35	1.33	0.99	1.07	1.22
	PE3	204	1.27	-	9.56	10.0	961	0.47	1.30	0.97	1.11	1.31
	PP4	211	1.23	-	4.03	16.8	2076	0.75	1.41	1.46**	0.97	1.24
	PP5	205	1.27	-	5.61	21.5	1812	0.85	1.27	1.29**	1.02	1.22
	PP6	203	1.28	-	9.61	32.0	1569	0.78	1.09	1.09**	1.06	1.25
								mean	1.31	1.12	1.04	1.24
								COV	12.0%	15.8%	5.5%	6.8%
[Lip10]	PL1	193	0.67	-	7.77	5.2	682	0.36	1.36	0.91**	1.03	1.16
	PL3	197	2.64	-	7.61	11.7	1324	0.54	1.16	1.06	1.08	1.29
	PL6	198	0.66	-	7.58	16.6	1363	0.71	1.30	1.77**	1.02	1.20
	PL7	197	1.32	-	7.61	27.6	1773	0.86	1.23	1.23	1.09	1.29
	PL8	200	2.60	-	7.50	-	2256	0.91	0.98	1.18	1.05	1.26
								mean	1.21	1.23	1.05	1.24
								COV	12.2%	26.5%	2.9%	4.7%
[Reg86]	V/1	118	0.46	-	6.78	-	170	0.33	1.35	1.17**	0.81	0.98
	V/2	118	1.44	-	6.78	-	280	0.50	1.37	1.10	0.94	1.18
	V/3	118	0.93	-	6.78	-	265	0.49	1.63	1.14	1.05	1.29
	V/4	118	0.86	-	6.78	-	285	0.53	1.35	1.15	1.02	1.26
	V/5	118	1.27	-	6.78	-	285	0.51	1.48	1.15	1.12	1.38
								mean	1.44	1.14	0.99***	1.22***
								COV	8.5%	2.2%	12.1%	12.5%
[Sis97]	L1	172	-	1.17	5.15	-	503	0.72	1.44	1.26	1.08	1.46
	L2	176	-	1.15	5.03	-	537	0.75	1.49	1.30	1.12	1.52
	L3	173	-	1.16	5.12	-	530	0.77	1.51	1.32	1.13	1.53
	L4	170	-	2.36	5.79	-	686	0.65	1.30	1.26	1.05	1.42
	L5	172	-	2.32	5.73	-	696	0.65	1.31	1.26	1.05	1.42
	L6	175	-	2.32	5.63	-	799	0.73	1.45	1.41	1.18	1.59
	L7	177	-	1.14	5.56	-	478	0.53	1.53	1.13	1.05	1.34
	L8	174	-	5.17	7.10	-	1111	0.55	1.28	1.25	1.11	1.51
	L9	172	-	5.22	7.18	-	1107	0.56	1.29	1.26	1.12	1.53
	L10	173	-	5.21	7.14	-	1079	0.54	1.25	1.22	1.08	1.48
								mean	1.39	1.27	1.10	1.48
								COV	7.9%	5.7%	3.7%	4.9%
								all tests, mean	1.34	1.18	1.05	1.30
								all tests, COV	11.3%	15.2%	6.7%	11.2%

* – reference test, Fernández Ruiz *et al.* [Fer10b]

** – $v_{R,max}$ is governing in the Eurocode 2 prediction

*** – d_g is not reported for these experiments, d_g = 16 mm [0.63 in.] is assumed (assuming d_g = 10 mm [0.39 in.] would give a mean of 1.04 and 1.28 for CSCT and Model Code 2010, respectively; assuming d_g = 20 mm [0.79 in.] would give 0.96 and 1.18)

Figure 5.13(b) confirms the CSCT [Mut08b] prediction that increasing specimen slenderness decreases its punching capacity. Consistently with the predictions of Model Code 2010 [FIB13] (Fig. 5.7), the effect is more pronounced for slabs with shear reinforcement.

(a)

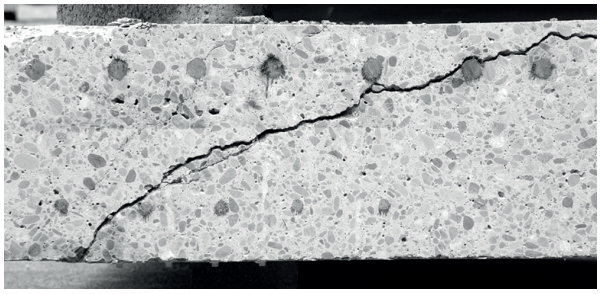

(b)

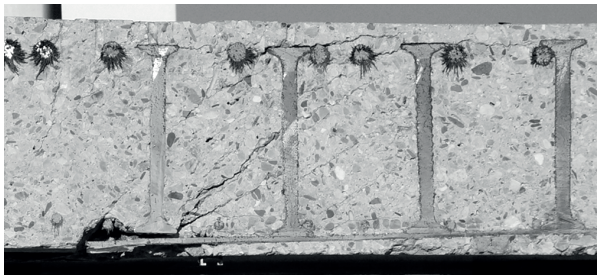

Figure 5.12 Photos of typical punching cracks on a saw-cut: (a) slab without shear reinforcement (PE7); (b) slab with shear reinforcement (PP4)

All the slabs analyzed in the present research failed below their respective flexural strengths (refer to the calculated $V_{R,test}/V_{flex}$ ratios in Table 5.2, where the values of V_{flex} are calculated using the yield line formulas given in Appendix B of the thesis. The $V_{R,test}/V_{flex}$ ratios increased with increasing column sizes and slenderness ratios. However, the load-rotation curves in Figure 5.10(d) suggest that a limit may have been reached for the specimens with shear reinforcement. These failures may be interpreted as failures due to combined effects of bending and shear. Such combined failures are also possible in continuous slabs in actual structures. However, the flexural strength of an actual slab may be higher than the flexural strength of an isolated test specimen. In Chapter 3, an extension of the CSCT was presented that allows predicting the punching capacities of continuous slabs and can also consider the influence of compressive membrane action in such slabs. Of the compared models, only the CSCT and the Model Code 2010 provide a physical method for assessing and comparing the behavior of both continuous and isolated slabs.

5.5 Comparison of test results to code predictions

Figure 5.14 compares the results of the present test campaign to the predictions of ACI 318 [ACI14], Eurocode 2 [CEN04], CSCT [Mut08b] and Model Code 2010 [FIB13] (Level of Approximation II). The details about the formulas used in the calculations can be found in Appendix A of the thesis. Previous results of similar campaigns by Lips *et al.* [Lip12] with variable column sizes, Regan [Reg86] with very small columns as well as Sistonen *et al.* [Sis97] with variable slab slender-

ness and column size to slab depth ratios are also included. The comparisons are shown as a function of c/d or d_c/d and specimen slenderness ratio ($B/2d$). The values are also given in Table 5.2.

The design formula of ACI 318 yields conservative predictions (the average measured-to-predicted strength of all the experiments is 1.34). However, the predictions are less conservative for larger column sizes in combination with lower reinforcement ratios and round columns (the lowest ratio of experimental load to prediction in current campaign is 1.02 for slab PE12). The slenderness effect is also neglected and thus a reduction in the margin of safety can be seen for higher slenderness ratios. The coefficient of variation (COV) for all the tests is 11.3%.

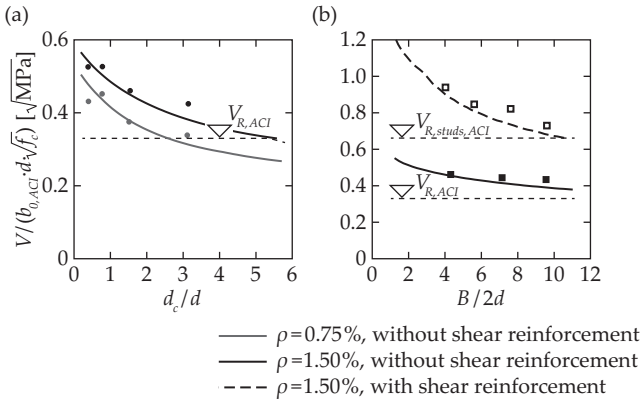

Figure 5.13 Normalized nominal shear stresses at failure on the ACI 318 control perimeter and comparison to the CSCT (continuous lines) and ACI 318 (dashed lines) predictions: (a) depending on column diameter (series I); (b) depending on specimen slenderness (series II)

The predictions of Eurocode 2 for the tests of the present test campaign fit the test results well if the governing verification is the one performed at the basic control perimeter located at $2d$ from the column edge. However, when the governing failure mode is exceeding $v_{R,max}$ at the column edge, the results show larger scatter. This limit also governs for the three slabs with shear reinforcement tested in the current campaign, as it assumes the same strength for both slabs with and without shear reinforcement. This lack of agreement has also been presented in previous studies [Lip12], showing a clear increase of punching capacity as a result of using shear reinforcement even in the case of small columns (with respect to slab depth). Thus, these predictions of Eurocode 2 are fairly conservative for these cases. On the contrary, Eurocode 2 gives excellent predictions for the five tests of Regan [Reg86] with c/d ratios between 0.46 and 1.44 where $v_{R,max}$ governs in only one case. These inconsistencies show that the Eurocode 2 verification of punching of small columns may not capture the actual influencing parameters correctly. For all the results, the average measured-to-predicted strength is 1.18 with a COV of 15.2%.

Regarding the predictions of both ACI 318 and Eurocode 2 for slabs with shear reinforcement (plotted with square markers with white fill in Fig. 5.14), a trend can be observed that leads to less conservative predictions for increasingly slender slabs. This is caused by the fact that although Eurocode 2 punching provisions account for the flexural reinforcement ratio, neither of the codes take the influence of slab slenderness into account.

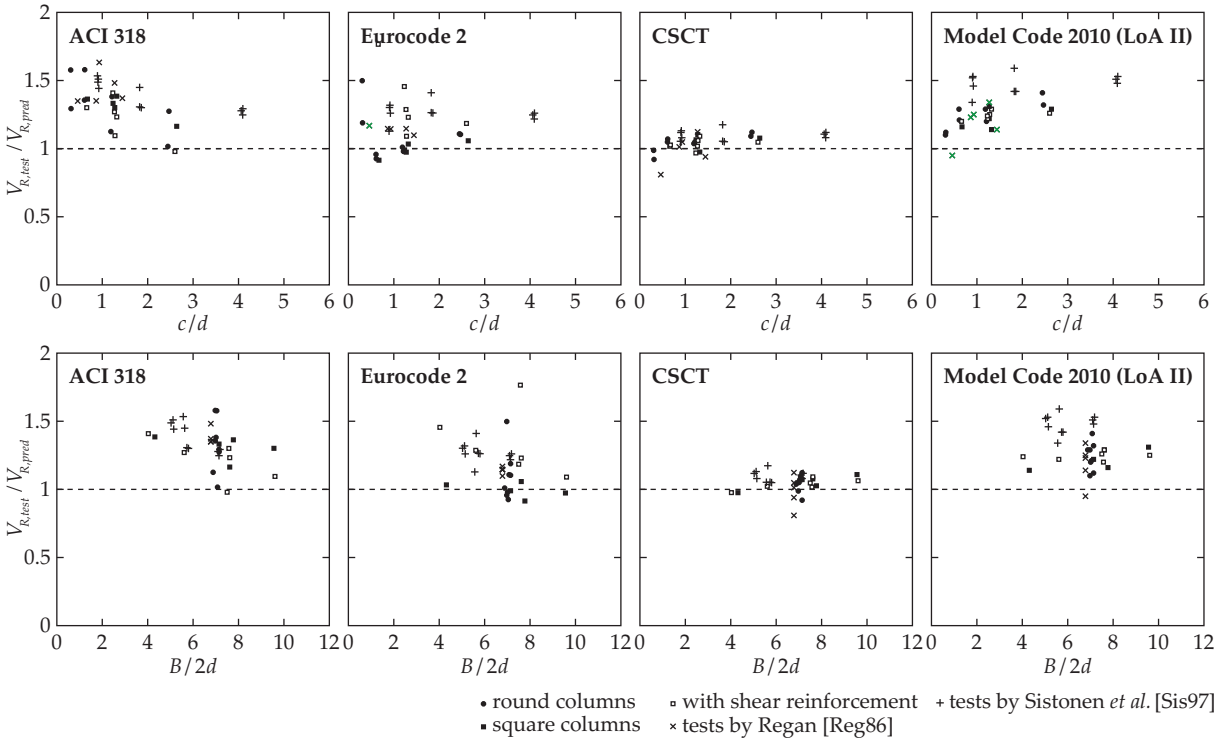

Figure 5.14 Comparison of test results to the codes of practice (for round columns, $c = \pi/4 \cdot d_c$)

The CSCT provides consistent results for all column size and specimen slenderness ratios. The mean ratio of experimental to predicted strength is 1.05 and the coefficient of variation 6.7%. For the smallest columns (PE6 and PE10 with d_c = 83 mm and V/1 of Regan [Reg86] with d_c = 54 mm), an overestimate of the punching strength can be seen. In these cases, the compressive stresses at failure under the column were close to $3 \cdot f_c$ (in other specimens, the average stress under the column plate always remained below f_c) and a different failure mode than typical to punching may have been attained in these tests. This hypothesis is also supported by the observations during the tests of the present experimental campaign and saw-cut patterns that showed a more gradual failure with crushing-like noise and steeper failure cracks.

The punching provisions of Model Code 2010 are based on the CSCT and the predictions are therefore similar. The differences can be explained by the different level of safety (the failure criterion curve of Model Code 2010 has been calibrated so that 5% of the experimental results are below the predicted strength, whereas the CSCT failure criterion corresponds to a mean of test results) and the fact that the non-linear load-rotation curve is replaced with a simplified parabolic relationship in Model Code 2010. The mean of the predictions is 1.30 and COV 11.2%. The influence of the two investigated parameters (column size with respect to slab depth and slab slenderness) is yet suitably reproduced.

5.6 Summary and conclusions

In this chapter, the results of an experimental campaign investigating the influence of specimen slenderness, column size and flexural reinforcement ratio on the shear strength of interior slab-column connections are presented. The results are compared to the predictions of ACI 318, Eurocode 2, the CSCT and Model Code 2010.

The main conclusions are:

- Experiments show that slenderness of a specimen influences the stiffness of its load-rotation response. Through influencing the crack widths, it also affects the punching strength. This effect is significant in the slabs with shear reinforcement and has to be considered when selecting the specimen size in the design of punching tests.
- Contrary to the experimental evidence, this parameter is not considered in the Eurocode 2 and ACI 318 punching provisions.
- Punching tests on slabs with varying support sizes indicate that the unitary nominal shear strength on a control perimeter at $d/2$ from the column face decreases with increasing column size. This effect can also be explained by the influence of cracking developing in the vicinity of the supported area.
- The decrease of the unitary nominal shear strength in ACI 318 for large columns may lead to an overestimate of the punching strength in the case of lower reinforcement ratios and thicker slabs. However, if the perimeter is located at $2d$ as in Eurocode 2, the punching strength of very small columns is overestimated. The deformation-dependent nominal shear stress of CSCT describes the punching phenomenon in a physical manner and provides good estimates for all different column sizes studied.
- The verification in Eurocode 2 that limits the shear stress at a control perimeter located at the column face neglects the influence of several important parameters and therefore may lead to very conservative results in the case of slabs with shear reinforcement.
- The CSCT and the punching provisions of Model Code 2010 consistently account for the influences of column size and slab slenderness. They provide the best mean and coefficient of variation for the ratio of experimental to predicted punching load amongst the compared models.

Chapter 6 Internal measurements

In the test campaign described in the previous chapter, development of cracking inside some selected specimens was tracked by means of a novel measurement system based on a coordinate measuring arm. This chapter analyzes these observations in detail and compares them to the measurements of the conventional instrumentation on slab surfaces. The main differences between the shear behavior of two-way specimens and that of previously studied one-way elements are discussed. This chapter is based on paper "Measurements of internal cracking in punching test slabs without shear reinforcement" submitted for publication in *Magazine of Concrete Research*.

6.1 Previous work

In shear tests of one-way elements (beams or slab strips), formation and propagation of flexural and shear cracks has been observed and measured by mechanical [Cam13, Vol14] or optical means [Cav15]. Through the rigorous experimental work, good overview of shear transfer actions in beams has been obtained, both in the case of elements with shear reinforcement [Cam13] as well as without it [Fer15].

In punching tests, the development of shear cracks is even more challenging to follow, as the cracking occurs inside the element. Several methods have been used to study the mechanism of punching failures. Moe [Moe61] tested slabs with large openings close to the slab-column connection and studied the growth of cracks on the sides of the openings. According to his observations, diagonal flexural cracks developed towards and eventually through the compression zone similarly to the behavior of one-way elements. Kinnunen and Nylander [Kin60] attempted to estimate the aggregate interlock stresses between the lips of the diagonal cracks. They eliminated this action in some of their test slabs by placing an impregnated cardboard cone in the place of the expected diagonal crack. The results showed a reduction in the failure load, in some cases very limited (10%), in another cases more significant (up to 54%). The disadvantage of this method was the predefined shape and length of the diagonal crack that may have influenced the results. In the tests of Regan [Reg83] and Ramos [Ram03], precast concrete blocks with strain gauges glued on the surfaces were placed in the punching specimens during their fabrication with the aim of measuring the magnitude and direction of radial strains inside the slab. These measurements showed the development of an inclined compression strut close to the column. However, this method could not detect concrete cracking, as cracks may have formed between the strain gauges. Crack openings have also been measured in the tests performed at EPFL, starting from Guandalini *et al.* [Gua09]. This has been done with LVDTs that have been fixed on the top and bottom surfaces of the slab measuring the thickness variation through a small hole drilled through the slab. Yet, these measurements only represent the vertical component of the opening of the internal cracks.

Although all the aforementioned experiments gave valuable information about the punching failure mechanism, information obtained with these methods was either incomplete or required significantly modifying the geometry or composition of the slab in a way that may have influenced its punching behavior. To avoid these shortcomings, Clément *et al.* [Cle12] performed three punching tests where the formation of cracks at various loading steps was followed using a robotic arm to measure the coordinates of a number of measurement points inside the slab. The same measurement system is used in the campaign described in the present chapter.

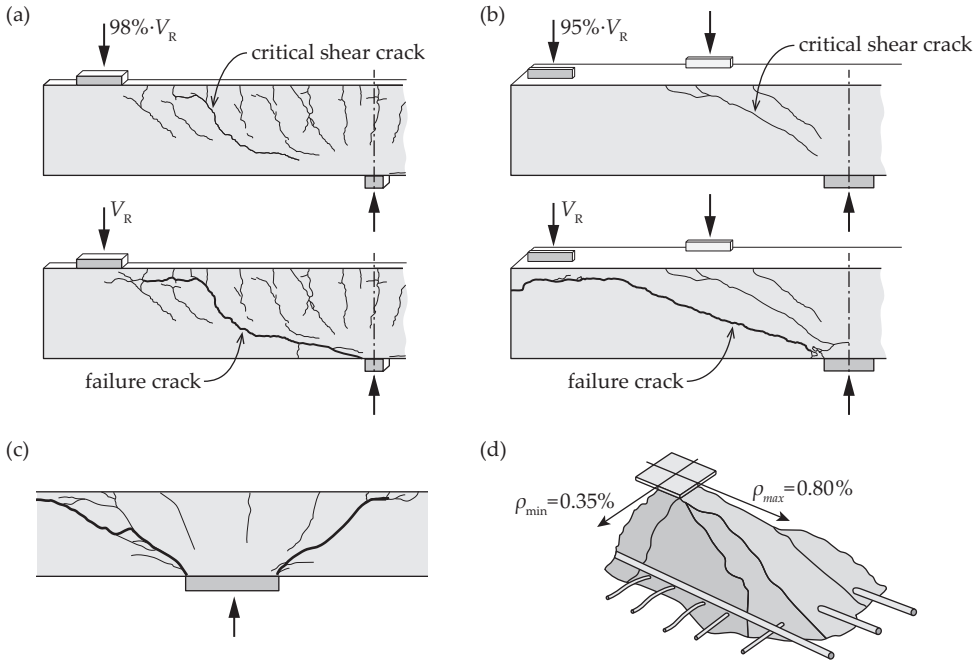

Figure 6.1 Comparison between the cracking patterns: (a) one-way (beam) specimen SC12b of Campana *et al.* [Cam13] (ρ = 1.5%); (b) saw-cut surface of two-way (slab) specimen PF22 of Clément *et al.* [Cle12] (ρ = 1.5%); (c) saw-cut surface of specimen PG3 of Guandalini *et al.* [Gua09] with low flexural reinforcement ratio (ρ = 0.33%); (d) punching cone of specimen PT23 of Sagaseta *et al.* [Sag11] with unequal reinforcement ratios in two directions

In Figure 6.1, cracking of some of the previously tested specimens is compared. In a sufficiently slender beam (such as SC12b [Cam13] shown in Fig. 6.1(a)), tension chord is normally cracked over the whole length of the element. The flexural cracks reach down to the neutral axis and may propagate into the compression chord. According to Fernández Ruiz *et al.* [Fer15], shear resistance of the element is controlled by one of these cracks, called the critical shear crack, which may either progress to become the failure crack (as in specimen SC12b shown in Fig. 6.1(a)) or trigger a sudden development of a new crack that leads to the failure [Cav15].

The cracking patterns observed on the saw-cut surfaces after a punching test is often different from the cracking on the sides of one-way elements [Mut10]. The internal measurements of Clement *et al.* [Cle12] indicated that the development of cracks differs as well. Figure 6.1(b) shows a two-way slab specimen (PF22 [Cle12]) with similar geometry (slab depth 400 mm, distance between the load

and the support 1380 mm) and reinforcement ratio (ρ = 1.5%) as the previously described beam SC12b. Flexural cracks on the saw-cut are concentrated in a zone located directly above the support. The furthermost flexural crack from the column edge (called the critical shear crack) is inclined at approximately 45°. This crack was detected by the internal measurement system after the appearance of flexural cracks on the surface of the slab and seen propagating to the vicinity of the compression chord, influencing its stress state. In contrast, the failure crack was not detected by the internal system even at the last measurement step at 95% of the failure load, which suggests its sudden appearance and propagation. Furthermore, this crack does not touch the critical shear crack. On the saw-cut, it can be seen as having much flatter inclination and straighter shape than the typical failure cracks in beam specimens (such as in SC12b in Fig. 6.1(a)).

However, it should be noted that in some other punching tests, different observations have been made. For instance, on the saw-cuts of specimen PG3 of Guandalini *et al.* [Gua09], which had low amount of flexural reinforcement (ρ = 0.33%), the failure cracks were seen having steeper angles (Fig. 6.1(c)) and turning quasi-vertical close to the tension chord. This suggests that these cracks had a flexural origin and that the flexural parts of the cracks were coincident with the critical shear crack. Moreover, in slabs with non-symmetric flexural reinforcement (as PT23 of Sagaseta *et al.* [Sag11] in Fig. 6.1(d)), the two types of failure cracks have been observed to occur in the same specimen. In the direction with lower amount of flexural reinforcement, a steeper failure crack can be seen, whereas the failure crack in the direction with higher reinforcement ratio has a lower angle similarly to that of PF22 (Fig. 6.1(b)).

This chapter describes in detail the measurements, both internal and external, performed during punching tests of six symmetric specimens (PE11, PE9, PE12, PE7, PE8 and PE5) from the test campaign presented in the previous chapter. Three different diameters of the support plate (166, 330 and 660 mm) and two flexural reinforcement ratios (nominal values 0.75% and 1.50%) were used. For further information about the specimens, refer to Chapter 5.

6.2 Measurement devices

6.2.1 External measurements

The slabs were instrumented with various measurement devices (Fig. 6.2(a)):

- the applied load was measured using four load cells on the load distribution elements and four load cells between the strong floor and the hydraulic jacks (Fig. 5.9);
- the slab rotation was tracked with four inclinometers on the main axes on the top surface close to the edges of the slab;
- vertical displacement profiles on the top and bottom slab surfaces were measured with linear variable differential transformers (LVDTs) on the E-W axis (west from the column)

(Fig. 6.2(b)). Additional four LVDTs measured the vertical displacement close to the four edges of the slab;

- column settlement and rotation were measured with three vertical LVDTs (in the analysis, it was assumed that the column plate did not deform);
- tangential concrete surface strains were measured with 3 strain gauges (base length 50 mm) glued on the concrete surface on the bottom face of the slab south from the column and perpendicular to the N-S axis;
- radial concrete surface strains were measured with 3 strain gauges oriented along the E-W axis west from the column.

All the measurement readings were set to zero before starting the test, assuming that the slab deformations under self-weight of the slab and the testing equipment were negligible (approximately 65 kN, added later to the measured load).

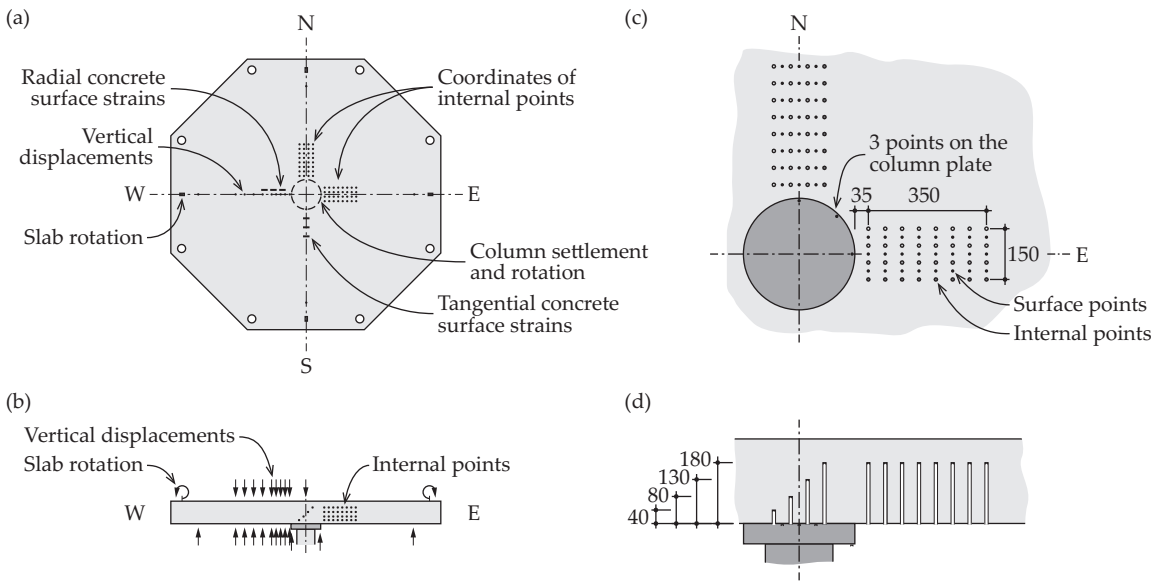

Figure 6.2 Instrumentation of the specimens: (a) plan view of the soffit of the specimen; (b) section view of the specimen (only LVDTs, inclinometers and internal points shown); (c) coordinate measurement points close to the column on the slab soffit; (d) section cut of the specimen through the internal coordinate measurement points

6.2.2 Internal measurements

The internal measurements were performed with a commercial coordinate measuring arm (FaroArm® Quantum) that could determine the location of its probe in the space by measuring the rotations of its 7 axes. In order to follow the internal cracking of the slab, 48 to 64 holes were drilled on the bottom surface (soffit) of each specimen with a 10 mm drill bit. The holes were cleaned of concrete dust and small steel cylinders with conical sockets as measurement points

were glued in the ends of the holes. To access the measurement points with the probe, the arm was extended with a stainless steel bar (length 200 mm, diameter 7 mm). Because the deformations of the extension bar, in comparison to the expected precision of the system, were not negligible, they were followed by means of strain gauges glued close to the fixed end of the extension bar. The obtained coordinates of the internal points were corrected using these strain measurements. The manufacturer-declared precision (radius of the point cloud) of the measuring arm was 0.020 mm. Calibration of the strain gauges on the extension bar, which was performed before each test, resulted in a standard deviation of the additional error below 0.010 mm.

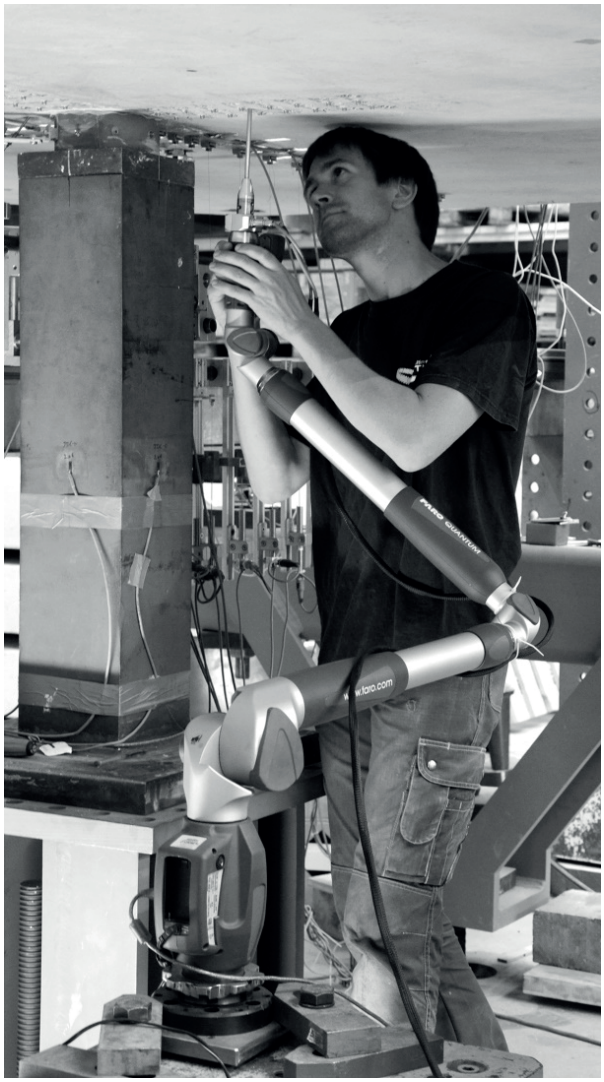

Figure 6.3 Performing the internal measurements with the robotic arm

The internal measurement points were located along the two main axes of the specimens in the north (strong axis) and east (weak axis) directions from the column in three or four lines (depending on the size of the column) with 8 points in each line (Fig. 6.2(c)). The distance between the points along each line, as well as between the lines was approximately 50 mm. The depth of the

holes for the internal points varied between 40 and 180 mm so that the points formed a regular mesh in a vertical plane (Fig. 6.2(d)). Reference points were glued on the slab surface between the holes, as well as on the column plate. The actual layout of the points varied slightly due to the precision of drilling and the need to avoid rebars.

The specimen was loaded by pumping oil into the hydraulic jacks. The load was applied in steps with larger load increments in the beginning of the test and smaller ones closer to the failure. After applying each load increment, the pumping was stopped which caused the load to decrease slightly. After approximately 10 minutes, when the rate of decrease of load had diminished, the coordinates of each point were measured sequentially (Fig. 6.3). One measurement step typically lasted for 10 to 15 minutes.

In addition to the accuracy of the measurement arm and the strain gauges on the extension bar, potential sources of erroneous measurements included accidental contacts of the extension bar with the walls of the drilled holes, dust or concrete debris on the measurement points, as well as loose points due to failure of the glue or cracks in concrete where the points were glued. As the points were located in narrow holes, these aspects were difficult to check visually. Also, slab movements or crack propagation during a measurement sequence may have influenced the calculated relative displacements between the points. In order to filter out inaccurate measurements, all the coordinates were carefully compared against the measurements at other load steps and the points that were judged clearly erroneous were removed from the analysis.

6.3 Test results

As explained in the previous chapter, all the analyzed specimens failed in punching with a sudden drop of the level of applied load. It is interesting to note that in several specimens, the failure occurred while the loading was stopped to perform measurements and the load had decreased below the maximum that had been reached. In these cases, the punching capacity V_R refers to the maximum load.

After the test, in order to observe the internal cracking patterns, all specimens were cut along the east-west (weak, Fig. 6.2(a)) axis, whereas the northern halves were additionally cut along the north-south (strong, Fig. 6.2(a)) axis. One wide crack, referred to as a "failure crack", was clearly distinguishable on all the saw-cut surfaces (Fig. 6.4). This crack extended from the edge of the column plate on the slab soffit to the tensile reinforcement layer (except on the east side of PE12, where the crack started at some distance from the column edge). The shapes and angles of this crack varied significantly between the specimens and even between the different sides of one specimen. On most saw-cut faces, some narrower flexural cracks were also visible above the column that extended from the top surface either to the bottom half of the slab or to the failure crack. The presence of the holes for internal measurements did not seem to have a significant influence on the cracking patterns and on punching performance compared to similar previously tested specimens.

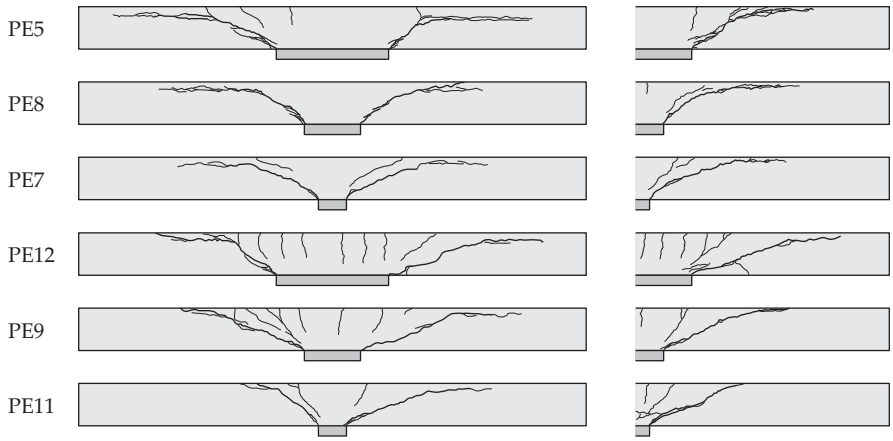

Figure 6.4 Saw-cuts of the specimens, along the weak axis (zone with holes for internal measurements is to the left (west) side of the column) and the strong axis (northern half)

6.3.1 Flexural response of specimens

According to the mechanical model of Kinnunen and Nylander [Kin60], the deformed shape of an axis-symmetric specimen can be approximated as conical between a radius r_0 (located at some distance from the column edge) and the edge of the specimen and as spherical within r_0 (Fig. 6.5(a)). The radius r_0 is determined by the location of the critical shear crack. It has been suggested to be selected as $r_0 = r_c + d$, which corresponds to an inclination of the critical shear crack of 45° [Mut08b]. Regarding the flexural response of a specimen, as shown in Figure 6.5(b), three phases can be observed, characterized by different stiffnesses of the load-rotation curve:

- Elastic uncracked phase before the first flexural cracks appear in the center of the slab. In this phase, slab deformations can be suitably predicted by means of linear-elastic slab theory;
- Cracked phase, where circular flexural cracks develop around the column. These cracks are inclined towards the center of the column due to the influence of shear stresses in the slab. The furthermost circular flexural crack (the critical shear crack) extends to the vicinity of the column edge. In addition, radial cracking starts spreading towards the edge of the slab. Starting from this phase, flexural behavior is suitably approximated by the conical model of Kinnunen and Nylander [Kin60].
- After yielding of radial reinforcement within the radius r_0, only tangential moments in the conical part can carry the additional load. The stiffness of the load-rotation response therefore decreases. Flexural strength of the specimen is reached when tangential reinforcement in the whole specimen reaches yielding.

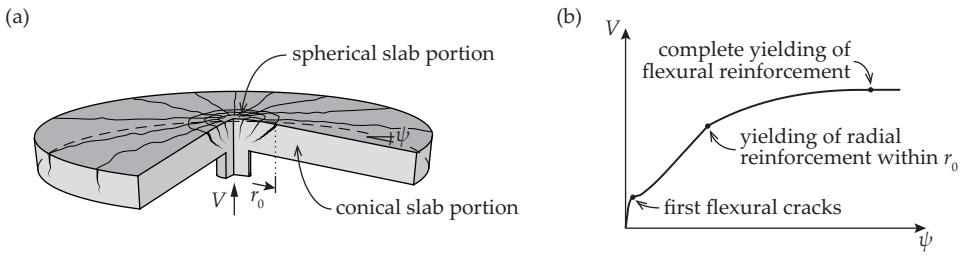

Figure 6.5 (a) Assumed deformed shape of a specimen [Kin60]; (b) Load-rotation curve

6.3.2 Deformations of the slab soffit

The behavior of punching test specimens cannot be characterized only by the flexural model. Figure 6.6(a) shows the deviations of the actual soffit deflections of specimen PE8 from the theoretical conical shape, measured with a series of LVDTs on the west side of the column. In the elastic uncracked phase, the slab has a curvature both in the tangential as well as in the radial direction, as predicted by the linear-elastic slab theory. Due to the radial curvature, compressive radial strains appear on the slab soffit (refer to the insert in Fig. 6.6(a)). After cracking of concrete due to the radial moments, this curvature starts to concentrate in the column region (the spherical slab portion in Fig. 6.5(a)) and thus the rate of increase of the radial compressive strains on the soffit decreases (at some distance from the column edge). After the circular cracks are fully developed, the radial strains on the soffit are nearly constant.

In addition, at already early stages of loading, penetration of the column plate into the slab is observed (this can be also in part explained by crushing of the thin layer of plaster placed between the column plate and the slab). However, the column penetration is only a local phenomenon as it does not have any effect on the radial soffit strains further from the column edge (Fig. 6.6(a)).

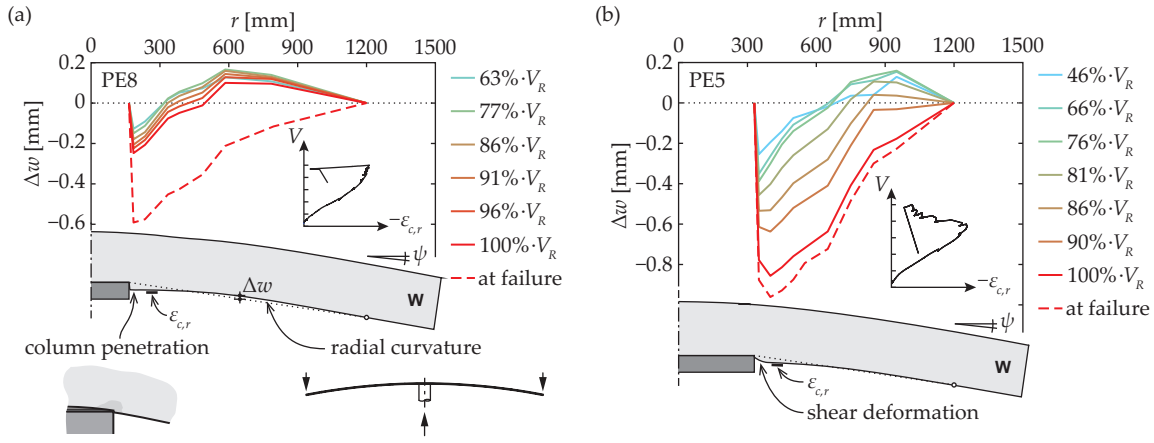

Figure 6.6 Deformations of the slab soffit: (a) deviations of the slab soffit from the assumed conical shape of specimen PE8; (b) deviations of the slab soffit of the specimen PE5

At load levels close to the punching strength, the development of strains on the slab soffit enters a new phase where the radial compression on the soffit begins to decrease. At failure, even tensile

strains have been measured in some of the previous experiments [Gua09]. Sometimes, this phase starts immediately before the failure (or even when the load is, in fact, decreasing, as in the specimen PE8 (Fig. 6.6(a)) or already at 80% of punching strength, as witnessed, for instance, in the specimen PE5 (Fig. 6.6(b)). The decrease of compressive strains is also measured by radial strain gauges further from the column edge (200 or 300 mm), although the reduction is less substantial there. Such slab behavior can be attributed to shear deformations of the slab soffit in the vicinity of the column (Fig. 6.6(b)). It can also be noted that the maximum soffit deviation from the conical shape (Δw_{max}) starts to increase faster in this phase than in the earlier stages of loading.

6.3.3 Internal cracking

Internal cracking of the specimens was monitored with the coordinate measuring arm on the eastern (weak axis) and the northern sides of the column (strong axis). Widths and opening directions of the cracks at different levels of load were calculated from the coordinates by dividing the mesh of measurement points into triangles. Strains on all sides of each triangle ($\varepsilon_{i\text{-}j} = \Delta l_{i\text{-}j}/l_{i\text{-}j}$) (Fig. 6.7(a)) were then converted into principal strains ($\varepsilon_{I,1\text{-}2\text{-}3}$ and $\varepsilon_{II,1\text{-}2\text{-}3}$ in Fig. 6.7(b)). The directions and magnitudes of the principal compressive strains in the triangles show the compressive stress field in the slab. However, the mesh of internal points was too coarse and the precision of the system too low to obtain reliable information about the compressive strains in concrete. In contrast, the precision was sufficient to follow the formation and kinematics of cracks. Crack widths w_{cr} and their opening directions at different load steps were calculated by multiplying the maximum principal tensile strain in each triangle with the length of the triangle in the direction of the strain (Fig. 6.7(c)). This represents an assumption that the tensile strain in a triangle was concentrated into a single crack that was perpendicular to the direction of the principal tension. The resulting crack widths and their opening directions are plotted in Figures 6.9(g)–6.14(g) for internal cracking on the weak axis and Figures 6.9(j)–6.14(j) for cracking on the strong axis, together with the cracks on the saw-cut surfaces. These plots confirm the assumption that the principal tensile strain directions are mostly perpendicular to the observed cracks.

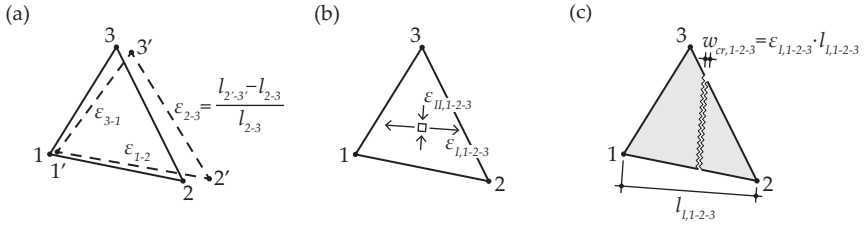

Figure 6.7 Conversion of the measured displacements to crack opening w_{cr}: (a) strains at the edges of the triangles; (b) principal strains; (c) crack opening in the direction of principal tensile strain

The cracks detected with the internal measurement system were always also found on the saw-cuts. On the other hand, in some places where no strains were measured before the failure in any of the measurement steps, wide failure cracks were present on saw-cut surfaces. Such cracks are

shown with dashed lines in Figures 6.9(f, g, i, j)–14(f, g, i, j) (for example on the strong axis of PE8 in Fig. 6.10(i, j)) in the locations where the absence of a crack was confirmed by reliable coordinate measurements. For all the measured cracks, the direction of crack opening did not change significantly between load steps and was approximately perpendicular to the crack lips (it should be noted that the plotted crack widths are projections on a vertical plane and some variability may thus be related to actual variations in crack angles between the measurement points). The exact centers of rotation of the slab sectors could not be detected due to the insufficient precision of the coordinate measurements. However, as the points on the slab soffit moved towards the column and the points deeper inside the slab moved further from the column, the vertical position of the center of rotation has to be located within the specimen.

6.4 Discussion of the test results

6.4.1 Development of the critical shear cracks

The critical shear crack (the furthermost circular crack of flexural origin) was followed in all the cases, except in the east direction (weak axis) of specimen PE8 (Fig. 6.10(g)). These cracks (1, 3, 5–11, 13–15 in Fig. 6.9–6.14) were first observed already at approximately 50% of the failure load. Widths of the critical shear cracks in different specimens, measured at the level of higher-most internal measurement points (approximately 170 mm from the bottom face of the slab), are shown as a function of slab rotation in Figure 6.8. The slabs with $\rho = 1.5\%$ are shown on the top and the ones with $\rho = 0.75\%$ on the bottom row. It can be seen that the cracks widths at a punching failure were larger in slabs with lower reinforcement ratios. The maximum measured crack width did not depend significantly on the column size.

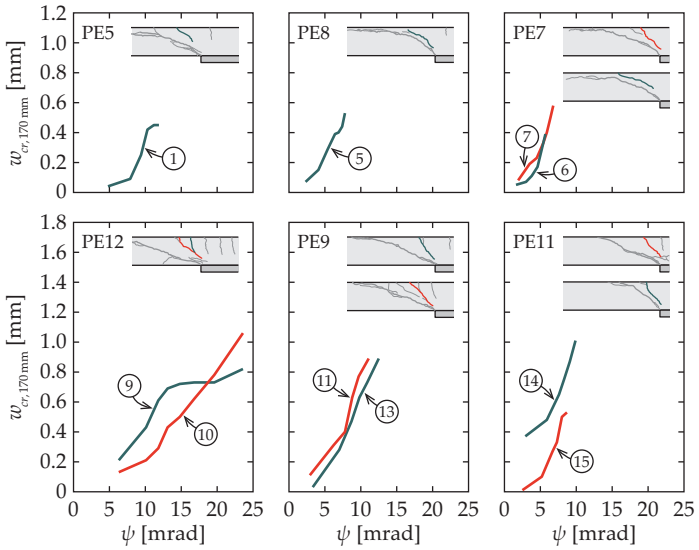

Figure 6.8 Widths of the flexural cracks as a function of slab rotation (average of the two directions in a corresponding axis)

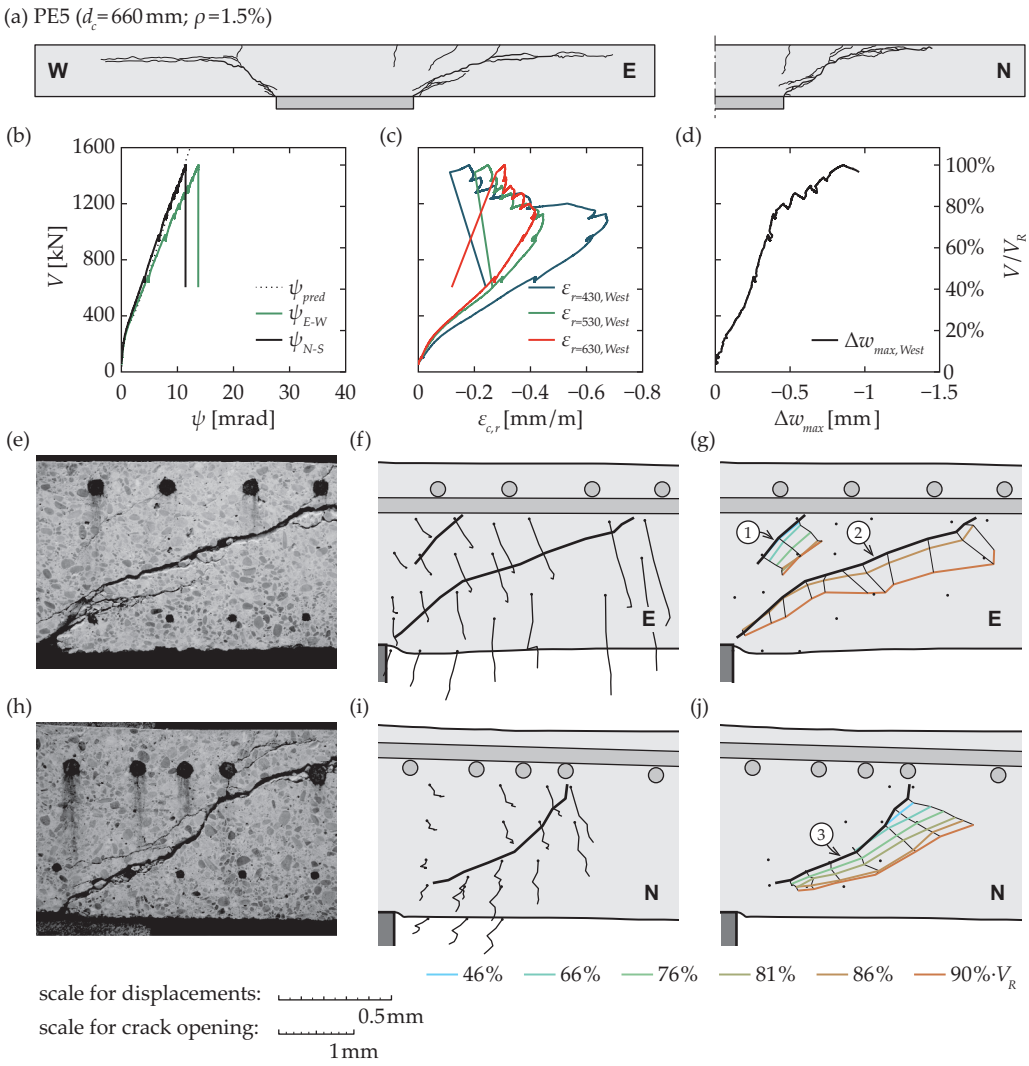

Figure 6.9 Specimen PE5: (a) cracks on saw-cuts; (b) rotations; (c) radial strains on soffit; (d) maximum negative deviation of the soffit from a conical shape; (e) cracks close to the column edge on the weak axis (E); (f) displacements (magnified) of the internal points relative to the edge of the column (E); (g) widths and opening directions of internal cracks (E); (h) cracks close to the column edge on the strong axis (N); (i) displacements (magnified) of the internal points relative to the edge of the column (N); (j) widths and opening directions of internal cracks (N)

However, it can be noted that in the case of larger columns, the cracks outside the perimeter of the column plate started opening at larger rotations. This can be explained by other flexural cracks closer to the center of the column developing first (outside of the monitored range). This is confirmed by the measurements performed on slab PE12, where two flexural cracks were located within the region of the internal measurement points (Fig. 6.12(j)). It can be seen that the crack that was closer to the center (crack 9) started opening at a lower rotation. However, another crack (crack 10) began opening further from the column and became the critical shear crack later. In the case of smaller columns, fewer circular cracks were located between the monitored region and the

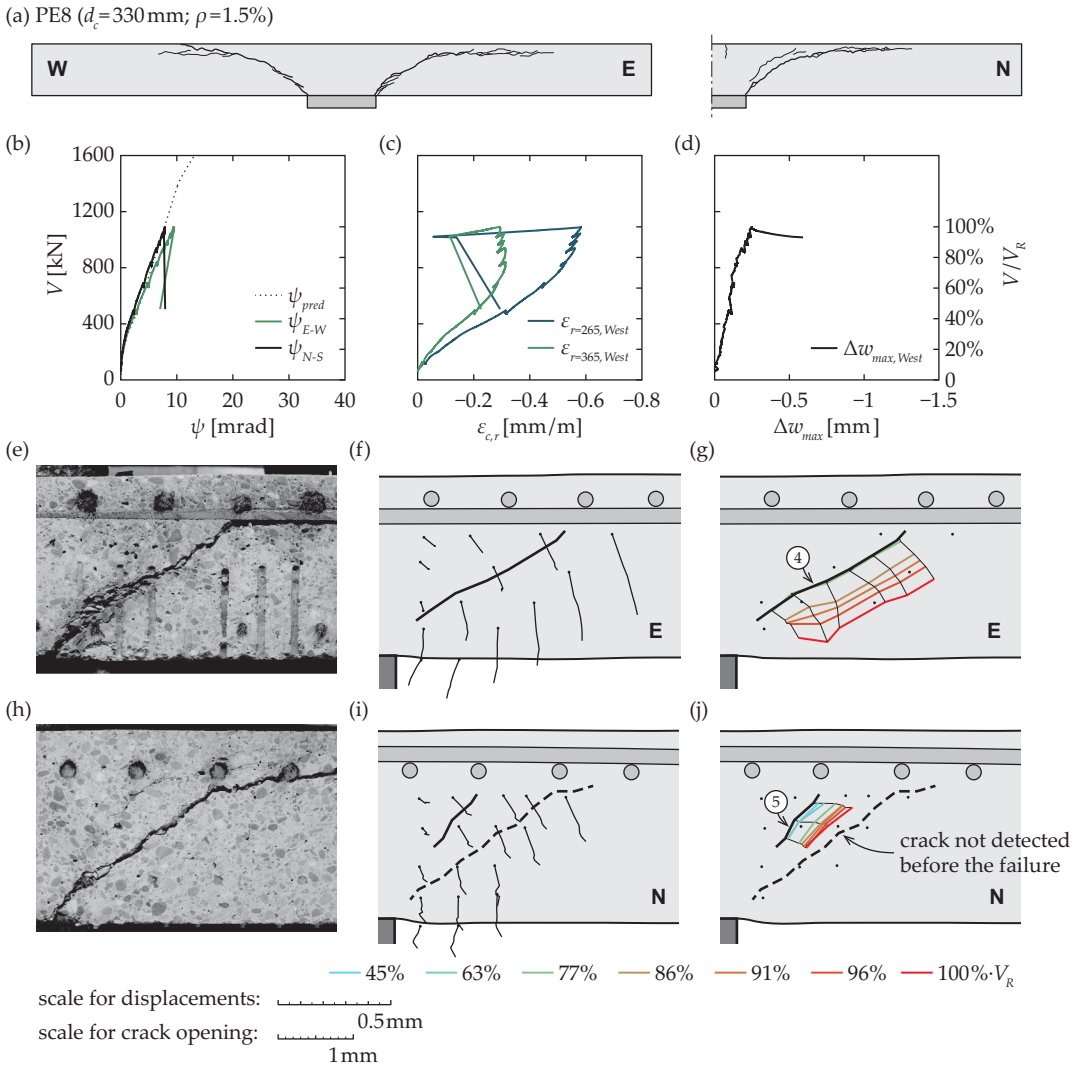

Figure 6.10 Specimen PE8: (a) cracks on saw-cuts; (b) rotations; (c) radial strains on soffit; (d) maximum negative deviation of the soffit from a conical shape; (e) cracks close to the column edge on the weak axis (E); (f) displacements (magnified) of the internal points relative to the edge of the column (E); (g) widths and opening directions of internal cracks (E); (h) cracks close to the column edge on the strong axis (N); (i) displacements (magnified) of the internal points relative to the edge of the column (N); (j) widths and opening directions of internal cracks (N)

center of the column and the development of the measured crack thus started at an earlier loading stage. It can be concluded that for an equal slab rotation, crack widths are lower if the column size is larger, as the flexural deformation is distributed between a larger number of cracks.

6.4.2 Development of the failure cracks

With the internal measurement system, two types of failure cracks could be distinguished. In some cases, the punching failures progressed along cracks that had been first observed as critical shear cracks. However, in the other cases, the failure cracks developed independently of the critical shear

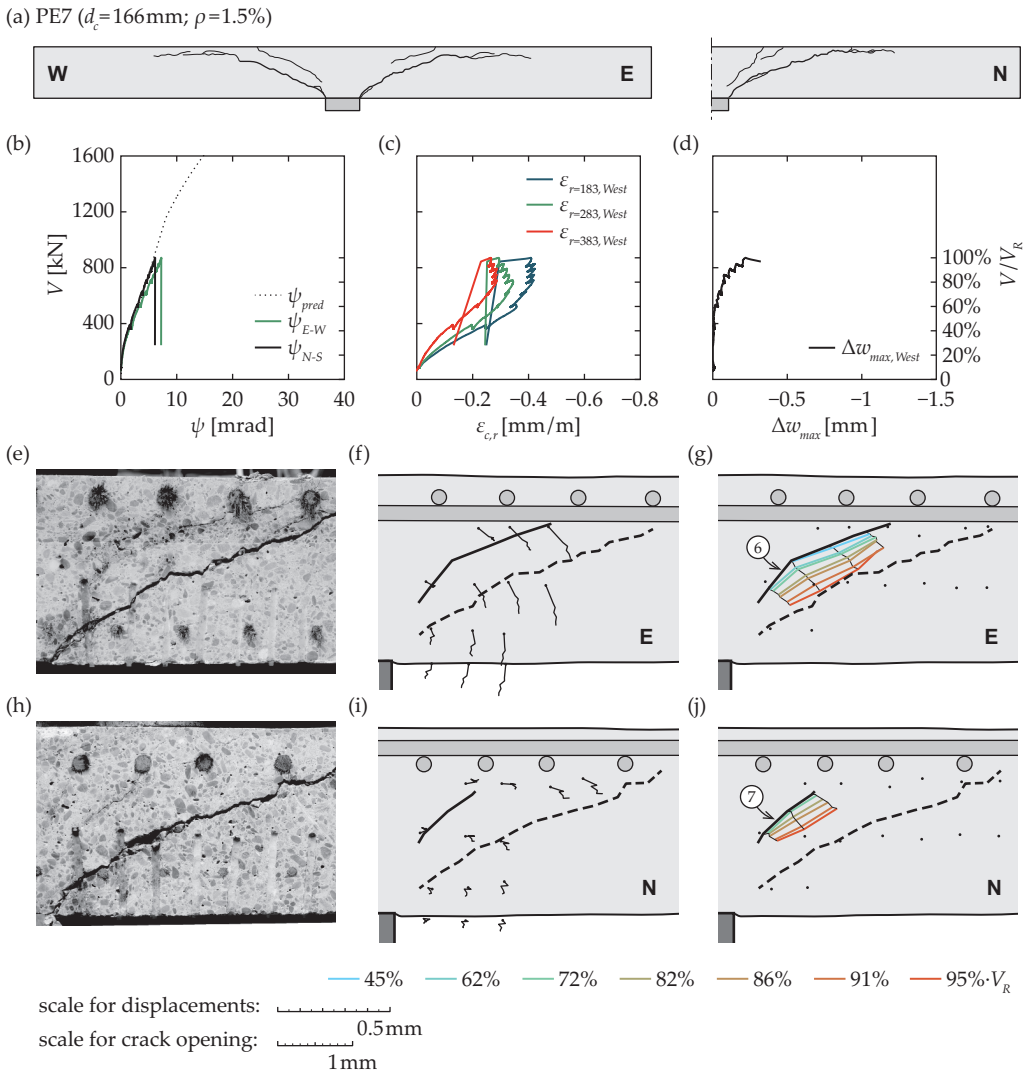

Figure 6.11 Specimen PE7: (a) cracks on saw-cuts; (b) rotations; (c) radial strains on soffit; (d) maximum negative deviation of the soffit from a conical shape; (e) cracks close to the column edge on the weak axis (E); (f) displacements (magnified) of the internal points relative to the edge of the column (E); (g) widths and opening directions of internal cracks (E); (h) cracks close to the column edge on the strong axis (N); (i) displacements (magnified) of the internal points relative to the edge of the column (N); (j) widths and opening directions of internal cracks (N)

cracks (refer to Fig. 6.1(c) and (b), respectively).

Development of the punching failure along the critical shear crack was observed in the specimens with the largest column sizes (d_c = 660 mm): on the north side of the column (strong axis) in specimen PE5 (crack 3 in Fig. 6.9(j)) and on the east side of the column (weak axis) in specimen PE12 (crack 8 in Fig. 6.12(g)). In both cases, the eventual failure cracks were first detected at load levels clearly below the punching capacity: at 76% of V_R in specimen PE5 and at 85% of V_R in specimen PE12. Yet, in both of these specimens, the failure cracks in the other monitored regions were of the second type and appeared in the slab portion below the critical shear crack. In specimen PE5, at the

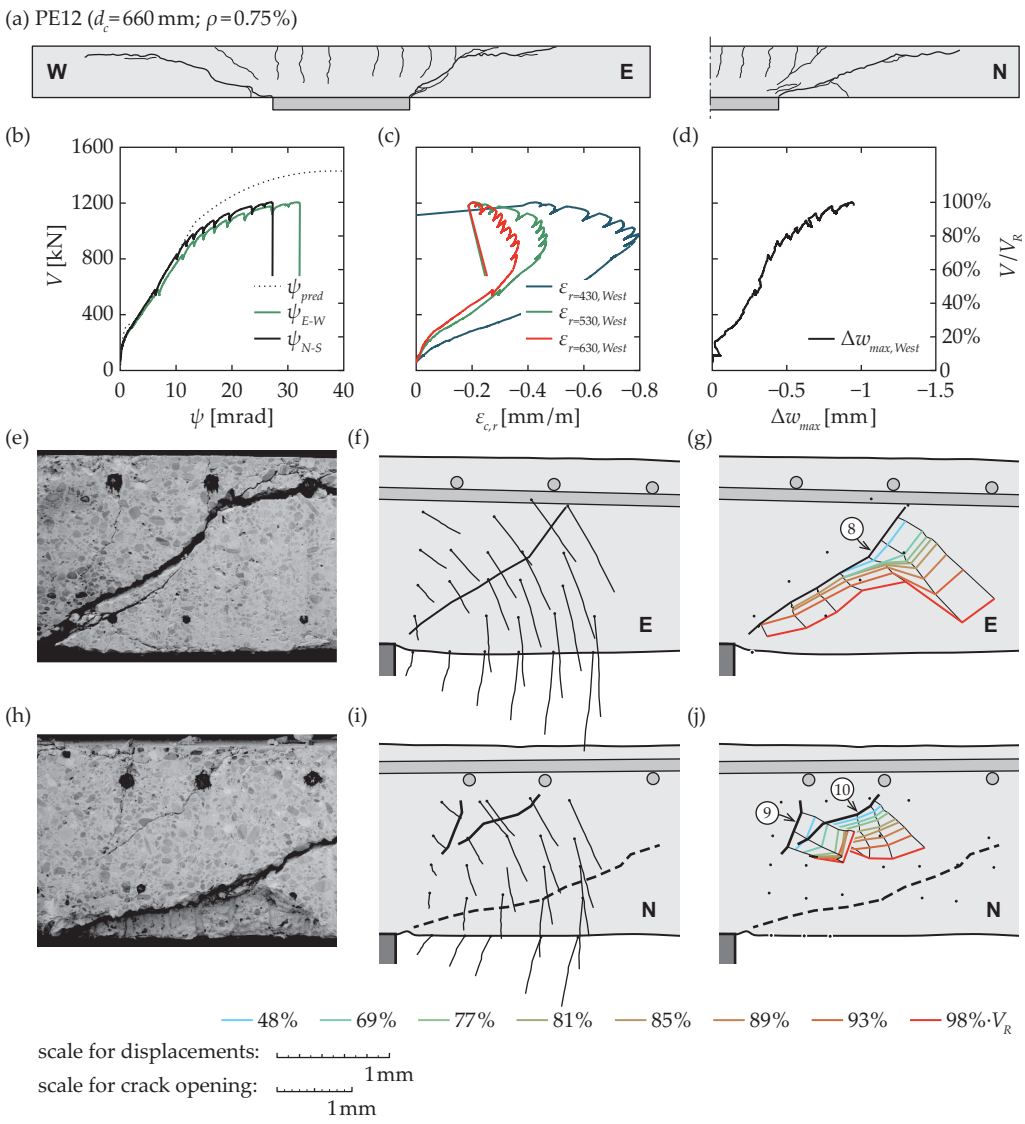

Figure 6.12 Specimen PE12: (a) cracks on saw-cuts; (b) rotations; (c) radial strains on soffit; (d) maximum negative deviation of the soffit from a conical shape; (e) cracks close to the column edge on the weak axis (E); (f) displacements of the internal points relative to the edge of the column (E); (g) widths and opening directions of internal cracks (E); (h) cracks close to the column edge on the strong axis (N); (i) displacements of the internal points (N); (j) widths and opening directions of internal cracks (N)

last measurement step at 90% of the maximum load, the failure crack on the east side of the column (inclined at 18° from horizontal) had a width of approximately 0.3 mm (crack 2 in Fig. 6.9(g)). However, in specimen PE12, where the failure crack on the east side of the column had even lower inclination, it was not detected even at the last measurement step, although the measurements were performed at 98% of V_R.

Regarding the deformations on the slab soffit, which were measured on the west side of the column, the development of shear deformations started already at approximately 75% of V_R in both specimens with the largest columns. This was indicated by the beginning of the reduction of radial

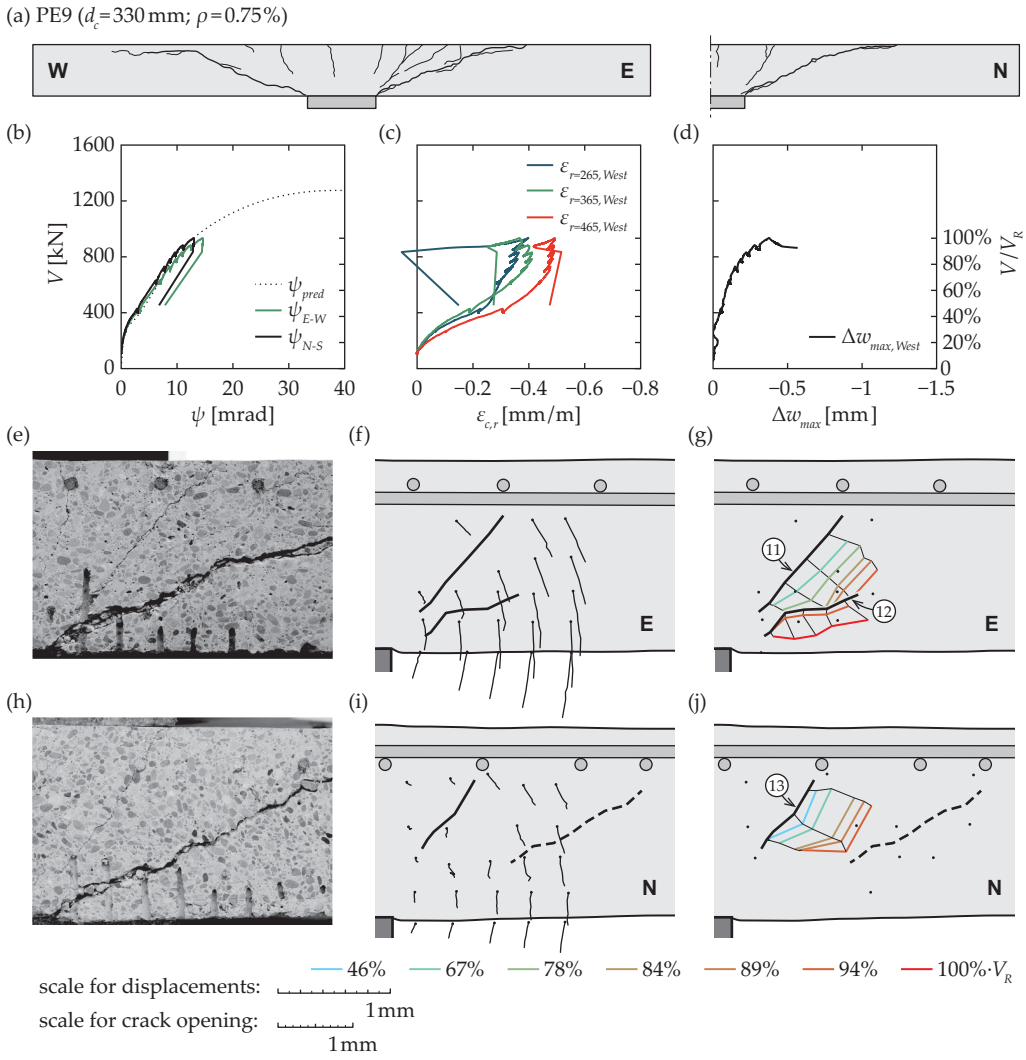

Figure 6.13 Specimen PE9: (a) cracks on saw-cuts; (b) rotations; (c) radial strains on soffit; (d) maximum negative deviation of the soffit from a conical shape; (e) cracks close to the column edge on the weak axis (E); (f) displacements (magnified) of the internal points relative to the edge of the column (E); (g) widths and opening directions of internal cracks (E); (h) cracks close to the column edge on the strong axis (N); (i) displacements (magnified) of the internal points relative to the edge of the column (N); (j) widths and opening directions of internal cracks (N)

compressive strains on the soffit (Fig. 6.9(c) and 6.12(c)) and concurrent increase of maximum deviation from the conical shape (Fig. 6.9(d) and 6.12(d)).

In the specimens with intermediate size columns (d_c = 330 mm: PE8 in Fig. 6.10 and PE9 in Fig. 6.13), the failure cracks developed independently of the critical shear cracks in every region with internal points. Both of the specimens failed during or after performing the internal measurements while the load had decreased below V_R. In the strong (north) direction, no strains were measured at the location of the eventual failure crack in either of the slabs. In contrast, on the east side of the column of specimen PE8, a failure crack (with an inclination of 30°) was observed to

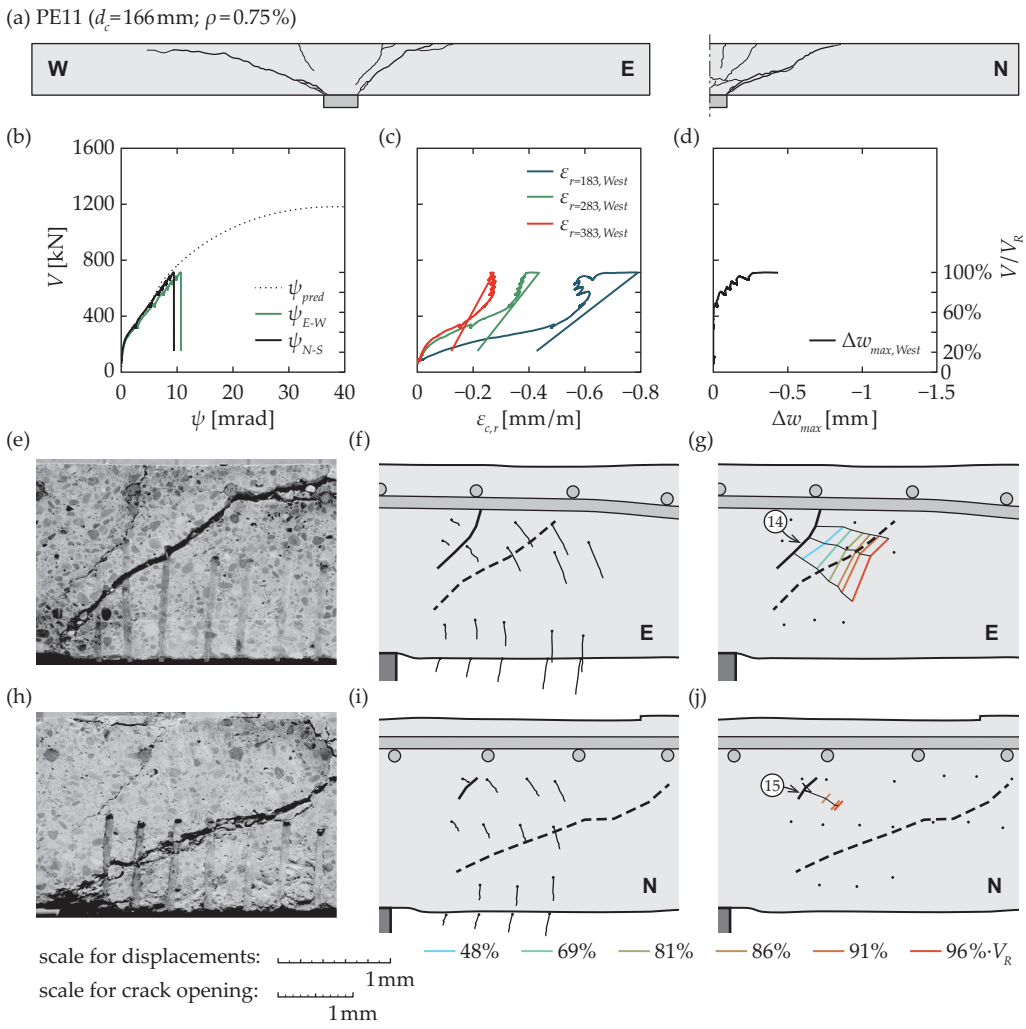

Figure 6.14 Specimen PE11: (a) cracks on saw-cuts; (b) rotations; (c) radial strains on soffit; (d) maximum negative deviation of the soffit from a conical shape; (e) cracks close to the column edge on the weak axis (E); (f) displacements (magnified) of the internal points relative to the edge of the column (E); (g) widths and opening directions of internal cracks (E); (h) cracks close to the column edge on the strong axis (N); (i) displacements (magnified) of the internal points relative to the edge of the column (N); (j) widths and opening directions of internal cracks (N)

start opening at 86% of V_R (Fig. 6.10(g)). The width of the crack, uniform over the whole measured length, increased to 0.7 mm before the failure.

However, on the west side of the column of PE8, shear deformations (Fig. 6.10(c) and (d)) started to increase only while performing the final measurements. The failure of the specimen occurred approximately 20 minutes after the loading was stopped, during which period the applied load had dropped from the maximum of 985 kN to 835 kN. In specimen PE9, the failure occurred while the measurements were being taken. During the final measurements, on the east side of the column, a failure crack with an opening of 0.3 mm (crack 12 in Fig. 6.13(g)) was detected. Yet, increas-

ing shear deformations were measured in this specimen on the west side of the column already at earlier loading stages (Fig. 6.13(d)).

In the specimens supported on the smallest columns (d_c = 166 mm), the failure cracks were not detected prior to punching in any of the cases. In specimen PE11, the radial compressive strains at the soffit, that had been decreasing before, started to grow again immediately before the failure. Similar behavior has also been observed in other specimens with even smaller column sizes (refer to Chapter 5) and in compact footings (by Simões *et al.* [Sim16]). This suggests that a different failure mode may govern in the case of very high compressive stresses in the punching region.

6.4.3 Tangential crack propagation

It is interesting to note that the development of failure cracks in two sectors of the same slab could be remarkably different, in spite of the specimens being nominally axisymmetric. In some slab sectors, the eventual failure cracks appeared at lower load levels than in the other sectors, sometimes already at 75–80% of V_R. This can be compared to the observations of Campana *et al.* [Cam13] as well as Cavagnis *et al.* [Cav15] regarding the shear behavior of beams, which showed that different cracking patterns, with consequent differences in mechanical shear transfer actions through the cracks, can emerge in beam specimens of similar geometries and mechanical properties. These differences can also explain the significant scatter between the shear strengths measured in various beam specimens.

In slab specimens, however, the detected initiation of a failure crack did not yet prompt a sudden punching failure. In several cases, the load could still be increased and the development of the failure crack could continue in a stable manner without significantly influencing the overall response of the specimen. This suggests that the reduction of the shear-carrying capacity of the sector elements with growing failure cracks was compensated by redistributing the shear force to adjacent sectors, where the failure cracks had not yet appeared. Similar redistribution of shear forces along the support has also been observed in non-symmetric punching test specimens by Sagaseta *et al.* [Sag11] and in shear tests of slabs with concentrated loads near linear supports by Natário *et al.* [Nat14].

Redistribution of shear forces in slabs also changes the associated moment fields. In axisymmetric punching test specimens, tangential shear redistribution due to the development of a failure crack should lead to locally reduced tangential moments in the slab sector with the failure crack (Fig. 6.15(a)). In most cases, this local reduction could not be directly observed, as the tangential soffit strains were measured in the experimental campaign only on one side of the column. However, the local reduction of bending moments was indirectly indicated by:

- in specimen PE7, decreasing tangential compression on the slab soffit was measured on the strong axis when the loading was stopped at 95%·V_R (Fig. 6.15(b));

– in the other specimens, the tangential soffit compression on the strong axis, which should have a linear dependence on slab rotation in axisymmetric slabs, started increasing faster at loads close to the failure, especially in the specimens with the largest column sizes, PE5 and PE12 (Fig. 6.15(c)). This may indicate the development of failure cracks and consequent decrease of tangential moments on the other sides of the column (on the weak axis);

– an increase of the average slab rotations in comparison to the predicted curves (shown with dashed lines in Figures 6.9(b)–14(b)) at load levels close to the punching failures. Again, this effect was observed to be stronger in specimens with larger column sizes (especially PE12, refer to Fig. 6.12(b)), where failure cracks were wider and detected at lower levels of load.

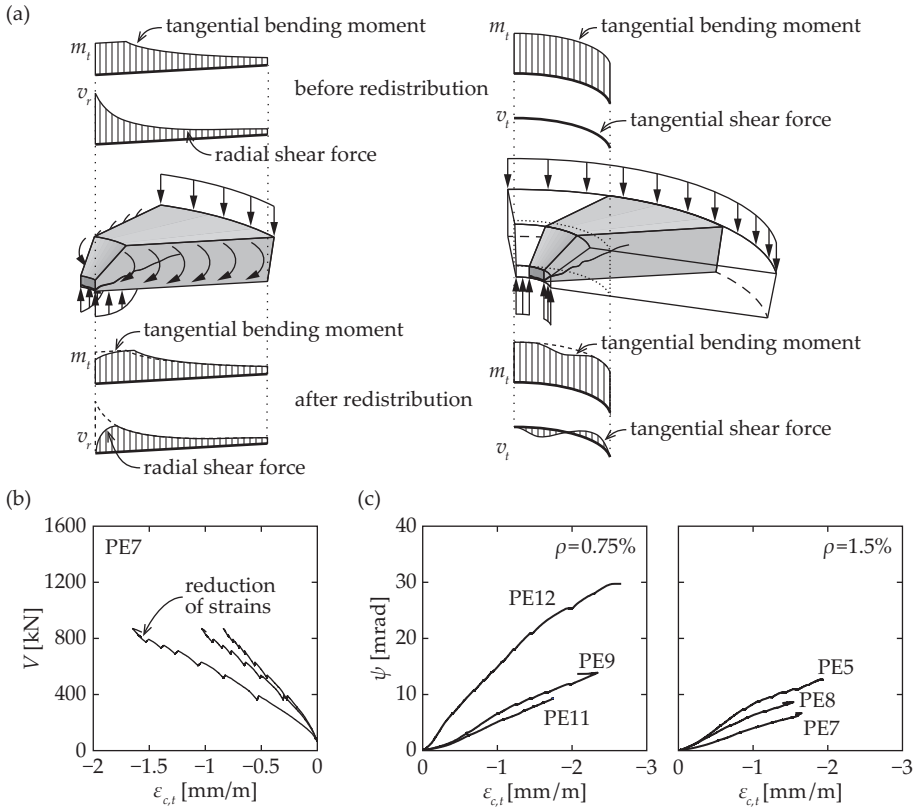

Figure 6.15 Redistribution of shear forces in axisymmetric specimens: (a) bending moments and shear forces associated to tangential shear redistribution; (b) measured tangential bottom surface strains in specimen PE7; (c) average slab rotation-tangential soffit strain curves for the axisymmetric specimens

It should also be noted that the ultimate tangential strains on the slab soffits (at 100 mm from the column edge) ranged from −1.5‰ to −2.6‰ (Fig. 6.15(c)). These strains are lower than the strains corresponding to the compressive strength of normal strength concrete in biaxial compression, as reported by Kupfer [Kup73]. Therefore, on the basis of these measurements, no strain-softening of concrete in compression was observed to have occurred.

6.5 Summary and conclusions

Formation and growth of cracks inside 6 full-scale punching test specimens was successfully monitored with a newly developed system for internal measurements. The results were also compared to conventional measurements performed on slab surfaces. Both flexural as well as the eventual failure cracks were tracked. The main conclusions made on the basis of the observations are:

- The main results (punching strengths and critical deformations) of the slabs with holes for internal measurements were consistent with the results of previously tested full slabs;
- Based on their mode of development, two types of cracks could be distinguished in the punching regions, namely the critical shear cracks and the punching failure cracks;
- The critical shear cracks were of flexural origin and developed as predicted by the sector model of Muttoni [Mut08b]. The directions of crack opening were approximately perpendicular to the crack lips. The widths of the furthermost flexural cracks depended on the total number of cracks within the supported area. Therefore, for equal rotations, the cracks were narrower in specimens with larger column sizes;
- The observed development of punching failure cracks was different between the specimens and even between the different sides of the column in the same specimen;
- Except for some sides of the largest columns, punching failures did not occur along the pre-existing critical shear cracks but by formation of new (lower-angled) failure cracks;
- The initiation of a failure crack did not always cause an immediate punching failure of the specimen. Instead, in several cases, the load could still be increased by up to 20%;
- The capacity of the specimens to resist increased loads after the formation of a failure crack can be explained by tangential redistribution of shear along the perimeter of the support. The associated changes of the moment field were also indicated by strain measurements on slab soffit.

Chapter 7 Punching failure model

This chapter proposes a new punching model for slabs without shear reinforcement. The model is based on the experimental evidence obtained in the test campaign presented in the previous chapter. The failure is assumed to be governed by a triaxial state of stresses in the compression strut around the edge of the support. Possible contribution of dowel action of tensile reinforcement is also considered. Size effect and the influence of crack propagation around the column are taken into account with semi-empirical factors. Comparison to 100 punching tests on slender specimens from the literature suggests a good agreement between the model predictions and the experimental results.

7.1 Mechanisms of shear transfer in reinforced concrete elements

7.1.1 Shear transfer mechanisms in beams and two-way slabs

Shear force in an element is associated with variations in acting bending moments. Bending moment in a beam can vary along the span either through changing the lever arm between the compression and tension chords with forces in them remaining constant, or by changing the forces in the chords. In the former case, the shear force in a beam is carried by the vertical component of the force in the compression chord. This mechanism is referred to as arching action. In the latter case, forces need to be transferred between the tension and compression chords. In cracked reinforced concrete elements without transverse reinforcement, the possible mechanisms of shear transfer include so-called beam shear transfer actions that were described by Kani [Kan64]. These mechanisms utilize tensile stresses in concrete, dowel action of tensile reinforcement and stress transfer through the cracks, which include aggregate interlocking stresses between crack lips and residual tensile strength of cracked concrete. The contributions of these actions in slender beams were recently studied by Fernández Ruiz *et al.* [Fer15], who used idealized crack shapes and kinematics and concluded that all the actions are eventually dependent on the widths of the cracks. However, a recent detailed experimental investigation by Cavagnis *et al.* [Cav15] has shown that force transfer through aggregate interlock stresses is strongly dependent on the shape of the cracks, which can be highly variable between similar specimens.

Experimental evidence and theoretical considerations have shown that shear behavior of a beam is strongly influenced by its shear slenderness ratio (defined as a/d for beams with concentrated loads or as M/Vd in a general case (Fig. 7.1(a)) and the relative contributions of the different mechanisms of shear transfer depend on this parameter [Kan64, Kan66]. In the case of compact beams, the compression chord can be inclined, allowing for the development of a direct strut, or arching action. Shear failures occur with a loss of capacity of the strut, which may be decreased due to trans-

verse tensile strains. In contrast, in slender beams, cracks developing through the direct strut limit its capacity and the strength of an element is governed by beam shear transfer actions and their capacities (aggregate interlock, dowel action or the tensile strength of concrete).

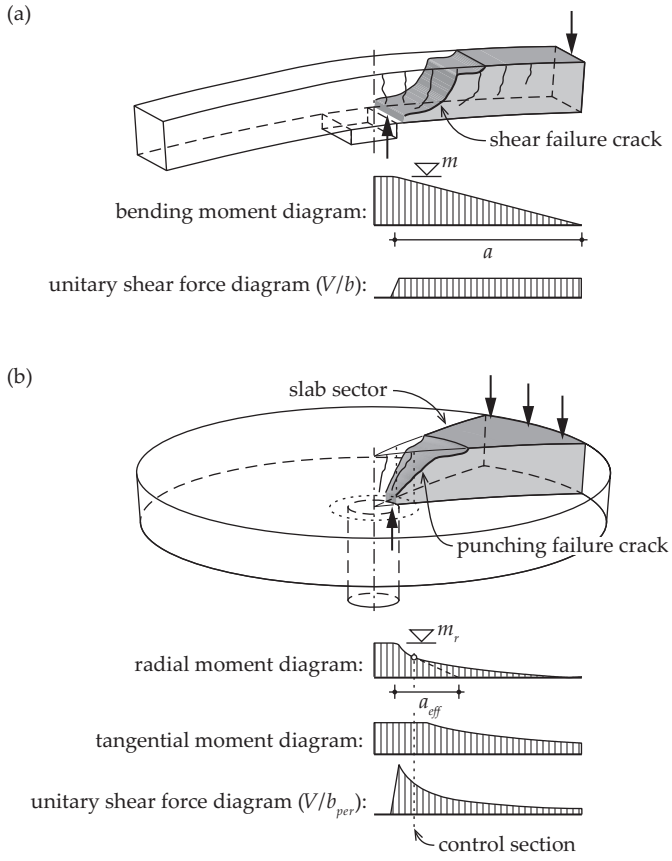

Figure 7.1 Distribution on bending moments and shear forces in (a) one-way beams and (b) two-way slabs

Shear behavior of two-way slabs in the vicinity of columns or concentrated loads differs from the behavior of beams in three important aspects. Firstly, with increasing distance from the column, the width of the slab sectors increases (Fig. 7.1(b)) and, consequently, shear force per unit width decreases. Therefore, the shear strength of a slab at some distance from the column, where the beam shear transfer actions would govern in beams, is normally sufficient and punching failure occurs instead in the immediate vicinity of the column edge. Secondly, as explained in Chapter 3 as well as shown in Figure 7.1(b), bending moments in two-way slabs can be distributed in two directions. Therefore, in comparison to beams with similar loads and distances between the loading points and the support, bending moments in a single direction are lower in two-way slabs. As a result, the effective shear slenderness ratio (M/Vd or a_{eff}/d (Fig. 7.1(b))) is reduced, meaning that, close to the column, shear force can be carried by the inclination of the compression strut [Mut10]. However, thirdly, unlike in beams where yielding of tensile reinforcement close to the support results in a flexural failure of the element, redistribution of bending moments into tangential direc-

tion means that the load can still increase in two-way slabs. Therefore, strains in the tensile reinforcement, as well as in the compression zone, can be significantly higher before a punching failure occurs in two-way slabs than at shear failure in compact beams. This leads to crack localization in slabs, whereas uniform softening of the strut governs the behavior of compact beams.

7.1.2 Contribution of aggregate interlock action

According to the CSCT of Muttoni [Mut08b], punching failures are caused by the failure of a radial compression strut that is intersected by an inclined flexural crack (referred to as the critical shear crack), which propagates through the strut into the radial compression zone (Fig. 7.2(a)). Shear stress is transferred via friction between the crack lips due to their macro-roughness (aggregate interlock) [Gui10a]. Capacity of the crack to carry shear stresses is assumed to be a function of its opening width, which is estimated to be proportional to $\psi \cdot d$, and of the roughness of the crack lips, which is assumed to depend on the maximum aggregate size d_g (Fig. 7.2(b)). The failure is expected to occur when the aggregate interlock capacity is exceeded (that can happen either at a large punching load V or due to large crack opening w_{cr}).

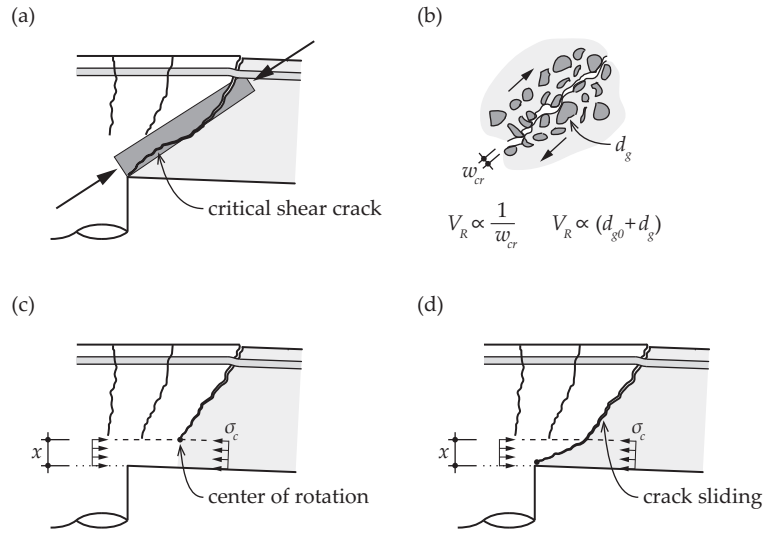

Figure 7.2 Critical Shear Crack Theory: (a) theoretical strut through the critical shear crack [Mut08b]; (b) aggregate interlock between sliding crack lips; (c) opening of the critical shear crack in the case of non-negligible depth of the compression zone; (d) opening of the critical shear crack after failure of the compression strut in the compression zone

Aggregate interlock stresses can be activated when crack lips slide relative to each other. However, as observed in the slabs described in Chapter 6, the measured crack opening displacements were in all cases larger than sliding displacements along the crack lips. It is suggested that this can be explained by the rigidity of the compression zone (Fig. 7.2(c)), due to which the sliding of crack lips could only occur after a compression zone failure (Fig. 7.2(d)). In the experiments, the failure of the compression strut in the compression zone, however, always led to an immediate collapse of the slab. In addition, in several cases, the failure did not develop along the existing critical shear

crack but by opening of a new, so-called failure crack. This crack appeared either prior to or at the moment of failure and often had a very low inclination.

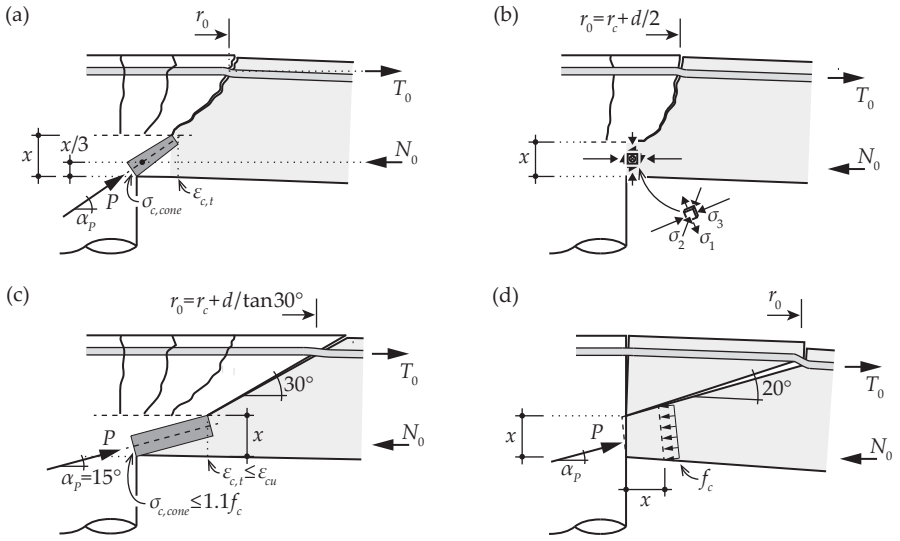

Figure 7.3 Contribution of the compression strut: (a) model of Kinnunen and Nylander [Kin60]; (b) model of Moe [Moe61]; (c) model of Broms [Bro90]; (d) model of Shehata and Regan [She89]

7.1.3 Previously proposed models based on the compression strut

Several previously proposed models account for the contribution of stresses in the compression strut below the flexural cracks to the punching capacity of a flat slab. The first mechanical model by Kinnunen and Nylander [Kin60] described the deformed shape of the slab by dividing it into a spherical part above the column and a conical part around it. The two parts were separated by an inclined flexural crack, which is referred to as the critical shear crack by Muttoni [Mut08b]. Shear force was assumed to be transferred from the conical part to the column through a cone-shaped shell at the tip of that crack, subjected to uniform compression $\sigma_{c,cone}$ (Fig. 7.3(a)). The geometry of the compression shell, including the inclination of the resultant force α_P, were calculated from the equilibrium equations of internal forces acting in the conical slab portion (including tangential moments not shown in Figure 7.3(a)). The failure criterion was defined as a function of strains and not stresses in the compression shell, as concrete strength was considered to be reduced by the large strains. A critical strain state was assumed to be attained with reaching a critical value of the tangential compressive strain on the slab soffit resulting from flexural deformations.

On the basis of experimental investigation, Moe [Moe61] assumed that most of the shear force is carried by the compression zone that is subjected to a complex non-uniform triaxial stress state. Moe did not attempt to model the realistic distribution of stresses nor the actual triaxial failure criterion, but showed that in most cases the largest principal stress in the compression zone was tensile (Fig. 7.3(b)). Therefore, splitting of concrete was considered to govern the punching resistance, making it a function of the tensile strength of concrete (assumed to be proportional to

square root of f_c). A simplification of this model, where the depth of the compression zone is assumed to be constant, is still used as a basis of the punching provisions of ACI 318 [ACI14].

The model of Kinnunen and Nylander was simplified and developed further by Broms [Bro90], who added an additional failure criterion for radial stresses in the conical shell ($\sigma_{cone} \leq 1.1 \cdot f_c$). This criterion governs the strength of stiffer slabs, where the tangential soffit strains had been observed to remain below the failure criterion of Kinnunen and Nylander (Fig. 7.3(c)). In addition, a factor accounting for the size effect was added and the model was simplified by assuming a constant $\alpha_P = 15°$.

Shehata and Regan [She89] proposed a model where the stress in the compression zone (after the formation of inclined flexural cracks) was assumed to remain constant but the inclination of the resultant force α_P varied (Fig. 7.3(d)). Splitting of the compression zone was predicted to occur when α_P reached 20°, causing the maximum principal stress in the compression zone to become tensile. In the model of Broms, as well as of Shehata and Regan, the inclination of the critical shear crack (variable in the model of Kinnunen and Nylander) was fixed to 30° and 20°, respectively. This was justified by the low angle of failure cracks typically observed on saw-cut surfaces of punching test specimens.

7.2 Stress-based failure model for the compression strut

The new punching model proposed in this chapter assumes, as originally suggested by Kinnunen and Nylander [Kin60], that the punching strength of a slab-column connection is governed by the failure of a cone-shaped shell below the flexural cracks in the direct compression strut. In accordance with the lower bound theorem of the theory of plasticity, stresses in the conical shell are assumed to be uniformly distributed. The strength of the conical shell is predicted using a stress-based yield criterion proposed by Ottosen [Ott77] (also adapted in Model Code 2010 [FIB13] as a general failure criterion for concrete under multi-axial loading). This approach was inspired by a global criterion of failure of the compression zone that was proposed by Gustafsson and Hillerborg [Gus88] to complement a linear-elastic finite element analysis of beams subjected to bending moment and shear force. Section 7.3 proposes a method to estimate the forces that are transferred through the critical shear crack by dowel action of the tensile reinforcing bars, accounting for the stresses in the reinforcement as well as the slip of the bars. Finally, in Section 7.4, a suitable effectiveness factor, which has to be applied when plastic behavior of concrete is assumed, is calibrated on the basis of experiments.

7.2.1 Critical surface in the conical shell

In the proposed model, the failure is expected to occur when a critical triaxial stress state is reached in the conical shell. Similarly to the previously proposed models and in agreement with the lower bound theorem of the theory of plasticity, an assumption is made that the distribution of stresses in the conical shell is uniform.

A triaxial stress state in the conical shell can be described by the maximal and the minimal principal stresses σ_1 (tension) and σ_3 (compression) on a radial vertical plane, inclined at an angle α_p from the horizontal (Fig. 7.4(a)), as well as a lateral stress due to the tangential bending moment, which acts horizontally and constitutes the intermediate principal stress $\sigma_t = \sigma_2$. In order to determine these stresses, a critical surface is regarded that cuts diagonally through the conical shell at an angle α. Stresses $\sigma_{//}$ along that surface and stresses σ_α perpendicular to it, as well as shear stresses τ_α act on that surface (Fig. 7.4(b)). For determining these stresses, a triangular element is considered that is limited by the critical surface, the slab soffit and a vertical plane at the intersection of the critical surface with the neutral axis of the slab (Fig. 7.4(b)). The forces $N_{\alpha,\varphi}$ and $V_{\alpha,\varphi}$ acting normal and parallel to the critical surface in a sector of that element with an angular width $\Delta\varphi$ are calculated from the equilibrium equations (it should be the noted that normal stress along the critical surface ($\sigma_{//}$) does not influence the equilibrium of forces acting on the triangular element):

$$N_{\alpha,\varphi} = N_{0,\varphi}\sin\alpha + V_{0,\varphi}\cos\alpha - N_t \cdot \Delta\varphi \cdot \sin\alpha \tag{7.1}$$

$$V_{\alpha\varphi} = -N_{0,\varphi}\cos\alpha + V_{0,\varphi}\sin\alpha + N_t \cdot \Delta\varphi \cdot \cos\alpha \tag{7.2}$$

where $N_{0,\varphi}$ and $V_{0,\varphi}$ are normal and shear forces, over an angular width $\Delta\varphi$, on a vertical section at the intersection of the critical surface with the neutral axis of the slab, located at a distance r_α from the center of the column, and N_t is the tangential force over the length of the triangular element, $r_\alpha - r_c$ (Fig. 7.4(b)). The distance r_α can be calculated as:

$$r_\alpha = r_c + x \cdot \cot\alpha \tag{7.3}$$

where r_c is the radius of the column.

The inclination of the critical surface α, which determines the geometry of the conical shell, is selected using the lower bound theorem of the theory of plasticity. This theorem states that any stress state is admissible if it is statically in equilibrium and remains below or equal to a yield criterion. Therefore, the governing inclination of the conical shell is the one that gives the highest load (V_R) for which the corresponding stress state is at the yield criterion. It should be noted that the geometry of the conical shell is independent of the location of the tip of the furthermost flexural crack (the critical shear crack). This assumption is supported by the observations of internal cracking described in Chapter 6 where, in several cases, the lower-angled failure cracks, which are typically seen on saw-cut surfaces, did not develop from the existing cracks of flexural origin but propagated as splitting cracks independently of them. Therefore, when the governing angle α is such that the conical shell reaches the neutral axis closer to the column than the tip of the critical shear crack, the failure of the conical shell is followed by opening of the previously existing critical shear crack, as occurred, for example, on the north side of the column in specimen PE5 (Fig. 7.4(c)). In the cases where the tip of the critical shear crack is closer to the column edge, which was a more common case in the tests described in Chapter 6, a new failure crack develops (as for example on the east side of the column in specimen PE5 in Fig. 7.4(d)).

Propagation of the failure crack in the region above the neutral axis is associated to very low concrete resistance and high brittleness (concrete subjected to triaxial tension). Therefore, the present model does not account for the potential contribution of this zone. Also, possible shear force transfer by dowel action of flexural reinforcement at the opening of the failure crack is not expected to contribute to the maximum punching capacity of the connection. It should be noted that dowel action of flexural reinforcement through the critical shear crack can reduce the force acting in the compression strut. This contribution will be discussed in Section 7.3.

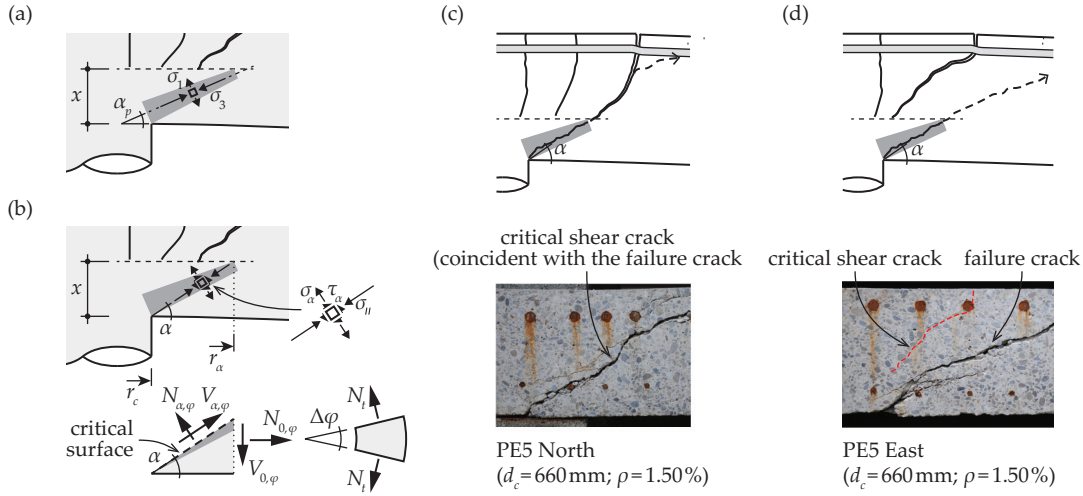

Figure 7.4 (a) Conical shell in the compression strut; (b) Critical surface in the conical shell, equilibrium of forces on a triangular sector element (positive directions shown); (c) Failure of the conical shell followed by opening of a flexural crack, north side of the column in specimen PE5; (d) Propagation of a new shear crack at failure, east side of the column in PE5

The geometry of the conical shell is influenced by the shape of the furthermost flexural crack (the critical shear crack). This crack is assumed to extend until the neutral axis of the slab, which defines the depth of the compression zone. The depth of the compression zone x of an element in bending can be calculated, assuming a fully cracked cross-section with linear-elastic behavior of concrete and steel and neglecting the influence of compression reinforcement, by solving an equation for x [Cle14]:

$$x = \frac{E_s}{E_c} \cdot \rho \cdot d \cdot \left(\sqrt{1 + \frac{2 \cdot E_c}{\rho \cdot E_s} - \frac{\sigma_r}{\sigma_s} \cdot \frac{2 \cdot E_c}{E_s} \cdot \frac{(d-x) \cdot h}{(\rho \cdot d)^2}} - 1 \right) \tag{7.4}$$

where σ_r is the average radial stress in the cross-section due to in-plane forces (compression is negative). In-plane forces may occur due to pre-stressing, but also due to edge restraints or slab continuity, as shown in Chapter 3. In isolated specimens, the in-plane forces are small and can be neglected. In this case, the depth of the flexural compression zone can be found directly [Mut08b]:

$$x = \frac{E_s}{E_c} \cdot \rho \cdot d \cdot \left(\sqrt{1 + \frac{2 \cdot E_c}{\rho \cdot E_s}} - 1 \right) \tag{7.5}$$

However, shear stresses may influence the development of flexural cracks. Due to these stresses, the critical shear crack, observed in the tests described in Chapter 6 to start developing at a distance approximately equal to d from the column edge, propagates towards the column in an inclined manner. In experiments, the inclination of the critical crack has been observed to be about 45° [Kin60, Mut08b]. As explained earlier, the magnitude of the stresses transferred through that crack is assumed to be limited in the proposed model. Therefore, the force in the tension chord at a perimeter $r_0 = r_c + d$, where the critical shear crack intersects the level of tensile reinforcement, has to be in equilibrium with compression in a narrower compression chord at r_α (Fig. 7.5(a, b)). Considering that the ratio between the lengths of the perimeters (and thus the widths of the compressed zone) is r_0/r_α, the depth of the compression zone at r_α, accounting for the influence of the inclined compression strut, can be calculated as:

$$x_\alpha = r_0 / r_\alpha \cdot x \tag{7.6}$$

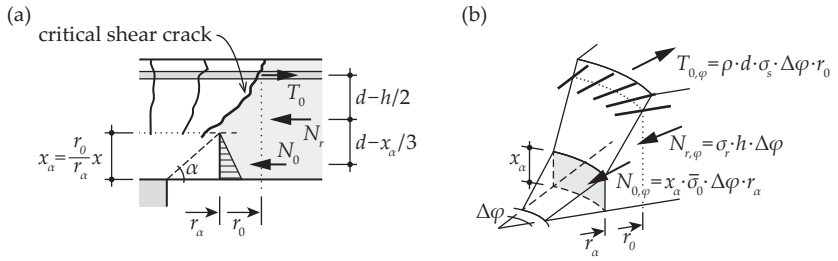

Figure 7.5 (a) Increase of the depth of the compressed zone due to the influence of inclined flexural cracks; (b) Radial forces in the tension and compression chords of a slab sector

7.2.2 Mean stresses on a vertical surface in the compression strut

In order to determine the radial horizontal force N_0 in the compression chord, the radial force T_0 in the tension chord has to be calculated. This can be done with the help of the kinematic model of Kinnunen and Nylander [Kin60] that allows calculating the load-rotation relationship of axisymmetric isolated slabs (Eq. 4.1) (refer to the specimen PE11 that is shown as an example in Figure 7.6(a)). Due to the assumption that the deformed shape of the slab within r_0 is spherical, radial curvatures are constant in this part of the slab ($\chi_r = -\psi / r_0$). Using the assumption of plane sections, the strain ε_s at the level of tensile reinforcement can then be calculated as $\varepsilon_s = -\chi_r \cdot (d - x)$ (Fig. 7.6(b)) and the stress σ_s in the reinforcing bars as:

$$\sigma_s = \min \begin{cases} \dfrac{\psi}{r_0} \cdot (d - x) \cdot \beta E_s \\ f_y \end{cases} \tag{7.7}$$

The value of factor β in Equation (7.7), which accounts for the reduced stiffness of the tension cord due to the orthogonal layout of reinforcing bars, has to be consistent with the one used in calculating ψ ($\beta = 0.6$ as suggested by Muttoni [Mut08b] is used in the present analysis). When constant depth of the compression zone is assumed (suitable for a cracked cross-section), stress in the radial

reinforcing bars at r_0 depends linearly on slab rotation up to yielding of reinforcement. An example of the load-reinforcement stress curve (for specimen PE11) is shown in Figure 7.6(c).

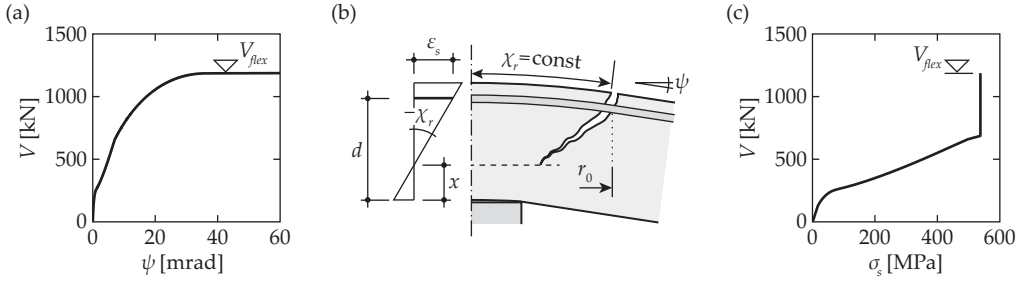

Figure 7.6 Radial force in the tension chord: (a) load-rotation curve of specimen PE11; (b) strains in the tension chord; (c) load-reinforcement stress curve for specimen PE11

The mean horizontal stress $\overline{\sigma}_0$ in the compression strut below the neutral axis at a cylindrical surface at r_α from the center of the column can be calculated using the equilibrium equations of radial forces and bending moments (Fig. 7.5(a)):

$$\overline{\sigma}_0 = -\frac{r_0}{r_\alpha} \cdot \frac{\rho \cdot d \cdot \sigma_s}{x_\alpha} - \frac{\sigma_r \cdot h}{x_\alpha} \cdot \frac{d - h/2}{d - x_\alpha/3} \tag{7.8}$$

If no in-plane stress is present in the slab, Equation (7.8) can be simplified:

$$\overline{\sigma}_0 = -\frac{r_0}{r_\alpha} \cdot \frac{\rho \cdot d \cdot \sigma_s}{x_\alpha} = -\frac{\rho \cdot d \cdot \sigma_s}{x} \tag{7.9}$$

The mean vertical stress on the same surface at r_α depends on the applied load V:

$$\overline{\tau}_0 = \frac{V_0}{x_\alpha \cdot 2\pi \cdot r_\alpha} = \frac{V - \sum V_{dow}}{x_\alpha \cdot 2\pi \cdot r_\alpha} \tag{7.10}$$

where ΣV_{dow} is the shear force carried by the dowel action of flexural reinforcing bars that will be discussed in Section 7.3.

The average tangential compression over the critical surface (that extends up to x_α) can be calculated by noting that within r_0, the deformed shape of the slab is spherical and radial and tangential stresses in the tension chord are therefore equal:

$$\overline{\sigma}_t = -\frac{\rho \cdot d \cdot \sigma_s}{x_\alpha} \tag{7.11}$$

7.2.3 Mean stresses on the critical surface

The mean stresses on the critical surface can be calculated using the equilibrium equations of horizontal and vertical forces acting on a sector of an element limited by the conical critical surface, a cylindrical surface at r_α and the slab soffit (Fig. 7.7). In addition to the forces on the cylindrical and inclined surfaces, tangential compressive forces have to be accounted for.

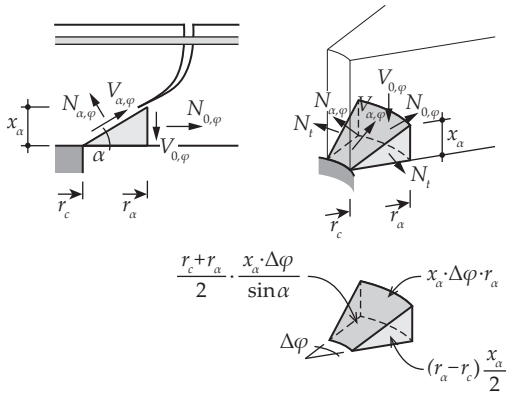

Figure 7.7 Forces acting on a sector of an element in the compression strut (positive directions are shown)

The mean normal and shear stresses on the critical surface are:

$$\overline{\sigma}_\alpha = \frac{2r_\alpha}{r_c + r_\alpha}\left(\overline{\sigma}_0 \sin^2\alpha + \overline{\tau}_0 \sin\alpha\cos\alpha\right) - \overline{\sigma}_t \sin^2\alpha \tag{7.12}$$

$$\overline{\tau}_\alpha = \frac{2r_\alpha}{r_c + r_\alpha}\left(-\overline{\sigma}_0 \sin\alpha\cos\alpha + \overline{\tau}_0 \sin^2\alpha\right) + \overline{\sigma}_t \sin\alpha\cos\alpha \tag{7.13}$$

Figure 7.8(a) shows the mean normal $\overline{\sigma}_\alpha$ and shear $\overline{\tau}_\alpha$ stresses on the critical surface of specimen PE11 (ρ = 0.75%; d_c = 166 mm) as a function of the applied punching load V and the angle α. If the critical surface is vertical (α = 90°), the mean shear stress $\overline{\tau}_\alpha$ (on the vertical axis) increases proportionally with the level of load. The mean normal stress $\overline{\sigma}_\alpha = \overline{\sigma}_0$ (on the horizontal axis) is proportional to the stresses in radial reinforcing bars σ_s (Eq. (7.9)) and thus reaches a plateau when the flexural reinforcement yields. For lower values of α (corresponding to flatter critical surfaces), the normal force N_α decreases and the shear force V_α increases. However, because a flatter surface also obtains a larger area, both mean stresses begin to decrease. If $\alpha \to 0°$, the mean value of both normal and shear stresses approaches zero (Fig. 7.8(a)).

However, it should be noted that the mean normal and shear stresses $(\overline{\sigma}_\alpha, \overline{\tau}_\alpha)$ and the tangential compression $\overline{\sigma}_t$ do not completely describe the stress state on the critical surface. In addition, a stress parallel to the critical surface $\sigma_{//}$ is present. This stress cannot be derived from the force equilibrium equations (Eq. (7.12) and (7.13)), because the area where this stress acts is infinitely small and the force therefore tends to zero. Instead, it is determined using the lower bound theorem of the theory of plasticity.

The complete state of mean stresses on a radial vertical plane on the critical surface can be represented by a Mohr's stress circle. Mohr's circle is a graphical representation of the stress state that shows the relationship between the principal stresses and stresses on surfaces that are at an angle θ_p from the principal stress directions (Fig. 7.8(b)).

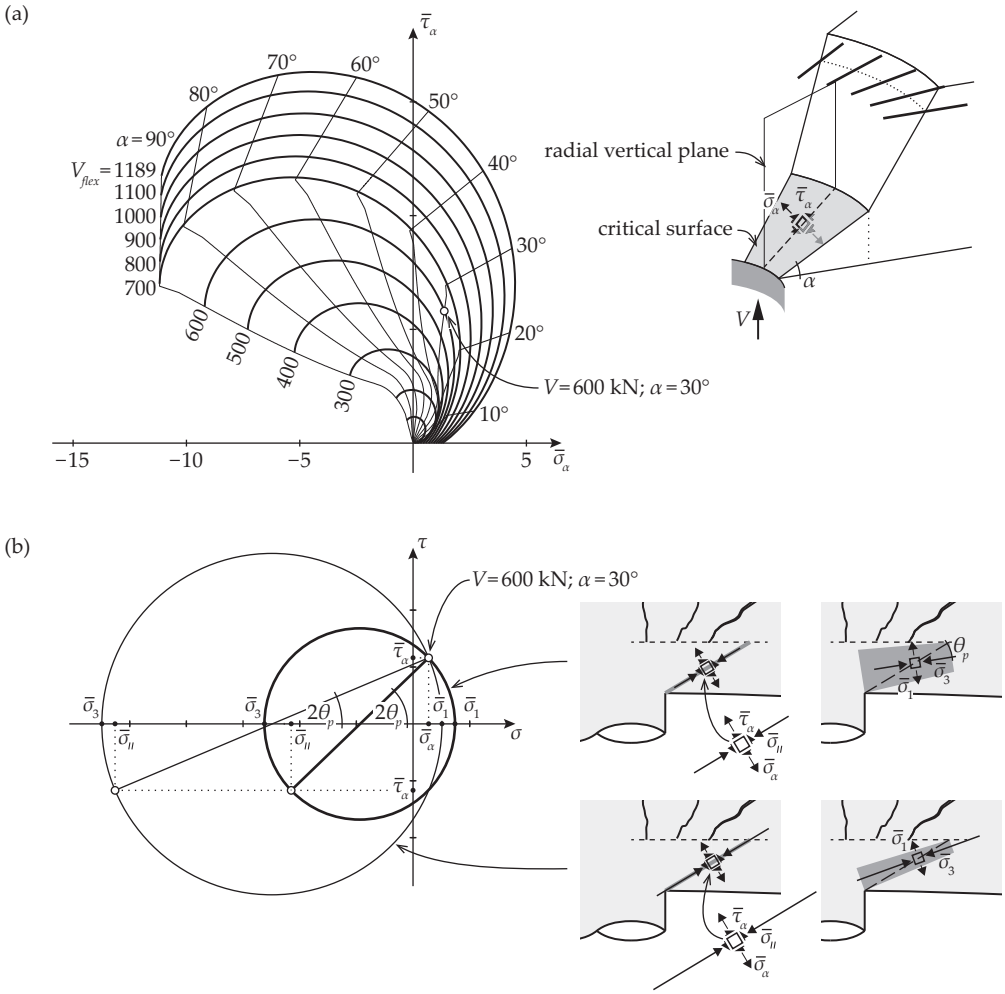

Figure 7.8 (a) The mean normal and shear stresses on the critical surface depending on the applied load V (in kN) and angle of the surface α in specimen PE11 ($\rho = 0.75\%$; $d_c = 166$ mm); (b) two examples of the possible mean stresses on the critical surface for the same shear force V and inclination of the critical surface (stresses in MPa)

Using the Mohr circle, the maximal and minimal principal stresses can be calculated:

$$\bar{\sigma}_1 = \bar{\sigma}_\alpha - \bar{\tau}_\alpha \cdot \frac{\cos 2\theta_p - 1}{\sin 2\theta_p} \tag{7.14}$$

$$\bar{\sigma}_3 = \bar{\sigma}_\alpha - \bar{\tau}_\alpha \cdot \frac{\cos 2\theta_p + 1}{\sin 2\theta_p} \tag{7.15}$$

where θ_p is the angle between the critical surface and the direction of principal stresses acting on it (Fig. 7.8(b)).

Examples of two of the possible stress circles are shown in Figure 7.8(b), corresponding to different values of $\sigma_{//}$ but to the same stresses $(\bar{\sigma}_\alpha, \bar{\tau}_\alpha)$ from Figure 7.8(a). In order for the stresses to be ad-

missible (according to the lower bound theorem of the theory of plasticity), the whole stress circle has to be located within a yield criterion. The limit state is thus attained when the circle touches the yield criterion at a single point.

7.2.4 Yield criteria for concrete

Several different multi-axial yield criteria have been proposed for concrete [Che82]. One of the simplest criteria that have given realistic results in various applications of theory of plasticity is the Mohr-Coulomb yield criterion that, as a function of principal stresses, can be expressed as:

$$f(\sigma_1,\sigma_3)=\frac{\sigma_1}{\frac{1-\sin\varphi}{1+\sin\varphi}\cdot f_c}-\frac{\sigma_3}{f_c}-1\le 0 \tag{7.16}$$

The angle of internal friction is normally selected as $\varphi = 37°$. This leaves only f_c as a required material parameter. The Mohr-Coulomb yield criterion is often augmented with Rankine's tension cut-off criterion, which assumes that the failure occurs when the maximum principal stress reaches the tensile strength of concrete f_{ct}. Rankine's yield surface is thus:

$$\sigma_1 \le f_{ct} \;;\; \sigma_2 \le f_{ct} \;;\; \sigma_3 \le f_{ct} \tag{7.17}$$

According to the Mohr-Coulomb criterion with Rankine's cut-off, yielding of concrete can occur either as a sliding failure if the Mohr-Coulomb criterion governs or as a separation failure if the Rankine's criterion is attained first. The criteria for different concrete strengths are shown on a σ-τ plane in Figure 7.9(a). The tensile strength of concrete f_{ct} is calculated with the formulas given in Model Code 2010 [FIB2013]:

$$f_{ct} = 0.3\cdot f_c^{2/3} \qquad \text{for } f_c \le 50\text{MPa} \tag{7.18}$$

$$f_{ct} = 2.12\cdot \ln\left(1+0.1\cdot\left(f_c+\Delta f_c\right)\right) \qquad \text{for } f_c > 50\text{MPa}$$

where $\Delta f_c = 8$ MPa.

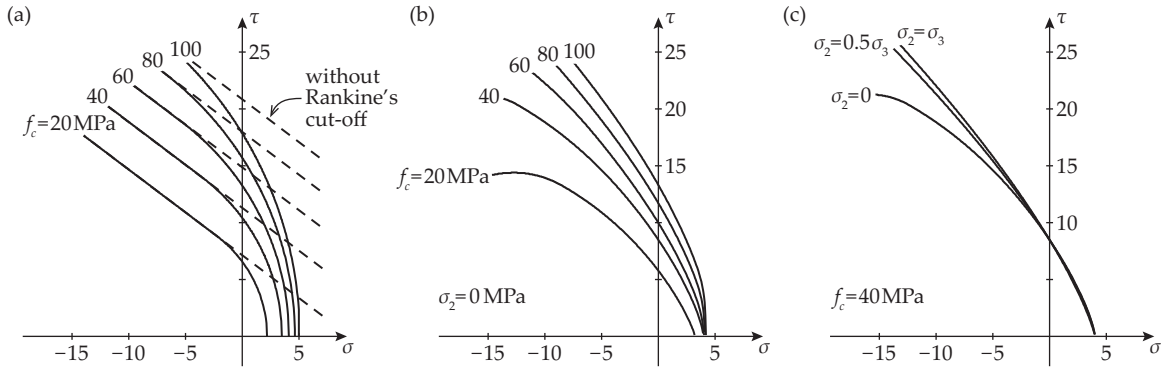

Figure 7.9 Multi-axial yield criteria for concrete on σ-τ plane: (a) Mohr-Coulomb criterion with Rankine's tension cut-off; (b) Ottosen criterion, without lateral stress; (c) Ottosen criterion, with lateral stress (stresses in MPa)

The Mohr-Coulomb criterion with a tension cut-off is a three-parameter yield criterion – three material parameters (compressive strength f_c, angle of internal friction φ and tensile strength f_{ct}) have to be known to predict a failure in a general multi-axial stress state. It should be noted that the criterion does not take into account the intermediate principal stress σ_2 and therefore cannot model the influence of lateral compression.

In order to model the triaxial behavior of concrete, Ottosen [Ott77] proposed a four-parameter yield criterion:

$$f(I_1, J_2, \cos 3\theta) = a\frac{J_2}{f_{cp}^2} + \lambda\frac{\sqrt{J_2}}{f_{cp}} + b\frac{I_1}{f_{cp}} - 1 = 0 \tag{7.19}$$

where I_1 and J_2 are stress invariants, a and b are coefficients and $\lambda(\cos 3\theta)$ is a function given as:

$$\lambda = k_1 \cos\left[\frac{1}{3}\cos^{-1}(k_2 \cos 3\theta)\right] \tag{7.20}$$

where θ is the angle of similarity k_1 and k_2 are additional coefficients.

Equation (7.19) constitutes a smooth and convex surface (Fig. 7.9(b)) and, unlike the Mohr-Coulomb criterion, also accounts for the influence of the intermediate principal stress (Fig. 7.9(c)). Experiments with four different stress states are needed to calibrate the yield criterion (typical calibration uses tests with uniaxial compressive strength, uniaxial tensile strength, compressive strength under equal biaxial stresses and triaxial compressive strength in the case where one of the compressive stresses is smaller than the other two). However, in this thesis, all the parameters are calculated from uniaxial compressive strength f_c following an approach given in Model Code 2010 [FIB13] (refer to Appendix C). The Ottosen criterion predicts slightly lower strengths than the Mohr-Coulomb criterion with Rankine's cut-off in the range where the maximal principal stress is tensile and the other principal stresses are compressive (that will be shown to be the governing case for punching).

7.2.5 Resistance of the compression strut

According to the lower bound theorem of the theory of plasticity, the conical shell can transfer a punching load V from the slab to the column until the stress state on a governing critical surface (inclined at α_R) is such that no Mohr's stress circle can be found that fits within a yield criterion for any values of θ_p. Graphically, that corresponds to a case where the stresses on the critical surface $(\bar{\sigma}_{\alpha,R}, \bar{\tau}_{\alpha,R})$, corresponding to ($V_R$, α_R) as shown in an example in Figure 7.8(a), are on the yield criterion that is tangent to the governing stress circle. Therefore, the normal of the yield criterion at the point $(\bar{\sigma}_{\alpha,R}, \bar{\tau}_{\alpha,R})$ defines the angle $2\theta_p$ and the magnitudes of the principal stresses.

Figure 7.10 shows the governing stress circles at failure loads for different yield criteria. Specimen PE11 is used as an example (for that specimen, the mean stresses on the potential critical surfaces

with varying inclinations at different load levels were shown in Fig. 7.8(a)). The Mohr-Coulomb yield criterion (Fig. 7.10(a)) has a constant slope on σ-τ plane (equal to the angle of internal friction that is usually assumed $\varphi = 37°$ for concrete). Therefore, its normal is inclined at 53° from the horizontal at every point. Due to this, the principal stresses can be directly calculated from Equations (7.14) and (7.15) and placed into the failure criterion that was given by Equation (7.16). Graphically, the punching resistance V_R is reached for a load V for which the corresponding curve in Figure 7.8(a) touches the Mohr-Coulomb yield criterion. If all the curves remain below the yield criterion, flexural failure governs the strength of the specimen.

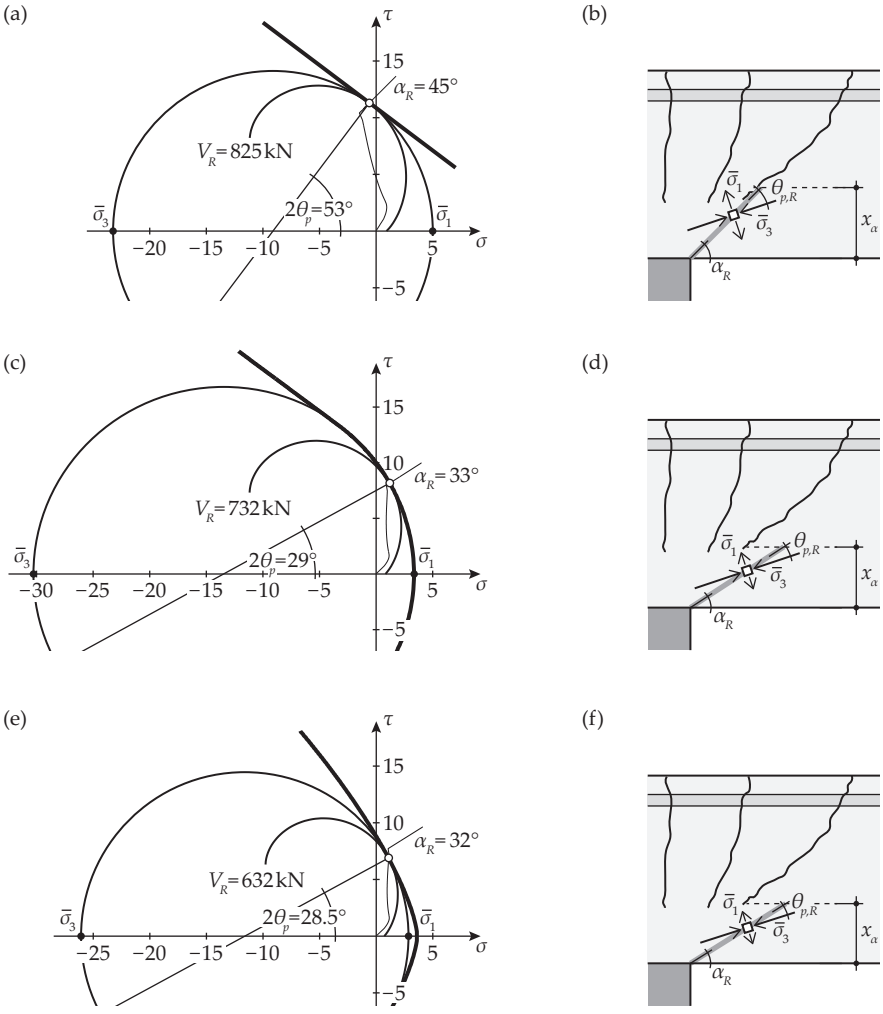

Figure 7.10 Mohr's stress circles (left), critical surfaces and principal stresses at maximum loads (right) according to various yield criteria for specimen PE11: (a, b) Mohr-Coulomb; (c, d) Mohr-Coulomb with Rankine's tension cut-off; (e, f) Ottosen criterion (stresses in MPa)

In the case of specimen PE11, the predicted punching failure load according to Mohr-Coulomb yield criterion is $V_R = 825$ kN and governing inclination of the critical surface α_R where the curves touch is 45°. Figure 7.10(b) shows the critical surface and directions of principal stresses at the edge of the column. However, it can be noted in Figure 7.10(a) that the maximum tensile stress σ_1 is ap-

proximately 5 MPa, which exceeds the uniaxial tensile strength of concrete. Therefore, if the Mohr-Coulomb failure criterion is applied together with Rankine's cut-off, the predicted punching strength decreases to V_R = 732 kN, because the separation criterion $\bar{\sigma}_1 \leq f_{ct}$ governs (Fig. 7.10(c)). The inclination of the governing critical surface α_R decreases but as the angle θ_p between the critical surface and principal stresses is lower as well, the direction of the principal compression in the conical shell stays similar (Fig. 7.10(d)). The mean principal compressive stress in the conical shell is higher and the tensile stress is lower than in the case where the Mohr-Coulomb criterion is applied.

The Ottosen yield criterion provides a smooth transition between the sliding and the separation criteria. The highest tensile stress can be reached at the hydrostatic axis (where $\sigma_1 = \sigma_2 = \sigma_3$) and deviations from it (as compressive stresses perpendicular to the principal tensile direction) reduce the capacity of concrete to withstand tensile stresses. Therefore, the maximum principal stress σ_1 on the critical surface at failure is lower than f_{ct} (2.8 MPa in the case of specimen PE11) and the predicted failure load decreases to V_R = 632 kN (Fig. 7.10(e, f)).

Table 7.1 Punching failure predictions of the proposed model with Ottosen yield criterion (without the effectiveness factors and contribution of dowel action)

	r_c mm	ρ %	B mm	r_q mm	α_R	$x_{\alpha,R}$ mm	σ_s MPa	σ_α MPa	τ_α MPa	$\theta_{p,R}$	σ_1 /f_{ct}	σ_t /f_c	σ_3 /f_c	$V_{R,pred}$ kN	$V_{R,test}$ kN	$V_{R,test}$ /$V_{R,pr}$
PE10	42	0.77	3000	1505	33°	82	397	0.85	7.68	14.7°	0.81	-0.19	-0.70	**485**	**530**	**1.09**
PE11	83	0.75	3000	1505	32°	79	470	1.11	6.86	14.3°	0.85	-0.25	-0.69	**632**	**712**	**1.13**
PE9	165	0.74	3000	1505	34°	76	538	1.64	6.72	13.5°	0.87	-0.26	-0.60	**968**	**935**	**0.97**
PE12	330	0.76	3000	1505	38°	71	538	1.76	5.57	12.7°	0.90	-0.32	-0.61	**1320**	**1206**	**0.91**
PE6	42	1.46	3000	1505	32°	96	285	0.92	7.33	14.5°	0.82	-0.24	-0.71	**631**	**656**	**1.04**
PE7	83	1.47	3000	1505	32°	92	355	1.17	7.40	14.0°	0.83	-0.28	-0.67	**845**	**871**	**1.03**
PE8	165	1.47	3000	1505	32°	89	420	1.56	6.55	13.2°	0.86	-0.35	-0.63	**1201**	**1091**	**0.91**
PE5	330	1.50	3000	1505	35°	87	446	1.68	5.46	12.3°	0.87	-0.44	-0.64	**1681**	**1476**	**0.88**
PE4	166	1.59	1700	765	38°	91	218	1.85	5.10	13.2°	0.95	-0.21	-0.57	**952**	**985**	**1.03**
PV1	166	1.50	3000	1505	32°	90	372	1.30	5.50	13.2°	0.87	-0.42	-0.71	**1023**	**978**	**0.96**
PE3	166	1.54	3900	1926	30°	85	471	1.15	6.11	13.0°	0.81	-0.51	-0.74	**1039**	**961**	**0.92**

7.2.6 Punching strength predictions

Similar analysis, using the Ottosen yield criterion, was performed for all the specimens presented in Chapter 5. The main results are shown in Table 7.1. It should be noted that this calculation does not account for the contribution of dowel action (Section 7.3) and the effectiveness factor, which has to be included due to the assumption of plastic behavior of concrete (Section 7.4). The governing angle of the critical surface was between 30° and 38° in all the specimens, whereas the direction of principal stresses was approximately 13° from it. The failure occurred in all the cases with principal tension in the conical shell being between 80–90% of the uniaxial tensile strength of concrete and principal compression about 60–70% of the uniaxial compressive strength. Comparison be-

tween the experimental results and model predictions shows a reasonable agreement, especially considering that only standard multi-axial strength parameters are used without any parameters specific to punching. It can also be seen that the punching capacity of specimens with larger column sizes is slightly overestimated. Due to similar slab depths (h = 250 mm; $d \approx 210$ mm), no conclusions can yet be made regarding the size effect.

7.3 Dowel action

In Chapter 6 of the thesis, an experimental observation was made that the direction of opening of the critical shear crack, which separates the spherical and conical slab portions, is approximately perpendicular to its lips. Because the opening direction of the inclined crack does not coincide with the direction of flexural reinforcement crossing it, the increase of crack width is accompanied by flexural deformations of rebars (Fig. 7.11(a)). Due to the bending moments appearing in the reinforcement, shear force V_{dow} is transferred between the lips of the critical shear crack by the bars. In this section, a simple method is presented to account for the contribution of dowel action of rebars crossing through the critical shear crack, considering the influences of tensile stresses in the reinforcement as well as the limited magnitude of dowel displacement before a punching failure. The dowel action of rebars through the failure crack is not considered, because it only appears when the other shear transfer mechanisms have already lost their capacities [Fer13].

7.3.1 Dowel action of tensile reinforcement in the critical shear crack

The flexural reinforcement in slab regions above the column is subjected to tensile stresses and can even reach yielding before a punching failure occurs. A formula for calculating the stress σ_s in reinforcing bars within a radius r_0 from the center of the column was given by Equation (7.7). The plastic flexural strength of a bar, reduced due to the stress σ_s, may be calculated in a simplified manner as:

$$M_{pl} = \frac{\Phi^3}{6} \cdot \left(f_y - \sigma_s \right) \tag{7.21}$$

where Φ is the diameter of the reinforcing bar. However, the plastic bending moment in the reinforcing bars may not be reached, as breakout of rebars may potentially occur due to the proximity of the surface of the slab on the right side of the crack in Figure 7.11(a). Pressure $\sigma_{c,dow}$ between concrete and the dowel can therefore be limited by the tensile strength of the concrete around the bar. Fernández Ruiz *et al.* [Fer10a] proposed that tensile failure of concrete will occur when the pressure reaches one of the criteria:

$$\frac{\sigma_{c,dow}}{f_{ct}} = \min\left(\frac{s_{top}}{\Phi_{top}} - 1;\quad 6;\quad 4 \cdot \frac{c_{top}}{\Phi_{top}} \right) \tag{7.22}$$

where s_{top} is the spacing of tensile reinforcing bars and c_{top} is the concrete cover.

Using the equilibrium equations of a free body shown in Figure 7.11(b) (a part of a dowel between the cross-sections with maximum moment and with maximum shear force), where the flexural strength of a rebar is calculated with Equation (7.21) and stress $\sigma_{c,dow}$, assumed to be uniformly distributed, with Equation (7.22), the maximum shear force that can potentially be transferred through dowel action of one bar can be calculated as:

$$V_{dow,max} = \frac{\Phi^2}{\sqrt{3}} \cdot \sqrt{\sigma_{c,dow} \cdot \left(f_y - \sigma_s\right)} \tag{7.23}$$

which is similar to the formula suggested by Rasmussen [Ras62] as $V_{dow,max} = k \cdot \Phi^2 \cdot \sqrt{f_c \cdot f_y}$, which assumes that the dowelling force is limited by flexural strength of the bars and the contact pressure $\sigma_{c,dow} \propto f_c$. The factor k in Rasmussen's formula was calibrated on the basis of experiments, $k = 1.5$ has been found suitable [Ran13].

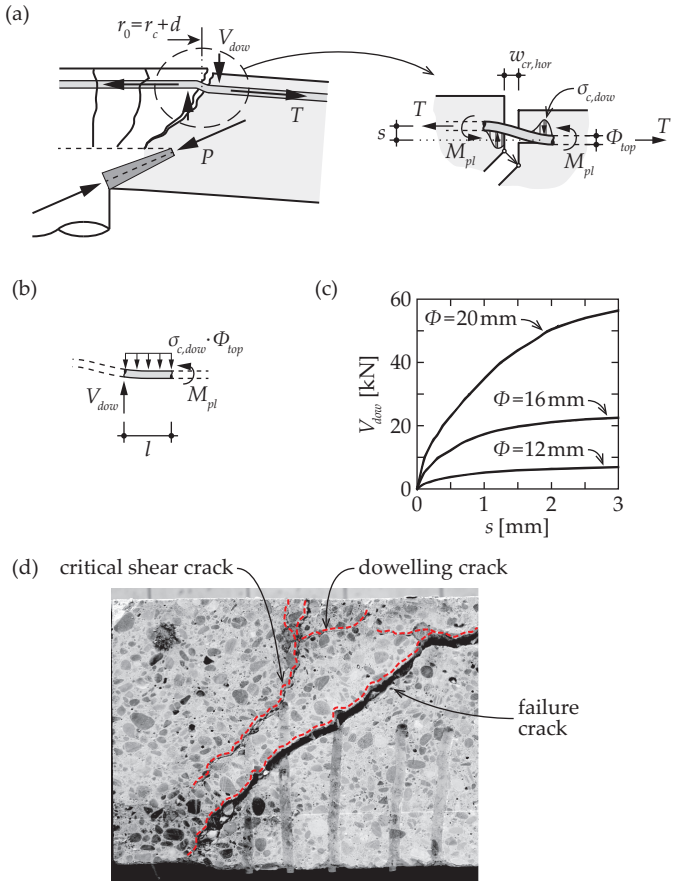

Figure 7.11 (a) Geometry of the critical shear crack and dowel action of top reinforcement; (b) Free body diagram of a tensile rebar between the cross-sections with zero moment and zero shear force used to determine the dowelling force; (c) Activation of dowel action according to the experiments of Randl [Ran07]; (d) Photo of cracks on saw-cuts associated to activation of dowel action (specimen PE11)

It should be noted that the $V_{dow,max}$ does not depend on the length of the bar section l where $\sigma_{c,dow}$ acts. Therefore, a delamination crack may start developing from to the critical shear crack without reducing the capacity of dowel action. In fact, cracking along the tensile reinforcement layer close to the critical shear crack could be observed on the saw-cuts, indicating the dowelling of the rebars (Figure 7.11(d)).

7.3.2 Activation of dowel action

Stress transfer through the crack by dowel action has to be accompanied by a displacement perpendicular to the axis of the dowel (shear slip s in Fig. 7.11(a)). The shear force calculated with Equation (7.23) assumes that the slip is sufficient for the plastic hinges in the dowel to develop. However, if the slip is limited, the shear force transferred by dowel action may be lower. Randl [Ran13] has shown that the activation of dowel action can be approximated by a parabolic formula that fits the experimental curves shown in Figure 7.11(c):

$$V_{dow} = V_{dow,max} \cdot \sqrt{\frac{s}{s_{max}}} \tag{7.24}$$

where s_{max} is the slip corresponding to the formation of a plastic hinge in the dowel (recommended to be taken approximately $0.10 – 0.20\Phi$ according to Model Code 2010 [FIB13]).

When the inclination of the critical shear crack is assumed to be 45°, the crack slip is equal to the horizontal crack opening w_{cr} (Fig. 7.11(a)). w_{cr} can be estimated from the reinforcement strains:

$$w_{cr} = \frac{\sigma_s}{\beta E_s} \cdot s_{cr} = s \tag{7.25}$$

where s_{cr} is the average crack spacing, which, in a simplified manner, is taken equal to 100 mm.

Dowel action of all the rebars at a perimeter $r_0 = r_c + d$ is:

$$\sum V_{dow} = \rho d \cdot 2\pi \cdot (r_c + d) \cdot k \cdot \sqrt{\sigma_{c,dow} \cdot (f_y - \sigma_s)} \cdot \sqrt{\frac{w_{cr}}{0.1 \cdot \Phi_{top}}} \tag{7.26}$$

The value of factor k in Equation (7.26) should be reduced in comparison to the corresponding factor in Rasmussen's formula to account for the lower post-peak stresses in the case when tensile behavior of concrete governs. In this thesis, a value of 0.6 has been found suitable.

According to Equation (7.26), no force is transferred by dowel action in the cases where flexural reinforcement reaches yielding before a punching failure occurs. However, in more rigid slabs with only small flexural deformations, the contribution of dowel action is reduced by the limited slip of the reinforcing bars that cross the flexural cracks. In the intermediate cases, the shear force carried by dowel action reduces the stresses in the compression strut. Its contribution to punching strength, shown in the parametric analysis in Section 7.5, does not normally exceed 10% of the total capacity (refer to Appendix E).

7.4 Effectiveness factor and size effect

A method to predict the failure of the conical shell in the compression strut was developed in Section 7.2 on the basis of the theory of plasticity. In that plastic approach, the material response was assumed to be perfectly rigid-plastic with an infinitely long yielding plateau [Nie11]. The actual response of concrete in compression exhibits a softening behavior after the peak load, which gets more brittle in the case of higher concrete strengths (Fig. 7.12(a)). In order to use the rigid-plastic material model, the plastic concrete strength has to be reduced with respect to the measured compressive strength values. In this thesis, a brittleness factor η_{fc} [SIA13] is applied (Fig. 7.12(b)):

$$f_{cp} = \eta_{fc} \cdot f_c = \left(\frac{30}{f_c}\right)^{1/3} \cdot f_c \tag{7.27}$$

The actual stress-strain response of concrete in tension differs even more from the assumption of plastic material behavior. The failure occurs at a very small tensile strain and shows only limited post-peak resistance. Therefore, the range of applicability of the theory of plasticity on concrete structures is often limited to the cases where tensile stresses can be carried by reinforcement. However, as shown (among others) by Nielsen and Hoang [Nie11], plasticity approaches can give good estimates of actual behavior even when brittle failure of concrete governs, provided that the effectiveness factor is suitably adjusted using relevant experimental results for calibration. Therefore, in order to determine an effectiveness factor applicable in the case of punching without shear reinforcement, the predictions of the proposed model are subsequently compared to test results.

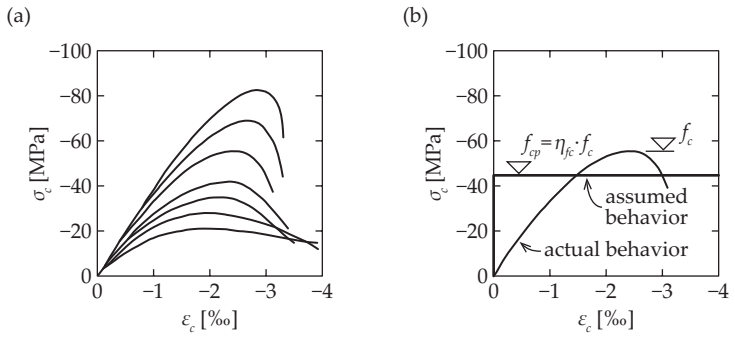

Figure 7.12 Compressive response of concrete: (a) stress-strain curves for concretes of different strength classes [ECP08]; (b) actual behavior and the assumed response in the model

7.4.1 Database of punching tests

In total, results of more than 500 punching tests have been made available [Osp11, Sib14]. However, the majority of the experiments have been performed on very thin slabs (<100 mm) that are not representative of real structures. For the analysis presented in this chapter, 119 test specimens have been selected, including slabs from the test campaign presented in this thesis as well as previous results reported in the literature.

The set of 87 specimens used by Muttoni [Mut08b] was selected for the present study. However, the specimens that failed at loads corresponding to the calculated flexural limit or within 5% from that were excluded (refer to Appendix B of the thesis for the formulas for calculating the flexural strengths of specimens). In addition, 31 recent full-scale punching tests performed at EPFL by previous researchers ([Gui10b], [Tas11], [Cle12], [Lip12]) or by the author ([Ein16a]), as well as 10 punching tests from elsewhere [Sis97] were included in the analysis. The list of the included test campaigns is shown in Table 7.2. Figure 7.13 illustrates the range of principal parameters (effective depth d, concrete strength f_c and flexural reinforcement ratio ρ). All the data necessary for calculations is given in Table E.1 of Appendix E of the thesis.

Table 7.2 Database of punching tests

	No.	Slender no.	d [mm]	ρ [%]	f_c [MPa]
Elstner and Hognestad (1956)	18	18	114–118	1.15–3.70	12.8–50.6
Kinnunen and Nylander (1960)	12	12	117–128	0.78–1.55	23.8–30.5
Moe (1961)	6	6	114	1.06–1.53	20.8–26.5
Tolf (1988)	8	8	98–200	0.34–0.81	22.6–28.2
Tomaszewicz (1993)	13	9	88–275	1.50–2.60	64.3–119
Hallgren (1996)	5	5	240–245	0.80–1.19	85.7–94.9
Ramdane (1996)	12	12	98–100	0.58–1.28	23.9–90.5
Sistonen *et al.* (1997)	10	-	170–176	0.45–1.17	19.0–25.8
Guandalini *et al.* (2009)	4	4	130–520	0.33–1.50	27.6–34.7
Guidotti (2010)	11	11	194–208	0.75–1.62	31.5–51.7
Tassinari (2011)	2	2	210–214	0.84–1.48	66.3–67.0
Clément *et al.* (2012)	3	-	346–350	0.75–1.52	31.6–33.9
Lips *et al.* (2012)	4	3	193–353	1.50–1.63	30.5–36.5
Einpaul *et al.* (2016)	11	10	197–218	0.74–1.59	31.1–44.1
	Σ 119	Σ 100			

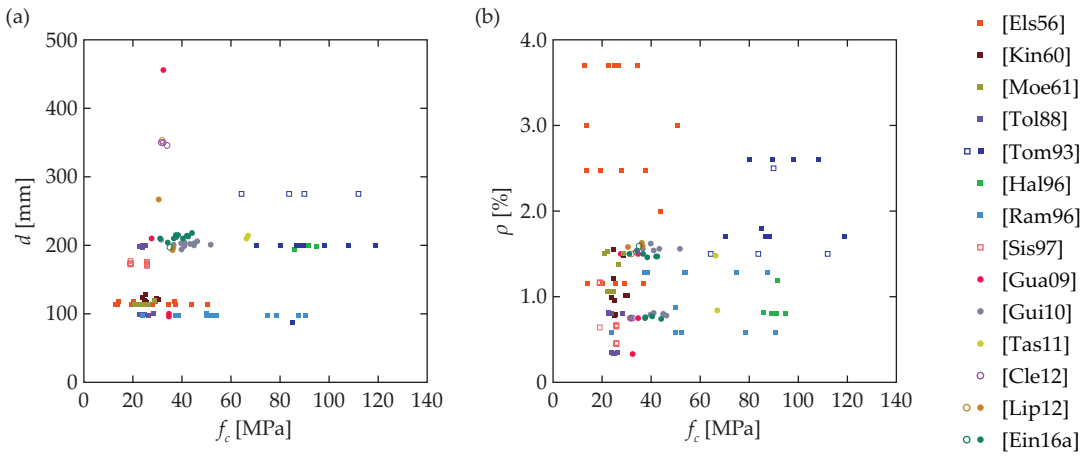

Figure 7.13 Database of 119 punching tests used for comparisons between the model predictions and experimental results (the empty markers indicate tests with distances between the loading points and the edge of the support $(r_q - r_c) < 4.5 \cdot d$)

Applying the previously described method to the 119 tests in Table 7.2 gives an average ratio of measured to predicted punching strengths of 1.04 with a coefficient of variation of 14.4%. It was

noted that for the specimens with relatively small distances between the loading points and the edge of the column, the predicted strengths were systematically lower than the experimental results (this will be further discussed and explained in Section 7.5.1). The 19 tests with $(r_q - r_c) < 4.5 \cdot d$ (shown with empty markers in Fig. 7.13) were excluded from the dataset used for calibrating the effectiveness factor. For the remaining tests, the average ratio was 1.03 and the coefficient of variation 13.7%.

7.4.2 Size effect

Brittle materials, where the failures occur by cracking, are known to exhibit size effect, according to which a proportional decrease of all the dimensions of an element (D) leads to an increase in its nominal resistance (σ_N). According to the principles of fracture mechanics this can be explained by the consideration of energy balance at crack propagation. Forming a new crack surface during the process of failure requires energy that is provided by a release of potential energy in the uncracked part of the element when the stress (and thus the elastic deformation) in it decreases. Consequently, the amount of released energy depends on the volume of the part of the element that is unloaded. Failure can only occur if that amount exceeds the energy required for crack formation. Thus, for proportionally larger size elements, the critical energy balance is reached at lower levels of nominal stress. Assuming linear-elastic material behavior, it can be shown that the nominal strength σ_N is inversely proportional to square root of element's characteristic size $D^{-1/2}$ [Wan96].

In spite of a nearly linear tensile stress-strain relationship of concrete, linear-elastic fracture mechanics (LEFM) has failed to provide good predictions for brittle failures of concrete. Hillerborg [Hil83] as well as Bažant [Baž84] have reasoned this with differences in the fracture process in concrete compared to more homogenous materials, such as steel or glass. In concrete, growth of a crack is preceded by a fracture process zone ahead of the propagating crack tip with a length that depends on the material parameters (according to Hillerborg's model) or accompanied by softening of a crack band, the width of which is a material property (according to Bažant's approach). Both models conclude that size effect has to be less strong for smaller element sizes where the relative length of the fracture process zone, or the width of the crack band, is larger compared to the element's size. The strength should only approach the LEFM predictions in the case of sufficiently large elements. On the basis of energy release analysis [Baž84], Bažant proposed a general format for the size effect factor in the case of quasi-brittle failures:

$$k_{size} = \frac{\sigma_N}{\sigma_0} = \frac{B}{\sqrt{1 + \frac{D}{D_0}}} \tag{7.28}$$

where σ_0 represents the plastic material strength, D is a characteristic element size, B is a constant and D_0 is a reference element size that represents a transitional size between the ranges where plastic behavior and LEFM govern. The reference size was assumed by Bažant to be proportional to maximum aggregate size but in the present thesis it is taken independent of this parameter on the

grounds of aggregate fracturing that was observed in the experiments. Bažant [Baž84] has suggested that the constants B and D_0 should be determined from regression analysis of test data, as their theoretical derivation is complex and requires many parameters whose values cannot be known precisely. Bažant and Cao performed such analysis for punching failures [Baž87] and found values of $B = 0.155$ and $D_0 = 181$ mm suitable. However, it should be noted that in their analysis, the nominal stress was calculated using the whole depth of a cross-section so that the influence of the amount of flexural reinforcement was neglected, as opposed to verifying the stresses in a conical shell in the compression strut as in the present model.

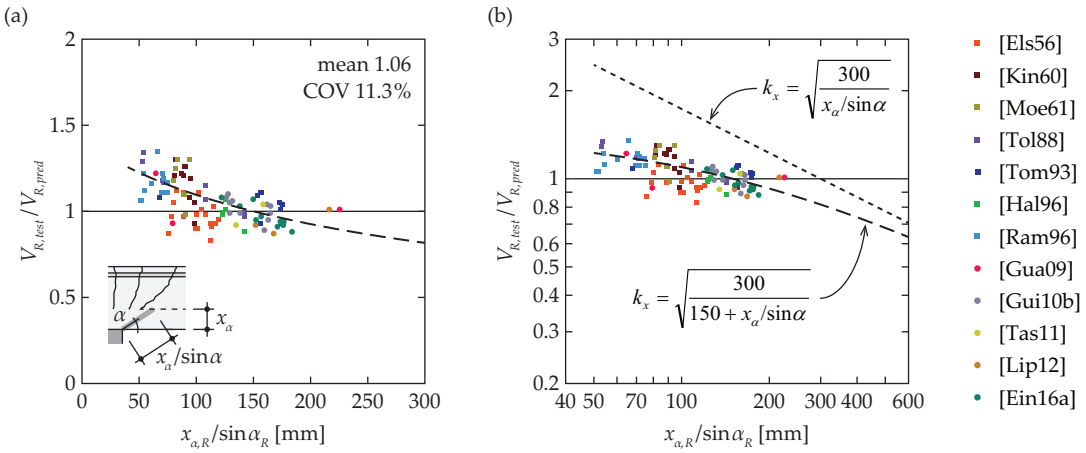

Figure 7.14 Ratios of measured to predicted punching strengths (100 specimens, without the size effect factor k_x) as a function of the depth of the critical surface and a suitable fit for the size effect factor k_x: (a) linear plot (b) double-logarithmic plot

Figure 7.14(a) shows the predictions of the proposed model for 100 punching tests of slender specimens (Table 7.2). The column size effect factor k_{col} (Section 7.4.3) is taken into account in this calculation. The mean value of the ratios between the experimental punching capacities and the predictions is 1.06 and the coefficient of variation 11.3%. The selected size parameter, shown in the horizontal axis, is the length of the governing critical surface on a radial vertical plane ($x_{\alpha,R} / \sin\alpha_R$), which represents the size of the conical compression shell in which plastic behavior is assumed.

To investigate the quasi-brittle size effect factors in the format of Equation (7.28), it is convenient to use double-logarithmic plots of nominal strength versus element size. In such plots, the LEFM size effect factor is a straight line with a slope of –1/2, the plastic limit is a horizontal line (no influence of size) and Equation (7.26) defines a curve that asymptotically approaches the plastic limit for $D/D_0 \to 0$ and the LEFM factor in the case of $D/D_0 \to \infty$. Figure 7.14(b) shows the comparison between test results and model predictions in such format. The size effect function k_x, selected on the basis of the experimental results and shown with a dashed line, is:

$$k_x = \sqrt{\frac{300}{150 + x_\alpha/\sin\alpha}} \tag{7.29}$$

that corresponds to $B = 1.41$ and $D_0 = 150$ mm (x_α is in millimeters).

7.4.3 Influence of column size

As suggested by the experimental results described in Chapter 6, the development of punching failure cracks does not start concurrently on the whole column perimeter. Due to local inhomogeneities in concrete, stresses at some points of the column perimeter reach the local material strength at lower levels of load than in the other points. However, the punching capacity of a slab-column connection is not necessarily determined by the weakest point on the column perimeter. As Sagaseta *et al.* [Sag11] and Natário *et al.* [Nat14] have demonstrated (for the cases of punching of slabs with unequal reinforcement ratios in two directions and for slabs with point loads close to linear supports, respectively), tangential redistribution of shear force may take place. This allows redistributing the load from the failed slab sectors, where the radial shear force transfer mechanism has lost all or part of its capacity, to adjacent sectors, where the capacity has not yet been reached. Chapter 6 presented some additional experimental evidence of the appearance of such redistribution even in nominally axisymmetric slabs.

At the moment when a slab-column connection fails in punching, some parts of the perimeter have already exceeded their peak shear capacities. Failure cracks, that had started opening in these parts of the perimeter, propagate tangentially to the slab sectors that have higher shear strength. This propagation is associated to a size effect similarly to the radial crack propagation discussed in Section 7.4.2.

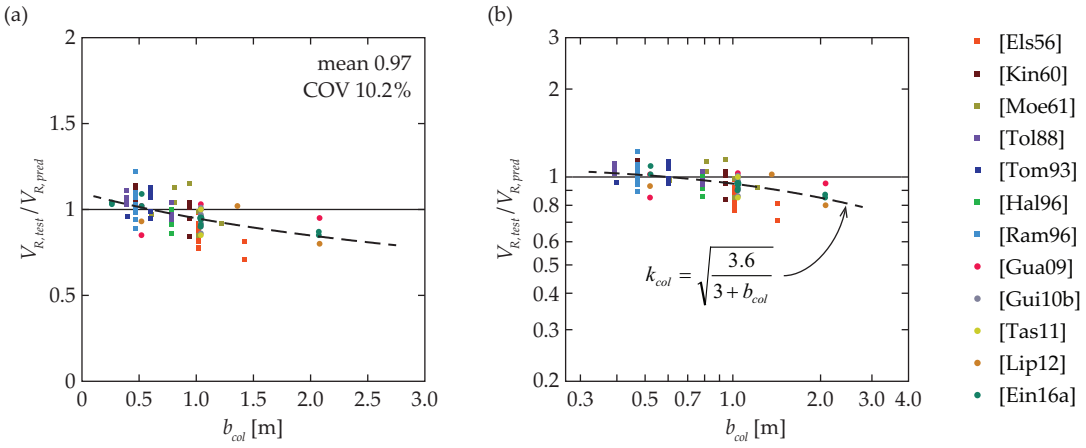

Figure 7.15 Ratios of measured to predicted punching strengths (100 specimens, without the column size effect factor k_{col}) as a function of column perimeter b_{col} and a suitable fit for the column size effect factor k_{col}: (a) linear plot (b) double-logarithmic plot

Figure 7.15(a) shows the predictions of the proposed model as a function of the length of the column perimeter b_{col} (the factor k_x for the size effect regarding the depth of the compression zone (Eq. (7.29) is accounted for in this calculation). A decreasing trend of the predictions for increasing column size can be clearly observed. A double-logarithmic plot in Figure 7.15(b) shows that this trend can be approximated in the format of Bažant's size effect law (Eq. (7.28)), but it is weaker (less dependent on size and thus closer to the range where the plastic approach is valid):

$$k_{col} = \sqrt{\frac{3.6}{3 + b_{col}}} \tag{7.30}$$

where b_{col} is the column perimeter in meters.

Regarding the range of validity of the column size effect factor given by Equation (7.28), it should be noted that one of the assumptions made in the development of the size effect formulation of Bažant (Eq. (7.28)) was that the work of external forces (displacement of the load application points) at the moment of failure is zero [Baž84]. That is the case in experiments with fixed grip conditions where the rigidity of the testing frame significantly exceeds the rigidity of the specimen.

In order for Bažant's size effect format to be applicable for the column size effect in punching, the tangential redistribution mechanism should be sufficiently stiff. In the vicinity of columns in two-way slabs, bending moments are negative (hogging) in both directions. Redistribution of shear in the tangential direction is accompanied by reduction of the tangential hogging moment. However, the sign of both moments typically remains the same (refer to the left side in Fig. 7.16). In contrast, close to a linear supports in one-way slabs, bending moments only act in the direction parallel to the support. Redistribution of shear forces along a linear support after the initiation of a failure crack will thus generate positive moments parallel to the support (refer to the right side of Fig. 7.16). When bending moments with different signs in two perpendicular directions act in a slab, the flexural compression zones are softened by transverse tensile strains acting in the tension chord of the other direction, considerably decreasing the stiffness of the slab response to both moments. In addition, shear failure cracks in slender elements develop at a greater distance from the edge of the support than punching failure cracks. Therefore, the flexural deformations associated to shear redistribution are significantly larger in the case of one-way shear than in punching. This increases the work of external forces which implies that more energy is available to propagate the failure crack along the support. Lateral crack propagation in one-way elements is therefore brittle and not significantly influenced by the element's width.

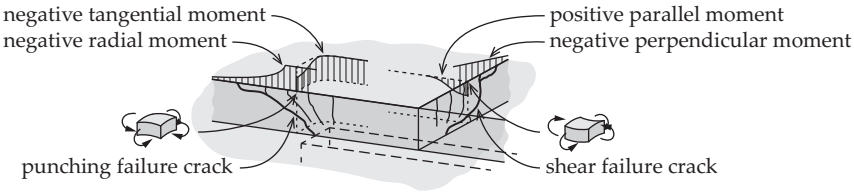

Figure 7.16 Redistribution of moments after the initiation of a punching failure crack in the case of two-way action (left side) and a shear failure crack in one-way slabs (right side)

It is important to note that the column size effect shown in Figure 7.15 does not provide a transition between shear strengths of one- and two-way slabs, because the mechanism of shear redistribution is markedly different in these two cases. The existence of stable crack propagation phase along the support and the associated column size effect is instead related to the distance between the failure crack and the support as well as the magnitude of hogging moments in the direction

parallel to the support. In the database used for calibrating Equation (7.30), all the specimens had columns that were sufficiently small so that the tangential redistribution mechanisms could be considered rigid.

7.5 Parametric analysis and comparison to the CSCT and test results

In this section, the influence of various parameters on punching capacity is analyzed according to the proposed model, the CSCT [Mut08b] and on the basis of experimental results (Table 7.2). For all the 119 specimens, the mean value of the ratios between experimental and predicted strengths is 1.03 and the coefficient of variation 12.4%. If 100 slender specimens are considered (($r_q - r_c$) > 4.5·d), the mean becomes 0.99 and the coefficient of variation is 8.8%. For the remaining 19 more compact slabs, the mean is 1.23 with a coefficient of variation of 10.3%. If the tests of Elstner and Hognestad [Els56] on thin slabs with very high reinforcement ratios are also excluded from the comparison (discussed in Section 7.5.5), the mean predicted to measured strength ratio of the 82 tests is 1.02 and the coefficient of variation 7.6%.

7.5.1 Slab slenderness

Shear slenderness of beam specimens is known to influence their shear capacity [Kan64]. Muttoni and Fernández Ruiz [Mut08a], similarly to Vecchio and Collins [Vec86], have explained the decreased shear strength of more slender beams by larger longitudinal tensile strains the element, which increase the opening of the critical shear crack [Mut08a], or decrease concrete strength in the compression field [Vec86]. According to the CSCT [Mut08b], punching strength of a slab is a function of its rotation and is thus also influenced by the specimen's slenderness, which affects the stiffness of its flexural response. Figure 7.17(a) shows the load-rotation curves for the case of three different slenderness ratios. The CSCT predicts the lowest punching strength for the most slender slab, justified by the widest critical shear cracks through the theoretical compression strut.

In the proposed model, punching strength is assumed to depend on the state of stresses in the compression strut in the vicinity of the column. The depth of the compression zone, after the formation of circular cracks, is assumed to be constant and the stresses to depend on the forces in radial tensile reinforcement. After the reinforcement has yielded, the punching strength is therefore independent of slab rotation (refer to the horizontal part of the failure criterion of the proposed model in Fig. 7.17(a)). Before yielding, forces in the reinforcement increase with increasing slab rotation (Eq. (7.6)), which leads to predicting that, in that range, the punching strength is higher for slabs that have larger slenderness ratios. However, the shear force carried by dowel action (shaded area in Fig. 7.17(a)), that contributes to the punching capacity only before yielding of reinforcement, can partially compensate for the reduced strength of the compression strut due to lower horizontal stresses.

Strains are not considered to influence the punching behavior due to the following reasons:

- Major part of the shear force is considered to be transferred through a conical shell in the compression strut. Tensile strains and cracking outside of the compression zone do not influence this capacity;
- Tangential and radial compressive strains measured on the soffits of slabs without shear reinforcement remained consistently below the strains that are associated to maximum stresses in biaxially compressed concrete and correspond to the beginning of the reduction of capacity due to large compressive strains (concrete crushing);
- Shifting of the rigid slab portions towards the center of the column and subsequent increase of compressive strains in the compression shell, suggested by Kinnunen and Nylander [Kin60], was not observed in test. Reduction of radial strains, measured on the soffits of tested slabs, can instead be attributed to the development of failure cracks.

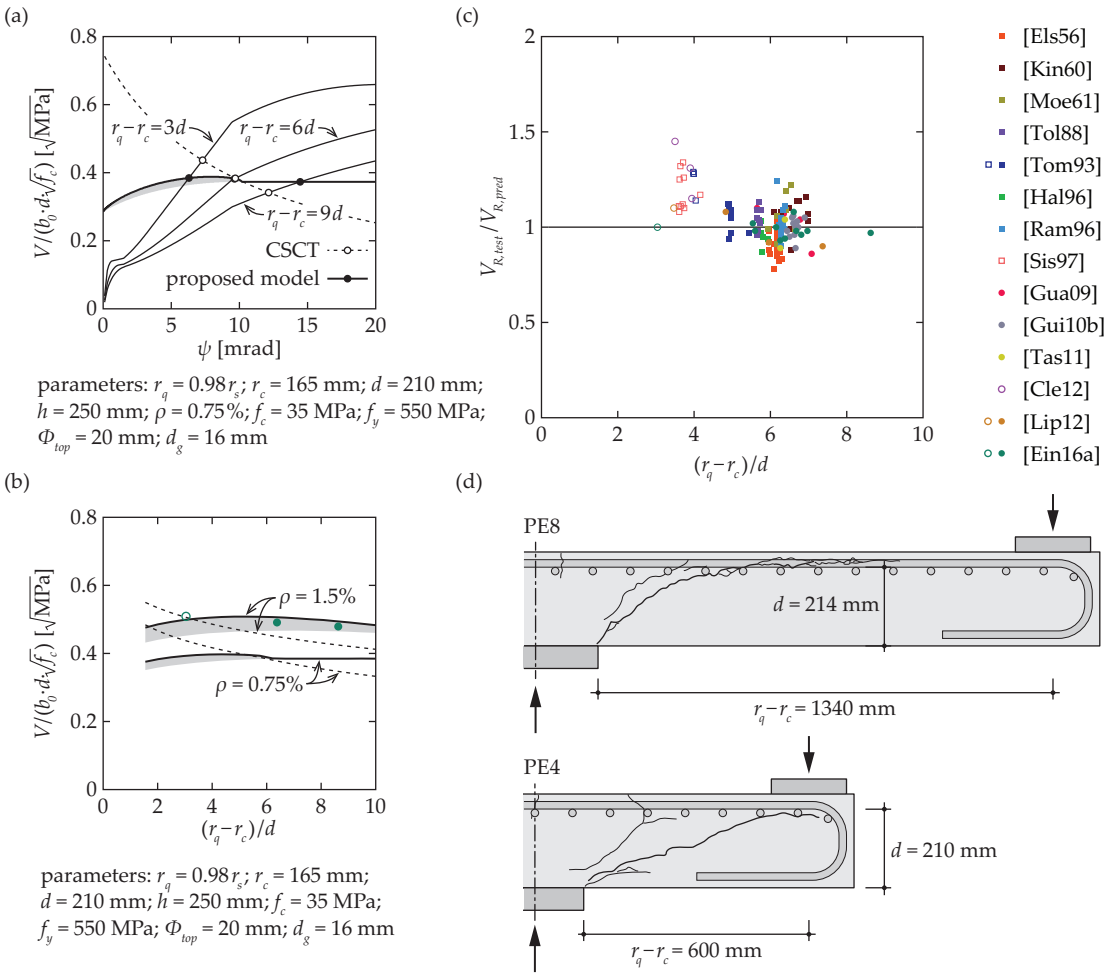

Figure 7.17 Influence of concrete strength: (a) load-rotation curves for slabs with different slenderness ratios and the failure criteria of the CSCT and the proposed model (shading – contribution of dowel action); (b) tests of the present thesis (continuous lines – predictions of the present model; dashed lines – predictions of the CSCT); (c) $V_{R,test}/V_{R,pred}$ ratios for 119 tests from the database for the proposed model; (d) an example of the failure cracks in slender specimens (PE8) and in compact specimens (PE4)

Figure 7.17(b) shows the punching strengths of specimens PE4, PV1 and PE3. The properties of the specimens were similar, apart from differences in the side lengths of slabs (between 1.7 x 1.7 m and 3.9 x 3.9 m) and loading spans. The predictions of the proposed model and CSCT are also shown. Consistently with the proposed model, the punching strengths of the slabs were very close, whereas the predictions of the CSCT for the smallest and the largest slab differ by approximately 15%.

Comparison between the experimental results and the predictions of the proposed model in Figure 7.17(c) shows that whereas the punching strengths of more slender specimens are well predicted, the model consistently underestimates the strength of more compact specimens (for slabs with $(r_q - r_c) < 4.5 \cdot d$, the mean value of the measured to predicted strength ratios is 1.23). This can be explained by the fact that, in compact specimens, part of the shear force can still be transferred by a direct strut between the loading points and column even after the formation of a failure crack (refer to the example of specimen PE4 in Fig. 7.17(d)).

7.5.2 Concrete strength

Experimental observations [Moe61] have shown that the punching strength of a slab-column connection is not directly proportional to the compressive strength f_c of the concrete in the slab. Based on these results, empirical formulas in the codes of practice assume proportionality to the square root [ACI14] or the cubic root of f_c [CEN04]. The CSCT and the punching provisions of Model Code 2010 [FIB13], which are based on the former, define the punching strength as a function of square root of f_c but do not assume direct proportionality (refer to the dashed lines in Fig. 7.18(a)).

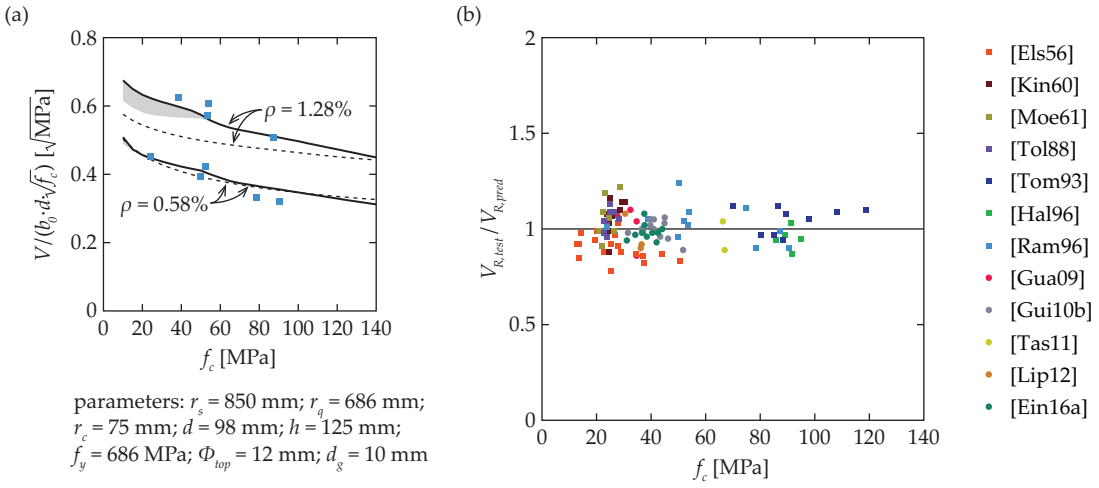

Figure 7.18 Influence of concrete strength: (a) tests of Ramdane [Ram96] (continuous lines – predictions of the present model; shaded area – contribution of dowel action; dashed lines – predictions of the CSCT); (b) $V_{R,test}/V_{R,pred}$ ratios for 100 slender tests from the database for the proposed model

Figure 7.18(a) shows the influence of f_c on punching strength (shown as a nominal shear stress on a control perimeter at $d/2$ from the edge of the column, normalized with square root of f_c) and compares the predictions to the test results of Ramdane [Ram96]. The earlier models where the plastic

strength of the compression strut can govern the punching capacity, such as the ones of Broms [Bro90] as well as Shehata and Regan [She89], assume that, in this failure mode, the punching strength is proportional to f_c. According to the model proposed herein, punching failures occur due to a triaxial stress state that is a combination of two compressive and one tensile stress, which makes the punching capacity dependent on the combination of compressive and tensile strengths. The influence of f_c on punching strength is weaker than proportional because the increase of tensile strength of concrete is slower than the increase of f_c (refer to Eq. (7.18)). In addition, a brittleness factor (Eq. (7.27)) is applied on the compressive strength of concrete to account for the decreased ductility of high strength concretes that further reduces the influence of f_c on punching strength. A comparison between the predictions and the test results from the database is shown in Figure 7.18(b). It should be noted that although the brittleness factor is not limited to 1 in this analysis, punching strengths of slabs with $f_c < 30$ MPa are not overestimated. This can be explained by the stronger beneficial effect of biaxial compression in lower strength, more ductile concretes.

7.5.3 Effective depth

Due to the size effect (Section 7.4.2), the increase of the punching strength of a slab is not proportional to the increase of the effective depth of its cross-section. Full-scale punching tests, where the specimen's depth is the main varied parameter and all the dimensions are kept proportional to it, are scarce in the literature. Figure 7.19(a) shows the results of such test campaign by Tolf [Tol88]. In these tests, two slab depths, 120 and 240 mm were used. All the other geometric parameters, including the diameters of flexural reinforcing bars (8 or 16 mm), concrete cover (12 or 24 mm) and maximum aggregate size (16 or 32 mm) as well as the slab and column sizes were kept proportional to the slab depth. The dashed lines in Figure 7.19(a), representing the CSCT predictions, show limited influence of slab depth, as the decrease of strength due to size effect is compensated by the increase of strength due to the larger aggregate size. The proposed model, that does not assume dependency of punching strength on aggregate size, predicts a more significant size effect for these specimens and fits the experimental results very well.

Figure 7.19(b) shows the predictions for three tests [Lip12, Ein16a] that have varying slab depths (h = 250 to 400 mm) and column sizes (c = 260 to 440 mm) but constant slab sizes (B = 3 m). With increasing slab depth, the slenderness ratios of those specimens thus decrease. According to the predictions of the CSCT, the nominal strength of these specimens is not expected to change significantly, as decreasing slenderness compensates for the size effect. The proposed model, in contrast, predicts the size effect to dominate. However, for $d > 280$ mm, the slenderness ratio of the specimens decreases below 4.5 in which case, as shown in Figure 7.17(c), the predictions of the proposed model underestimate the actual strength.

The comparison of the model predictions to the test results, which is shown in Figure 7.19(c), highlights the scarcity of test data on thick but slender slabs. In total, only two punching tests on slender slabs where the depth of the compression zone exceeds 200 mm are known to the author. More

experimental data is needed to evaluate whether the size effect factor (Eq. (7.29)) of the proposed model is too strong and thus provides too conservative predictions for thicker specimens.

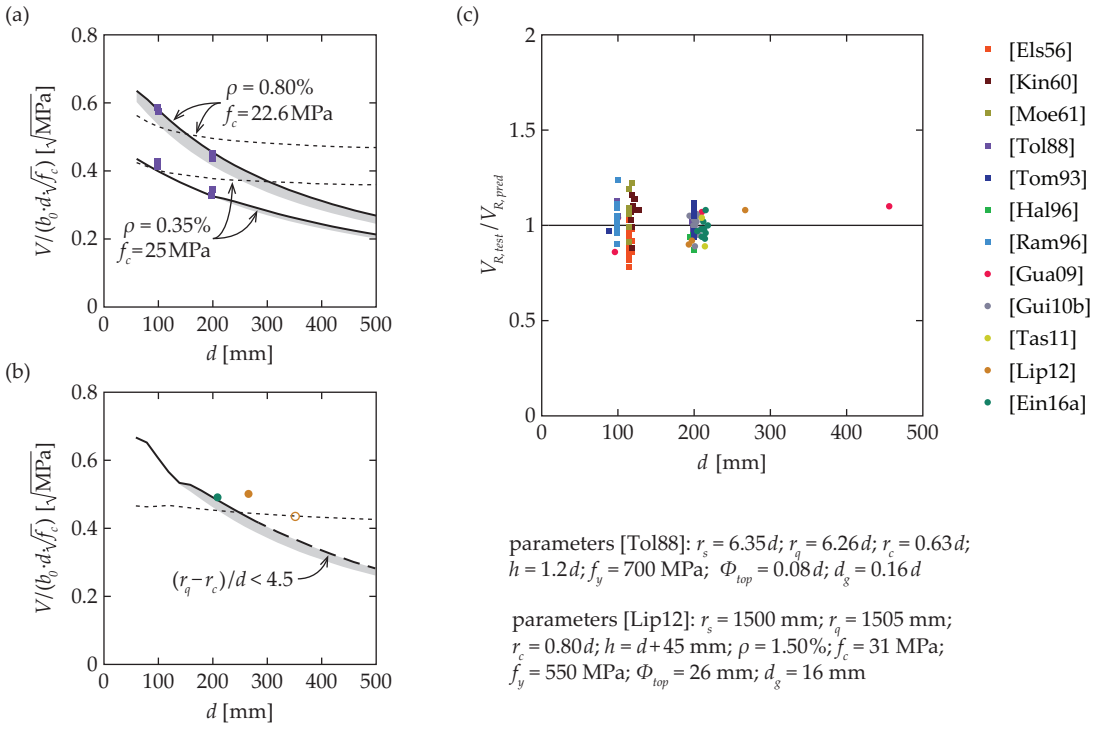

Figure 7.19 Influence of effective depth: (a) tests of Tolf [Tol88]; (b) tests PV1 [Fer10b], PL4 and PL5 [Lip12] (continuous lines – predictions of the present model; shaded area – contribution of dowel action; dashed lines – predictions of the CSCT); (c) $V_{R,test}/V_{R,pred}$ ratios for 100 slender tests from the database for the proposed model

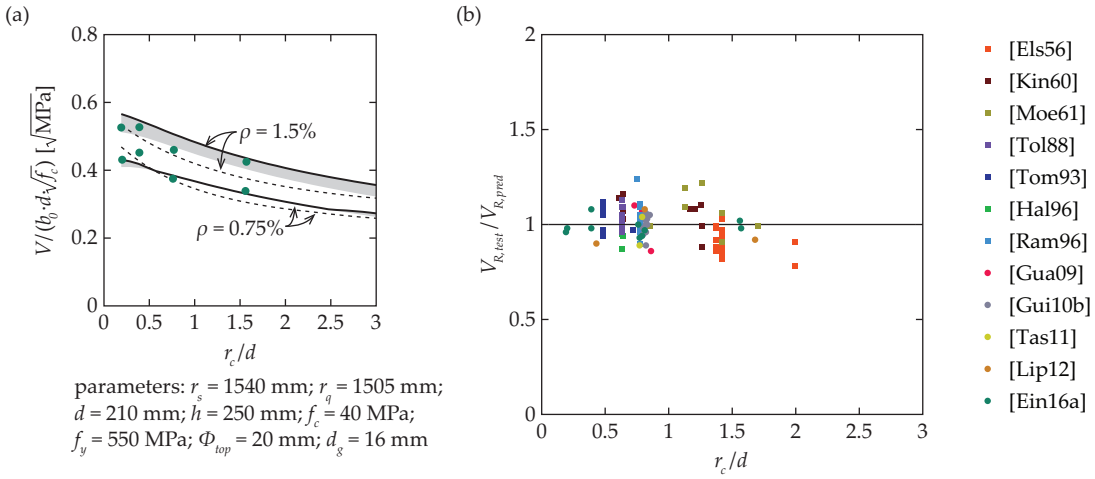

Figure 7.20 Influence of column size: (a) tests of the present thesis (continuous lines – predictions of the present model; shaded area – contribution of dowel action; dashed lines – predictions of the CSCT); (b) $V_{R,test}/V_{R,pred}$ ratios for 100 slender tests from the database for the proposed model

7.5.4 Column size

The influence of column size is accounted for in the proposed model by modifying the effectiveness factor with a term that is a function of column size (Eq. (7.30)). This term is calibrated on the basis of available experiments. Therefore, a comparison between the test results and the predictions expectedly shows good correlation (Fig. 7.20(a, b)). In the CSCT, the influence of column size is similar to the proposed model, although the reduction of nominal punching strength with increasing column size was justified by an increase of the width of the critical shear crack (as was further explained in Chapter 3).

7.5.5 Reinforcement ratio

The amount of flexural reinforcement (Fig. 7.21(a)) affects the punching strength mainly by changing the depth of the compression zone. This was calculated (Eq. (7.5)) by assuming linear-elastic concrete response. In the case of high reinforcement ratios, especially in combination with relatively low concrete strengths, non-linear deformations may start to occur in concrete, which can lead to overestimated depth of the compression zone and thus overestimate the punching strength. That may explain the apparent unconservative predictions in the case of very high values of ρ that can be seen in Figure 7.21(b). However, it should be noted that all such specimens are from the test campaign of Elstner and Hognestad [Els56] on relatively thin slabs (nominal effective depths d = 114 to 118 mm, actual values not reported) with large diameter rebars as tensile reinforcement (19 or 25 mm) and small concrete cover (15 or 13 mm), whereas the maximum aggregate size was 25 to 38 mm. As such, these slabs did not conform to the current codes of practice [CEN04, FIB13], which require that concrete cover of rebars be at least equal to the bar diameter in order to achieve adequate bond. In addition, in real slabs, reinforcement ratios over 2% are uncommon. Therefore, these specimens were kept in the database but the statistical parameters were also calculated for a dataset where these slabs were excluded.

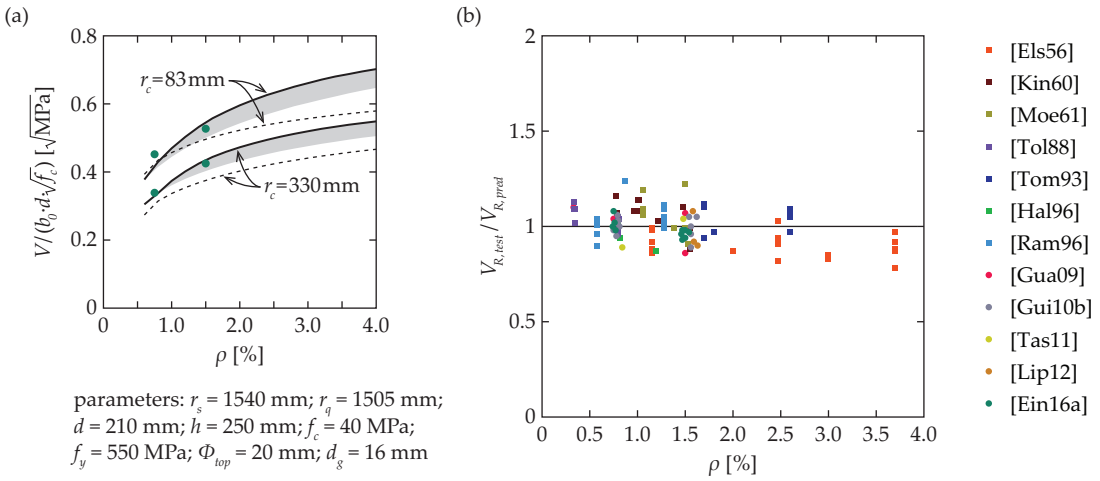

Figure 7.21 Influence of reinforcement ratio: (a) tests of the present thesis (continuous lines – predictions of the present model; shaded area – contribution of dowel action; dashed lines – predictions of the CSCT); (b) $V_{R,test}/V_{R,pred}$ ratios for 100 slender tests from the database for the proposed model

7.5.6 In-plane forces

If in-plane forces, caused for example by pre-stressing, are present in the slab, the effective depth should be calculated by solving Equation (7.4). The increased force in the compression chord due to σ_n should also be accounted for in Equation (7.8). The magnitude of the in-plane forces at the column perimeter and the slab rotation can be predicted with the axisymmetric model that was introduced in Chapter 3.

An experimental investigation on punching of pre-stressed slabs was performed by Clément *et al.* [Cle14]. Parametric analysis and a comparison to the results of this campaign are shown in Figure 7.22. Specimens of the first series of the campaign (series N) had centric in-plane compression applied by means of an external loading frame. Three different levels of pre-stress (1.25, 2.5 and 5 MPa) were applied on slabs with two different flexural reinforcement ratios (0.79% and 1.55%). Figure 7.22(a) shows the predictions of the proposed model (continuous lines) and the CSCT (dashed lines) with the modifications to account for the influence of in-plane forces on the load-rotation response, as well as on the failure criterion [Cle13, Cle14]. Both the proposed model and the CSCT predict that the punching strength increases with increasing pre-stress levels and according to both models, that increase is limited. In the CSCT, this limit arises from the formulation of the failure criterion, where the maximum normalized nominal stress, corresponding to slab rotation $\psi = 0$, is 0.75. According to the proposed model, the reduction of the efficiency of high levels of prestressing is related to a shift from a separation-governed failure mode to a sliding-type failure, between which the applied yield criterion predicts a smooth transition. The trend of reducing efficiency of prestressing is well predicted by the proposed model. However, the estimates are slightly conservative.

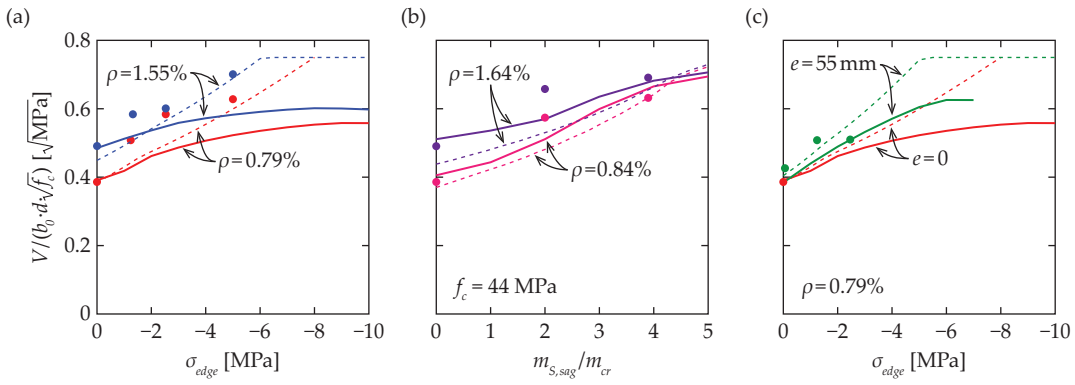

Figure 7.22 Influence of pre-stressing, specimens of Clément *et al.* [Cle14]: (a) slabs with different levels of applied edge compression without eccentricity (reference specimens PG11 [Gui10a] and PV1 [Fer10b]); (b) specimens with applied edge moments; (c) specimens with ρ = 0.8%, with centric prestressing cables and with prestressing eccentricity of 55 mm (continuous lines – proposed model; dashed lines – CSCT (Clément *et al.* [Cle14]); parameters, if not shown otherwise: r_s = 1540 mm; r_q = 1505 mm; r_c = 165 mm; d = 210 mm; h = 250 mm; f_c = 35 MPa; f_y = 584 MPa; Φ_{top} = 16 mm; d_g = 16 mm)

Four specimens in the campaign of Clément *et al.* [Cle14] (series M) investigated the influence of positive bending moments in the slab. These moments normally arise due to the eccentricity of prestressing cables. In series M, however, the positive (sagging) moment was applied at the edges of the specimens with a special loading frame. The non-linear analysis presented in Chapter 3 showed that the total bending moment remains negative (hogging) in the center of the slab, but in-plane compressive forces arise due to the restraint provided by the applied edge moments. Accounting for this compression increases the depth of the compression zone and thus, according to the proposed model, enhances the punching strength. Figure 7.22(b) shows the influence of the applied positive moments at specimen's edge, predicted with the proposed model and with the CSCT [Cle14]. The predictions of both models are similar and fit the observed trends.

The three specimens of series P [Cle14] were reinforced with prestressing cables with an eccentricity of 55 mm. The effects of in-plane compression and positive bending moments were thus combined. Figure 7.22(c) shows the influence of the prestressing stress according to the investigated models. Similarly to series N (Fig. 7.22(a)), the predictions of the CSCT are limited by the maximum punching strength. The proposed model could be applied until the level of prestressing was such that the positive moments due to eccentricity completely cancelled the negative moments due to shear loading in the punching region.

7.5.7 Edge restraints

Ospina *et al.* [Osp01], and later Choi and Kim [Cho12] tested specimens with passive flexural edge restraints that modelled actual continuous slabs, allowing for redistributions between hogging and sagging moments. The main investigated parameters were the provided amounts of hogging and sagging reinforcement. Although the ratios of hogging reinforcement were notably different, the flexural response of the edge-restrained specimens did not vary as much. This can be explained by the emergence of in-plane forces due to the confinement in the hogging moment portion of the specimen provided by a tension ring in the sagging moment portion, as predicted by the analysis presented in Chapter 3.

Table 7.3 Comparison between the test results of edge-restrained slabs and the predictions of the CSCT (accounting for the compressive membrane action, failure criterion of Eq. (2.1)) as well as of the proposed model (* – cyclic tests)

Ref.	Test	ρ_{hog}, [%]	ρ_{sag}, [%]	$V_{R,test}/b_0\,d\sqrt{f_c}$ [√MPa]	CSCT $V_{R,pred}/b_0\,d\sqrt{f_c}$ [√MPa]	Proposed $V_{R,pred}/b_0\,d\sqrt{f_c}$ [√MPa]
[Osp01]	ER1-VS	0.92	0.14	0.469	0.411	0.504
[Cho12]	MRA*	1.06	0.31	0.345	0.433	0.531
	MRB*	0.83	0.43	0.327	0.427	0.519
	MRC*	0.58	0.57	0.335	0.409	0.537

According to the proposed model, the increase of punching strength arising from the confinement can be predicted by accounting for the compressive in-plane stresses in the column perimeter. The

results of the analysis are shown in Table 7.3. The predicted strengths for all the specimens are very similar in spite of the differences in the distribution of reinforcement. The predictions for the tests of Choi and Kim [Cho12] are consistently higher than the measured strengths due to a cyclic loading at 80–100% of the failure load.

7.6 Simplifications of the model

7.6.1 Constant inclination of the critical surface

According to the punching strength model proposed in this thesis, the inclination of the critical surface α in the compression strut and the angle of principal stresses θ_p relative to that surface are defined by the state of normal and shear stresses on the critical surface where the σ_α-τ_α curve touches a yield criterion, as was shown in Figure 7.10. In Figure 7.23(a), it can be seen that the Ottosen yield criterion and the curves, that describe the mean normal (σ_α) and shear stresses (τ_α) as a function of punching load V and α, are nearly parallel in a relatively long range. Therefore, the angle α does not have a strong influence on the punching capacity V_R. In addition, the angle of the principal stresses θ_p, which is related to the slope of the yield criterion, does not change significantly either. Thus, constant values can be selected for α and θ_p without a noticeable loss of precision of the predictions. Based on the governing values for the 119 tests in the database, $\alpha = 30°$ and $\theta = 12°$ were selected (refer to Fig. 7.23(b) and (c) for α and θ_p, respectively).

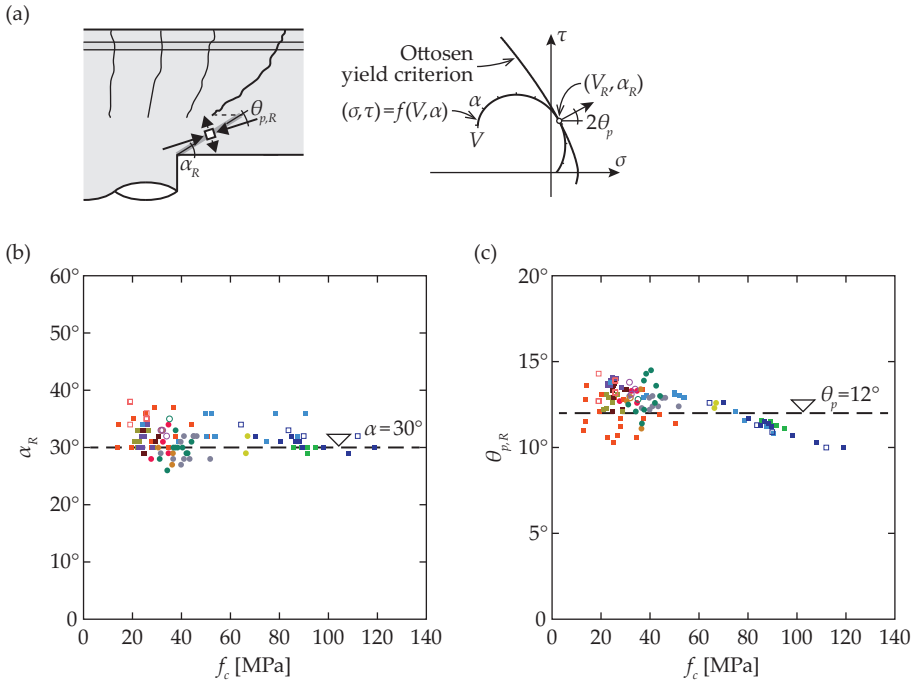

Figure 7.23 Inclination of the critical surface α and direction of principal compression θ_p: (a) determination of angles α and θ_p; (b) governing angles α_R for the 119 tests in the database; (c) governing angles $\theta_{p,R}$ for the 119 tests in the database

7.6.2 Stress in flexural reinforcement

In the proposed model, punching strength of a slab-column connection is assumed to be a function of the force in the tension chord of the slab. This force depends on the flexural deformations of the slab around to the connection and increases with increasing level of load. However, after the load reaches a level that causes yielding of radial flexural reinforcement, forces in the tension chord and thus the punching capacity are constant.

In addition, the shear force that is transferred to the column by dowel action of tensile reinforcement depends on the stresses in the rebars. An example of the evolution of punching strength as a function of slab rotation was shown in Figure 7.17(a). As a simplification in order to avoid the need to use iterations to determine the punching strength, stress in tensile reinforcement σ_s can be assumed to be constant at a level equal to the yield strength of reinforcing steel f_y (refer to the calculation example given in Appendix D of the thesis).

Table 7.4 shows the ratios of the experimental to the predicted capacities for the 100 slender specimens from the literature, using firstly the proposed model with the governing angles α and θ_p calculated through iterations. In the second calculation, constant angles of $\alpha = 30°$ and $\theta = 12°$ are assumed. Negligible differences between the simplified and the iterated results can be seen. Finally, the punching strengths are calculated using constant stresses in the flexural reinforcement of $\sigma_s = f_y$, which results in slightly increased scatter of the predictions. Table E.2 in Appendix E of the thesis lists the calculated $V_{R,test}/V_{R,pred}$ ratios for all the specimens.

Table 7.4 $V_{R,test}/V_{R,pred}$ ratios for the slender slabs according to the proposed model

	No.	variable angles		$\alpha = 30°$; $\theta = 12°$		constant σ_s	
		mean	COV	mean	COV	mean	COV
Elstner and Hognestad [Els56]	18	0.90	7.2%	0.90	7.0%	0.97	12.4%
Kinnunen and Nylander [Kin60]	12	1.08	8.4%	1.08	8.4%	1.08	7.8%
Moe [Moe61]	6	1.04	9.3%	1.04	9.3%	1.05	8.8%
Tolf [Tol88]	8	1.04	5.6%	1.05	5.2%	1.11	4.4%
Tomaszewicz [Tom93]	9	1.05	6.7%	1.05	6.8%	1.06	6.5%
Hallgren [Hal96]	5	0.95	5.8%	0.95	5.9%	0.96	5.1%
Ramdane [Ram96]	12	1.03	9.1%	1.02	9.4%	1.03	9.8%
Guandalini *et al.* [Gua09]	4	1.02	13.0%	1.01	13.1%	1.06	14.1%
Guidotti [Gui10b]	11	1.02	10.3%	1.02	10.2%	1.04	6.2%
Tassinari [Tas11]	2	0.97	-	0.97	-	0.99	-
Lips *et al.* [Lip12]	3	0.97	10.2%	0.97	10.1%	1.10	10.0%
Einpaul *et al.* [Ein16a]	10	0.98	4.2%	0.99	4.4%	1.07	5.4%
	Σ 100	1.00	9.0%	1.00	9.1%	1.04	9.4%
without Elstner and Hognestad	**Σ 82**	**1.02**	**7.8%**	**1.02**	**7.9%**	**1.05**	**8.0%**

As explained in Section 7.5.5, the proposed model overestimates the strength of the thin specimens with very high amounts of flexural reinforcement tested by Elstner and Hognestad [Els56], possibly due to the detailing of the reinforcement in these specimens, which does not conform to the modern requirements. The mean and the coefficient of variation for the experimental to the pre-

dicted strength ratios are thus also given for all the other specimens from the database, excluding this campaign.

Table 7.5 $V_{R,test}/V_{R,pred}$ ratios for the slender slabs according to the CSCT [Mut08b], Model Code 2010 [FIB13] (Level of Approximation II) and Eurocode 2 [CEN04]

	No.	CSCT		MC2010 (LoA II)		Eurocode 2	
		mean	COV	mean	COV	mean	COV
Elstner and Hognestad [Els56]	18	0.98	7.7%	1.14	7.6%	1.17	9.5%
Kinnunen and Nylander [Kin60]	12	1.06	8.3%	1.23	8.2%	1.21	9.8%
Moe [Moe61]	6	1.04	9.0%	1.24	8.8%	1.25	9.8%
Tolf [Tol88]	8	0.99	10.0%	1.18	9.6%	1.11	13.8%
Tomaszewicz [Tom93]	9	1.10	6.1%	1.31	5.9%	1.10	9.1%
Hallgren [Hal96]	5	0.96	3.8%	1.18	5.1%	0.97	4.2%
Ramdane [Ram96]	12	1.10	10.5%	1.44	7.5%	1.27	12.5%
Guandalini *et al.* [Gua09]	4	1.08	8.9%	1.29	8.9%	1.08	13.4%
Guidotti [Gui10b]	11	1.09	9.8%	1.29	9.6%	1.05	5.1%
Tassinari [Tas11]	2	1.07	-	1.27	-	1.02	-
Lips *et al.* [Lip12]	3	1.08	3.8%	1.21	5.1%	1.01	8.2%
Einpaul *et al.* [Ein16a]	10	1.05	5.8%	1.23	7.5%	1.07	15.9%
	Σ 100	1.05	9.2%	1.25	10.3%	1.14	12.9%
without Elstner and Hognestad	**Σ 82**	**1.06**	**9.0%**	**1.27**	**9.8%**	**1.13**	**13.5%**

Table 7.5 shows experimental-to-predicted strength ratios for other punching models: the CSCT [Mut08b], Model Code 2010 (level of approximation II) [FIB13] and Eurocode 2 [CEN04]. The CSCT shows a low scatter (mean ratio is 1.06 and COV 9.0%). The results of Model Code 2010 punching provisions are conservative but also with a low scatter (mean 1.27 and COV 9.8%). For the considered tests, the predictions of Eurocode 2 have clearly the largest scatter (mean 1.13 and COV 13.5%). All the results can be found in Table E.2 in Appendix E of the thesis.

7.7 Summary

In this chapter, a new calculation model was proposed that allowed predicting the punching strength of slab-column connections. The model assumed that the shear force is transferred from the slab to the column by an inclined compression strut and, in a smaller part, by dowel action of tensile reinforcement. The strength of a conical shell, located below the flexural cracks in the compression strut, is predicted using the lower bound theorem of the theory of plasticity and the general triaxial stress-based yield criterion of Ottosen [Ott77].

The proposed model assumed that punching failures occur due to crack localization in the compression strut. Therefore, applying the theory of plasticity requires that relevant effectiveness factors be used on the yield stress of concrete. It is explained that in the case of punching, the effectiveness factor should depend on the slab depth to account for the size effect, but it should also be a function of column size in order to consider the propagation of the failure crack along a support perimeter. A semi-empirical effectiveness factor is calibrated on the basis of a selection of experimental results.

A comparison to test results suggests that the proposed model can successfully predict the punching strength of slender specimens, where the formation of a direct strut between the load and the support is avoided. The contribution of dowel action is shown to be up to approximately 10% of the capacity. A simplified form of the model is also given that allows calculating the punching strength without iterations.

The proposed model can be also used to predict the punching strength of pre-stressed slabs by considering the influence of in-plane forces on the location of the neutral axis. Enhanced punching strength of continuous or confined slabs can also be predicted when the magnitude of the in-plane compression, which arises due to confinement, is calculated with the axisymmetric numerical model described in Chapter 3.

Chapter 8 Summary and conclusions

The present thesis consisted of an analytical study on the behavior of continuous reinforced concrete flat slabs, an experimental campaign of punching tests on isolated specimens with a focus on investigating the failure mechanism by means of internal measurements, and a development of a new model for axisymmetric punching that is based on the assumption that the shear force is mostly transferred to the column through a direct compression strut. This chapter contains a brief summary of the achieved results, the main conclusions of the work and an outlook for further research.

8.1 Summary

The earlier mechanical models for punching have analyzed the behavior of actual slabs by considering axisymmetric isolated slab elements limited by the points of moment contraflexure around the slab-column connection. In the present thesis, the behavior of continuous slabs was studied on the basis of slab portions that extend to the mid-span symmetry line of the slab. Due to the nonlinear flexural response of reinforced concrete members, caused by cracking of concrete and yielding of reinforcement, redistribution between hogging and sagging moments occurs in continuous slabs. The adopted approach allowed accounting for this effect as well as the consequent shifting of the line of moment contraflexure. In addition, compressive membrane action may arise after flexural cracking of continuous slabs due to restrained slab dilation, which can be provided either by the lateral rigidity of the adjoining structural elements or by the radially uncracked sagging moment portion of the slab itself. Comparisons of the model predictions to the results of punching test on various edge-restrained specimens confirmed the accuracy of the model. The model, as well as the test results, shows that due to the effect of self-confinement, even only flexural edge restraints can generate compressive membrane forces around the column. On the basis of the numerical model, a simplified formula for calculating the load-rotation response of continuous slabs was proposed, adapted for use together with the punching provisions of Model Code 2010.

In the experimental part of the thesis, thirteen 250 mm deep isolated punching test specimens were tested to failure. Ten specimens had no shear reinforcement, whereas three specimens were equipped with double-headed shear studs. The main investigated parameters were column size and specimen slenderness ratio. The obtained punching strengths were compared to the predictions calculated using the punching provisions of the major codes of practice (ACI 318, Eurocode 2 and Model Code 2010) as well as the Critical Shear Crack Theory (CSCT). In some specimens, detailed investigation of the failure mechanism was conducted. Using a novel technique based on a coordinate measuring arm, displacements of measurement points arranged in a grid pattern inside

the specimen were tracked. This allowed following the initiation and development of internal cracking in the vicinity of the column.

Finally, a new method was proposed to calculate the punching resistance of interior slab-column connections. Experimental observations on the kinematics of internal cracks in two-way slabs suggested that the transfer of shear stresses through the cracks of flexural origin was not significant. According to the proposed model, punching failures are considered to occur due to localization of a failure crack in the direct compression strut below the flexural cracks. The failure crack may then propagate to join pre-existing flexural cracks or develop further independently of them. The critical state of in-plane and shear stresses that causes the crack localization is predicted using the lower bound theorem of the theory of plasticity in combination with a general triaxial yield criterion. Because the actual behavior of concrete in the case of punching failures is brittle and not plastic, effective values of concrete strength parameters have to be used. These values should also account for the structural size effect that is known to affect the behavior of brittle elements. In this thesis, the effectiveness factor was shown to depend on the slab depth and column size. The new model can also be used to predict the punching strength of slabs with in-plane forces, such as prestressed slabs or slabs where membrane forces are generated due to slab continuity.

8.2 Conclusions

8.2.1 Punching of continuous slabs

The size of the isolated test specimens, which corresponds to the location of moment contraflexure points in actual slabs, is normally selected assuming linear-elastic slab behavior. A non-linear analysis presented in this thesis shows that this location actually varies with the level of load in continuous slabs. Together with the compressive membrane action, it may lead to a stiffer response of the continuous slabs than has been assumed on the basis of isolated elements. According to the CSCT, where the punching strength of slab-column connections is a function of slab rotation, it results in increased punching capacity of actual slabs.

Especially significant differences between isolated specimens and continuous slabs appear in slabs with low amounts of hogging reinforcement or in shear-reinforced slabs, where tensile reinforcement in the vicinity of the slab-column connection reaches yielding before a punching failure occurs. In continuous slabs, this leads to redistribution of bending from hogging to sagging moments and a subsequent shift of the moment contraflexure line towards the column, which increases the stiffness of the load-rotation response and thus the punching strength. These phenomena cannot occur in isolated specimens and may thus lead to conservative estimates of the punching strengths of corresponding actual slabs.

Due to the described effects, edge-restrained specimens are better suited for modeling the punching behavior of actual flat slabs than conventional isolated elements. Whereas the development of design formulas for punching shear on the basis on tests on isolated slabs is believed to be conservative, the provisions for more precise calculations (such as for assessment of existing struc-

tures) should take into account the experimental and analytical evidence obtained from tests on slabs with flexural edge restraints.

8.2.2 Experimental investigation

The campaign of punching tests on isolated specimens with variable column sizes confirmed the well-known observation that the nominal shear strength on a control perimeter close to the column edge decreases with increasing column size. Despite the experimental evidence, the punching provisions of ACI 318 assume constant shear strength on a control perimeter at $d/2$ from the column edge for column side lengths up to $4d$. In the Eurocode 2 provisions, the influence of column size is accounted for by verifying the nominal shear stress on a control perimeter located further away (at $2d$) from the column edge. However, in order to avoid decreasing the factor of safety in the case of small column sizes, an empirical limit for the maximum nominal shear stress at the column perimeter has been added. Yet, comparisons between the code predictions and the test results show a considerable scatter, in part because the punching verification of small columns in Eurocode 2 does not account for the beneficial influence of shear reinforcement, which has been experimentally observed.

The CSCT explains the reduced nominal punching strengths of larger columns by greater slab rotations at load levels close to the failure and consequently increased crack widths that decrease the capacity of concrete to carry shear stresses from the slab to the column. In the experimental campaign, however, the flexural crack widths reached before punching failures occurred were not observed to be significantly affected by column size, because in the case of larger columns, the slab deformation was distributed between a larger number of cracks. Nonetheless, the CSCT provides the best punching strength estimates of the compared models. The predictions of the Model Code 2010 punching provisions (in the level of approximation II) are based on the CSCT and thus show similar tendencies, while being more conservative.

The influence of slab slenderness is not accounted for in the punching provisions of ACI 318 and Eurocode 2. In the tests on isolated specimens, the slab slenderness ratio had a significant influence on the punching capacity of slabs with shear reinforcement. However, as all these specimens failed after yielding of flexural reinforcement, these results do not directly predict the behavior of actual continuous slabs. Regarding the slabs without shear reinforcement tested in the present research, the influence of slab slenderness on the punching strength was not observed to be significant.

By means of the measurements of internal cracking during punching tests, two types of cracks could be distinguished. Propagation of flexural cracks, inclined towards the column due to the influence of shear, could be observed around the column. However, in most cases, the eventual punching failures did not take place along these cracks. Instead, new lower-angled failure cracks developed. On some sides of the column in some specimens, these cracks were first detected already below 80% of the maximum load. However, on the other side of the column or in other specimens, they appeared suddenly only at the moment of failure.

8.2.3 Proposed punching model

The model for axisymmetric punching proposed in this thesis uses the theory of plasticity and assumes uniform distribution of stresses in a conical shell in the compression strut around the support. In this model, the actual non-uniform stress distribution is taken into account by using the effective values of concrete strength. The effectiveness factor is shown to be a function of the slab depth as well as the column size. The column size effect, caused by the shear redistribution that occurs along the support, can explain the reduction of the nominal shear strength of larger slab-column connections that was observed in the test campaign described in the present thesis. A comparison between the model predictions and 82 tests from the literature shows a very good agreement (average tested-to-predicted strength ratio is 1.02 with a coefficient of variation if 7.8%).

In the proposed model, the punching strength does not directly depend on the slab rotation. Therefore, in the case of sufficiently slender elements, where the development of a direct strut between the loading points and the support is avoided, the punching strength is not significantly influenced by the slenderness ratio of the slab. However, more slender slabs show higher deformation capacities compared to the more compact ones.

The beneficial influence of in-plane compressive stresses in the slab around the connection can be accounted for by modifying the inclination of the compression strut. The enhanced punching strength of continuous slabs can therefore be explained by the compressive membrane action, which was shown to generate compressive forces in the slab even in the case of specimens with only flexural edge restraints.

8.3 Outlook

Regarding the punching behavior of continuous slabs, it should be noted that axisymmetric geometries, which were assumed in the models presented in this thesis, exist in practice only in very rare cases. Actual slabs may have openings in the vicinity of the columns or in the confinement-providing mid-span tension ring that, depending on their size, can restrain or completely eliminate the influence of compressive membrane action. Furthermore, compressive membrane action due to self-confinement appears only partly in the case of edge columns. In continuous slabs, moment redistribution may also influence the distribution of shear forces between the columns. It might be useful to study these effects on the basis of non-linear finite element analyses, which can be adapted to more complex geometries.

Punching resistance under sustained or cyclic loading has not received sufficient research attention. In self-confined continuous slabs, the influence of sustained loading may be even more important due to the tensile creep of concrete in the tension ring that may reduce its stiffness and thus increase the slab rotation around the columns. The influence of pre-existing cracks in concrete due to previously applied loading cycles should also be further investigated.

In the study of continuous slabs, the differences found between the load-rotation responses of continuous slabs and isolated specimens were especially significant in the case of using highly efficient shear reinforcement. This highlighted that tests on isolated specimens might not always be suitable for modeling the behavior of actual shear-reinforced slabs. However, tests on continuous or edge-restrained slabs with modern shear reinforcement are extremely scarce in the literature. More such experimental data are needed to assess the level of safety of the presently used design approaches.

The size effect factor used in the proposed punching model was calibrated on the basis of test results from the literature. However, the majority of the experiments have been performed on slabs that are thinner than the ones typically used in practice. Due to laboratory constraints, many of the thicker punching test specimens have also had lower slenderness ratios. In order to validate the applicability of proposed punching models on actual thick slabs, more punching tests should be performed on thick but sufficiently slender specimens.

Further investigation is also needed on the redistribution of shear forces along the support in axisymmetric slabs. A numerical study should be performed on the influence of tangential shear redistribution on the moment field and the deformations of the slab. The obtained results should be compared to detailed experimental measurements of soffit deformations and strains at several locations along the column perimeter, possibly also to the distribution of reaction forces along the edge of the support plate. These analyses can lead to proper assessment of slab deformations associated to shear redistribution and allow for deriving a column size effect factor on the basis on energy balance considerations. Such approach can also be suitable for modelling the behavior of slabs in the vicinity of wall corners, where high concentrations of shear stresses may occur, potentially leading to an initiation of the failure cracks at relatively low levels of load.

The proposed punching model can also be extended for slabs with shear reinforcement by accounting for the forces in the reinforcement units that cross the critical surface. In such cases, depending on the location and the size of the first units, the governing critical surface would be steeper and the failure mode would shift closer to a sliding than a separation failure, which matches with the experimental observations.

The punching model proposed in the present thesis predicts the failure of a conical shell in the compression strut using the theory of plasticity together with a general yield criterion and a semi-empirical effectiveness factor calibrated on the basis of experimental results. The actual mechanisms of failure inside the conical shell were not studied. A more detailed numerical analysis, which considers the micro-mechanical behavior and fracture propagation in concrete under triaxial stress and strain state, and more refined experimental investigation could give more information about the actual low-level behavior of that region.

References

[**ACI71**] American Concrete Institute "Building code requirements for structural concrete (ACI 318-71)," Farmington Hills, Michigan, USA, 1971, 78 p.

[**ACI14**] American Concrete Institute "Building code requirements for structural concrete (ACI 318-14)," Farmington Hills, Michigan, USA, 2014, 519 p.

[**Ale87**] Alexander, S. D. B., Simmonds, S. H. "Ultimate strength of slab-column connection," *ACI Structural Journal*, Vol. 84, No. 3, 1987, pp. 255–261

[**Ale99**] Alexander, S. D. B. "Strip design for punching shear," *ACI Special Publication*, Vol. 183, 1999, pp. 161–179

[**And81**] Andrä, H. P. "Zum Tragverhalten von Flachdecken mit Dübelleisten-Bewehrung im Auflagerbereich [The strength of the support zones of flat slabs reinforced with shear combs]," *Beton- und Stahlbetonbau*, Vol. 76, No. 3, 1981, pp. 53–57 (in German)

[**ASC74**] Joint ASCE-ACI Task Committee 426 on Shear and Diagonal Tension, "The shear strength of reinforced concrete members – slabs," *Journal of the Structural Division, ASCE*, Vol. 100, No. 8, 1974, pp. 1543–1591.

[**Baž84**] Bažant, Z. P. "Size effect in blunt fracture: concrete, rock, metal," *Journal of Engineering Mechanics*, Vol. 110, No. 4, 1984, pp. 518–538

[**Baž87**] Bažant, Z. P., Cao, Z. "Size effect in punching shear failure of slabs," *ACI Structural Journal*, Vol. 84, No. 1, 1987, pp. 44–53

[**Bel15**] Belletti, B., Walraven, J. C., Trapani, F. "Compressive membrane action in confined RC and SFRC circular slabs," *Engineering Structures*, Vol. 95, 2015, pp. 25–39

[**Ben00**] Bentz, E. C. "Sectional analysis of reinforced concrete members," PhD Thesis, Department of Civil Engineering, University of Toronto, Canada, 2000, 310 p.

[**Bra80a**] Braestrup, M. W. "Dome effect in RC slabs: Rigid-plastic analysis," *Journal of the Structural Division – ASCE*, Vol. 106, No. 6, 1980, pp. 1237–1253

[**Bra80b**] Braestrup, M. W., Morley, C. T. "Dome effect in RC slabs: Elastic-plastic analysis," *Journal of the Structural Division – ASCE*, Vol. 106, No. 6, 1980, pp. 1255–1262

[**Bro90**] Broms, C. E. "Punching of flat plates – a question of concrete properties in biaxial compression and size effect," *ACI Structural Journal*, Vol. 87, No. 3, 1990, pp. 292–304

[**BSI85**] British Standards Institution "BS 8110-1:1985 Structural use of concrete. Code of practice for design and construction," London, UK, 1985, 124 p.

[**Cam13**] Campana, S., Fernández Ruiz, M., Anastasi, A., Muttoni, A. "Analysis of shear-transfer actions on one-way RC members based on measured cracking pattern and failure kinematics," *Magazine of Concrete Research,* Vol. 56, No. 6, 2013, pp. 386–404

[**Cav15**] Cavagnis, F., Fernández Ruiz, M., Muttoni, A. "Shear failures in reinforced concrete members without transverse reinforcement: An analysis of the critical shear crack development on the basis of test results," *Engineering Structures*, Vol. 103, 2015, pp. 157–173

[**CEB93**] Comité Euro-International du Béton "CEB-FIP Model Code 1990," Thomas Telford, London, UK, 1993, 460 p.

[**CEN04**] European Committee for Standardization (CEN) "Eurocode 2: Design of concrete structures – Part 1: General rules and rules for buildings," Brussels, Belgium, 2004, 225 p.

[**CEN10**] European Committee for Standardization (CEN) "EN 1992-1-1/AC:2010 Corrigendum for: Design of concrete structures – Part 1: General rules and rules for buildings," Brussels, Belgium, 2010, 23 p.

[**CEN14**] European Committee for Standardization (CEN) "EN 1992-1-1/A1:2014 Amendment for: Design of concrete structures – Part 1: General rules and rules for buildings," Brussels, Belgium, 2014, 4 p.

[**Cha92**] Chana, B. S., Desai, S. B. "Membrane action, and design against punching shear," *The Structural Engineer*, Vol. 70, No. 19, 1992, pp. 339–343

[**Che82**] Chen W. F. "Plasticity in reinforced concrete," McGraw-Hill, New York, USA, 1982, 474 p.

[**Cho12**] Choi, J.-W., Kim, J.-H. J. "Experimental investigations on moment redistribution and punching shear of flat plates," *ACI Structural Journal*, Vol. 109, No. 3, 2012, pp. 329–338

[**Cle12**] Clément, T., Fraccaro, M., Muttoni, A., Fernández Ruiz, M. "Essais de poinçonnement sur dalles en béton armé – Mesures internes [Punching tests on reinforced concrete slabs – internal measurements]," Test report, IBETON, EPFL, Lausanne, Switzerland, 2012, 74 p. (in French)

[**Cle13**] Clément, T., Ramos, A. P., Fernández Ruiz, M., Muttoni, A. "Design for punching of prestressed concrete slabs," *Structural Concrete*, Vol. 14, No. 2, 2013, pp. 157–167.

[**Cle14**] Clément, T., Pinho Ramos, A., Fernández Ruiz, M., Muttoni, A., "Influence of prestressing on the punching strength of post-tensioned slabs," *Engineering Structures*, Vol. 72, 2014, pp. 56–69

[**CSA94**] Canadian Standards Association, "Design of concrete structure for buildings – Standard CSA-A23.3-M94," Ottawa, Ontario, Canada, 1994, 199 p.

[**ECP08**] European Concrete Platform, "Eurocode 2 Commentary," Brussels, Belgium, 2008, 168 p.

[**Ein15**] Einpaul, J., Fernández Ruiz, M., Muttoni, A. "Influence of moment redistribution and compressive membrane action on punching strength of flat slabs," *Engineering Structures*, Vol. 86, 2015, pp. 43–57

[**Ein16a**] Einpaul, J., Bujnak, J., Fernández Ruiz, M., Muttoni, A. "Study on the influence of column size and slab slenderness on punching strength," *ACI Structural Journal*, Vol. 113, No. 1, 2016, pp. 135–145

[**Ein16b**] Einpaul, J., Brantschen, F., Fernández Ruiz, M., Muttoni, A. "Performance of punching shear reinforcement under gravity loading: Influence of type and detailing," *ACI Structural Journal*, accepted for publication

[**Ein16c**] Einpaul, J., Ospina, C. E., Fernández Ruiz, M., Muttoni, A. "Punching shear capacity of continuous slabs," *ACI Structural Journal*, accepted for publication

[**Els56**] Elstner, R. C., Hognestad, E. "Shearing strength of reinforced concrete slabs," *ACI Materials Journal*, Vol. 53, No. 2, 1956, pp. 29–58

[**Eyr16**] Eyre, J. R. "Surround stiffness to membrane action in concrete slabs," *Magazine of Concrete Research*, Vol. 59, No. 2, 2007, pp. 107–119

[**Fer09**] Fernández Ruiz, M., Muttoni, A. "Applications of Critical Shear Crack Theory to punching of reinforced concrete slabs with transverse reinforcement," *ACI Structural Journal*, Vol. 106, No. 4, 2009, pp. 485–494

[**Fer10a**] Fernández Ruiz, M., Plumey, S., Muttoni, A. "Interaction between bond and deviation forces in spalling failures of arch-shaped members without transverse reinforcement," *ACI Structural Journal*, Vol. 107, No. 3, 2010, pp. 346–354

[**Fer10b**] Fernández Ruiz, M., Muttoni, A., Kunz, J. "Strengthening of flat slabs against punching shear using post-installed shear reinforcement," *ACI Structural Journal*, Vol. 107, No. 4, 2010, pp. 434–442

[**Fer13**] Fernández Ruiz, M., Mirzaei, Y., Muttoni, A. "Post-punching behavior of flat slabs," *ACI Structural Journal*, Vol. 110, No. 5, 2013, pp. 801–812

[**Fer15**] Fernández Ruiz, M., Muttoni, A., Sagaseta, J. "Shear strength of concrete members without transverse reinforcement: A mechanical approach to consistently account for size and strain effects," *Engineering Structures*, Vol. 99, 2015, pp. 360–372

[**FIB01**] Fédération internationale du béton, "*fib* Bulletin 12: Punching of structural concrete slabs," Lausanne, Switzerland, 2001, 307 p.

[**FIB13**] Fédération internationale du béton, *"fib* Model Code for Concrete Structures 2010," Ernst & Sohn, Germany, 2013, 434 p.

[**Gua05**] Guandalini, S. "Poinçonnement symétrique des dalles en béton armé [Symmetric punching in R/C slabs]," Doctoral thesis, EPFL, No. 3380, Lausanne, Switzerland, 2005, 289 p. (in French)

[**Gua09**] Guandalini S., Burdet O., Muttoni A. "Punching tests of slabs with low reinforcement ratios," *ACI Structural Journal*, Vol. 106, No. 1, 2009, pp. 87–95

[**Gui10a**] Guidotti, R. "Poinçonnement des planchers-dalles avec colonnes superposées fortement sollicitées [Punching of flat slabs with superposed heavily loaded columns]," Doctoral thesis, EPFL, No. 4812, Lausanne, Switzerland, 2010, 230 p. (in French)

[**Gui10b**] Guidotti, R., Fernández Ruiz, M., Muttoni, A. "Essais de poinçonnement de dalles en béton vibré et béton autocompactant avec différentes tailles maximales du granulat [Punching tests of slabs of vibrated and self-compacting concrete with variable maximum aggregate size]," Test report, IBETON, EPFL, Lausanne, Switzerland, 2009, 67 p. (in French)

[**Gus88**] Gustafsson, J., Hillerborg, A. "Sensitivity in shear strength of longitudinally reinforced concrete beams to fracture energy of concrete," *ACI Structural Journal*, Vol. 85, No. 3, 1988, pp. 286–294

[**Hal96**] Hallgren, M. "Punching shear capacity of reinforced high strength concrete slabs," Doctoral thesis, KTH, Stockholm, Sweden, 1996, 206 p.

[**Hew75**] Hewitt, B. E., Batchelor, B. "Punching shear strength of restrained slabs," *Journal of the Structural Division – ASCE*, Vol. 101, No. 9, 1975, pp. 1837–1853

[**Hil76**] Hillerborg, A., Modéer, M., Petersson, P. "Analysis of crack formation and crack growth in concrete by means of fracture mechanics and finite elements," *Cement and Concrete Research*, Vol. 6, No. 6, 1976, pp. 773–781

[**Hil83**] Hillerborg, A. "Analysis of a single crack," Fracture mechanics of concrete, edited by F. H. Wittmann, Elsevier science publishers B.V., Amsterdam, Netherlands, 1983, pp. 223–249

[**Hoa98**] Hoang, L. C., Nielsen, M. P. "Plasticity approach to shear design," *Cement and Concrete Composites*, Vol. 20, No. 6, 1998, pp. 437–453

[**Kan64**] Kani, G. N. J. "The riddle of shear failure and its solution," *ACI Journal*, Vol. 61, No. 4, 1964, pp. 441–467

[**Kan66**] Kani G. N. J. "Basic facts concerning shear failure," *ACI Journal,* Vol. 63, No. 6, 1966, pp. 675–692

[**Kin60**] Kinnunen, S., Nylander, H. "Punching of concrete slabs without shear reinforcement," *Transactions of the Royal Institute of Technology*, No. 158, Stockholm, Sweden, 1960, 112 p.

[**Kin63**] Kinnunen, S. "Punching of concrete slabs with two-way reinforcement," *Transactions of the Royal Institute of Technology*, No. 198, Stockholm, Sweden, 1963, 108 p.

[**Kir84**] Kirkpatrick, J., Rankin, G. I. B., Long, A. E. "Strength evaluation of M-Beam bridge deck slabs," *The Structural Engineer*, Vol. 62B, No. 3, 1984, pp. 60–68

[**Kua93**] Kuang, J. S., Morley, C. T. "A plasticity model for punching shear of laterally restrained slabs with compressive membrane action," *International Journal of Mechanical Science*, Vol. 35, No. 5, 1993, pp. 371–385

[**Kup73**] Kupfer, H. B., Gerstle, K. H. "Behavior of concrete under biaxial stresses," *ASCE Journal of Engineering Mechanics*, Vol. 99, No. 4, 1973, pp. 853–866

[**Lad77**] Ladner, M., Schaeidt, W., Gut, S. "Experimentelle Untersuchungen an Stahlbeton-Flachdecke [Experimental study on reinforced concrete flat slabs]," EMPA Bericht No. 205, Switzerland, 1977, 96 p. (in German)

[**Lip12**] Lips, S., Fernández Ruiz, M., Muttoni, A. "Experimental investigation on punching strength and deformation capacity of shear-reinforced slabs," *ACI Structural Journal*, Vol. 109, No. 6, 2012, pp. 889–900

[**Mar98**] Marti, P., Alvarez, M., Kaufmann, W., Sigrist, V. "Tension chord model for structural concrete," *Structural Engineering International*, Vol. 8, No. 4, 1998, pp. 287–298

[**Mel98**] Melo, G. S., Regan, P. E. "Post-punching resistance of connections between flat slabs and interior columns," *Magazine of Concrete Research*, Vol. 50, No. 4, 1998, pp. 319–327

[**Moe61**] Moe, J. "Shearing strength of reinforced concrete slabs and footings under concentrated loads," PCA Bulletin D47, Skokie, Illinois, USA, 1961, 135 p.

[**Mut96**] Muttoni, A., Schwartz, J., Thürlimann, B. "Design of concrete structures with stress fields," Birkhäuser Verlag, Basel, Switzerland, 1996, 143 p.

[**Mut08a**] Muttoni, A., Fernández Ruiz, M. "Shear strength of members without transverse reinforcement as function of critical shear crack width," *ACI Structural Journal*, Vol. 105, No. 2, 2008, pp. 163–172

[**Mut08b**] Muttoni, A. "Punching shear strength of reinforced concrete slabs without transverse reinforcement," *ACI Structural Journal*, Vol. 105, No. 4, 2008, pp. 440–450

[**Mut10**] Muttoni, A., Fernández Ruiz, M. "Shear in slabs and beams: may they be treated in the same way?" In: *fib* Bulletin 57: Shear and punching shear in RC and FRC elements, Fédération internationale du béton, Lausanne, Switzerland, 2010, pp. 1–24.

[**Mut13**] Muttoni, A., Fernández Ruiz, M., Bentz, E. C., Foster, S. J., Sigrist, V. "Background to the Model Code 2010 shear provisions – Part II Punching shear," *Structural Concrete*, Vol. 14, No. 3, 2013, pp. 195–203

[**Nat14**] Natário, F., Fernández Ruiz, M., Muttoni, A. "Shear strength of RC slabs under concentrated loads near clamped linear supports," *Engineering Structures*, Vol. 76, 2014, pp. 10–23

[**Nie84**] Nielsen, M. P. "Limit analysis and concrete plasticity," Prentice-Hall, Englewood Cliffs, New Jersey, USA, 1984, 420 p.

[**Nie11**] Nielsen, M. P., Hoang, L. C. "Limit analysis and concrete plasticity. 3rd edition," CRC Press, Boca Raton, Florida, USA, 2011, 788 p.

[**Nyl90**] Nylander, H., Kinnunen, S. "Dimensionering med hänsyn till genomstansning vid koncentrerat stöd [Design for punching of concentrated loads]," Betonghandboken – Konstruktion, 2nd edition, AB Svensk Byggtjänst, Stockholm, Sweden, 1990, pp. 648–675 (in Swedish)

[**Ock55**] Ockleston, A. J. "Load tests on a three storey reinforced concrete building in Johannesburg," *The Structural Engineer*, Vol. 33, No. 10, 1955, pp. 304–322

[**Osp01**] Ospina, C. E., Alexander, S. D. B., Cheng, J. J. R. "Behaviour of concrete slabs with fibre-reinforced polymer reinforcement," Structural Engineering Report No. 242, University of Alberta, Canada, 2001, 355 p.

[**Osp11**] Ospina, C. E., Birkle, G., Widianto, W. "ACI 445 punching shear collected databank," Network for Earthquake Engineering Simulation (database), Dataset, 2011.

[**Ott77**] Ottosen, N. S. "A failure criterion for concrete," *ASCE Journal of Engineering Mechanics*, Vol. 103, No. 4, 1977, pp. 527–535

[**Par80**] Park, R., Gamble, W. L. "Reinforced concrete slabs," John Wiley & Sons, Hoboken, New Jersey, USA, 1980, 618 p.

[**Ran07**] Randl, N. "Load bearing behaviour of cast-in shear dowels," *Beton- und Stahlbetonbau*, Vol. 102, Special Edition, 2007, pp. 31–37

[**Ran13**] Randl, N. "Design recommendations for interface shear transfer in *fib* Model Code 2010," *Structural Concrete*, Vol. 14, No. 3, 2013, pp. 230–241

[**Ram96**] Ramdane, K.-E. "Punching shear of high performance concrete slabs," In: Proceedings of the fourth international symposium on utilization of high-strength / high performance concrete, Vol. 3, Laboratoire Central des Ponts et Chaussées, Paris, France, 1996, pp. 1015–1026

[**Ram03**] Ramos, A. P. "Punçoamento em lajes fungiformes pré-esforçadas [Punching of pre-stressed flat slabs]," Doctoral thesis, Instituto Superior Tecnico, Universidade Tecnica de Lisboa, Lisbon, Portugal, 2003, 292 p. (in Portuguese)

[**Ras62**] Rasmussen, B. H. "Strength of transversely loaded bolts and dowels embedded in concrete," Laboratoriet for Bygningsstatik, Denmark Technical University, Vol. 34, No. 2, Meddelelse, Denmark, 1962, pp. 39–55

[**Reg83**] Regan, P. E. "Punching shear in prestressed concrete slab bridges," Engineering Structures Research group, Polytechnic of Central London, London, UK, 1983, 249 p.

[**Reg86**] Regan, P. E. "Symmetric punching of reinforced concrete slabs," *Magazine of Concrete Research*, Vol. 38, No. 136, 1986, pp. 115–128

[**Sag11**] Sagaseta, J., Muttoni, A., Fernández Ruiz, M., Tassinari L. "Non-axis-symmetrical punching shear around internal columns of RC slabs without transverse reinforcement," *Magazine of Concrete Research*, Vol. 63, No. 6, 2011, pp. 441–457

[**Sag14**] Sagaseta, J., Tassinari, L., Fernández Ruiz, M., Muttoni, A. "Punching of flat slabs supported on rectangular columns," *Engineering Structures*, Vol. 77, 2014, pp. 17–33

[**Sch84**] Schäfers, U. "Konstruktion, Bemessung und Sicherheit gegen Durchstanzen von balkenlosen Stahlbetondecken im Bereich von Innenstützen [Construction, dimensioning and safety with respect to punching shear of reinforced concrete flat plates in the vicinity of internal columns]," Deutscher Ausschuss für Stahlbeton, No. 357, Berlin, Germany, 1984, 83 p. (in German)

[**She89**] Shehata, I. A. E. M., Regan, P. E. "Punching in R.C. slabs," *Journal of Structural Engineering*, Vol. 115, No. 7, 1989, pp. 1726–1740

[**SIA03**] Swiss Society of Engineers and Architects "SIA 262:2003 Concrete structures," Zürich, Switzerland, 2003, 94 p.

[**SIA13**] Swiss Society of Engineers and Architects "SIA 262:2013 Concrete structures," Zürich, Switzerland, 2013, 102 p.

[**Sib14**] Siburg, C. "Zur einheitlichen Bemessung gegen Durchstanzen in Flachdecken und Fundamenten [A uniform design method for punching shear of flat slabs and footings]," Doctoral thesis, RWTH Aachen, IMB, Vol. 40, Aachen, Germany, 2014, 198 p. (in German)

[**Sim87**] Simmonds, S. H., Alexander, S. D. B. "Truss model for edge colum-slab connections," *ACI Structural Journal*, Vol. 84, No. 4, 1987, pp. 296–303

[**Sim16**] Simões, J. T., Bujnak, J., Fernández Ruiz, M., Muttoni, A. "Investigation on the punching shear strength and behavior of RC footings based on detailed experimental measurements," *Structural Concrete*, submitted for publication

[**Sis97**] Sistonen, E., Lydman, M., Huovinen, S. "Teräsbetonilaatan lävistyskapasiteetin laskentakaavan geometrinen malli [The geometrical model of the calculation formula of the punching shear capacity of the reinforced concrete slab]," Report No. 69, Helsinki University of Technology, Espoo, Finland, 1997, 95 p. (in Finnish)

[**Sta01**] Staller, M. "Empirical model by Staller," In: *fib* Bulletin 12: Punching of structural concrete slabs, Fédération internationale du béton, Lausanne, Switzerland, 2001, pp. 56–61

[**Ste07**] Stein, T., Ghali, A., Dilger, W. H. "Distinction between punching and flexural failure modes of flat plates," *ACI Structural Journal*, Vol. 104, No. 3, 2007, pp. 357–365

[**Tas11**] Tassinari, L. "Poinçonnement non symétrique des dalles en béton armé [Non-symmetric punching of reinforced concrete slabs]," Doctoral thesis, EPFL, No. 5030, Lausanne, Switzerland, 2011, 197 p. (in French)

[**Tol88**] Tolf, P. "Plattjocklekens inverkan pa betongplattors hallfasthet vid genomstansning. Försök med cikulära plattor [Influence of the slab thickness on the strength of concrete slabs at punching. Tests with circular slabs]," KTH, Dep. of Structural Mechanics and Engineering, Bulletin 146, Stockholm, Sweden, 1988, 64 p. (in Swedish)

[**Tom93**] Tomaszewicz, A. "High strength concrete. SP2 – Plates and shells. Report 2.3 Punching shear capacity of reinforced concrete slabs," SINTEF Structure and Concrete, Report No. STF70 A93082, Trondheim, Norway, 1993, 36 p.

[**UKH02**] UK Highway Agency "BD 81/02 Use of compressive membrane action in bridge decks, Design manual for roads and bridges," Vol. 3, Section 4, Part 20, 2002, 20 p.

[**Van72**] Vanderbilt, M. D. "Shear strength of continuous plates," *Journal of the Structural Division, ASCE*, Vol. 98, No. 5, 1972, pp. 961–973

[**Vaz08**] Vaz Rodrigues, R., Fernández Ruiz, M., Muttoni, A. "Shear strength of R/C bridge cantilever slabs," *Engineering Structures*, Vol. 30, 2008, pp. 3024–3033

[**Vec86**] Vecchio, F. J., Collins, M. P. "The modified compression-field theory for reinforced concrete elements subjected to shear," *ACI Structural Journal*, Vol. 83, No. 2, 1986, pp. 219–231

[**Vol14**] Vollum, R. L., Fang, L. "Shear enhancement in RC beams with multiple point loads," *Engineering Structures*, Vol. 80, 2014, pp. 389–405

[**Wal80**] Walraven, J. C. "Aggregate interlock: A theoretical and experimental analysis," Doctoral thesis, TU Delft, Delft, Netherlands, 1980, 197 p.

[**Wan96**] Wang, C. H. "Introduction to fracture mechanics," DSTO Aeronautical and Maritime Research Laboratory, Melbourne, Australia, 1996, 73 p.

[**Woo61**] Wood, R. H. "Plastic and elastic design of slabs and plates," Thames and Hudson, London, United Kingdom, 1961, 344 p.

Appendix A Punching provisions in codes

This appendix presents the formulas used for calculating the code predictions in Chapter 3 of the thesis. In the present analysis, mean values are used for material strength and all the safety factors are taken equal to one.

In all of the considered codes, punching verification is performed by comparing the nominal shear strength of the slab v_R to a nominal shear stess on a control perimeter around a column or a loaded area v:

$$v = \frac{V}{b_0 d} \tag{A.1}$$

where V is concentrated load, b_0 is length of the control perimeter and d effective depth of the slab.

A.1 ACI 318-14

In ACI 318-14 [**ACI14**], the perimeter where punching resistance is verified is located at a distance $0.5d$ from the column edge. In the case of square or rectangular columns, the corners of the control perimeter do not have to be rounded. For square interior columns with $c < 4d$ and normal strength concrete, the nominal shear strength is calculated as:

$$v_{R,c,ACI} = 0.33 \cdot f_c^{1/2} \tag{A.2}$$

The contribution of shear reinforcement is added to a reduced value of concrete $v_{R,c}$. The reduction factor is 0.5 and only shear reinforcement within a distance d from the column edge is taken into account. For slabs with double-headed studs as shear reinforcement, the maximum punching resistance is limited to twice the value obtained with Equation (A.2).

For large interior columns, the shear strength is reduced with a factor $10 \cdot d / b_{0,ACI}$.

A.2 Eurocode 2

According to the punching provisions of Eurocode 2 [CEN04], the nominal shear strength at a control perimeter located at a distance $2d$ from the edge of the loaded area is:

$$v_{R,c,EC2(2d)} = 0.18 \cdot k \cdot (100 \cdot \rho)^{1/3} \cdot f_c^{1/3} \geq 0.035 \cdot k^{3/2} \cdot f_c^{1/2} \tag{A.3}$$

where ρ is the flexural reinforcement ratio (geometric mean of two perpendicular directions in a strip extending to $3d$ on both sides of the column, taken at most 2.0%, f_c is concrete cylinder compressive strength [MPa] and factor $k = \left(1 + \sqrt{200/d}\right) \leq 2$ (d in mm) takes into account the size effect.

An additional verification has to be performed at the edge of the loaded area, where shear stress has to be lower than (according to an amendment of Eurocode 2 published in 2010 [CEN10]):

$$v_{R,EC2(0d)} = 0.24 \cdot \left(1 - \frac{f_c}{250}\right) \cdot f_c \tag{A.4}$$

In slabs with shear reinforcement, the contribution of shear reinforcing units that are located closer than 1.5d to the edge of the column is considered with an effective stress of $f_{yt,ef} = 1.15 \cdot (250 + 0.25 \cdot d)$ [MPa, mm] that is added to 0.75 times the resistance calculated with Equation (A.2). According to an amendment published in 2014 [CEN14], the maximum punching resistance of slabs with shear reinforcement is defined as k_{max} times the punching strength calculated with Equation (A.3) (recommended value of k_{max} is 1.5 but higher values may be used, depending on the type and efficiency of the shear reinforcement system, if they are experimentally validated). The limitation of nominal shear stress at the edge of the column (Eq. A.4) is also applicable for slabs with shear reinforcement.

A.3 Model Code 2010

The punching formulation of Model Code 2010 [FIB13] is based on the CSCT [Mut08]. The nominal punching strength depends on the rotation ψ of the slab:

$$v_{R,c,CSCT} = \frac{1}{1.5 + 0.9 \cdot \psi \cdot d \cdot k_{dg}} \cdot f_c^{1/2} \tag{A.5}$$

where $k_{dg} = 2/(1 + d_g/d_{g0}) \geq 0.75$, d_{g0} = 16 mm and in the Level of Approximation II (recommended for a typical design of new structures), slab rotation can be estimated with a simplified parabolic relationship depending on the acting moment in the column strip:

$$\psi = 1.5 \cdot \frac{r_s}{d} \cdot \frac{f_y}{E_s} \cdot \left(\frac{m_S}{m_R}\right)^{3/2} \tag{A.6}$$

where r_s is the radius of an isolated slab or 0.22L in case of a continuous slab with regular span lengths, f_y and E_s are the yield strength and modulus of elasticity of flexural reinforcement, respectively, m_R is the moment capacity of the slab and m_S is the average acting moment in the column strip for interior columns (in slabs with sufficiently regular geometry, m_S can be approximated as $m_S = V/8$)

The contribution of shear reinforcing units located between 0.35d and d is taken into account. Stresses in the transverse reinforcement are found by considering the strains due to flexural deformations. For large amounts of transverse reinforcement, the punching strength is limited to k_{sys} times Equation (A.5). In the case of double-headed studs, k_{sys} = 2.8. However, it should be noted that the increase of punching load is smaller than k_{sys} because with increased load, the slab rotation ψ increases as well, thus decreasing the nominal punching strength.

Appendix B Flexural capacities of test specimens

This appendix presents governing yield line mechanisms and formulas for calculating the flexural capacities for some of the most common types of punching test specimens.

For round specimens supported on round columns with equal displacements applied along the specimen edge ([Kin60], [Hal96], [Tol88], [Ram96]), flexural strength can be calculated as:

$$V_{flex} = 2\pi \cdot \frac{D}{2b_q} \cdot m_{R,average} \tag{B.1}$$

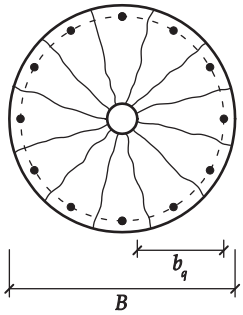

Figure B.1 Yield line pattern for a circular specimen

For square or octagonal specimens with equal loads applied at points close to the slab edge (statically determined elements, such as [Gua09] (slabs with $h = 250$ mm), [Gui10b], [Tas11], [Cle12], [Lip12], [Ein16a]), the governing mechanism is attained by formation of yield lines parallel to the level of upper-most reinforment layer:

$$V_{flex} = 8 \cdot \frac{B}{2(b_{q1} + b_{q2})} \cdot m_{R,weak} \tag{B.2}$$

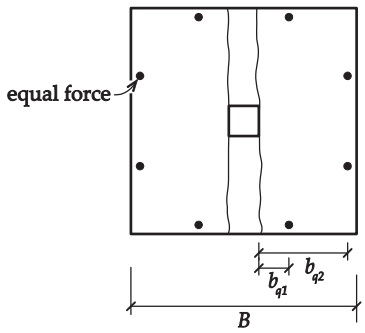

Figure B.2 Yield line pattern for a statically determined square specimen

For square specimens with equal displacements applied at points close to the slab edge (statically undetermined elements, such as specimens PG-3, PG-6 and PG-7 of Guandalini *et al.* [Gua09]), the governing mechanism has yield lines in both directions. The flexural capacity is approximately:

$$V_{flex} \approx 8 \cdot \frac{B}{2(b_{q1} + b_{q2})} \cdot m_{R,average} \tag{B.3}$$

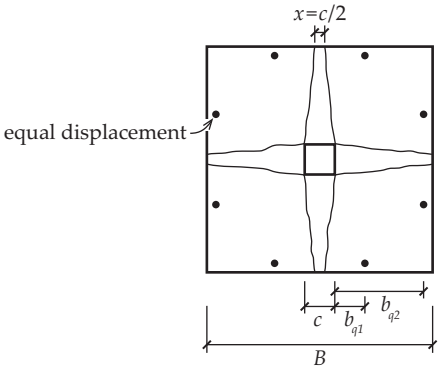

Figure B.3 Yield line pattern for a statically undetermined square specimen

For square specimens that are supported close to the edges with corners free to lift up from the supports, where the load is applied through a square column stub or plate in the center of the slab (tests by [Moe61], [Tom93], [Els56]):

$$V_{flex} = \frac{8}{b_q}\left[\frac{\left(\sqrt{2}-1\right)^2}{2} \cdot c + \left(\sqrt{2}-1\right) \cdot B\right] \cdot m_{R,average} \tag{B.4}$$

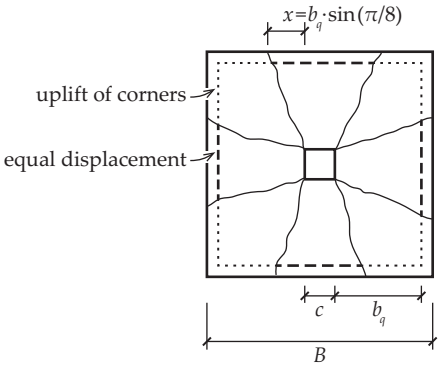

Figure B.4 Yield line pattern for a square specimen simply supported at the edges, square column

For square specimens that are supported close to the edges with corners free to lift up from the supports, where the load is applied through a round column stub or plate (tests by [Sis97]):

$$V_{flex} \approx \frac{8}{b_q}\left[\frac{\left(\sqrt{2}-1\right)^2}{4}\cdot d_c + \left(\sqrt{2}-1\right)\cdot B\right]\cdot m_{R,average} \tag{B.5}$$

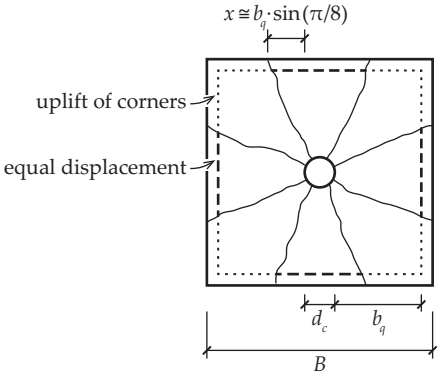

Figure B.5 Yield line pattern for a square specimen simply supported at the edges, round column

In the presented formulas, the average flexural capacity of the slab is calculated as:

$$m_{R,average} = \rho_{average}\cdot f_y \cdot d^2_{average}\cdot\left(1-\frac{\rho_{average}\cdot f_y}{2\cdot f_{cp}}\right) \tag{B.6}$$

where the effective concrete strength is calculated as $f_{cp} = \eta_{fc}\cdot f_c$, where $\eta_{fc} = \left(30/f_c\right)^{1/3} \le 1$ takes into account the increased brittleness of high strength concrete.

Flexural capacity in the weak direction is:

$$m_{R,weak} = \rho_{weak}\cdot f_y \cdot d^2_{weak}\cdot\left(1-\frac{\rho_{weak}\cdot f_y}{2\cdot f_{cp}}\right) \tag{B.7}$$

The reinforcement ratios are calculated as an average of the whole slab, $\rho_{average} = \sum A_s \big/ B\cdot d_{average}$ or $\rho_{weak} = \sum A_s \big/ B\cdot d_{weak}$, where $\sum A_s$ the total area of flexural reinforcement in the considered direction.

Appendix C Triaxial yield criterion for concrete

This appendix presents the formulas used in Chapter 7 to predict the failure of the compression zone close to the column. The four-parameter triaxial yield criterion was first developed by Ottosen [Ott77] by fitting a smooth and convex failure surface to available test results using membrane analogy.

The yield criterion, given in Haigh-Westergaard coordinates (hydrostatic stress ξ, deviatoric stress ρ and angle of similarity θ [Che82]), is formulated as:

$$f(I_1, J_2, \cos 3\theta) = a\frac{J_2}{f_{cp}^2} + \lambda\frac{\sqrt{J_2}}{f_{cp}} + b\frac{I_1}{f_{cp}} - 1 = 0 \tag{C.1}$$

where $I_1 = \sqrt{3}\cdot\xi$ and $J_2 = 3/4\cdot\rho^2$ are stress invariants, a and b are coefficients and $\lambda(\cos 3\theta)$ is a function given as:

$$\lambda = k_1 \cos\left[\frac{1}{3}\cos^{-1}(k_2 \cos 3\theta)\right] \tag{C.2}$$

where k_1 and k_2 are additional coefficients. f_{cp} is the plastic strength of concrete that accounts for the steeper descending branch of the stress-strain curve of concretes with $f_c \geq 30$ MPa:

$$f_{cp} = \left(\frac{30}{f_c}\right)^{1/3}\cdot f_c \tag{C.3}$$

As the calibration tests were performed on concrete cubes, cube strength should be used as the concrete strength $f_c = f_{c,cyl} / 0.8$.

From the principal stresses σ_1, σ_2 and σ_3, the stress invariants can be calculated as:

$$I_1 = \sigma_1 + \sigma_2 + \sigma_3 \tag{C.4}$$

$$J_2 = \frac{1}{6}\left[(\sigma_1 - \sigma_2)^2 + (\sigma_2 - \sigma_3)^2 + (\sigma_3 - \sigma_1)^2\right] \tag{C.5}$$

$$J_3 = (\sigma_1 - I_1/3)(\sigma_2 - I_1/3)(\sigma_3 - I_1/3) \tag{C.6}$$

and the angle of similarity θ can is:

$$\cos 3\theta = \frac{\sqrt{2}\cdot J_3}{\tau_{oct}^3} \tag{C.7}$$

where the deviatoric octahedral stress τ_{oct} is:

$$\tau_{oct} = \sqrt{\frac{2}{3} \cdot J_2} \tag{C.8}$$

Coefficients a, b, k_1 and k_2 in the failure criterion (Equation (C.1)) can be calibrated using results of tests on concrete specimens with different combinations of uniaxial and multi-axial stresses. Ottosen used the following types of tests:

- uniaxial compressive test ($\sigma_1 = 0$; $\sigma_2 = 0$; $\sigma_3 = -f_{cp}$; $\theta = 60°$);
- uniaxial tensile test ($\sigma_1 = f_{ct}$; $\sigma_2 = 0$; $\sigma_3 = 0$; $\theta = 0°$);
- biaxial compressive test ($\sigma_1 = 0$; $\sigma_2 = -f_{2c} \cdot f_{cp}$; $\sigma_3 = -f_{2c} \cdot f_{cp}$);
- a triaxial test with stresses on the compressive meridian ($\sigma_1 = \sigma_2 > \sigma_3$, $\theta = 60°$ (compression is negative)).

The coefficient values can be determined by solving a system of Equations (C.1) and (C.2) in the case of the afforementioned stress states with the coefficients α, β, k_1 and k_2 as unknowns. Table C.1 shows their values depending on the ratio of f_{ct}/f_{cp} ($f_{2c} = 1.16$; $(\xi/f_{cp}, \rho/f_{cp}) = (-5, 4)$).

Table C.1 Coefficient values as a function of the ratio f_{ct}/f_{cp}

f_{ct}/f_{cp}	a	b	k_1	k_2
0.06	2.6944	5.5973	19.0831	0.9982
0.07	2.1875	4.7393	16.4548	0.9954
0.08	1.8076	4.0962	14.4863	0.9914
0.10	1.2759	3.1962	11.7365	0.9801
0.12	0.9218	2.5969	9.9110	0.9647

Model Code 2010 [FIB13] provides closed form solutions for the coefficients a, b, k_1 and k_2. The biaxial concrete strength f_{c2c} is taken as:

$$f_{c2c} = \left(1.2 - \frac{f_{cp}}{1000}\right) \cdot f_{cp} \tag{C.9}$$

Triaxial failure is assumed to occur at $\sigma_{com} = -240$ MPa and and octahedral shear stress τ_{com}:

$$\tau_{com} = 185 - 180 \cdot \frac{f_{cp}}{100} + 260 \cdot \left(\frac{f_{cp}}{100}\right)^2 - 84\left(\frac{f_{cp}}{100}\right)^3 \tag{C.10}$$

A parameter h is defined as:

$$h = -\frac{\sqrt{2} \cdot \sigma_{com}/f_{cp} + \tau_{com}/f_{cp}}{\frac{\tau_{com}/f_{cp}}{\sqrt{2}} - \frac{1}{3}} \tag{C.11}$$

Coefficients can then be calculated as:

$$b = \frac{\sqrt{2} - \dfrac{3 \cdot \tau_{com}/f_{cp}}{f_{c2c}/f_{cp} \cdot f_{ct}/f_c}}{h - \dfrac{9 \cdot \tau_{com}/f_{cp}}{f_{c2c}/f_{cp} - f_{ct}/f_c}} \tag{C.12}$$

$$a = \frac{h \cdot b - \sqrt{2}}{\tau_{com}/f_{cp}} \tag{C.13}$$

$$\lambda_c = \lambda(\theta = 60°) = \left(1 - \frac{h}{3 \cdot \tau_{com}/f_{cp}}\right) \cdot \sqrt{3} \cdot b + \sqrt{3} + \frac{\sqrt{2}}{\sqrt{3} \cdot \tau_{com}/f_{cp}} \tag{C.14}$$

$$\lambda_t = \lambda(\theta = 0°) = \left(2 \cdot \sqrt{3} - \frac{f_{c2c}/f_{cp} \cdot h}{\sqrt{3} \cdot \tau_{com}/f_{cp}}\right) \cdot b + \frac{\sqrt{3}}{f_{c2c}/f_{cp}} + \frac{\sqrt{2} \cdot f_{c2c}/f_{cp}}{\sqrt{3} \cdot \tau_{com}/f_{cp}} \tag{C.15}$$

$$k_2 = 1 \qquad \text{for } \lambda_c/\lambda_t \le 1/2 \tag{C.16}$$

$$k_2 = \cos\left\{3 \cdot \arctan\left[\left(2 \cdot \lambda_c/\lambda_t - 1\right)/\sqrt{3}\right]\right\} \qquad \text{for } \lambda_c/\lambda_t > 1/2 \tag{C.17}$$

$$k_1 = \left(2 \cdot \cos\theta - 1\right) \cdot \lambda_t + 4 \cdot \left(1 - \cos\theta\right) \cdot \lambda_c \qquad \text{for } \lambda_c/\lambda_t \le 1/2 \tag{C.18}$$

$$k_1 = \frac{\lambda_c}{\cos\left(\pi/3 - 1/3 \cdot \arccos k_2\right)} \qquad \text{for } \lambda_c/\lambda_t > 1/2 \tag{C.19}$$

In the absence of other data, tensile strength of concrete f_{ct} is calculated according to the Model Code 2010 [FIB13]:

$$f_{ct} = 0.3 \cdot f_c^{2/3} \qquad \text{if } f_c \le 50 \text{ MPa} \tag{C.20}$$

$$f_{ct} = 2.12 \cdot \ln\left(1 + 0.1 f_c\right) \qquad \text{if } f_c > 50 \text{ MPa} \tag{C.21}$$

Appendix D Calculation example

This appendix gives a calculation example of the punching strength model presented in Chapter 7 of the thesis. Specimen PE8 is selected for the example.

Input data:

- column radius r_c = 165 mm
  (for square columns, radius of a round column with the same perimeter should be used)
- effective depth of the slab d = 214 mm
  (arithmetic average of two directions)
- concrete strength f_c = 42.0 MPa
  (cylinder compressive strength)
- yield strength of reinforcing steel f_y = 542 MPa
- reinforcement ratio ρ = 1.47%

Capacity of the slab-column connection is verified for an applied punching load V = 1096 kN.

Calculation of mean stresses on the critical surface:

- relative column size:

$$r_c / d = 0.771$$

- modulus of elasticity of concrete [FIB13]:

$$E_c = 10000 \cdot f_c^{1/3} = 10000 \cdot 42^{1/3} = 34760\text{MPa}$$

- modulus of elasticity of reinforcing steel is assumed to be $E_s = 205000\text{MPa}$
- relative depth of the compression zone (without accounting for the influence of the inclined shera strut):

$$\frac{x}{d} = \frac{E_s}{E_c} \cdot \rho \cdot \left(\sqrt{1 + \frac{2 \cdot E_c}{\rho \cdot E_s}} - 1 \right) = \frac{205000}{34760} \cdot 0.0147 \cdot \left(\sqrt{1 + \frac{2 \cdot 34760}{0.0147 \cdot 205000}} - 1 \right) = 0.339 \qquad (7.5)$$

- the critical surface is assumed to be inclined with an angle α = 30° from the horizontal. Depth of the compression zone due to influence of the inclined strut x_α and the radius where the critical surface intersects with the neutral axis r_α should be calculated by solving the system of two equations:

$$r_\alpha = r_c + x_\alpha \cdot \cot 30° \qquad (7.3)$$

$$x_\alpha = r_0 / r_\alpha \cdot x \qquad (7.6)$$

The solution of the equation system gives a parameter k_α:

$$k_\alpha = \frac{1}{2} + \frac{1}{2}\sqrt{1 + 4\sqrt{3}\cdot\frac{x}{d}\cdot\frac{r_c/d+1}{(r_c/d)^2}} = \frac{1}{2} + \frac{1}{2}\sqrt{1 + 4\sqrt{3}\cdot 0.339\cdot\frac{0.771+1}{0.771^2}} = 1.915 \tag{D.1}$$

which can be used to calculate r_α and x_α:

$$r_\alpha = k_\alpha \cdot r_c = 1.915\cdot 165 = 316\text{mm} \tag{D.2}$$

$$x_\alpha = \frac{k_\alpha - 1}{\sqrt{3}}\cdot r_c = \frac{1.915-1}{\sqrt{3}}\cdot 165 = 87.2\text{mm} \tag{D.3}$$

– stress in tensile reinforcement can be calculated from slab rotation (Eq. **(7.7)**). Alternatively, tensile reinforcement can be assumed to be yielding:

$$\sigma_s = f_y = 542\text{MPa} \tag{7.7}$$

– the effectiveness factors k_x and k_{col} are:

$$k_x = \sqrt{\frac{300}{150 + x_\alpha/\sin\alpha}} = \sqrt{\frac{300}{150 + 87.2/\sin 30°}} = 0.962 \tag{7.29}$$

$$k_{col} = \sqrt{\frac{3.6}{3 + b_{col}}} = \sqrt{\frac{3600}{3000 + 2\cdot\pi\cdot 165}} = 0.944 \tag{7.30}$$

– radial normal stress in the compression zone at r_α:

$$\overline{\sigma}_0 = -\frac{\rho\cdot d\cdot\sigma_s}{x}\Big/ k_x k_{col} = -\frac{0.0147\cdot 542}{0.339\cdot 0.962\cdot 0.944} = -25.88\text{MPa} \tag{7.9}$$

– shear stress in the compression zone at r_α ($V_{dow} = 0$ because $\sigma_s = f_y$):

$$\overline{\tau}_0 = \frac{V - \sum V_{dow}}{x_\alpha\cdot 2\pi\cdot r_\alpha}\Big/ k_x k_{col} = \frac{1096000}{87.2\cdot 2\cdot\pi\cdot 316\cdot 0.962\cdot 0.944} = 6.97\text{MPa} \tag{7.10}$$

– tangential normal stress in the compression zone within r_0:

$$\overline{\sigma}_t = -\frac{\rho\cdot d\cdot\sigma_s}{x_\alpha}\Big/ k_x k_{col} = -\frac{0.0147\cdot 214\cdot 542}{87.2\cdot 0.962\cdot 0.944} = -21.53\text{MPa} \tag{7.11}$$

– normal and shear stresses on the critical surface:

$$\begin{aligned}\overline{\sigma}_\alpha &= \frac{2r_\alpha}{r_c + r_\alpha}\left(\overline{\sigma}_0\sin^2\alpha + \overline{\tau}_0\sin\alpha\cos\alpha\right) - \overline{\sigma}_t\sin^2\alpha = \\ &= \frac{2\cdot 316}{165+316}\cdot\left(-25.88\cdot\frac{1}{4} + 6.97\cdot\frac{\sqrt{3}}{4}\right) + 21.53\cdot\frac{1}{4} = 0.85\text{MPa}\end{aligned} \tag{7.12}$$

$$\begin{aligned}\overline{\tau}_\alpha &= \frac{2r_\alpha}{r_c + r_\alpha}\left(-\overline{\sigma}_0\sin\alpha\cos\alpha + \overline{\tau}_0\sin^2\alpha\right) + \overline{\sigma}_t\sin\alpha\cos\alpha = \\ &= \frac{2\cdot 316}{165+316}\cdot\left(25.88\cdot\frac{\sqrt{3}}{4} + 6.97\cdot\frac{1}{4}\right) - 21.53\cdot\frac{\sqrt{3}}{4} = 7.69\text{MPa}\end{aligned} \tag{7.13}$$

– principal stresses on the critical surface (angle $\theta_p = 12°$ is assumed):

$$\bar{\sigma}_1 = \bar{\sigma}_\alpha - \bar{\tau}_\alpha \cdot \frac{\cos 2\theta_p - 1}{\sin 2\theta_p} = 0.85 - 7.69 \cdot \frac{\cos 24° - 1}{\sin 24°} = 2.48\text{MPa} \tag{7.14}$$

$$\bar{\sigma}_2 = \bar{\sigma}_t = -21.53\text{MPa}$$

$$\bar{\sigma}_3 = \bar{\sigma}_\alpha - \bar{\tau}_\alpha \cdot \frac{\cos 2\theta_p + 1}{\sin 2\theta_p} = 0.85 - 7.69 \cdot \frac{\cos 24° + 1}{\sin 24°} = -35.33\text{MPa} \tag{7.15}$$

Calculation of the stress invariants:

$$I_1 = \sigma_1 + \sigma_2 + \sigma_3 = 2.48 - 21.53 - 35.33 = -54.38\text{MPa} \tag{C.4}$$

$$J_2 = \frac{1}{6}\left[(\sigma_1 - \sigma_2)^2 + (\sigma_2 - \sigma_3)^2 + (\sigma_3 - \sigma_1)^2\right] = \tag{C.5}$$
$$= \frac{1}{6}\left[(2.48 + 21.53)^2 + (-21.53 + 35.33)^2 + (-35.33 - 2.48)^2\right] = 366\text{MPa}^2$$

$$J_3 = (\sigma_1 - I_1/3)\cdot(\sigma_2 - I_1/3)\cdot(\sigma_3 - I_1/3) = \tag{C.6}$$
$$= (2.48 + 54.38/3)\cdot(-21.53 + 54.38/3)\cdot(-35.33 + 54.38/3) = 1206\text{MPa}^3$$

$$\tau_{oct} = \sqrt{\frac{2}{3}\cdot J_2} = \sqrt{\frac{2}{3}\cdot 366} = 15.62\text{MPa} \tag{C.8}$$

$$\cos 3\theta = \frac{\sqrt{2}\cdot J_3}{\tau_{oct}^3} = \frac{\sqrt{2}\cdot 1206}{15.62^3} = 0.448 \tag{C.7}$$

Calculation of the strength parameters for the triaxial yield criterion:

– concrete cube strength:

$$f_{c,cube} = f_{c,cyl}/0.8 = 42/0.8 = 52.5\text{MPa}$$

– plastic concrete cube strength:

$$f_{cp} = \left(\frac{30}{f_c}\right)^{1/3}\cdot f_c = \left(\frac{30}{42}\right)^{1/3}\cdot 52.5 = 46.9\text{MPa} \tag{C.3}$$

– concrete tensile strength:

$$f_{ct} = 0.3\cdot f_c^{2/3} = 0.3\cdot 42^{2/3} = 3.62\text{MPa} \tag{C.20}$$

– biaxial concrete compressive strength:

$$f_{c2c} = \left(1.2 - \frac{f_{cp}}{1000}\right)\cdot f_{cp} = \left(1.2 - \frac{46.9}{1000}\right)\cdot 46.9 = 54.08\text{MPa} \tag{C.9}$$

– concrete strength in a triaxial stress state:

$$\sigma_{com} = -240\text{MPa} \tag{C.9}$$

$$\tau_{com} = 185 - 180\cdot\frac{f_{cp}}{100} + 260\cdot\left(\frac{f_{cp}}{100}\right)^2 - 84\left(\frac{f_{cp}}{100}\right)^3 = \tag{C.10}$$
$$= 185 - 180\cdot\frac{46.9}{100} + 260\cdot\left(\frac{46.9}{100}\right)^2 - 84\left(\frac{46.9}{100}\right)^3 = 149.1\text{MPa}$$

Calculation of coefficients [FIB13]:

$$h = -\frac{\sqrt{2}\cdot\sigma_{com}/f_{cp} + \tau_{com}/f_{cp}}{\frac{\tau_{com}/f_{cp}}{\sqrt{2}} - \frac{1}{3}} = -\frac{\sqrt{2}\cdot -240/46.9 + 149.1/46.9}{\frac{149.1/46.9}{\sqrt{2}} - \frac{1}{3}} = 2.119 \tag{C.11}$$

$$b = \frac{\sqrt{2} - \frac{3\cdot\tau_{com}/f_{cp}}{f_{c2c}/f_{cp}\cdot f_{ct}/f_c}}{h - \frac{9\cdot\tau_{com}/f_{cp}}{f_{c2c}/f_{cp} - f_{ct}/f_c}} = \frac{\sqrt{2} - \frac{3\cdot 149.1/46.9}{54.08/46.9\cdot 3.62/42}}{2.119 - \frac{9\cdot 149.1/46.9}{54.08/46.9 - 3.62/42}} = 3.823 \tag{C.12}$$

$$a = \frac{h\cdot b - \sqrt{2}}{\tau_{com}/f_{cp}} = \frac{2.119\cdot 3.823 - \sqrt{2}}{149.1/46.9} = 2.103 \tag{C.13}$$

$$\lambda_c = \left(1 - \frac{h}{3\cdot\tau_{com}/f_{cp}}\right)\cdot\sqrt{3}\cdot b + \sqrt{3} + \frac{\sqrt{2}}{\sqrt{3}\cdot\tau_{com}/f_{cp}} = \tag{C.14}$$

$$= \left(1 - \frac{2.119}{3\cdot 149.1/46.9}\right)\cdot\sqrt{3}\cdot 3.823 + \sqrt{3} + \frac{\sqrt{2}}{\sqrt{3}\cdot 149.1/46.9} = 7.139$$

$$\lambda_t = \left(2\cdot\sqrt{3} - \frac{f_{c2c}/f_{cp}\cdot h}{\sqrt{3}\cdot\tau_{com}/f_{cp}}\right)\cdot b + \frac{\sqrt{3}}{f_{c2c}/f_{cp}} + \frac{\sqrt{2}\cdot f_{c2c}/f_{cp}}{\sqrt{3}\cdot\tau_{com}/f_{cp}} = \tag{C.15}$$

$$= \left(2\cdot\sqrt{3} - \frac{54.08/46.9\cdot 2.119}{\sqrt{3}\cdot 149.1/46.9}\right)\cdot 3.823 + \frac{\sqrt{3}}{54.08/46.9} + \frac{\sqrt{2}\cdot 54.08/46.9}{\sqrt{3}\cdot 149.1/46.9} = 13.345$$

$$\lambda_c/\lambda_t = 7.139/13.345 = 0.535$$

$$k_2 = \cos\left\{3\cdot\arctan\left[\left(2\cdot\lambda_c/\lambda_t - 1\right)/\sqrt{3}\right]\right\} = \cos\left\{3\cdot\arctan\left[\left(2\cdot 0.535 - 1\right)/\sqrt{3}\right]\right\} = 0.9927 \tag{C.17}$$

$$k_1 = \frac{\lambda_c}{\cos\left(\pi/3 - 1/3\cdot\arccos k_2\right)} = \frac{7.139}{\cos\left(\pi/3 - 1/3\cdot\arccos 0.9927\right)} = 13.357 \tag{C.19}$$

$$\lambda = k_1\cos\left[\frac{1}{3}\cos^{-1}\left(k_2\cos 3\theta\right)\right] = 13.357\cdot\cos\left[\frac{1}{3}\cos^{-1}\left(0.9927\cdot 0.448\right)\right] = 12.453 \tag{C.2}$$

The yield criterion is:

$$f\left(I_1, J_2, \cos 3\theta\right) = a\frac{J_2}{f_{cp}^2} + \lambda\frac{\sqrt{J_2}}{f_{cp}} + b\frac{I_1}{f_{cp}} - 1 = 2.103\cdot\frac{366}{46.9^2} + 12.453\cdot\frac{\sqrt{366}}{46.9} - 3.823\cdot\frac{54.38}{46.9} - 1 = -0.003 \approx 0$$

The load V = 1096 kN is therefore very close to the yield criterion.

Appendix E Database of punching tests

This appendix presents the main properties of the specimens in the database that was used to validate the punching model described in Chapter 7. The main properties of the specimens are shown in Table E.1, a comparison between the experimental results and the model predictions are shown in Table E.2.

Table E.1 Main parameters of the specimens in the punching test database (specimen type and dimensions b_{q1} and b_{q2} – refer to the figures in Appendix B)

Series	Specimen	h	d	c	d_c	*speci-men type*	B	b_{q1}	b_{q2}	f_c	d_g	f_y	ρ	Φ	$V_{R,test}$	$V_{R,test}$ /V_{flex}
		mm	mm	mm	mm		mm	mm	mm	Mpa	mm	Mpa	%	mm	kN	
[Els56]	A-1a	152	118	254	-	(B.4)	1829	763	-	14.1	25	332	1.15	19	**303**	0.81
	A-1b	152	118	254	-	(B.4)	1829	763	-	25.3	25	332	1.15	19	**365**	0.91
	A-1c	152	118	254	-	(B.4)	1829	763	-	29.1	25	332	1.15	19	**356**	0.88
	A-1d	152	118	254	-	(B.4)	1829	763	-	36.9	25	332	1.15	19	**351**	0.86
	A-1e	152	118	254	-	(B.4)	1829	763	-	20.3	25	332	1.15	19	**356**	0.90
	A-2a	152	114	254	-	(B.4)	1829	763	-	13.7	25	321	2.47	25	**334**	0.56
	A-2b	152	114	254	-	(B.4)	1829	763	-	19.5	25	321	2.47	25	**400**	0.60
	A-2c	152	114	254	-	(B.4)	1829	763	-	37.5	25	321	2.47	25	**467**	0.63
	A-7b	152	114	254	-	(B.4)	1829	763	-	27.9	25	321	2.47	25	**512**	0.71
	A-3a	152	114	254	-	(B.4)	1829	763	-	12.8	25	321	3.70	25	**356**	0.53
	A-3b	152	114	254	-	(B.4)	1829	763	-	22.6	25	321	3.70	25	**445**	0.48
	A-3c	152	114	254	-	(B.4)	1829	763	-	26.6	25	321	3.70	25	**534**	0.55
	A-3d	152	114	254	-	(B.4)	1829	763	-	34.6	25	321	3.70	25	**547**	0.53
	A-5	152	114	356	-	(B.4)	1829	763	-	27.8	25	321	2.47	25	**534**	0.73
	A-6	152	114	356	-	(B.4)	1829	763	-	25.1	25	321	3.70	25	**498**	0.51
	B-9	152	114	254	-	(B.4)	1829	763	-	43.9	38	341	2.00	22	**505**	0.76
	B-11	152	114	254	-	(B.4)	1829	763	-	13.5	38	409	3.00	25	**329**	0.46
	B-14	152	114	254	-	(B.4)	1829	763	-	50.6	38	325	3.00	25	**578**	0.63
[Kin60]	IA15a-5	149	117	-	150	(B.1)	1840	818	-	25.5	32	441	0.79	12	**255**	0.81
	IA15a-6	151	118	-	150	(B.1)	1840	818	-	24.9	32	454	0.78	12	**275**	0.85
	IA15b-9	150	117	-	150	(B.1)	1840	818	-	24.7	32	446	1.21	12	**275**	0.59
	IA15b-10	150	117	-	150	(B.1)	1840	818	-	24.7	32	448	1.21	12	**275**	0.59
	IA15c-11	153	121	-	150	(B.1)	1840	818	-	30.5	32	436	1.02	12	**333**	0.78
	IA15c-12	154	122	-	150	(B.1)	1840	818	-	29.4	32	439	1.01	12	**332**	0.77
	IA30a-24	158	128	-	300	(B.1)	1840	780	-	25.1	32	455	0.96	12	**430**	0.89
	IA30a-25	154	124	-	300	(B.1)	1840	780	-	23.8	32	451	0.99	12	**408**	0.88
	IA30b-28	151	119	-	300	(B.1)	1840	780	-	24.6	32	437	1.55	12	**368**	0.60
	IA30b-29	151	119	-	300	(B.1)	1840	780	-	24.6	32	445	1.55	12	**417**	0.67
	IA30c-30	151	120	-	300	(B.1)	1840	780	-	28.6	32	436	1.48	12	**490**	0.80
	IA30c-31	151	119	-	300	(B.1)	1840	780	-	28.6	32	448	1.50	12	**539**	0.87
[Moe61]	S2-60	152	114	254	-	(B.4)	1829	763	-	22.1	38	399	1.53	16	**356**	0.64

	S1-70	152	114	254	-	(B.4)	1829	763	-	24.5	38	483	1.06	16	**392**	0.81
	S5-60	152	114	203	-	(B.4)	1829	789	-	22.2	38	399	1.06	16	**343**	0.88
	S5-70	152	114	203	-	(B.4)	1829	789	-	23.0	38	483	1.06	16	**378**	0.81
	R2	152	114	152	-	(B.4)	1829	814	-	26.5	10	328	1.38	16	**311**	0.76
	M1A	152	114	305	-	(B.4)	1829	738	-	20.8	38	481	1.50	19	**433**	0.66
[Tol88]	S2.1	240	200	-	250	(B.1)	2540	1128	-	23.9	32	657	0.80	16	**603**	0.46
	S2.2	240	199	-	250	(B.1)	2540	1128	-	22.6	32	670	0.80	16	**600**	0.45
	S2.3	240	200	-	250	(B.1)	2540	1128	-	25.0	32	668	0.34	16	**489**	0.80
	S2.4	240	197	-	250	(B.1)	2540	1128	-	23.8	32	664	0.35	16	**444**	0.73
	S1.1	120	100	-	125	(B.1)	1270	564	-	28.2	16	706	0.80	8	**216**	0.60
	S1.2	120	99	-	125	(B.1)	1270	564	-	22.6	16	701	0.81	8	**194**	0.56
	S1.3	120	98	-	125	(B.1)	1270	564	-	26.3	16	720	0.35	8	**145**	0.89
	S1.4	120	99	-	125	(B.1)	1270	564	-	24.8	16	712	0.34	8	**148**	0.93
[Tom93]	ND65-1-1	320	275	200	-	(B.4)	3000	1150	-	64.3	16	500	1.50	25	**2050**	0.45
	ND65-2-1	240	200	150	-	(B.4)	2600	1025	-	70.2	16	500	1.70	20	**1200**	0.45
	ND95-1-1	320	275	200	-	(B.4)	3000	1150	-	83.7	16	500	1.50	25	**2250**	0.48
	ND95-1-3	320	275	200	-	(B.4)	3000	1150	-	89.9	16	500	2.50	25	**2400**	0.32
	ND95-2-1	240	200	150	-	(B.4)	2600	1025	-	88.2	16	500	1.70	20	**1100**	0.41
	ND95-2-1D	240	200	150	-	(B.4)	2600	1025	-	86.7	16	500	1.70	20	**1300**	0.48
	ND95-2-3	240	200	150	-	(B.4)	2600	1025	-	89.5	16	500	2.60	20	**1450**	0.37
	ND95-2-3D	240	200	150	-	(B.4)	2600	1025	-	80.3	16	500	2.60	20	**1250**	0.32
	ND95-2-3D+	240	200	150	-	(B.4)	2600	1025	-	98.0	16	500	2.60	20	**1450**	0.36
	ND95-3-1	120	88	100	-	(B.4)	1500	500	-	85.1	16	500	1.80	12	**330**	0.51
	ND115-1-1	320	275	200	-	(B.4)	3000	1150	-	112	16	500	1.50	25	**2450**	0.52
	ND115-2-1	240	200	150	-	(B.4)	2600	1025	-	119	16	500	1.70	20	**1400**	0.51
	ND115-2-3	240	200	150	-	(B.4)	2600	1025	-	108.1	16	500	2.60	20	**1550**	0.39
[Hal96]	HSC 0	240	200	-	250	(B.1)	2540	1138	-	89.1	18	643	0.80	16	**965**	0.70
	HSC 1	245	200	-	250	(B.1)	2540	1138	-	91.3	18	627	0.80	16	**1021**	0.76
	HSC 2	240	194	-	250	(B.1)	2540	1138	-	85.7	18	620	0.82	16	**889**	0.69
	HSC 4	240	200	-	250	(B.1)	2540	1138	-	91.6	18	596	1.19	20	**1041**	0.55
	N/HSC 8	242	198	-	250	(B.1)	2540	1138	-	94.9	18	631	0.80	16	**944**	0.71
[Ram96]	1	125	98	-	150	(B.1)	1700	611	-	78.4	10	550	0.58	12	**224**	0.86
	2	125	98	-	150	(B.1)	1700	611	-	49.9	10	550	0.58	12	**212**	0.82
	3	125	98	-	150	(B.1)	1700	611	-	23.9	10	550	0.58	12	**169**	0.68
	4	125	98	-	150	(B.1)	1700	611	-	52.2	10	550	0.58	12	**233**	0.90
	6	125	98	-	150	(B.1)	1700	611	-	90.5	10	550	0.58	12	**233**	0.89
	12	125	98	-	150	(B.1)	1700	611	-	53.6	10	550	1.28	12	**319**	0.59
	13	125	98	-	150	(B.1)	1700	611	-	38.7	10	550	1.28	12	**297**	0.56
	14	125	98	-	150	(B.1)	1700	611	-	54.0	10	550	1.28	12	**341**	0.63
	16	125	98	-	150	(B.1)	1700	611	-	87.4	10	550	1.28	12	**362**	0.65
	21	125	98	-	150	(B.1)	1700	611	-	37.2	20	650	1.28	12	**286**	0.47
	22	125	98	-	150	(B.1)	1700	611	-	74.8	20	650	1.28	12	**405**	0.63
	23	125	100	-	150	(B.1)	1700	611	-	50.1	20	650	0.87	10	**341**	0.74
[Sis97]	L1	197	172	-	202	(B.5)	1770	684	-	25.8	16	621	0.46	10	**503**	0.73
	L2	201	176	-	202	(B.5)	1770	684	-	25.8	16	621	0.45	10	**537**	0.76
	L3	198	173	-	201	(B.5)	1770	685	-	25.8	16	621	0.45	10	**530**	0.77
	L4	197	170	-	402	(B.5)	1970	684	-	25.8	16	612	0.67	12	**686**	0.65
	L5	199	172	-	399	(B.5)	1970	686	-	25.8	16	612	0.66	12	**696**	0.65
	L6	202	175	-	406	(B.5)	1970	682	-	25.8	16	612	0.65	12	**799**	0.73
	L7	204	177	-	201	(B.5)	1970	785	-	19.0	16	586	0.64	12	**478**	0.54
	L8	205	174	-	899	(B.5)	2470	686	-	19.0	16	576	1.16	16	**1111**	0.54

	L9	203	172	-	897	(B.5)	2470	687	-	19.0	16	576	1.17	16	**1107**	0.55
	L10	204	173	-	901	(B.5)	2470	685	-	19.0	16	576	1.16	16	**1079**	0.53
[Gua09]	PG-1	250	210	260	-	(B.2)	3000	470	1250	27.6	16	573	1.50	20	**1023**	0.49
	PG-3	500	456	520	-	(B.3)	6000	960	2320	32.4	16	520	0.33	16	**2153**	0.85
	PG-6	125	96	130	-	(B.3)	1500	235	625	34.7	16	526	1.50	14	**238**	0.53
	PG-7	125	100	130	-	(B.3)	1500	235	625	34.7	16	550	0.75	10	**241**	0.89
[Gui10b]	PG11	250	208	260	-	(B.2)	3000	470	1250	31.5	16	570	0.75	16	**763**	0.66
	PG19	250	206	260	-	(B.2)	3000	470	1250	46.2	16	510	0.78	16	**860**	0.80
	PG20	250	201	260	-	(B.2)	3000	470	1250	51.7	16	551	1.56	20	**1094**	0.53
	PG23	250	199	260	-	(B.2)	3000	470	1250	41.0	32	510	0.81	16	**839**	0.81
	PG24	250	194	260	-	(B.2)	3000	470	1250	39.8	32	551	1.62	20	**1102**	0.57
	PG25	250	203	260	-	(B.2)	3000	470	1250	45.0	8	510	0.79	16	**935**	0.89
	PG26	250	204	260	-	(B.2)	3000	470	1250	41.0	8	551	1.54	20	**1175**	0.57
	PG27	250	200	260	-	(B.2)	3000	470	1250	44.9	16	510	0.80	16	**900**	0.87
	PG28	250	202	260	-	(B.2)	3000	470	1250	43.3	16	551	1.56	20	**1098**	0.54
	PG29	250	203	260	-	(B.2)	3000	470	1250	39.7	32	510	0.79	16	**854**	0.81
	PG30	250	201	260	-	(B.2)	3000	470	1250	36.6	32	551	1.56	20	**1049**	0.52
[Tas11]	PT22	250	214	260	-	(B.2)	3000	470	1250	67.0	16	552	0.84	16	**989**	0.73
	PT31	250	210	260	-	(B.2)	3000	470	1250	66.3	16	540	1.48	20	**1433**	0.66
[Cle12]	PF21	409	350	220	-	(B.2)	3000	470	1250	31.6	16	541	0.75	20	**1838**	0.58
	PF22	405	346	220	-	(B.2)	3000	470	1250	33.9	16	520	1.52	26	**2007**	0.36
	PF23	405	350	440	-	(B.2)	3000	470	1250	32.3	16	541	0.75	20	**2685**	0.85
[Lip12]	PL1	250	193	130	-	(B.2)	3000	535	1315	36.2	16	583	1.63	20	**682**	0.37
	PL3	250	197	520	-	(B.2)	3000	340	1120	36.5	16	583	1.59	20	**1324**	0.55
	PL4	320	267	340	-	(B.2)	3000	430	1210	30.5	16	531	1.58	26	**1625**	0.45
	PL5	400	353	440	-	(B.2)	3000	380	1160	31.9	16	580	1.50	26	**2491**	0.35
[Ein16a]	PE10	250	210	-	83	(B.2)	3000	559	1339	40.4	16	538	0.77	16	**530**	0.51
	PE11	250	215	-	166	(B.2)	3000	517	1297	37.5	16	538	0.75	16	**712**	0.64
	PE9	250	218	-	330	(B.2)	3000	435	1215	44.1	16	538	0.74	16	**935**	0.74
	PE12	250	212	-	660	(B.2)	3000	270	1050	37.6	16	538	0.76	16	**1206**	0.80
	PE6	250	215	-	83	(B.2)	3000	559	1339	38.4	16	542	1.46	20	**656**	0.33
	PE7	250	213	-	166	(B.2)	3000	517	1297	42.5	16	542	1.47	20	**871**	0.42
	PE8	250	214	-	330	(B.2)	3000	435	1215	42.0	16	542	1.47	20	**1091**	0.48
	PE5	250	210	-	660	(B.2)	3000	270	1050	36.7	16	542	1.50	20	**1476**	0.54
	PE4	250	197	260	-	(B.2)	1700	100	600	35.1	16	517	1.59	20	**985**	0.38
	PV1	250	210	260	-	(B.2)	3000	470	1250	31.1	16	709	1.50	20	**978**	0.38
	PE3	250	204	260	-	(B.2)	3900	470	1700	34.2	16	517	1.54	20	**961**	0.48

Appendix E Database of punching tests

Table E.2 Main parameters of the specimens, predicted contribution of dowel action to the punching strenght and comparison of the experimenal capacities to the predictions of the proposed model, CSCT, Model Code 2010 (LoA II) and Eurocode 2

Series	Specimen	$(r_q-r_c)/d$	f_c	d	r_c/d	ρ	$V_{R,dow}/V_{R,pred}$	$V_{R,test}/V_{R,pred}$					
								proposed model	constant α and θ_p	constant σ_s	CSCT	MC2010 (LoA II)	EC2
			Mpa	mm		%							
[Els56]	A-1a	6.0	14.1	118	1.37	1.15	0%	0.98	0.97	0.97	0.99	1.19	1.13
	A-1b	6.0	25.3	118	1.37	1.15	0%	0.92	0.91	0.91	0.99	1.16	1.12
	A-1c	6.0	29.1	118	1.37	1.15	0%	0.88	0.88	0.88	0.93	1.08	1.04
	A-1d	6.0	36.9	118	1.37	1.15	0%	0.86	0.86	0.86	0.86	0.99	0.95
	A-1e	6.0	20.3	118	1.37	1.15	0%	0.99	0.97	0.97	1.04	1.22	1.17
	A-2a	6.2	13.7	114	1.42	2.47	4%	0.92	0.92	1.04	0.99	1.16	1.10
	A-2b	6.2	19.5	114	1.42	2.47	3%	0.94	0.94	1.00	1.02	1.19	1.17
	A-2c	6.2	37.5	114	1.42	2.47	0%	0.82	0.82	0.82	0.91	1.07	1.10
	A-7b	6.2	27.9	114	1.42	2.47	1%	1.03	1.03	1.05	1.12	1.31	1.33
	A-3a	6.2	12.8	114	1.42	3.70	6%	0.92	0.91	1.25	1.04	1.23	1.20
	A-3b	6.2	22.6	114	1.42	3.70	5%	0.88	0.87	0.99	1.01	1.15	1.24
	A-3c	6.2	26.6	114	1.42	3.70	5%	0.97	0.97	1.07	1.13	1.28	1.41
	A-3d	6.2	34.6	114	1.42	3.70	4%	0.87	0.88	0.93	1.04	1.17	1.33
	A-5	6.1	27.8	114	1.99	2.47	0%	0.91	0.91	0.91	0.98	1.15	1.19
	A-6	6.1	25.1	114	1.99	3.70	5%	0.78	0.79	0.89	0.89	1.01	1.15
	B-9	6.2	43.9	114	1.42	2.00	0%	0.87	0.86	0.86	0.93	1.09	1.13
	B-11	6.2	13.5	114	1.42	3.00	7%	0.85	0.85	1.20	0.92	1.09	1.09
	B-14	6.3	50.6	114	1.42	3.00	0%	0.83	0.83	0.83	0.91	1.06	1.23
[Kin60]	IA15a-5	7.0	25.5	117	0.64	0.79	0%	1.07	1.07	1.07	1.03	1.20	1.15
	IA15a-6	6.9	24.9	118	0.64	0.78	0%	1.16	1.16	1.16	1.10	1.29	1.23
	IA15b-9	7.0	24.7	117	0.64	1.21	0%	1.03	1.03	1.03	0.99	1.15	1.08
	IA15b-10	7.0	24.7	117	0.64	1.21	0%	1.03	1.03	1.03	0.99	1.15	1.08
	IA15c-11	6.8	30.5	121	0.62	1.02	0%	1.14	1.14	1.14	1.10	1.28	1.22
	IA15c-12	6.7	29.4	122	0.61	1.01	0%	1.14	1.15	1.15	1.10	1.28	1.22
	IA30a-24	6.1	25.1	128	1.17	0.96	0%	1.08	1.07	1.07	1.07	1.24	1.27
	IA30a-25	6.3	23.8	124	1.21	0.99	0%	1.08	1.07	1.07	1.08	1.25	1.27
	IA30b-28	6.6	24.6	119	1.26	1.55	2%	0.88	0.88	0.90	0.89	1.04	1.05
	IA30b-29	6.6	24.6	119	1.26	1.55	3%	0.99	0.99	1.02	1.01	1.18	1.19
	IA30c-30	6.5	28.6	120	1.25	1.48	0%	1.10	1.10	1.10	1.12	1.31	1.33
	IA30c-31	6.6	28.6	119	1.26	1.50	0%	1.22	1.22	1.22	1.24	1.45	1.47
[Moe61]	S2-60	6.2	22.1	114	1.42	1.53	1%	0.91	0.91	0.92	0.89	1.06	1.10
	S1-70	6.2	24.5	114	1.42	1.06	0%	1.06	1.06	1.06	1.02	1.23	1.32
	S5-60	6.4	22.2	114	1.13	1.06	0%	1.09	1.09	1.09	1.07	1.26	1.30
	S5-70	6.4	23.0	114	1.13	1.06	0%	1.19	1.19	1.19	1.13	1.35	1.42
	R2	6.7	26.5	114	0.85	1.38	0%	0.99	0.98	0.98	1.13	1.35	1.12
	M1A	5.9	20.8	114	1.70	1.50	5%	0.99	0.99	1.08	0.99	1.20	1.26
[Tol88]	S2.1	5.6	23.9	200	0.63	0.80	9%	0.96	0.97	1.08	0.88	1.04	0.95
	S2.2	5.7	22.6	199	0.63	0.80	9%	0.98	0.99	1.12	0.91	1.06	0.97
	S2.3	5.6	25.0	200	0.63	0.34	0%	1.09	1.09	1.09	0.94	1.14	1.01
	S2.4	5.7	23.8	197	0.63	0.35	0%	1.02	1.02	1.02	0.88	1.07	0.95
	S1.1	5.6	28.2	100	0.63	0.80	8%	1.05	1.06	1.16	1.11	1.30	1.29
	S1.2	5.7	22.6	99	0.63	0.81	9%	1.04	1.05	1.17	1.10	1.29	1.26
	S1.3	5.8	26.3	98	0.64	0.35	0%	1.09	1.08	1.08	1.03	1.24	1.21
	S1.4	5.7	24.8	99	0.63	0.34	0%	1.13	1.13	1.13	1.07	1.29	1.25

[Tom93]	ND65-1-1	4.0	64.3	275	0.46	1.50	7%	1.29	1.28	1.29	1.15	1.39	1.15
	ND65-2-1	4.9	70.2	200	0.48	1.70	8%	1.12	1.12	1.16	1.14	1.37	1.09
	ND95-1-1	4.0	83.7	275	0.46	1.50	7%	1.28	1.29	1.25	1.14	1.40	1.15
	ND95-1-3	4.0	89.9	275	0.46	2.50	7%	1.14	1.15	1.09	1.08	1.23	1.09
	ND95-2-1	4.9	88.2	200	0.48	1.70	7%	0.94	0.95	0.96	0.96	1.16	0.92
	ND95-2-1D	4.9	86.7	200	0.48	1.70	7%	1.12	1.12	1.14	1.14	1.38	1.10
	ND95-2-3	5.0	89.5	200	0.48	2.60	8%	1.08	1.09	1.08	1.17	1.33	1.15
	ND95-2-3D	5.0	80.3	200	0.48	2.60	8%	0.97	0.97	0.98	1.05	1.20	1.03
	ND95-2-3D+	5.0	98.0	200	0.48	2.60	8%	1.05	1.06	1.04	1.12	1.29	1.11
	ND95-3-1	5.4	85.1	88	0.72	1.80	5%	0.97	0.97	1.01	1.07	1.36	1.29
	ND115-1-1	4.0	112.0	275	0.46	1.50	7%	1.28	1.32	1.22	1.10	1.39	1.14
	ND115-2-1	4.9	119.0	200	0.48	1.70	7%	1.10	1.12	1.11	1.08	1.34	1.06
	ND115-2-3	5.0	108.1	200	0.48	2.60	8%	1.09	1.10	1.07	1.15	1.33	1.15
[Hal96]	HSC 0	5.8	89.1	200	0.63	0.80	0%	0.97	0.97	0.97	0.97	1.20	0.98
	HSC 1	5.8	91.3	200	0.63	0.80	0%	1.03	1.03	1.03	1.02	1.26	1.03
	HSC 2	5.9	85.7	194	0.64	0.82	0%	0.94	0.94	0.94	0.95	1.17	0.96
	HSC 4	5.8	91.6	200	0.63	1.19	3%	0.87	0.87	0.90	0.92	1.10	0.92
	N/HSC 8	5.8	94.9	198	0.63	0.80	0%	0.95	0.95	0.95	0.95	1.17	0.96
[Ram96]	1	6.3	78.4	98	0.77	0.58	0%	0.90	0.89	0.89	0.92	1.28	1.04
	2	6.3	49.9	98	0.77	0.58	0%	0.96	0.93	0.93	1.00	1.37	1.15
	3	6.2	23.9	98	0.77	0.58	0%	1.01	1.00	1.00	1.02	1.36	1.17
	4	6.3	52.2	98	0.77	0.58	0%	1.04	1.02	1.02	1.09	1.49	1.24
	6	6.3	90.5	98	0.77	0.58	0%	0.90	0.90	0.90	0.91	1.28	1.04
	12	6.3	53.6	98	0.77	1.28	0%	1.02	1.02	1.02	1.16	1.47	1.30
	13	6.3	38.7	98	0.77	1.28	5%	1.05	1.05	1.10	1.22	1.53	1.35
	14	6.3	54.0	98	0.77	1.28	0%	1.09	1.09	1.09	1.23	1.56	1.38
	16	6.3	87.4	98	0.77	1.28	0%	0.99	1.00	1.00	1.08	1.42	1.25
	21	6.3	37.2	98	0.77	1.28	8%	0.99	0.99	1.08	1.12	1.37	1.31
	22	6.4	74.8	98	0.77	1.28	3%	1.11	1.11	1.14	1.19	1.51	1.47
	23	6.2	50.1	100	0.75	0.87	0%	1.24	1.24	1.24	1.23	1.61	1.56
[Sis97]	L1	3.7	25.8	172	0.59	0.46	7%	1.26	1.25	1.34	1.08	1.45	1.27
	L2	3.6	25.8	176	0.57	0.45	7%	1.32	1.31	1.40	1.12	1.50	1.32
	L3	3.7	25.8	173	0.58	0.45	7%	1.34	1.32	1.41	1.14	1.53	1.34
	L4	3.7	25.8	170	1.18	0.67	7%	1.10	1.09	1.17	1.05	1.40	1.28
	L5	3.7	25.8	172	1.16	0.66	7%	1.12	1.10	1.18	1.06	1.41	1.28
	L6	3.6	25.8	175	1.16	0.65	7%	1.25	1.23	1.33	1.18	1.57	1.43
	L7	4.2	19.0	177	0.57	0.64	7%	1.17	1.17	1.29	1.06	1.33	1.14
	L8	3.6	19.0	174	2.58	1.16	9%	1.11	1.08	1.39	1.10	1.50	1.26
	L9	3.6	19.0	172	2.61	1.17	9%	1.11	1.09	1.40	1.12	1.52	1.28
	L10	3.6	19.0	173	2.60	1.16	9%	1.08	1.05	1.36	1.08	1.47	1.23
[Gua09]	PG-1	6.4	27.6	210	0.79	1.50	9%	1.07	1.07	1.22	1.18	1.33	1.08
	PG-3	5.7	32.4	456	0.73	0.33	0%	1.10	1.10	1.10	1.02	1.38	0.92
	PG-6	7.1	34.7	96	0.86	1.50	0%	0.86	0.87	0.87	0.98	1.12	1.07
	PG-7	6.8	34.7	100	0.83	0.75	0%	1.04	1.04	1.04	1.13	1.33	1.27
[Gui10b]	PG11	6.4	31.5	208	0.80	0.75	2%	0.98	0.98	1.00	1.01	1.23	0.98
	PG19	6.5	46.2	206	0.80	0.78	0%	0.95	0.95	0.95	1.03	1.25	0.97
	PG20	6.7	51.7	201	0.82	1.56	6%	0.89	0.89	0.94	1.06	1.20	0.98
	PG23	6.7	41.0	199	0.83	0.81	0%	1.00	1.00	1.00	0.98	1.17	1.03
	PG24	6.9	39.8	194	0.85	1.62	7%	1.05	1.04	1.13	1.11	1.26	1.13
	PG25	6.6	45.0	203	0.82	0.79	0%	1.06	1.06	1.06	1.23	1.53	1.09

	PG26	6.6	41.0	204	0.81	1.54	7%	1.05	1.05	1.13	1.32	1.48	1.12
	PG27	6.7	44.9	200	0.83	0.80	0%	1.03	1.03	1.03	1.13	1.38	1.07
	PG28	6.6	43.3	202	0.82	1.56	7%	0.96	0.96	1.03	1.13	1.27	1.04
	PG29	6.6	39.7	203	0.82	0.79	0%	1.02	1.02	1.02	0.99	1.18	1.04
	PG30	6.7	36.6	201	0.82	1.56	7%	1.00	1.00	1.09	1.04	1.18	1.06
[Tas11]	PT22	6.3	67.0	214	0.77	0.84	0%	0.89	0.89	0.89	0.94	1.16	0.91
	PT31	6.4	66.3	210	0.79	1.48	5%	1.04	1.04	1.08	1.19	1.38	1.13
[Cle12]	PF21	3.9	31.6	350	0.40	0.75	7%	1.31	1.31	1.43	1.13	1.30	1.10
	PF22	3.9	33.9	346	0.40	1.52	8%	1.15	1.15	1.33	1.05	1.12	0.94
	PF23	3.5	32.3	350	0.80	0.75	7%	1.45	1.44	1.54	1.29	1.53	1.36
[Lip12]	PL1	7.4	36.2	193	0.43	1.63	9%	0.90	0.91	1.04	1.04	1.14	0.91
	PL3	6.0	36.5	197	1.68	1.59	8%	0.92	0.92	1.04	1.09	1.26	1.06
	PL4	4.8	30.5	267	0.81	1.58	8%	1.08	1.08	1.23	1.12	1.23	1.06
	PL5	3.5	31.9	353	0.79	1.50	8%	1.10	1.10	1.28	1.00	1.08	0.99
[Ein16a]	PE10	7.0	40.4	210	0.20	0.77	6%	0.98	1.00	1.07	0.92	1.11	1.19
	PE11	6.6	37.5	215	0.39	0.75	4%	1.08	1.09	1.13	1.05	1.28	0.96
	PE9	6.1	44.1	218	0.76	0.74	0%	1.00	1.00	1.00	1.04	1.28	1.01
	PE12	5.5	37.6	212	1.56	0.76	0%	1.02	1.02	1.02	1.10	1.39	1.11
	PE6	6.8	38.4	215	0.19	1.46	8%	0.96	0.97	1.15	0.99	1.10	1.50
	PE7	6.7	42.5	213	0.39	1.47	7%	0.98	0.99	1.09	1.07	1.20	0.93
	PE8	6.3	42.0	214	0.77	1.47	6%	0.93	0.93	1.00	1.05	1.19	0.98
	PE5	5.6	36.7	210	1.57	1.50	8%	0.98	0.98	1.08	1.12	1.31	1.10
	PE4	3.0	35.1	197	0.84	1.59	8%	1.00	0.98	1.07	0.98	1.12	1.03
	PV1	6.4	31.1	210	0.79	1.50	11%	0.94	0.94	1.13	1.08	1.20	0.99
	PE3	8.6	34.2	204	0.81	1.54	6%	0.97	0.96	1.02	1.12	1.29	0.97

Curriculum Vitae

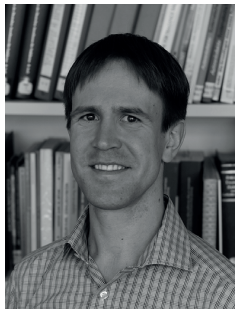

NAME	**Einpaul**
FIRST NAME	**Jürgen**
DATE OF BIRTH	11 May 1983
NATIONALITY	Estonian
E-MAIL	jyrgen.einpaul@gmail.com

EDUCATION

- Doctoral candidate in Civil Engineering, Ecole Polytechnique Fédérale de Lausanne **01.2011 – 03.2016**
  thesis "Punching strength of continuous flat slabs"
- MSc in Civil and Building Engineering, Tallinn University of Technology **09.2002 – 06.2010**
  thesis "Structural analysis of columns in a multi-storey reinforced concrete sway frame"

EMPLOYMENT HISTORY

- EPFL, Lausanne, Switzerland, doctoral assitant **01.2011 – 02.2016**
  - experimental and analytical research on punching of flat slabs
  - teaching assistantship for courses "Structures", "Concrete structures", "Advanced concrete structures", "Concrete bridges" and several semester and master projects
- EstKONSULT OÜ, Tallinn, Estonia, structural engineer **11.2007 – 12.2010**
  - design of cast-in-place and prefabricated reinforced concrete buildings
  - management of design projects
- Loodesystem OÜ, Tallinn, Estonia, structural engineer **06.2006 – 11.2007**
  - design of prefabricated cold-formed steel frame buildings and façade panels

AWARDS

- Estonian Concrete Association, award for the best Master's thesis on concrete in 2010

JOURNAL PUBLICATIONS

- Einpaul J., Fernández Ruiz M., Muttoni A. "Measurements of internal cracking in punching test slabs without shear reinforcement," *Magazine of Concrete Research*, submitted for publication
- Einpaul J., Ospina C. E., Fernández Ruiz M., Muttoni A. "Punching shear capacity of continuous slabs," *ACI Structural Journal*, accepted for publication
- Einpaul J., Brantschen F., Fernández Ruiz M., Muttoni A. "Performance of punching shear reinforcement under gravity loading: Influence of type and detailing," *ACI Structural Journal*, accepted for publication
- Einpaul J., Bujnak J., Fernández Ruiz M., Muttoni A. "Study on the influence of column size and slab slenderness on punching strength," *ACI Structural Journal*, Vol. 113, No. 1, 2016, pp. 135–145
- Burdet O., Einpaul J., Muttoni A. "Experimental investigation of soil-structure interaction for transition slabs of integral bridges," *Structural Concrete*, Vol. 16, No. 4, 2015, pp. 470–479
- Einpaul J., Fernández Ruiz M., Muttoni A. "Influence of moment redistribution and compressive membrane action on punching strength of flat slabs," *Engineering Structures*, Vol. 86, 2015, pp. 43–57
- V. Faria D. M., Einpaul J., P. Ramos A. M., Fernández Ruiz M., Muttoni A. "On the efficiency of flat slabs strengthening against punching using externally bonded fibre reinforced polymers," *Construction and Building Materials*, Vol. 73, 2014, pp. 366–377

LANGUAGES

- **Estonian:** mother tongue; **English:** fluent; **French:** intermediate; **Russian:** intermediate; **German:** beginner